

# Development of an Acoustic Emission Waveguide-based System for Monitoring of Rock Slope Deformation Mechanisms

by

*Daniela Codeglia*

A Doctoral Thesis

Submitted in partial fulfilment of the requirements for the award of  
Doctor of Philosophy of Loughborough University

September 2017

© by Daniela Codeglia 2017

© 2017 Daniela Codeglia

**in** [danielacodeglia](#)  
**✈** [@dcodeglia](#)  
**🌐** [researchgate.net/profile/daniela\\_codeglia](#)

**↓** Download available from [The Loughborough University Repository](#)



This work is made available according to the conditions of the Creative Commons Attribution-NonCommercial-NoDerivatives 4.0 International License



# Abstract

Hundreds of thousands of landslides occur every year around the world impacting on people's lives. Monitoring techniques able to foresee imminent collapse and provide a warning in time useful for action to be taken are essential for risk reduction and disaster prevention.

Acoustic emission (AE) is generated in soil and rock materials by rearrangement of particles during displacement or increasing damage in the microstructure preceding a collapse; therefore AE is appropriate for estimation of slope deformation.

To overcome the high attenuation that characterise geological materials and thus to be able to monitor AE activity, a system called Slope ALARMS that makes use of a waveguide to transmit AE waves from a deforming zone to a piezoelectric transducer was developed. The system quantifies acoustic activity as Ring Down Count (RDC) rates. In soil applications RDC rates have been correlated with the rate of deformation, however, the application to rock slopes poses new challenges over the significance of the measured AE trends, requiring new interpretation strategies.

In order to develop new approaches to interpret acoustic emission rates measured within rock slopes, the system was installed at two trial sites in Italy and Austria. RDC rates from these sites, which have been measured over 6 and 2.5 years respectively, are analysed and clear and recurring trends were identified.

The comparison of AE trends with response from a series of traditional instruments available at the sites allowed correlation with changes in external slope loading and internal stress changes. AE signatures from the limestone slope at the Italian site have been identified as generated in response to variations in the ground-water level and snow loading. At the conglomerate slope in Austria, AE signatures include the detachment of small boulders from the slope surface caused by the succession of freeze-thaw cycles during winter time.

Consideration was also given to laboratory testing of specific system elements and field experiments. A framework towards strategies to interpret measured acoustic emission trends is provided for the use of the system within rock slopes.

**Keywords** Acoustic Emission (AE) · Landslides · Monitoring system · Waveguide · Rock slope · Rock mass stability · Early warning · Field monitoring · Instrumentation

# Acknowledgement

The development of the Slope ALARMS system used in the field studies reported in this work was funded by the UK Engineering and Physical Sciences Research Council (EPSRC Grant ref. EP/H007261/1).

Installation of instruments at Passo della Morte, Italy, was funded by the Research Institute for Geo-Hydrological Protection of the Italian National Research Council (CNR–IRPI). The Grossreifling, Austria, field trial was funded by the VIF 2011 program of the Austrian Research Promotion Agency and the Austrian Railway OeBB. Particular thanks are due to Reinhard Hendricks and Dr. Thomas Meisel from INGLAS GmbH for their collaboration on the Grossreifling SART project and their help on site.

I would like to express my gratitude to my supervisors Prof. Neil Dixon and Dr. Gary Fowmes for their guidance. Their knowledge and experience have been an invaluable resource and their enthusiasm and support have greatly helped me during the challenging times.

Very heartfelt thanks to Dr. Gianluca Marcato from the CNR–IRPI for supervising the work at Passo della Morte and, in particular, for constantly supporting me throughout these years.

I would like also to thank Dr. Alister Smith for his help getting my head around the Slope ALARMS sensors during the early stages of this project and for his help on site.

I will always remember the many colleagues and friends I met in “The Hub”; their camaraderie, the useful (and not-so-useful) discussions over lunch (or coffee breaks), their help and the many things I learnt from them. It has been a pleasure meeting you all.

Finally, but most importantly, an enormous thank you to my friends, my family and to Jamie. Words cannot describe how grateful I am for your patience, your support, for listening and encouraging me. I could not have completed this work without you!

# Publications

Parts of this PhD study have been published in the following peer-reviewed papers:

**Codeglia, D.**, N. Dixon, G. J. Fowmes, and G. Marcato (2017). “Analysis of Acoustic Emission patterns for monitoring of rock slope deformation mechanisms”. In: *Engineering Geology* 219, pp. 21–31. doi: [10.1016/j.enggeo.2016.11.021](https://doi.org/10.1016/j.enggeo.2016.11.021)

Smith, A., N. Dixon, **D. Codeglia**, and G. J. Fowmes (2016). “An acoustic emission slope displacement rate sensor: Comparisons with established instrumentation”. In: *Geotechnical News* December, BiTech Publishers, pp. 22–25. url: [dspace.lboro.ac.uk/2134/23549](https://dspace.lboro.ac.uk/2134/23549)

**Codeglia, D.**, N. Dixon, G. J. Fowmes, and G. Marcato (2015). “Strategies for rock slope failure early warning using acoustic emission monitoring”. In: *IOP Conference Series: Earth and Environmental Science* 26, p. 012028. doi: [10.1088/1755-1315/26/1/012028](https://doi.org/10.1088/1755-1315/26/1/012028)

Dixon, N., **D. Codeglia**, A. Smith, G. J. Fowmes, and P. Meldrum (2015). “An acoustic emission slope displacement rate sensor — case studies”. In: *Proceedings of the Ninth International Symposium on Field Measurements in Geomechanics*. Ed. by P. Digh. Perth, Australia: Australian Centre for Geomechanics, pp. 743–756. url: [dspace.lboro.ac.uk/2134/19021](https://dspace.lboro.ac.uk/2134/19021)

# Contents

<b>Abstract</b>	<b>ii</b>
<b>Acknowledgement</b>	<b>iii</b>
<b>Publications</b>	<b>iv</b>
<b>Abbreviations and conventions</b>	<b>xviii</b>
<b>1 Introduction</b>	<b>1</b>
1.1 Research topic and justification . . . . .	1
1.2 Aim and objectives . . . . .	4
1.3 Thesis structure . . . . .	4
<b>2 Literature review</b>	<b>6</b>
2.1 Landslide classification and stability of rock masses . . . . .	7
2.1.1 Shear strength of jointed rock masses . . . . .	12
2.1.1.1 Stick-slip behaviour . . . . .	12
2.1.2 Shear strength of isotropic rock masses . . . . .	15
2.1.3 Landslide triggers . . . . .	15
2.2 Landslide monitoring and early warning . . . . .	16
2.3 Acoustic emission (AE) fundamentals . . . . .	21
2.3.1 AE in deforming geological materials . . . . .	23
2.3.2 AE properties . . . . .	24
2.4 AE monitoring . . . . .	29
2.4.1 Waveguide . . . . .	30
2.4.2 Piezoelectric transducer . . . . .	36
2.4.3 Signal conditioning . . . . .	37
2.4.3.1 Pre-amplifier . . . . .	37

2.4.3.2	Band-pass filter . . . . .	38
2.4.3.3	Analog-to-digital converter . . . . .	39
2.4.3.4	Comparator . . . . .	40
2.4.4	AE monitoring systems in literature . . . . .	40
2.5	Summary . . . . .	46
<b>3</b>	<b>Methodology</b>	<b>49</b>
3.1	Research methods . . . . .	50
3.2	Measurement system . . . . .	52
3.2.1	The Slope ALARMS system . . . . .	55
3.2.2	System modifications . . . . .	58
3.2.2.1	Grouted waveguides . . . . .	59
3.2.2.2	Waveguides . . . . .	60
3.2.2.3	Sensor node versions MK1 and MK2 . . . . .	62
3.2.2.4	Monitoring periods and downsampling . . . . .	64
3.2.3	Limitations of the Slope ALARMS . . . . .	65
3.3	Trial sites . . . . .	66
3.3.1	Passo della Morte (PdM) . . . . .	67
3.3.2	Grossreifling (SART) . . . . .	72
3.4	Laboratory testing of system elements and field experiments . . . . .	76
3.4.1	Controlled AE generator . . . . .	77
3.4.2	Laboratory testing . . . . .	78
3.4.2.1	Comparison of versions MK1 and MK2 (Test A) . . . . .	78
3.4.2.2	Transducer mounting on threaded waveguide (Test B) . . . . .	79
3.4.2.3	Attenuation in threaded waveguides (Test C) . . . . .	81
3.4.3	Field experiments . . . . .	83
3.4.3.1	Attenuation along waveguides on site (Test D) . . . . .	84
3.4.3.2	Extent of monitoring (Test E) . . . . .	86
3.4.3.3	External sources of AE (Test F) . . . . .	87
3.5	Summary . . . . .	88
<b>4</b>	<b>Laboratory testing of system elements and field experiments</b>	<b>90</b>
4.1	Laboratory testing . . . . .	91
4.1.1	Comparison of versions MK1 and MK2 (Test A) . . . . .	91

4.1.1.1	Results . . . . .	92
4.1.2	Transducer mounting on threaded waveguide (Test B) . . . .	95
4.1.2.1	Results . . . . .	96
4.1.3	Attenuation in threaded waveguides (Test C) . . . . .	97
4.1.3.1	Results . . . . .	98
4.2	Field experiments . . . . .	102
4.2.1	Attenuation along waveguides on site (Test D) . . . . .	102
4.2.1.1	Results . . . . .	103
4.2.2	Monitoring extent (Test E) . . . . .	106
4.2.2.1	Results . . . . .	106
4.2.3	External sources of AE (Test F) . . . . .	107
4.2.3.1	Results . . . . .	108
4.3	Summary . . . . .	111
<b>5</b>	<b>The Passo della Morte site</b>	<b>114</b>
5.1	Site description . . . . .	114
5.1.1	Geologic overview . . . . .	116
5.1.2	Rock mass description . . . . .	118
5.1.3	Hydrogeology . . . . .	121
5.1.4	Conceptual failure model . . . . .	124
5.2	Measurement system . . . . .	126
5.2.1	Acoustic Emission . . . . .	126
5.2.2	Other available instruments . . . . .	129
5.2.2.1	Temperature probe . . . . .	130
5.2.2.2	Rain gauge . . . . .	130
5.2.2.3	Snow gauge . . . . .	130
5.2.2.4	Crackmeters . . . . .	131
5.2.2.5	Piezometer . . . . .	131
5.3	Analysis of field monitoring results . . . . .	132
5.3.1	Acoustic Emission . . . . .	133
5.3.1.1	Daily and weekly trends . . . . .	138
5.3.1.2	Recurring patterns . . . . .	141
5.3.2	Variation of groundwater level . . . . .	143
5.3.3	Snowfall . . . . .	152

5.3.4	Displacement on discontinuities . . . . .	154
5.3.5	Earthquakes . . . . .	161
5.4	Summary . . . . .	167
<b>6</b>	<b>The Grossreifling site</b>	<b>169</b>
6.1	Site description . . . . .	170
6.1.1	Geologic overview . . . . .	172
6.1.2	Ground model and material characterisation . . . . .	173
6.1.3	Expected failure mechanisms . . . . .	174
6.2	Measurement system . . . . .	174
6.2.1	Acoustic Emission . . . . .	174
6.2.2	Detection fence . . . . .	178
6.2.3	Weather station . . . . .	182
6.3	Analysis of field monitoring results . . . . .	183
6.3.1	Solar exposure . . . . .	186
6.3.2	Water seepage . . . . .	187
6.3.3	High RDC/h peaks . . . . .	192
6.3.4	Freeze-thaw weathering . . . . .	193
6.4	Summary . . . . .	202
<b>7</b>	<b>Framework</b>	<b>204</b>
7.1	Interpretation of AE trends . . . . .	204
7.2	Recommendations for future work . . . . .	208
<b>8</b>	<b>Conclusions</b>	<b>210</b>
<b>Appendix A Instruments specifications</b>		<b>224</b>
<b>Appendix B Additional graphs</b>		<b>228</b>
<b>Appendix C Additional tables</b>		<b>230</b>
<b>Appendix D Coding</b>		<b>239</b>

# List of Tables

2.1	A summary of Varnes's (1978) classification system . . . . .	7
2.2	Instruments typically used in rock slope stability monitoring . . . . .	20
3.1	Specifications of smooth and threaded waveguide types used in this work and and type of cement used to grout the waveguides . . .	61
3.2	Technical specifications of piezoelectric transducers. R3 $\alpha$ is used in the Slope ALARMS MK2 version while R3 $\alpha$ was used in the previous MK1 version of the system . . . . .	64
3.3	Example of downsampling RDC/15min to RDC/hour . . . . .	65
3.4	Specifications of instruments installed at Passo della Morte site . . .	70
3.5	Specifications of AE monitoring installation at Passo della Morte site	71
3.6	Parameters and specifications of Grossreifling site installation . . . .	75
3.7	Range of instruments available for comparison at SART . . . . .	75
4.1	The five mounting configurations tested (B1 – B5). B0 represents the reference test conducted on a smooth waveguide. Figure 3.11 shows a diagram of the configurations . . . . .	96
4.2	Attenuation along waveguide obtained from Test C . . . . .	100
4.3	Attenuation along waveguide obtained by Smith (2015) . . . . .	101
5.1	Rock mass joint sets, after Codeglia (2011) . . . . .	120
5.2	Percentage of monitoring periods equal to 0 RDC/h for every sensor and each series . . . . .	135
5.3	Minimum local magnitude values for triggering of different landslide types . . . . .	162
5.4	Earthquakes . . . . .	165
5.5	Theoretical acceleration calculated for Passo della Morte as a consequence of earthquakes with local magnitude $M_L$ greater than 4.5 occurred in the last thirty years in the South-Eastern Alps. Modified after Zoppè (2015) . . . . .	166



6.1 Example of impact detected by sensor No.12. . . . . 180

6.2 Detection fence sensors . . . . . 181

# List of Figures

2.1	Representation of the influence of scale on the type of rock mass behaviour model . . . . .	11
2.2	Spring-block model illustrating the principle of stick-slip behaviour	14
2.3	Conceptual model of joint shear behaviour . . . . .	14
2.4	Characteristic AE event waveform with main parameters indicated	25
2.5	Attenuation versus frequency by material group . . . . .	29
2.6	Block diagram representing the major components of an AE monitoring system typically used in the field . . . . .	30
2.7	Longitudinal and shear waves. Modified after Construction and Design (2017) . . . . .	32
2.8	Rayleigh surface wave. Modified after Construction and Design (2017) . . . . .	32
2.9	Exaggerated schematic of Lamb wave modes. Left: asymmetric or flexural mode; Right: symmetric or extensional mode. After Marks et al. (2016) . . . . .	32
2.10	The concept of active waveguide in soil slopes . . . . .	34
2.11	The active waveguide proposed by Nakajima et al. (1995). A fibreglass-reinforced resin wave-generator is placed within a steel pipe . . . . .	35
2.12	The active waveguide proposed by Cheon et al. (2011) . . . . .	36
2.13	Principle of signal amplification with single amplifier . . . . .	38
2.14	Analog-to-digital conversion . . . . .	39
2.15	Monitoring system proposed by Amitrano et al. (2005) and example of results . . . . .	41
2.16	Underground waveguide array proposed by Hardy (1994) . . . . .	42
2.17	Waveguide monitoring system proposed by Shiotani et al. (2001b)	43
2.18	Criteria for evaluation of damage proposed by Cheon et al. (2011)	44

2.19 Parameters influencing the acoustic emission detected by the Slope ALARMS in soil slopes . . . . .	45
3.1 Methodological approach . . . . .	52
3.2 Simplified schematic of Slope ALARMS installed within a rock slope and installation at one of the sites . . . . .	56
3.3 Generalised concept of Ring Down Count . . . . .	58
3.4 32 mm outer diameter self-drilling threaded pipes . . . . .	61
3.5 Photograph of Passo della Morte (Italy) taken towards north-east, along the Tagliamento River valley. Modified after Codeglia et al., 2017 . . . . .	67
3.6 Schematic of the unstable limestone rock mass outcrop and monitoring system . . . . .	69
3.7 Grossreifling (Austria) site location: <b>(a)</b> schematic map of the site with waveguides and detection fence location, note the railway line at the base of the slope; <b>(b)</b> image of the conglomerate slope with location of the sensor nodes and projection of the steel bars . .	72
3.8 Rockfall occurred at the Grossreifling site landing on the rail track .	73
3.9 The controlled AE source generator developed by Smith (2015) . .	77
3.10 Test B set-up. The transducer and AE source were installed at a constant centre-to-centre distance of 0.2 m . . . . .	80
3.11 The five transducer mounting configurations considered in Test B .	81
3.12 Transducer mounting on flattened threads obtained by filing (B5) .	81
3.13 Schematic representing Test C set-up . . . . .	82
3.14 Test C. A threaded waveguide is positioned on a stand made of sponges, the transducer is placed on a flat surface and tied to the waveguide . . . . .	82
3.15 The 12 m waveguide employed in Test C . . . . .	83
3.16 10,000 RPM DC motor connected to the control box through a 50 m cable . . . . .	85
3.17 Test D. The small AE wave-generator being inserted in one of the waveguides at Passo della Morte . . . . .	85
3.18 Schematic of Test D. For each waveguide (AEWG1, AEWG2, AEWG3) the positions where the wave-generator was triggered are detailed. The schematic also shows at which distance from the end the waveguide enters the rock mass . . . . .	86

3.19	Sensor H108L cover. The locations where the rock was hit to perform Test E are indicated with a circle (E1,E2,E3). The waveguide (red dashed line) enters the rock mass at an angle to the left-hand side . . . . .	87
4.1	Results of Test A. Comparison of RDC responses given by the Slope ALARMS MK1 and MK2; <b>(a)</b> Test A1, 1 second burst of vibration; <b>(b)</b> Test A2, 10 seconds burst of vibration . . . . .	94
4.2	Results of Test B. RDC responses of five different mounting configurations (B1 to B5) compared to the response of a standard steel pipe (B0). 1 second burst of vibration to the left and 10 seconds to the right . . . . .	97
4.3	Results of Test C. The trendline is calculated on the average of the RDC results for each wave-generator position. Each 3 m rod length is identified by a dashed line . . . . .	99
4.4	Results of the test performed by Smith (2015) on smooth waveguides. RDC induced by 10 s vibration vs propagation distance. <b>(a)</b> loose couplings; <b>(b)</b> tight couplings. The values referring to the 0.1 voltage threshold test (light blue) are here not considered .	101
4.5	Percentage of signal loss after couplings: <b>(a)</b> for Test C; <b>(b)</b> . . . . .	102
4.6	Percentage of signal loss after couplings. After Smith (2015) . . . . .	102
4.7	Results of Test D. RDC vs distance from free end of waveguide. The black dotted line represents the location of the transducer along the waveguide and the grey dashed line represents the point where the waveguide enters the rock mass, both refer to the x-axis. <b>(a)</b> AEWG1; <b>(b)</b> AEWG2; <b>(c)</b> AEWG3 . . . . .	105
4.8	Results of Test E. Refer to Figure 3.19 for E1, E2, E3 locations. E1 is approximately 0.30 m from the grouted part of the waveguide, E2 about 0.60 m and E3 about 1.10 m . . . . .	107
4.9	Results of Test F1. The test consisted in pouring water from a watering can onto sensors covers at SART site . . . . .	109
4.10	Results of Test F2. <b>(a)</b> drumming onto sensors covers for 5 seconds (3 repetitions); <b>(b)</b> hitting the cover with the shank of a screwdriver (3 repetitions) . . . . .	110
4.11	Results of Test F3. Three masses of 80 kg, 60 kg and 10 kg were dropped 5 times each on the ground surrounding sensor VE10U . .	111
5.1	Passo della Morte (Italy) site location . . . . .	115

5.2	Bedrock geology and superficial deposits map of Passo della Morte. The unstable limestone outcrop is highlighted in yellow. The camera icon indicates the approximate position and orientation used to photograph the west rock mass face (e.g. Figure 5.4 and 5.9). A'-A'' indicates approximately the cross-section in Figure 5.3. Modified after Codeglia (2013) . . . . .	116
5.3	Indicative cross-section of Passo della Morte . . . . .	117
5.4	The limestone rock mass face photographed from the west. The structural elements described in the text are outlined: A is the contact between dolomite and limestone; B the sector characterised by tight bedding; C the sector with open bedding and marl infill; D the sector with shallower dip angle and E are small folds. The dolomite bedrock is coloured in light orange and the small faults are marked in red. The Rio Sccluses flows along A during rainfall events. Some openings in the Passo della Morte tunnel are visible . . . . .	119
5.5	Side tunnel, also referred to as opening on the side of Passo della Morte tunnel. The red arrow indicate the location of piezometer P22 (in this photo it was not yet installed) . . . . .	122
5.6	Typical yearly rainfall and piezometric level for the site. To note the variations of groundwater level which can be greater than 15 m	122
5.7	Location of sensors AEWG1 and AEWG2 within the PdM tunnel (yellow circles). The dashed line represents the projection of waveguide AEWG2; waveguide AEWG1 enters the rock mass approximately perpendicular to the photograph, which makes not possible to indicate the waveguide . . . . .	127
5.8	Plastic enclosure protecting AE equipment at Passo della Morte site placed in a niche formed within the road tunnel lining . . . . .	127
5.9	West rock mass face with projection of waveguides (dashed lines) and position of the Slope ALARMS sensors (stars, AEWG1,2,3) and locations of crackmeters (EXT4,5,6) . . . . .	129
5.10	Location of rain gauge and snow gauge with respect to Passo della Morte . . . . .	131
5.11	Schematic of the unstable limestone rock mass outcrop and monitoring system . . . . .	132
5.12	Example. (A) represents a population of data with 75% zero values; (B) represents the same data with zeroes removed to show distribution of data greater than zero . . . . .	134
5.13	Data distribution . . . . .	136

5.14	Number of hourly AE monitoring periods above zero <b>(a)</b> by hour of the day; <b>(b)</b> by day of the week, for each sensor. The y axis upper limit is set to the actual total number of monitoring periods (hours) existing per each hour of the day and day of the week, respectively, for the time interval considered (13/10/2014 20:00:00 to 20/06/2016 12:00:00) . . . . .	140
5.15	Type A, Type B and Type C acoustic emission patterns at Passo della Morte. Generally, Type A is in the order of hundreds RDC/h, Type B in the order of tens of thousands RDC/h and Type C in the order of hundreds of thousands RDC/h . . . . .	141
5.16	Groundwater level variation events analysed . . . . .	144
5.17	Event 1. <b>(a)</b> full graph (representing temperature, snowfall, AEWG1, AEWG2, AEWG3, rainfall and piezometric level) vs time; <b>(b)</b> acoustic emission (RDC/h) vs variation of groundwater level (m); <b>(c)</b> acoustic emission (RDC/h) vs rainfall (mm/h) . .	146
5.18	Acoustic emission (RDC/h) vs variation of groundwater level (m) graphs for: <b>(a)</b> Event 2; <b>(b)</b> Event 3; <b>(c)</b> Event 4; <b>(d)</b> Event 5; <b>(e)</b> Event 6 . . . . .	149
5.19	Acoustic emission (RDC/h) vs rainfall (mm/h) graphs for: <b>(a)</b> Event 2; <b>(b)</b> Event 3; <b>(c)</b> Event 4; <b>(d)</b> Event 5; <b>(e)</b> Event 6 . . . . .	150
5.20	Examples of AE rates (RDC/h) in response to snow load. The high count events last for short time. They are clustered around the times when the snowfall occurs and are clearly not correlated with piezometric level changes or rainfall events . . . . .	154
5.21	Crackmeters measurements. A, B C, D correspond to the events analysed in this Section . . . . .	155
5.22	Event A – EXT4 cumulative displacement 1 mm; EXT5 cumulative displacement 1.5 mm . . . . .	159
5.23	Event B – EXT4 displacement 3 mm; EXT5 displacement 2 mm . . .	159
5.24	Event C – EXT4 displacement 2 mm . . . . .	160
5.25	Event D – EXT4 displacement 0.8 mm main event; 0.2 mm minor event . . . . .	160
5.26	Extract of the Seismic Hazard Map of Italy . . . . .	161
5.27	Map showing the location of the earthquakes considered in the analysis. The numbers refer to Table 5.4 . . . . .	164
6.1	Map of the Grossreifling, Styria (Austria) area. The SART site (yellow star) is located about 1.0 km NW of Grossreifling. Weather data are collected at Mooslandl weather station (blue star), about 4.5 km SE of the SART site along the Enns River valley	171

6.2	Indicative SW–NE cross-section of the study slope with elements mentioned in the text and geological setting . . . . .	171
6.3	Geological map of Austria 1:50,000 – Nr. 100 Hieflau. The Grossreifling site is indicated with a yellow star . . . . .	173
6.4	The small cave formed by localised washout of conglomerate material; sensor H108L is indicated with a yellow star . . . . .	176
6.5	Grossreifling (Austria) site location: <b>(a)</b> schematic map of the site with waveguides and detection fence location, note the railway line at the base of the slope; <b>(b)</b> image of the conglomerate slope with location of the sensor nodes and projection of the steel bars . .	177
6.6	Schematic of the Detection Fence design. Modified after Hendricks et al. (2014) . . . . .	179
6.7	Schematic of the southernmost part of the detection fence below acoustic sensors H108L and H209R. The schematic includes the movement sensors locations, (P) = post, (SC) = support cable . . .	181
6.8	Comparison of rainfall data measured at Grossreifling and Mooslandl	183
6.9	Boxplots representing sensors H108L, H209R and VE10U AE data distribution. The lowest whisker represents the 1% mark and the highest whisker represents the 99% mark, thus outliers are the highest 1% of the data range. RDC/h = 0 is not considered . . . . .	184
6.10	Equidistant stereographic Sun Path chart at Grossreifling site coordinates. The diagram is superimposed to the study slope strike and dip direction (in red) . . . . .	186
6.11	Acoustic emission vs rainfall for the three sensors H108L, H209R and VE10U. The number of monitoring periods considered (same for each sensors) is 1896 one-hour monitoring periods . . . . .	188
6.12	<b>(a)</b> AE rates (RDC/h) in response to major rainfall events. The highest AE peaks recorded are a stronger response to the rainfall and could be generated with processes triggered by the rainfall; <b>(b)</b> graphs showing the relationship between rainfall rates (mm/h) and AE rates (RDC/h) for each waveguide. The time window considered is 17/05/2015 to 02/06/2015, cutting out the very high event shown in (a) occurred around 14/05/2015 to give emphasis to the rainfall–AE proportionality . . . . .	191
6.13	High RDC/h rates events. The spike shape is due to the one-monitoring period duration. Note that RDC/h ranges differ amongst the sensors and between event <b>(a)</b> and event <b>(b)</b> . . . . .	193
6.14	Hourly temperature and acoustic emission observations for 37 representative days . . . . .	195

6.15	Acoustic emission (RDC/h) versus Temperature (°C) graphs for the three sensors H108L, H209R and VE10U. Data represented are same as Figure 6.14. H108L and H209R higher acoustic rates are concentrated at temperatures greater than 0 °C whereas VE10U shows higher rates at temperatures lower than 0 °C. The red line represents the 0 °C . . . . .	197
6.16	AE rates due to freeze-thaw cycles for the period 11/02/2015 to 21/02/2015. H108L and H209R show rates during warm hours, VE10U shows rates during cold hours. Lines represent photos triggered by detection fence sensors and taken by Camera 2 (does not apply to sensor VE10U due to its location) . . . . .	200
6.17	Material detached as consequence of freeze-thaw weathering. Samples of photos taken by Camera 2 (viewpoint 1) in the period 10–21/02/2015. For camera location reference to Figure 6.7 .	201
7.1	Typical AE trend due to variation of water pressure conditions (sharp increase and slow decrease) . . . . .	206
7.2	Typical AE trends due to snow load (sharp spikes) . . . . .	206



# Abbreviations and conventions

Auto	Automatic
AE	Acoustic Emission
EWS	Early Warning System
GWL	Groundwater level
Lat	Latitude
Lon	Longitude
M <sub>L</sub>	Local magnitude
OeBB	Austrian Federal Railways
PDM	Passo della Morte site
RDC	Ring Down Count
RPM	Revolutions per minute
SART	Grossreifling site
SMS	Short Message Service
SW	Smooth waveguide
TW	Threaded waveguide
UTC	Coordinated Universal Time
WG	Waveguide

- Measurement units are given using the International System of Units (SI) convention where possible;
- Coordinates are given in decimal degrees and refer to the WGS84 Web Mercator projection;
- Time is given in 24-hour clock format, in which the day is divided into 24 hours stating at 00:00 and ending at 23:59.

# Chapter 1

## Introduction

### 1.1 Research topic and justification

Hundreds of landslides occur every year around the world, causing several thousands of fatalities. A study by Petley (2012) states that the total numbers of landslides and victims could be even underestimated due to lack of reports by some countries (e.g. North Korea, Ethiopia, etc.). There is also a potential for this number to grow in the coming years as global incidence of landslides is rising dramatically as a response to a number of rapidly changing natural and anthropic factors. Slope stability is demonstrably influenced by climate and, consequently, slope susceptibility to collapse is function of a range of variables that govern interdependent processes which respond, at different time scales, to climate change (Dijkstra and Dixon, 2010). Increasing climate variability, and consequent increasing frequency of extreme weather events, accelerates slope degradation and creates the conditions for slope instabilities to develop. At the same time human activity also affect the temporal and spatial occurrence of landslides (Crozier, 2010). Expanding urbanization, uncontrolled land-use and environmental degradation are increasing the size of vulnerable areas. All these factors together result in greater exposure of population, infrastructures and economic activities to landslide risk.

From a perspective of risk management, it is often impracticable or uneconomical to adopt structural measures for hazard reduction or to move settlements and infrastructures at risk from potential affected areas. However, it is possible to significantly decrease the risk of loss of lives and cost of emergency repairs by reducing the vulnerability. Depending on the landslide characteristics (i.e. volume, material type, movement type, expected velocity, etc.) it is possible to act on the exposed number of people (e.g. evacuation), to plan defence actions or to implement maintenance plans. The need to adopt affordable and reliable non-structural mitigation strategies has increased the interest in new types of monitoring technology and the demand of instrumentation able to provide continuous, remote, near-real time information on slope status and give warning of accelerating slope movement at an early stage.

It is extremely rare in fact that slope failure occurs suddenly, without any indications prior to collapse (Saito, 1965). Often is the scale of the problem that we are considering that prevents us to appreciate the precursors of a failure. In brittle rock slopes, for example, deformation preceding a collapse might be of very small magnitude and developing cracks might not be clearly recognisable, thus requiring monitoring instruments with suitable sensitivity to be able to identify a developing phenomenon. However, instruments with high sensitivity are often very expensive or have technical limitations, as emphasised by practitioners (Michoud et al., 2013).

Acoustic emission can be used as an early indicator of large scale events as in rocks it is generated by micro-crack growth and displacement along existing discontinuities. In fact acoustic emission is not a new technique in the monitoring of rock stability. It has been used since the 1930s in the tunnelling and mining industry, however, the application to natural rock slopes has been hindered by attenuation-related issues. In tunnels and mines the source of AE is expected to be near recently excavated areas (Hardy, 1992) and placing the accelerometers in key locations is relatively straight-forward. In natural rock slopes there can be much more un-

certainty about the location of potential shear zone or critical discontinuities and hence attenuation could prevent the stress waves from reaching the transducer. A relatively recent approach to reduce attenuation problems is the use of waveguides made of low attenuation solids to direct AE waves to the monitoring sensor.

A waveguide acoustic emission system with active granular backfill was developed by Dixon et al. (2003) and used in conjunction with the sensor developed by Dixon et al. (2010). This system was specifically conceived for the use in fine-grained soils, which attenuation is even higher than in rock masses. This system is becoming an established approach to monitor the stability of soil slopes and has the potential to be an affordable early warning system for slope instability. A relationship between AE rate and deformation is available and displacement rates as little as 0.0018 mm/day were recorded. However, the application to rock slopes poses new challenges over the significance of the measured AE trends and require new interpretation strategies to be developed.

## 1.2 Aim and objectives

The aim of this research work is the development of a waveguide-based system for monitoring of acoustic emission activity (AE) generated by the deformation and fracture propagation occurring within rock slopes prior to collapse, in order to be able to provide warning in time to be of use for the authorities in charge to take action.

In particular the project focuses on the adaptation, improvement and optimisation for the application to rock slopes of the Slope ALARMS monitoring technique which was developed specifically for use within soil slopes. In order to achieve the primary aim, the following objectives need to be fulfilled:

- (1) To define factors and processes that lead to generation of detected AE activity and to differentiate between AE generated by deformation and other sources;
- (2) To validate modifications made to the system for installation at rock sites;
- (3) To produce a framework that can be used to associate AE generated by key processes and mechanisms.

## 1.3 Thesis structure

This thesis is organised in eight Chapters and four Appendices.

Chapter 1 defines the aim and objectives of this research work and puts the research into context.

Chapter 2 provides a discussion of the existing literature in the field of landslide behaviour, slope instability monitoring techniques and Acoustic Emission. The chapter is aimed to justification of the aim and objectives, identifying the areas in the literature that have not yet been developed, to assure that this research work will constitute an original and unique contribution to knowledge.

Chapter 3 explains the research methodology and details the research methods that were followed in order to fulfil the aim and objectives.

Chapter 4 discusses the results of a series of tests carried out in the laboratory and in the field to address key variables influencing the performance of the system and eliminate associated uncertainties.

Chapter 5 provides a description of Passo della Morte (Italy) trial site and a discussion of field measurements collected at this site.

Chapter 6 describes the Grossreifling (Austria) trial sites and provides an analysis of the measurements collected.

Chapter 7 provides a discussion towards strategies to interpret measured acoustic emission trends in rock slopes and provides recommendations for further development of this research topic.

Chapter 8 is the concluding chapter where findings and results achieved in this study are summarised and recommendations for further work are given.

Appendix A reports manufacturer's technical sheets for piezoelectric transducers and waveguides.

Appendix B reports additional graphs.

Appendix C reports the numerical data obtained from experiments.

Appendix D reports coding used for data selection and analysis.

# **Chapter 2**

## **Literature review**

The review provided in this Chapter serves the purpose of identifying the areas of the subject that have not been developed yet and ensure that the research carried out is an original contribution to knowledge. It also provides the reader with all the elements necessary to understand the research topic.

The review is split into five sections. Section 2.1 reports a description of landslide-forming materials and explains the parameters that influence the stability of rock masses. An overview of existing monitoring methods and technology is then provided in Section 2.2. AE parameters are reported in Section 2.3, which also explains the reasons why acoustic emission is suitable to be used for the monitoring of the early stages of developing instability in a rock slope. Section 2.4 explores existing AE monitoring techniques and their application to rock slopes. Finally, Section 2.5 summarizes the key findings and gaps in knowledge identified.

## 2.1 Landslide classification and stability of rock masses

The most widely used landslide classification was originally proposed by Varnes (1978) and updated afterwards by Cruden and Varnes (1996). Modifications have been made over the years to adapt the classification to modern usage by integrating the definitions developed by Hutchinson (1988) and Hungr (2001). The most recent version is the one published by Hungr et al. (2014), which appears as reported in Table 2.1. The classification mainly differentiates landslide processes by the type of movement (falls, topples, slides, lateral spreading and flows) and the type of geological material in which the movement takes place.

**Table 2.1:** A summary of Varnes' (1978) classification system. After Hungr et al. (2014)

Movement type	Rock	Engineering soils	
		Debris	Earth
Fall	Rockfall	Debris fall	Earth fall
Topple	Rock topple	Debris topple	Earth topple
Rotational sliding	Rock slide	Debris slide	Earth slide
Translational sliding	Rock slide	Debris slide	Earth slide
Lateral spreading	Rock spread	—	Earth spread
Flow	Rock creep	Talus flow	Dry sand flow
		Debris flow	Wet sand flow
		Debris avalanche	Quick dry flow
		Solifluction	Earth flow
		Soil creep	Rapid earth flow
Complex	Rock slide – debris avalanche	Cambering, valley bulging	Loess flow
			Earth slump – earth flow



Geotechnical materials are traditionally differentiated into two very broad categories: rock, or bedrock, and soil, or engineering soil. Although a more accurate differentiation of landslide-forming materials has been proposed by Hungr et al. (2014) to reflect the accepted geotechnical and geological terminology, this mainly regards a more detailed differentiation of the soil types (which are now "Clay", "Mud", "Silt, sand, gravel, and boulders" and "Debris") and introducing other categories of material such as "Peat" and "Ice". The general, broader distinction between rock and soil is still valid and will suffice to the purposes of this research.

The term *soil* is used to describe an aggregate of solid particles, generally of minerals and rock that either was transported or was formed by the weathering of rock. Particles are not cemented together or are characterised by weak bonding. In slope stability analysis, soils are divided in two broad sub-categories based on their grain distribution: earth, fine-grained material in which 80% or more of the particles are smaller than 2mm, and debris, coarse-grained material in which 20% to 80% of the particles are larger than 2mm.

The term *rock* is used to describe an aggregate of particles (minerals or rock fragments) which are cemented together or are characterised by strong bonding between particles. Generally, the stability of rock is mainly controlled by the presence of discontinuities, hence the term *rock mass*, which considers intact rock and discontinuities as a whole, is more accurate for slope stability purposes.

A rock mass is, ideally, composed of a system of intact rock blocks separated by discontinuities to form a material in which all elements behave in mutual dependence (Palmström, 2001). Discontinuities can occur in the form of bedding planes, faults, joints, fissures, cracks, etc. which denote different dimensions and genesis. Nevertheless, the collective terms joint and weakness zone are generally used in rock mechanics to represent most macroscopic types of discontinuities.

This work concerns mainly the stability of rock masses but there will be also references to fine-grained soils.

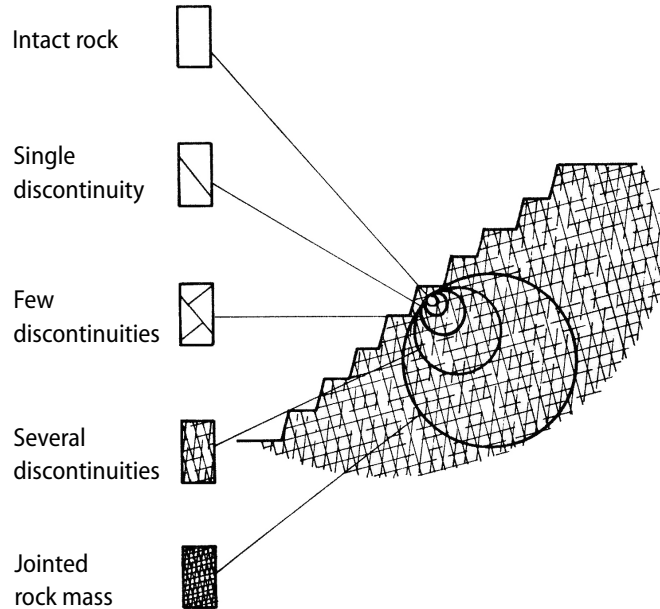
Rock mass behaviour and its strength properties are controlled by both the strength of discontinuities and the strength of intact rock (Hoek, 1983). The proportion of strength given by one or the other depends on the structure and characteristics of the rock mass, such as the number, orientation, persistence, spacing and shear strength of discontinuities, and the nature of the material.




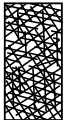
The mechanical behaviour of rock masses changes also with the scale of the problem, i.e. scale effect (Hoek, 1983). For a given problem scale, the behaviour is controlled by the orientation of discontinuity planes with respect to the slope. In the example shown in Figure 2.1, considering a portion of the slope that does not contain any discontinuities, the mechanical behaviour is controlled by the intact rock strength parameters; when considering a bigger portion, which includes one or a few discontinuities, the failure mechanism strength parameters depend on the orientation and strength of the discontinuities; increasing the portion even more, at the slope scale the rock appears so subdivided in small blocks that can be considered isotropic and therefore an equivalent–continuum model (i.e. analogue to soils) can be used to evaluate the strength parameters. This means that the scale the problem is related to has to be carefully evaluated. It also means that in practice it is very difficult to obtain samples for laboratory testing that are representative of the scale of interest. Therefore, the use of empirical methods and parameters evaluated on the basis of field observations is widely used in rock mass failure criteria.

The shear strength of a rock mass and its failure behaviour are controlled by (Hoek, 1983; Sonmez et al., 1998):

- *strength of intact rock*, when no discontinuities are present (ideal condition);
- *strength of discontinuities*, when the rock mass, or the scale of the problem considered, is characterised by one or few sets of discontinuities with unfavourable orientation;
- *strength of intact rock and discontinuities together*, when the rock mass, or the

scale of the problem considered, is closely jointed and no dominant discontinuities are present.



	Description	Strength characteristics	Strength testing
	Hard intact rock	Brittle, elastic and generally isotropic	Triaxial testing of rock specimens in laboratory relatively simple and inexpensive and results usually reliable
	Intact rock with single inclined discontinuity	Highly anisotropic, depending on shear strength, orientation and inclination of discontinuity	Triaxial testing of core with inclined joints difficult and expensive but results reliable. Direct shear testing of joints simple, inexpensive but results require
	Massive rock with a few sets of discontinuities	Anisotropic, depending on number, shear strength and continuity of discontinuities	Laboratory testing very difficult because of sample disturbance and equipment size limitation
	Heavily jointed rock	Reasonably isotropic. Highly dilatant at low normal stress levels with particle breakage at high normal stress	Triaxial testing of undisturbed core samples extremely difficult due to sample disturbance and preparation problems

**Figure 2.1:** Schematic representation of the influence of scale on the type of rock mass behaviour model. Modified after Hoek (1983)

## 2.1.1 Shear strength of jointed rock masses

The shear strength of discontinuities controls the mechanical behaviour when a slope is characterised by one or few dominant discontinuities (e.g. persistent joints, faults, bedding planes, etc.) which have an unfavourable orientation with respect to the slope. The failure mechanism depends on the number and orientation of discontinuities and can occur as translational sliding. The available strength resisting the movement is only given by the strength and characteristics of the discontinuities (Romana, 1993).

The mechanisms leading to the failure in shear of a jointed rock mass are fundamentally two:

1. The joint dilates and overrides asperities, when the normal stress acting on the asperities is low;
2. Asperities are crushed, when the normal stress is higher than the compressive strength of asperities.

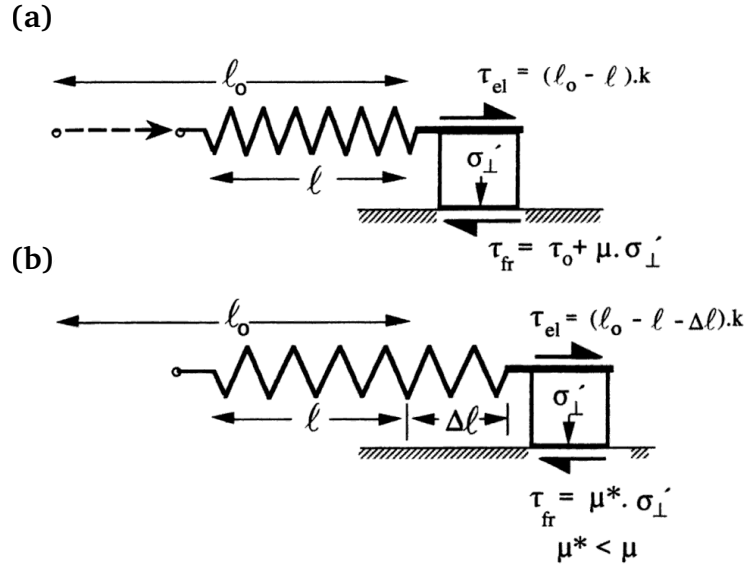
As the normal stress increases during joint dilation, also mixed mechanisms are possible; if the build up of normal stress exceeds the compressive strength, asperities can be crushed. On the other hand, the motion of joint dilation can also be stopped if the normal stress becomes greater but doesn't exceed the compressive strength. This generates a stick-slip behaviour which has the potential to degrade the asperities and lead to failure with time.

### 2.1.1.1 Stick-slip behaviour

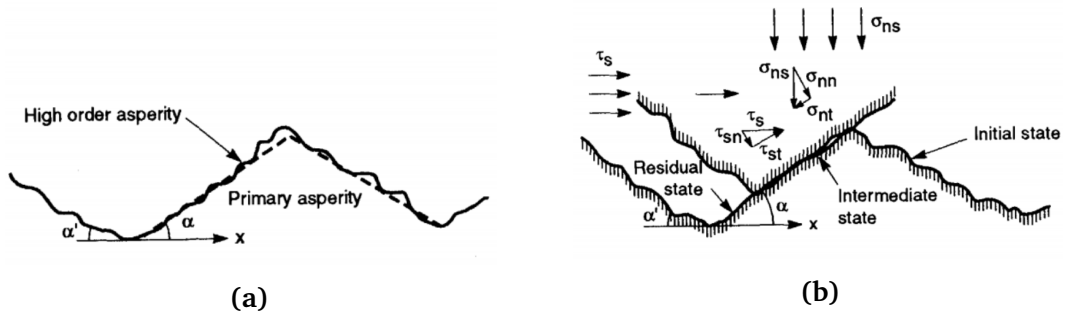
The shear stress builds up during the *stick* phase and when the applied shear stress on a discontinuity exceeds the mobilized shear strength, joint *slip* begins. The slip will continue until an increase in joint shear resistance, either through an increase in normal stress or due to asperity locking, increases the ability of the joint to resist

the relative motion (Ghosh et al., 1996). The principle of stick-slip is demonstrated by means of a spring-block analogue model, which is shown in Figure 2.2. During *stick* phase, the friction force builds up but the block holds its position. When the applied force becomes greater than the frictional force resisting the relative motion, that is the static friction, *slip* occurs at the interface.

The stick-slip behaviour and its extent in rock joints is a function of joint roughness, material properties of the joint surfaces, local strength of asperities and the applied stress field (Ghosh et al., 1996). A rock joint surface is rarely planar, it may be curved and contain dominant asperities, primary asperities, which could be either large or small. There also exist higher order asperities that have much smaller size, called secondary asperities (Mandl, 2000). Primary and secondary asperities both contribute to the joint shear resistance; a schematic is shown in Figure 2.3a along with a diagram of the forces acting on them in Figure 2.3b. After several stick-slip cycles the shear resistance of the secondary asperities degrades and the joint can more easily override the asperities and failure can occur.



**Figure 2.2:** Spring-block model illustrating the principle of stick-slip behaviour. (a) situation at the end of *stick* phase and incipience of slip,  $\tau_{el} = \tau_{fr}$  where  $\tau_{el}$  is the elastic driving stress and  $\tau_{fr}$  is the resisting frictional stress; (b) situation at arrest of *slip*, the spring has bounced forward when  $\tau_{fr}$  was exceeded.  $k$  is the elastic stiffness of the spring,  $\mu$  is the static friction,  $\mu^*$  is the kinetic friction. After Mandl (2000)



**Figure 2.3:** Conceptual model of joint shear behavior. (a) orders of asperities; (b) diagram of stresses and forces acting on a joint.  $\sigma_{ns}$  is the vertical stress,  $\tau_{sn}$  is the horizontal stress. After Ghosh et al. (1996)

## 2.1.2 Shear strength of isotropic rock masses

The shear strength of the rock mass as a whole controls the mechanical behaviour when no dominant discontinuities are present, the fracturing is statistically isotropic and the scale of the problem is such that no specific discontinuity is able to control the failure mechanism of the slope. When these conditions are satisfied, the slope can be regarded as a continuum–equivalent and the most likely failure mechanism would be rotational sliding.

## 2.1.3 Landslide triggers

Gravity is the major driving force for landslides to occur. However, in most cases there needs to be a triggering factor for a slope movement to be initiated. A landslide trigger decreases the factor of safety to less than one, which means that driving forces are greater than resisting forces, and failure will occur. Several factors can trigger a landslide, including:

1. **Water pressure:** rapid groundwater level increase due to intense rainfall or snowmelt generates greater pressure within pores or fractures. The build-up of pressure within the slope causes the forces resisting the motion to decrease and the landslide movement can be initiated;
2. **Seismic activity:** ground shaking due to earthquakes can cause an instantaneous increase of shear stress on a slope;
3. **Loading on upper slopes:** the addition of mass on an upper slope acts unfavourably to stability as it cause driving forces to grow;
4. **Weathering:** the action of rainwater, extremes of temperature (e.g. freeze-thaw) and biological activity on rocks can cause the degradation of bonds between particles that form the rock or rock mass. Differential weathering



on weaker layers can also cause undercutting at the toe, promoting failure of the slope;

**5. Any of the above or other triggers can also combine to cause failure.**

The landslide triggers described above are pertinent to the sites considered in this work. Several other triggers exist, which may include volcanic activity or undercutting by river erosion, for example. These are not discussed here as not relevant to the sites subject of this research.

Monitoring over time of parameter changes associated with landslide triggers (e.g. rainfall, groundwater level, snow, seismic activity) along with other parameters intrinsic to the rock mass, may help identification of approaching conditions favourable for a landslide to occur.

## **2.2 Landslide monitoring and early warning**

In the field of slope stability, the purposes of a monitoring system can be summarised into three main areas:

- **Knowledge acquisition**, to correctly identify the extent of the phenomenon, predict possible evolutionary scenarios, define the associated risk and to design remediation;
- **Hazard reduction** validating design, and assessing performance of stabilization systems;
- **Reduction of elements at risk** identifying forerunners and disseminating alerts and/or alarms (i.e. early warning) in order to take actions .

For any of the purposes set out above, the parameters that may be monitored include those related to the movement itself, such as surface deformations, subsurface deformations and generation of acoustic emission; parameters that induce

destabilising forces to grow, such as variations of piezometric level and seismicity; and environmental parameters in close correlation to the phenomenon, such as precipitation, snow height and temperature.

A large number of monitoring techniques and technologies are today available for the monitoring of these physical parameters, such as (Angeli et al., 2000; Gili et al., 2000; Michoud et al., 2013; Savvaidis, 2003; Uhlemann et al., 2016):

- **surface displacement:** Extensometers, Crackmeters, Tiltmeters, Global Navigation Satellite System (GNSS), Total Station Theodolites, terrestrial remote sensing methods (e.g. Ground-based Interferometric Synthetic Aperture Radar (GB-InSAR), Terrestrial Laser Scanning (TLS), Terrestrial Photogrammetry) and airborne/spaceborne remote sensing methods (e.g. Airborne Light Detection and Ranging (LiDAR), Airborne Photogrammetry, Spaceborne InSAR);
- **sub-surface displacement:** Manual-reading inclinometer, Borehole in-place inclinometer (remotely read), Time Domain Reflectometry (TDR), Borehole TDR-cable, Borehole multi-base extensometer, ShapeAccelArray (SAA);
- **water conditions:** Piezometers, Water-pressure transducers.

Each one of these methods offers advantages and disadvantages over the others and therefore they are suitable to answer specific questions and to be used at different stages of risk management, depending on their characteristics (Corsini, 2008; Dunnicliff, 1988). For example, airborne/space-borne remote sensing techniques are generally expensive and hence performed with low-temporal resolution (see also Table 2.2); hence these techniques are suitable to be employed for the monitoring of large areas or areas with difficult access in a phase of hazard identification but cannot be used for operative early warnings.

Sites that have restricted access (e.g. due to geographical position, adverse conditions such as snow cover for prolonged periods, etc.) are often monitored with

low sensitivity or low temporal resolution systems (e.g. remote sensing, manual-reading inclinometer, etc.) as other automated systems are too power demanding or too expensive. These traditional methods seldom provide real-time information for use in early warning of instability and have high labour costs associated. Therefore, there is a clear demand for high sensitivity, continuous and near-real time systems that can provide information on the state of slope stability.

Hence, the methods that can be used for warning of impending landslides need to have high sensitivity and high temporal resolution. Also high life expectancy, robustness, low price, low maintenance and running costs, low noise level of the sensors (to avoid false alarms) are factors highly regarded in the choice of instrumentation (Michoud et al., 2013).

Table 2.2 summarises the typical characteristics of the most common instruments employed for the monitoring of rock slopes. The table clearly shows that there are several sensitive (i.e. resolution  $< \text{mm}$ ) instruments that have the potential of being used for warning of an impending collapse (e.g. crackmeters, extensometers, in-place inclinometers) however they must be automatically read and must be connected to a wider EWS to provide communication functions. Moreover, a number of devices must be used to achieve higher spatial resolution. Other instruments (e.g. terrestrial remote sensing) have high spatial resolution but their sensitivity is lower (mm to cm), and the cost associated is very high.

To assess the current state of practice, to identify advantages and limitations of current monitoring/early warning systems and how they can be improved Michoud et al. (2013) submitted a questionnaire to a number of institutions in charge of the management of 23 different landslides EWSs. The report highlights some key elements that the practitioners agreed need improvement such as long-term sensors robustness, as monitoring network are often located in hostile environments that make installation and maintenance challenging. The survey also highlights the importance to take into consideration the technical limitations of sensors to improve

reliability and pertinence of automatic alarms in order to decrease the frequency of false alarms.

Although many types of monitoring methods are available today, there is still a need for development of reliable, high temporal-resolution systems that are able to give warning at an early stage of instability development. It is also essential that the sensor is robust and has low operating costs associated, in terms of initial purchase price but also in terms of power demand, labour and maintenance.

Table 2.2: Instruments typically used in rock slope stability monitoring

Instrument/Tech-nique	Early warning of instability	Integrated communication sys	Rate and magnitude	Resolution/Accuracy/Precision	Reading frequency	Spatial Resolution	False alarms	Cost
Crackmeter	YES if auto	NO	YES	0.01 mm to 1mm	High	Point like	NO	Low
Extensometer	YES if auto	NO	YES	0.01 mm to 1mm	High	Point like	NO	Low
GNSS	NO	NO	Requires consecutive surveys	mm to cm	Low	Depends on number of markers	/	High
Geophone/Accelerometer	YES	NO	Partially	Acceleration: 0.1m/s <sup>2</sup> , Velocity: 0.01 mm/s	High	Low for single instrument	YES	Moderate
Inclinometer (probe)	NO	NO	YES	0.1 mm/m	Low (manual)	Relatively low (2D)	NO	Moderate
Inclinometer (in-place)	YES	NO	YES	0.04 mm/m	High (auto)	Point-like to relatively low (2D)		Moderate
Terrestrial remote sensing (e.g. GB-InSAR)	YES	NO	YES	mm to cm	Low (manual) to High (auto)	High	YES	High
Airborne/spaceborne remote sensing	NO	NO	YES	mm to m	Low	Very high	/	Very high
TDR Cables	YES if auto	NO	(?) Entity of deformation, not total magnitude	mm to cm, depends on length	Low (manual) to High (auto)	Relatively low (2D)	NO	High
Fibre Optic Cables	YES	NO	(?) Entity of deformation, not total magnitude	0.01% can be detected (0.001 m over 1 m)	High	Relatively low (2D)	NO	High
Tiltmeter	YES if rotational component	NO	Partially (not displacement)	Precision 0.2% to 1%	Low (manual) to High (auto)	Low	YES	Low
Total Station	Possibly	NO	YES	precision 0.5 – 5 mm depends on measured distance	Low (manual) to High (auto)	Depends on number of prisms	?	High

## 2.3 Acoustic emission (AE) fundamentals

Any material undergoing irreversible changes within its structure generates transient stress waves due to rapid release of energy, which radiate in an omnidirectional manner from localised sources and propagate through materials surrounding the generation source. Acoustic emission (AE) is the recommended term for general use by the American Society for Testing and Materials (ASTM Standard E1316, 2016) and is defined by the same standard as: *"The class of phenomena whereby transient elastic waves are generated by the rapid release of energy from localised sources within a material, or the transient waves so generated."* The term *acoustic emission*, or its acronym *AE*, will be used throughout this thesis work, although other terms have been used in the literature to refer to the same phenomenon. Examples from the geotechnical literature include terms such as: microseismic emission (Arosio et al., 2009), microsonic activity (McCauley, 1976; Plona et al., 1997), microseismicity (Cai et al., 2001; Helmstetter and Garambois, 2010) and rock noise (Amitrano et al., 2010); some authors differentiate the terminology with respect to the scale of the problem, using the term acoustic emission when working at the laboratory scale and the term microseismic activity for applications at the field scale (Hardy, 2003; Amitrano et al., 2010).

The monitoring of acoustic emission signals is an established non-destructive testing (NDT) technique for material health monitoring. It has been used in many engineering and construction fields to monitor cracks growth, fibres breaking and many other processes of active damage in stressed materials, such as corrosion and leakages in oil and gas or water pipe networks (e.g. Anastasopoulos et al., 2009; Long et al., 2003), damage assessment of reinforced concrete (e.g. Noorsuhada, 2016), deterioration of rotating machines (e.g. bearings, engines, gearboxes and pumps), structural health monitoring (e.g. Farrar and Worden, 2007).

AE monitoring is not a new technique in geotechnical investigation. The acoustic emission technique for the monitoring of rock masses was initiated in the late

1930s in the mining industry and developed since the 1970s. AE has also been described in classical geotechnical instrumentation (e.g. Dunnicliff, 1988) and landslide investigation texts (e.g. Schuster and Krizek, 1978) as an established technique for the monitoring of rock structures in the mining and tunnelling industry.

AE monitoring has been successfully used in mining and tunnelling activities because attenuation (i.e. the decay of AE waves with the distance from the source, see Section 2.3.2) is not a primary concern. In fact the source of AE is generally expected to be in the proximity of recently excavated areas and therefore the instruments are strategically located to be relatively close to the source of AE (Hardy, 1992). In natural slopes there is much more uncertainty as where deformation is being generated and thus where the source of AE is located (i.e. movement along discontinuities, shear zones, etc.) which makes it difficult to place a transducer with sufficient precision.

In recent years most effort has been focussed on laboratory studies (for example Zhang et al., 2016; Stierle et al., 2016) rather than field studies and therefore only few examples are available in literature. Examples of acoustic emission monitoring of rock structures in mining environment are common in the literature but few are found concerning the monitoring of natural slopes.

The application to natural slopes has been mainly inhibited by:

- (1) **attenuation** related issues;
- (2) **technology** related issues.

To overcome attenuation (defined in Section 2.2) problems and being able to monitor a larger portion of the slope, low frequency methods (1 Hz – 1,000 Hz) have been used by many authors (e.g. Amitrano et al., 2005; Senfaute et al., 2009; Spillmann et al., 2007; Tonnellier et al., 2013). However, the main limitation of this method is that it is not suitable to be used in sites with high ambient noise (i.e. from anthropic activities) as this is characterised by the same frequency range and

could affect the monitoring. Other authors (e.g. Dixon et al., 2003; Shiotani et al., 2001b; Hardy, 1992) have partially overcome attenuation using metal waveguides installed within the unstable slopes to direct AE to transducers (see Section 2.4).

Technology issues are mainly connected to the size of the equipment, power consumption and maintenance, which makes the technology not suitable for remote sites or difficult access areas. Dixon and Spriggs (2010) addressed this problem patenting a unitary battery-operated sensor that is portable, thus solving problems connected to transport and placement at site; uses reduced power, which means that there is no need for mains to be present in the area; and it is placed at the ground level (not grouted or buried) which makes maintenance or replacement relatively effortless.

### 2.3.1 AE in deforming geological materials

In a deforming *soil* mass, AE is generated by frictional grain-to-grain slip and particle collision, restructuring of particle contact network and mechanical interaction (Koerner et al., 1981; Michlmayr et al., 2012; Michlmayr and Or, 2014).

In *rock* materials, acoustic emission is generated by nucleation and propagation of new fractures, damage accumulation and/or displacement along existing discontinuities (Amitrano, 2006; Hardy, 2003). Evans (1978) demonstrated that the detected AE event rate depends on the stress intensity, which is the basic concept for the primary use of acoustic emission as a failure indicator.

Due to the complexity of rock masses, the sources of acoustic emission can be associated (Amitrano, 2006; Hardy, 2003; Kranz, 1983; Matcharashvili et al., 2011; Thompson et al., 2009):

- at the micro-level AE activity may originate as a result of micro-cracks from stress concentrators, which are small defects in the rock, such as voids, pores, inclusions;



- at the macro-level by initiation and propagation of fractures through and between mineral grains ;
- at the mega-level by fracturing and failure of large areas of material or relative motion along pre-existing discontinuity planes, e.g. stick-slip behaviour (Section 2.1.1.1).

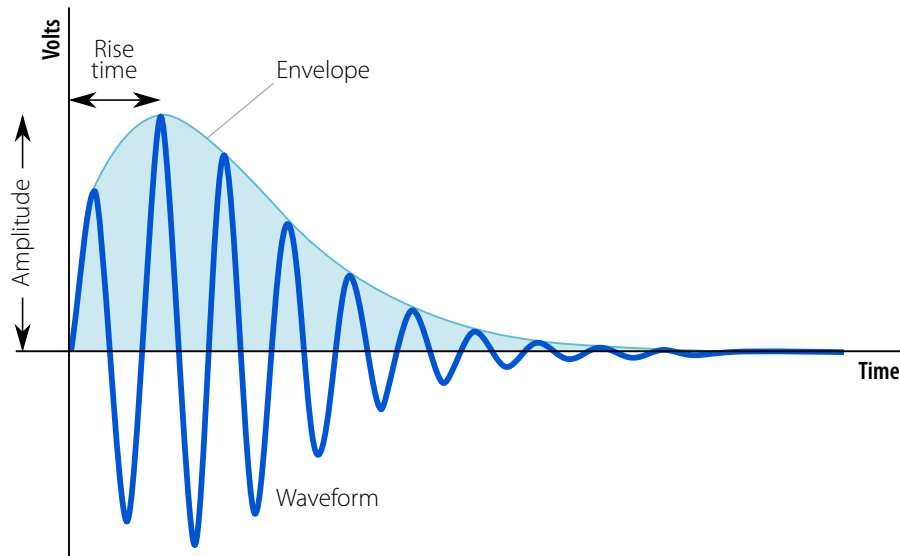
In fact, deformation in rock masses occurs predominantly along pre-existing discontinuities. Stick-slip displacement (Section 2.1.1.1) on rock joints radiates energy in the form of acoustic emission (Matcharashvili et al., 2011; Thompson et al., 2009).

Generally, the micro-cracking in rock is found to be stress and time-dependent (because of slow crack growth), resulting in an acoustic emission rate that depends on the details of the stress history to which the material is subject (Evans, 1978).

AE so generated is able to travel in the soil or rock masses for limited distances, which depend on the intrinsic characteristics of the material and its structure, as explained in Section 2.3.2.

#### 2.3.2 AE properties

Figure 2.4 shows a characteristic acoustic emission event waveform. The AE signal is indicated as a solid line. The (upper) signal envelope outlines the signal extremes and is determined by connecting all positive amplitude points. The time employed to reach the peak amplitude is called rise time.



**Figure 2.4:** Characteristic AE event waveform with main parameters indicated

The typical frequencies of interest for geotechnical field and laboratory applications in rock and soil mechanics varies between 20 kHz and 1 MHz. Below 20 kHz ambient noise generated by anthropic activities (machinery vibration, traffic, construction activities, etc.) interfere with the measurements (Moradian et al., 2016). In most rock monitoring AE applications these high frequencies are normally used to overcome the problem of background noise. These studies are generally carried out in sites with relatively high environmental noise either of anthropic or natural origin. Environmental noise is typically characterised by low frequencies ( $<10$  kHz), thus an extensive filtration of low frequencies is needed. The upper limit (1 MHz) is imposed by the extent of rock that needs to be tested/monitored, due to attenuation issues of the materials involved (e.g. Mathiyaparanam, 2006; Moradian et al., 2016). In fact, high frequencies are attenuated much more than low frequencies, hence the higher the frequency, the smaller the volume that can be investigated (by a single sensor).

As an elastic wave propagates through the medium surrounding the source, the amplitude of such wave significantly decreases over the travel distance. The term used to describe this loss of energy is *attenuation*. Attenuation is caused by a num-

ber of factors, the most important being geometric spreading, material damping, scattering and mode conversion (Barton, 2007; Hardy, 2003; Long et al., 2003):

- **Geometric spreading** is due to wave radiation away from the source and it decays with the inverted squared distance of propagation. For a stress wave propagating from a point source, considering geometric spreading alone, the amplitude  $A$  at a distance  $r$  from the source is equal to

$$A_{(r)} = A_0 \cdot \frac{1}{r^2} \quad (2.1)$$

where  $A_0$  is the amplitude at the source. Acoustic emission waves propagate in all directions as spherical waves. As the wave front moves away from a point source, the energy is spread out over a spherical surface of ever increasing size. Since the wave amplitude is equivalent to the energy per unit area, it decreases with the square of the distance from the source. This factor depends only on geometry and is independent of the materials and frequencies involved.

- **Material damping** is the loss of amplitude due to conversion of the mechanical (sound) energy to thermal energy caused by inelastic behaviour of the material.
- **Scattering** is the reflection of the stress wave in directions other than its original direction of propagation when travelling through an inhomogeneous media. It occurs when the wavelength ( $\lambda$ ) of the stress wave is comparable with the particle size ( $d$ )

$$d \approx \lambda \quad \text{with } \lambda = \frac{v}{f} \quad (2.2)$$

where  $v$  is the velocity of propagation and  $f$  is the frequency of the incident stress wave. For geological media the inhomogeneities are grains in materials such as soil or blocks of rock separated by discontinuities in rock masses. When the acoustic wave meets the grain/block along the path this result in

the generation of secondary waves which radiate in a variety of directions interfering with the general flow of energy.

- **Mode conversion** happens when one form of wave energy is transformed into another form. For instance the non-normal incidence of a longitudinal wave on an interface, can cause some of the energy to start particle movement in a transverse direction generating a shear wave. This effect can only be generated by the non-normal incidence of the stress wave on an interface between two materials of different acoustic impedances. Impedance ( $Z$ ) depends on the density ( $\rho$ ) and velocity ( $v$ ) of the material

$$Z = \rho v \quad (2.3)$$

The impedance contrast between the two materials causes refracted and reflected components to be generated (depending on the Snell's Law, e.g. Long et al. (2003), Aster (2005), and Shehadeh et al. (2008)), dissipating energy and consequently reducing the acoustic wave amplitude. The larger the impedance contrast between the two materials, the more the sound is refracted.

In this work, Equation 2.4 will be used to derive the attenuation coefficient of a decaying wave, taking into account all forms of attenuation (i.e. geometric spreading, material damping, scattering, mode conversion):

$$A_{(r)} = A_0 e^{-\alpha r} \quad (2.4)$$

where  $\alpha$  is the attenuation coefficient,  $A_{(r)}$  is the wave amplitude at a distance  $r$  from the source,  $A_0$  is the amplitude at the source (i.e. non-attenuated) and  $e$  is Euler's number. To derive the attenuation coefficient, Equation 2.4 must be rearranged to:

$$-\alpha = \frac{1}{r} \ln \frac{A_{(r)}}{A_0} \quad (2.5)$$

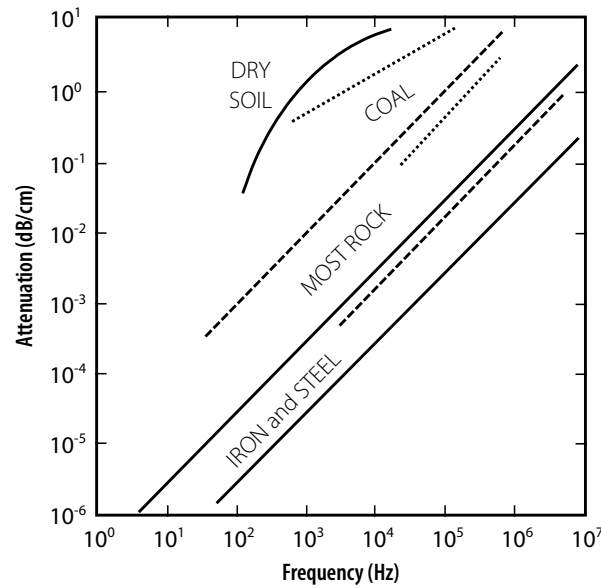
Equation 2.5 produces the attenuation coefficient in Neper per metre (Np/m). To

convert the output to the more commonly used units of decibel per metre (dB/m), Equation 2.6 will be used:

$$1 \text{ Np/m} \approx 0.1151 \text{ dB/m} \quad (2.6)$$

In general, geological materials are characterised by high attenuation, which means that only relatively small volumes can be investigated (from a single point sensor). Granular materials such as soils attenuate much more than intact rock. Figure 2.5 provides attenuation ranges for soil  $>10 \text{ dB/cm}$  and for intact rock in the order  $10^{-1}$  to  $10^{-3} \text{ dB/cm}$  for frequencies of about 20 kHz. However, this graph does not account for discontinuities, which are the primary cause of attenuation in rock masses. The graph also shows clearly that attenuation is highly frequency-related for all materials.

To partially overcome signal attenuation problems and to be able to monitor larger volumes of material, bars or pipes composed of a low attenuation solid such as steel ( $<10^{-4} \text{ dB/cm}$ ), referred to as waveguides, have been used in many monitoring fields to create a preferential path for AE signals to reach AE sensors (Section 2.4.1).

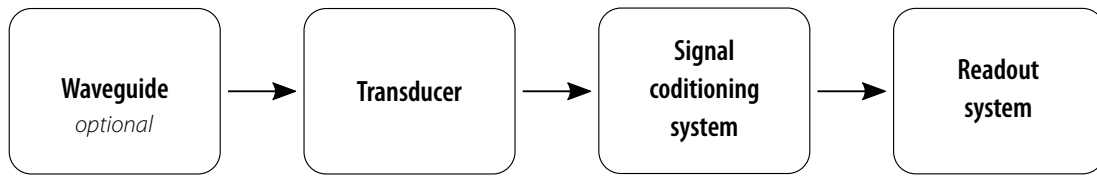


**Figure 2.5:** Attenuation versus frequency by material group. Intact rock attenuates more than iron and steel but much less than soils. It is also evident how attenuation is highly frequency-related. After Koerner et al. (1981)

## 2.4 AE monitoring

An acoustic emission monitoring system is typically composed of three main elements: the transducer, which detects the sound waves, the signal conditioning system, which prepares the signal for being analysed, and the readout system which allows the signal to be read by the end user. An optional component is the waveguide, which can help overcome problems related to attenuation and can be employed both in laboratory experiments (few centimetres long) or in field applications (up to tens of metres). In a traditional AE monitoring system the waveguide is not employed and the transducer is attached directly to the structure that is being monitored or placed within a borehole, an example of this type of application is provided by Amitrano et al. (2005), see Section 2.4.4.

In Figure 2.6 a diagram of the major components that constitute an AE monitoring system typically used in the field is provided.



**Figure 2.6:** Block diagram representing the major components of an AE monitoring system typically used in the field. Modified after Hardy (2003)

### 2.4.1 Waveguide

As discussed in Section 2.3.2, geological materials attenuate AE signals significantly and thus only regions surrounding the transducer can be investigated. To partially overcome this problem the use of a waveguide has been found useful to direct AE signals from within the monitored body to the transducer, creating a preferential low attenuation path (Chichibu et al., 1989; Dixon et al., 2003; Koerner et al., 1981; Nakajima et al., 1988; Shiotani and Ohtsu, 1999). Hardy (2003) defines a waveguide as a component normally formed of a low attenuation solid, such as steel, used to convey an AE signal from a test specimen located in a hostile environment or a remote area, to a transducer located in a convenient and benign environment.

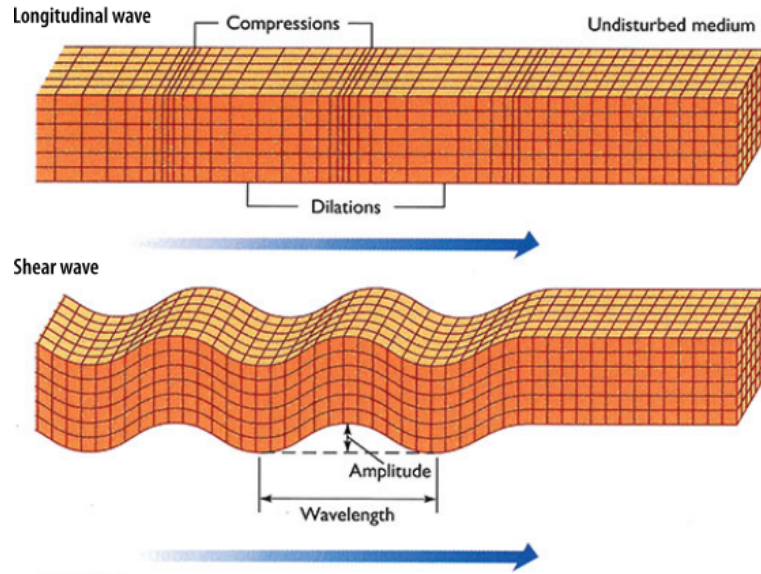
The transmission of AE waves through the waveguide is not only improved by the low attenuation material they are formed of, but is also favoured by their geometrical properties. As previously discussed in Section 2.3.2, acoustic emissions propagate as spherical waves. As the waves expand into a three-dimensional space, the signal dissipates following the inverse squared law of the distance from the source. Waveguides work on the principle of reducing the component of attenuation due to geometrical spreading, physically constraining the wave expansion to one dimension. This way the waveguide enables the signal to propagate with minimal loss of energy.

Acoustic emission waves propagate within a waveguide in four principle modes

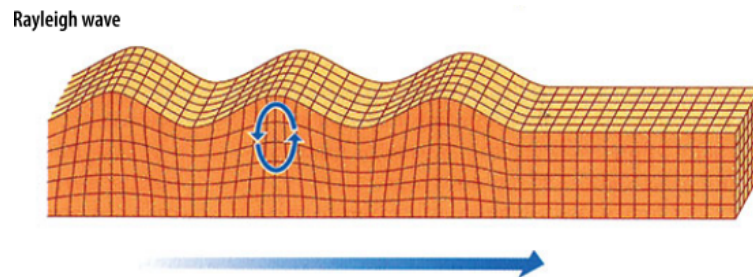
that depend on the particle motion. AE propagates as longitudinal waves and shear waves through the material, as Rayleigh waves on the surface; as the waveguide is composed of a relatively thin material bounded by two surfaces (tube), also Lamb waves are generated (Maji et al., 1997; Paipetis et al., 2012; Sikorska and Pan, 2004; Zelenyak et al., 2015):

- **Longitudinal waves**, particles oscillate parallel to the direction of wave propagation. They are also called compressional waves as particles in the material are compressed and dilated (see Figure 2.7);
- **Shear waves**, the particles oscillation occurs in the direction transverse to the direction of propagation (Figure 2.7). Shear waves are usually generated using some of the energy from longitudinal waves and therefore are relatively weaker when compared to longitudinal waves;
- **Rayleigh waves** travel on the surface of a solid penetrating to a depth of one wavelength. Particles move in an elliptic orbit motion where major axis of the ellipse is perpendicular to the surface of the solid (Figure 2.8). The width of the elliptical motion decreases with depth from the surface. Rayleigh waves are very sensitive to surface defects and are able to follow the surface around curves;
- **Lamb waves**, can only be generated in materials that are bounded by two surfaces, i.e. their thickness must be only a few wavelengths thick (e.g. plate or tube). The propagation of the Lamb waves occurs throughout the thickness of the material and depends on the density and the elastic material properties and is influenced by frequency and material thickness. The primary Lamb wave modes are symmetrical and asymmetrical. The *symmetrical mode*, also called the extensional mode, stretch and compress the plate/tube in the wave propagation direction. The *asymmetrical mode*, also called the flexural mode, moves mainly in a normal direction to the waveguide, and a little proportion occurs in the direction parallel to the waveguide (see Figure 2.9).

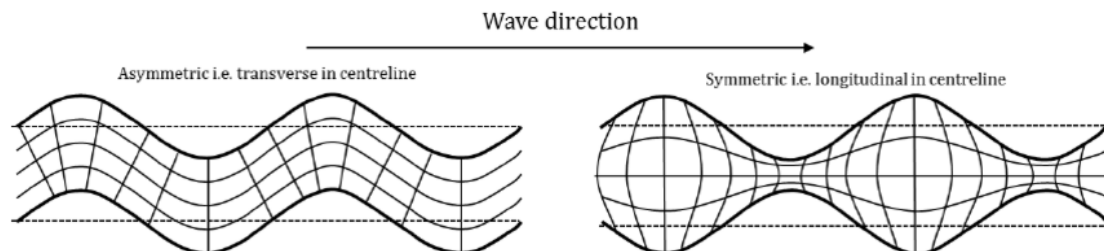




**Figure 2.7:** Longitudinal and shear waves. Modified after Construction and Design (2017)



**Figure 2.8:** Rayleigh surface wave. Modified after Construction and Design (2017)



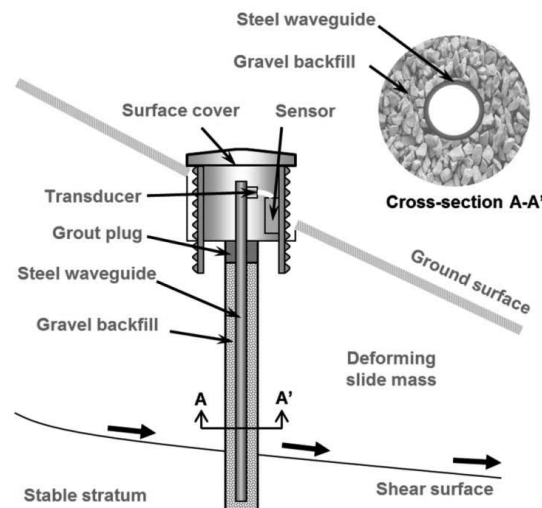
**Figure 2.9:** Exaggerated schematic of Lamb wave modes. Left: asymmetric or flexural mode; Right: symmetric or extensional mode. After Marks et al. (2016)

The effectiveness of using a waveguide rather than placing a sensor on the ground to investigate the soil covering loss on AE was firstly studied by Lord et al. (1982). The standard waveguides commonly employed in slope stability monitoring are metal rods or pipes, the first term referring to a solid bar and the second to a hollow tube, installed into pre-drilled boreholes. The ideal condition for monitoring of slopes is to install the waveguide through existing or expected shear surfaces, active discontinuities or zones of deformation. This is particularly important when using active waveguides as the measured AE is generated by the strain of the granular wave-generator (Dixon et al., 2003; Dixon et al., 2010; Smith et al., 2014a).

Waveguides can be active or passive, depending on whether the system comprises a wave-generator or not:

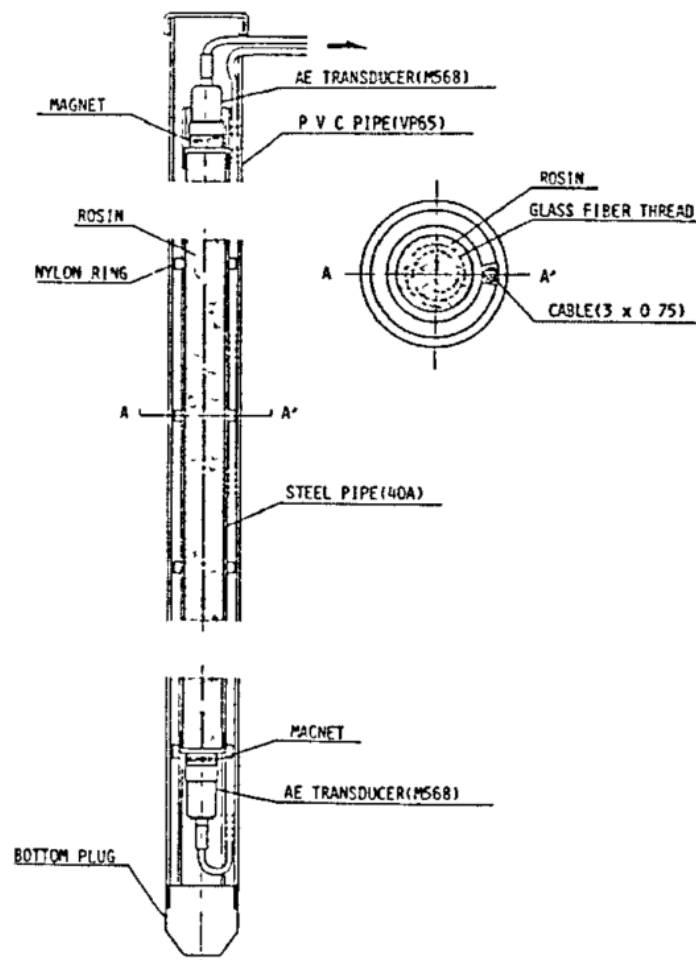
- an *active* waveguide is surrounded by (e.g. Dixon et al., 2003) or filled with (e.g. Nakajima et al., 1995) a wave-generator which emits AE when deformed by the host slope. The wave-generator can be a coarse-grained material such as gravel (Dixon et al., 2003) or a brittle material such as the fibreglass-reinforced resin that Nakajima et al. (1995) used for their wave-generator or made of cement mortar mixed with sands to achieve an increased brittleness (Cheon et al., 2011). As the slope deforms, the waveguide and the wave-generator also deform. The stress/strain of gravel particles or the cracking of the mortar generate increased rates and strength of AE that can propagate along the waveguide;
- a *passive* waveguide (e.g. Shiotani et al., 2001b; Shiotani et al., 2001a) is not expected to be the primary source of measurable acoustic emission and it is usually grouted with regular mortar or mortar designed specifically to match the brittleness of the surrounding (rock) material to ensure continuity for the stress waves generated within the hosting slope to propagate to the waveguide.

Active waveguides with granular backfill are formed by placing hollow metal tube within a pre-drilled borehole and backfilling the gap between the pipe and the borehole wall with coarse-grained material (Figure 2.10). This type of active waveguides are successfully (Dixon et al., 2015c; Dixon et al., 2015b; Smith et al., 2014a) used for the monitoring of fine-grained (e.g. clay) soil slopes. Fine-grained slopes naturally generate low AE activity that is also highly attenuated in a short distance from the source, hence the signal would not be measurable without the addition of a noisier material to generate an increased amplitude signal. However, granular active waveguides are not suitable to be employed in brittle rock slopes as the expected displacements pre-failure are so small that the movement would not be large enough to create strain within the grained backfill and generate stronger acoustic activity (Shiotani et al., 2001b). Moreover, in rock slopes there is often the necessity of drilling non-vertical boreholes to install the waveguide through potentially critical discontinuities; the granular backfill would be very difficult to install within such configuration.



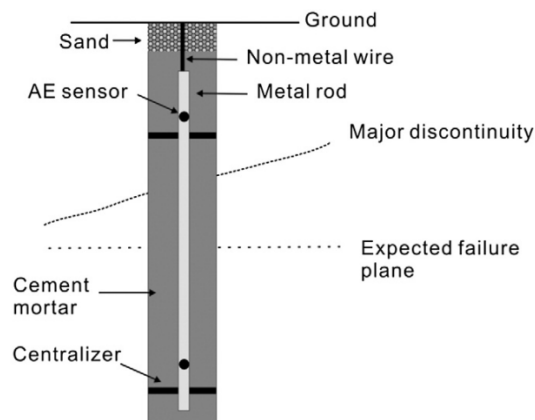
**Figure 2.10:** The concept of active waveguide in soil slopes: a hollow tube surrounded by a wave-generator backfill (i.e. gravel) is installed in a borehole which crosses any shear surfaces. After Dixon et al. (2014)

The resin and fibreglass wave-generator waveguide filling proposed by Nakajima et al. (1988) and Nakajima et al. (1995) (see Figure 2.11) was installed within a soil slope and gave good results to deformation when compared to strain gauge results. However, the total length of the waveguide tested in the field trial appears to be approximately 2.5 m, hence it is not clear whether this method would be suitable for longer lengths, and no trials were performed to assess accuracy and reliability of the proposed waveguide in the long-term (i.e. effects of degradation of the wave-generator material).



**Figure 2.11:** The active waveguide proposed by Nakajima et al. (1995). A fibreglass-reinforced resin wave-generator is placed within a steel pipe

A third type of active waveguide is the one proposed by Cheon et al. (2011) which consist of a metal rod grouted into a borehole (Figure 2.12). The grout used as wavegenerator, specifically designed to have high brittleness properties, is made of a super high-early-strength cement and Jumunjin sand, which is a standard sand in Korea.



**Figure 2.12:** The active waveguide proposed by Cheon et al. (2011)

### 2.4.2 Piezoelectric transducer

A piezoelectric transducer is a device that consists of a membrane made of piezoelectric material, usually ceramics, which generates electric charge in response to an applied mechanical stress. Piezoelectric sensors are commonly used to convert acceleration to an electric voltage and therefore are commonly used in the detection of acoustic emission. The two types of piezoelectric transducers to choose from are broadband and resonant. Broadband piezoelectric transducers respond to emissions over a large frequency bandwidth. Resonant transducers have normally higher sensitivity but can detect only emissions in the frequencies around the resonant frequency (Ozevin et al., 2006). It is normally advantageous to employ resonant transducers when working with a relatively narrow range of fre-

quencies to maximise the sensitivity within the range of interest and attenuate the frequencies that fall outside of it (Scruby, 1987). In geotechnical applications Dixon and Spriggs (2010) use resonant transducers (for details see Table 3.2 in Section 3.2.2.3), but other authors do not report the type of transducer used.

In general, the sensitivity of transducers is maximum for mechanical signals propagating in a direction parallel to the axis of the sensing element. However, it is important to note that the sensitivity of most accelerometers are independent of the mounting direction (i.e. vertical, horizontal or at an angle) (Hardy, 2003).

### **2.4.3 Signal conditioning**

Spontaneous AE emitted by a deforming material is often characterised by low amplitude and low signal-to-noise ratio (SNR). SNR is the ratio of the signal carrying useful information to the unwanted noise interference. The signal can be improved using pre-amplifiers and filters before being sampled.

#### **2.4.3.1 Pre-amplifier**

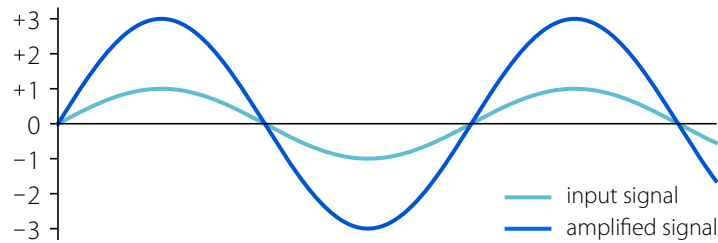
The mechanical signals associated with AE activity are often of very low amplitude (e.g.  $v \approx 10^{-7}$  m/s in some cases as indicated by Hardy, 2003) and a high gain pre-amplifier is generally required to prevent signal loss and minimize the noise interference contributed by surrounding circuitry (Mathiyaparanam, 2006). The pre-amplifier is an electronic component which purpose is to prepare the weak signal for further processing through increasing the signal amplitude above the noise floor. The amplifier works by taking power from an external source (e.g. power supply, battery, solar panel, etc.) and modulating the output power based on the characteristics of the input signal. The result is a signal which waveform is identical to the input but with larger amplitude (Figure 2.13). The amplification factor, also called gain, represents the quantity an analog amplifier would increase the signal amplitude. The decibel [dB] is the most common way of quantifying the

gain of an amplifier. Decibel is a logarithmic scale which is calculated by:

$$[dB] = 20 \log_{10} \frac{V_o}{V_i} \quad (2.7)$$

where  $V_o$  is the output voltage and  $V_i$  is the input voltage. Therefore, if the gain is 70dB the AE signal from the sensor [V] gets amplified by a factor of about 3000.

However, a single standard amplifier multiplies the input signal and the noise contribution of the electronic circuitry, by the gain of the amplifier. So while the amplitude of the input signal gets larger, so does the input noise, resulting in no improvement to the signal-to-noise ratio (SNR). In order to improve signal-to-noise ratio, multiple amplifiers are commonly used in a summing configuration (i.e. connected in parallel). For example, with two amplifiers the input signal amplitude increases by 2 as the two signals are correlated; however, the electronic noise increases only as  $\sqrt{2}$  as the two noise sources are uncorrelated. To significantly improve the signal-to-noise ratio, this principle can be extended to N amplifiers.



**Figure 2.13:** Principle of signal amplification with single amplifier. In the example the output-to-input signal ratio is 3:1, which corresponds to a 9.5 dB gain

#### 2.4.3.2 Band-pass filter

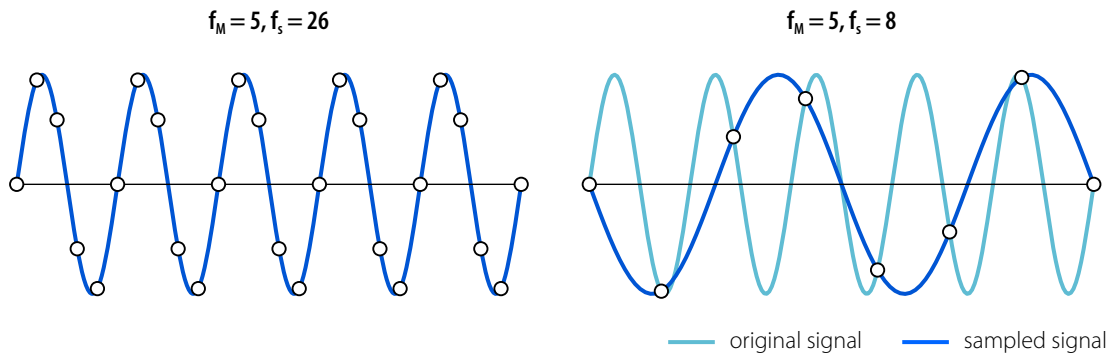
A band-pass filter is usually composed by a high-pass filter and a low-pass filter. Combining the effect of the two filters results that frequencies within a certain range (passband) are free to pass, whilst all other frequencies are significantly attenuated. This is needed to improve the SNR ratio and to ensure correct analog-to-digital conversion at the next step.

### 2.4.3.3 Analog-to-digital converter

The analog-to-digital converter is a device that samples a continuous-time analog signal [V] to a discrete-time digital number that represents the signal amplitude. The analog signal is sampled at a constant sampling frequency. The Nyquist-Shannon sampling theorem gives a rule for the minimum sampling frequency that has to be used in order to capture all the information from a continuous-time signal. The theorem states that to be able to reconstruct an unambiguous (univocal) signal of finite bandwidth from its samples, the sampling frequency ( $f_s$ ) must be at least double the maximum frequency ( $f_M$ ) of the original signal:

$$f_s \geq 2f_M \quad (2.8)$$

If the sampling frequency is lower, than more than one signal can be represented with the same points. This phenomenon is called aliasing. An example of correctly sampled signal and an example of a misidentified signal (aliasing) are provided in Figure 2.14 left and right respectively.



**Figure 2.14:** Analog-to-digital conversion. Left: signal adequately sampled. Right: example of aliasing. The original signal is represented in light blue and the signal interpreted from its samples is represented in dark blue

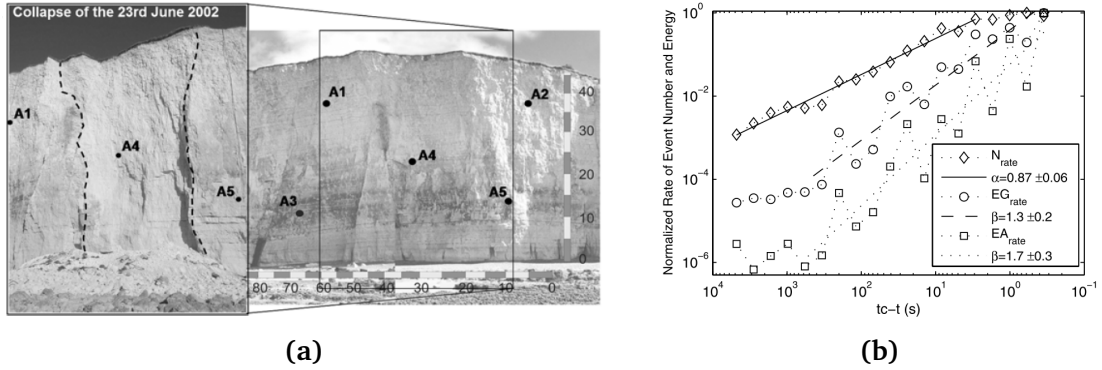


#### **2.4.3.4 Comparator**

The comparator is an electronic device that compares an input voltage with a set voltage threshold indicating which one is greater by providing a binary response: 0 for values lower than the threshold, 1 for values higher than the threshold. The sum of all the binary values assigned within an established monitoring period (e.g. 15 minutes) results in the number of times the acoustic input exceeds the threshold voltage. The name given to this process is ring-down counting and the number of counts takes the name of ring-down count (RDC) (e.g. Koerner et al., 1981).

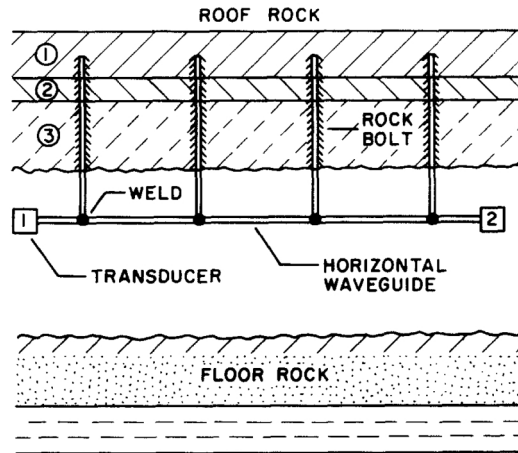
#### **2.4.4 AE monitoring systems in literature**

An interesting example of AE monitoring of a natural slope is provided by Senfaute et al. (2009) and Amitrano et al. (2005) who recorded the actual collapse of a slope and observed how the wave parameters evolved approaching failure. They installed a network of five seismic stations for monitoring of a natural chalk cliff in northern France made unstable by sea erosion. Each seismic station is composed of a seismometer (40 Hz – 1.5 kHz) and an accelerometer (2 Hz – 10 kHz) connected to a 40/60 dB pre-amplifier and a band-pass filter (170 – 10 kHz). All the seismic stations are connected to an acquisition system (40 kHz, 16 bits). The sensors were cemented in two 10 m vertical and three 6 m horizontal boreholes. The sensors are installed at a maximum distance of 50 m. Amitrano et al. (2005) analysed the statistical pattern of AE registered by one of the sensors before a cliff collapse. The analyses show that a power law acceleration of events rate number is defined on 3 orders of magnitude, within 2 hours from the collapse time and, at the same time, the average size of the seismic events (in terms of energy, which is function of signal amplitude) increases towards the time to failure (Figure 2.15). Amitrano et al. (2005) was the first to observe simultaneous power-law increase of seismic events and b-value decrease of a slope prior to collapse, recorded by a sensor located at about 5 m of the rupture surface during the 2 hours preceding a 10,000 m<sup>3</sup> collapse.



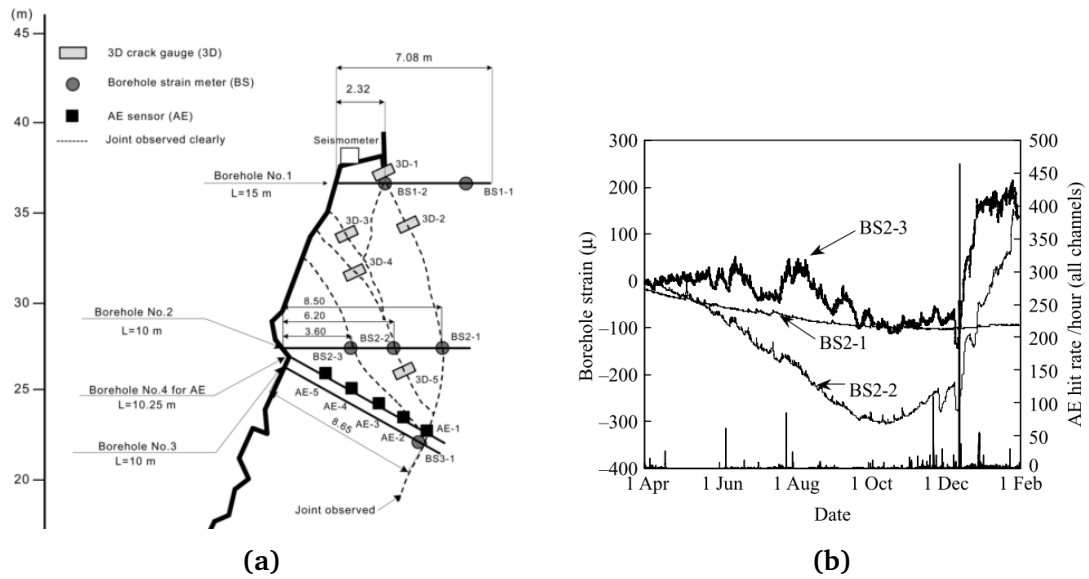
**Figure 2.15:** (a) Chalk cliff before and after collapse with location of the seismic stations; (b) Example of results obtained by Amitrano et al. (2005). Events rate number in event/s (diamonds), and reduced seismic energy rate ( $dE/dt$  divided by its maximal value) for the geophone (circles) and for the accelerometer (squares), as function of the time to collapse ( $tc-t$ ),  $tc$  being the time of collapse. The time axis is reversed. After Amitrano et al. (2005)

In the field of AE monitoring by means of waveguides, Hardy (1992) was among the first to apply this method to the monitoring of mine and tunnel roof stability. The system (Figure 2.16) was designed as an array of vertical bolts installed within the roof, and each bolt was connected to a horizontal waveguide, to transfer the AE signal generated within the rock to two transducers placed at the opposite ends of the horizontal rod. This configuration allowed to identify the approximate source of the roof instability and its severity. Using the difference in terms of arrival-time of the signal at the two transducers (procedure known as linear 1D source location) placed at the opposite ends of the horizontal waveguide, it was possible to determine which vertical bolt the acoustic emission was coming from.



**Figure 2.16:** Underground waveguide array obtained connecting several bolts by means of an horizontal waveguide for the monitoring of underground roof sections. After Hardy (1994)

Shiotani et al. (2001b), Shiotani (2004), and Shiotani (2006) proposed a system called the WEAD (WaveguideE for Acoustic emission waves due to rock Deformation) for the acoustic monitoring of rock slopes. The WEAD system comprises a waveguide on which multiple equally-spaced transducers (60 kHz resonant) are mounted in order to establish with great precision the source location. The typical mounting configuration is illustrated in Figure 2.17a. The sensors record the whole waveform data which is sent to a control room for data processing. The waveguide is placed within a pre-drilled borehole and grouted with a cement mix specifically designed to match the rock mechanical properties. The rock is sampled during borehole drilling and the parameters are obtained from laboratory tests. Shiotani et al. (2001b) and Shiotani (2006) report a field test of the system in a hornfels rock slope dipping  $80^\circ$ . 5 sensors are mounted on a waveguide (which is called a reinforcement) and cemented in a 10 m long borehole (Figure 2.17a). In situ measurements and comparison with 3 strain-meters installed in an adjacent borehole suggest a correlation between AE and strain increase. Typical results are reported in Figure 2.17b, which show a significantly higher AE hit at the beginning of a borehole strain increment.



**Figure 2.17:** (a) Installation at the site; (b) Example of results obtained by Shiotani et al. (2001b). Comparison between strain increment and AE hit hourly rates (AE hits are equivalent to RDC). Higher AE activity corresponds to strain increment. After Shiotani et al. (2001b)

More recently, Cheon et al. (2011) proposed an improvement to the WEAD system in order to overcome issues caused by wave attenuation and variable rock conditions. The improved system makes use of only two sensors at the opposite ends of the waveguide to determine the acoustic emission source; the grout surrounding the waveguide is designed to have a high brittleness becoming a wave-generator itself, rather than being designed on rock characteristics. In this system external background noise is excluded installing the sensor in the borehole and sealing the first two metres with high damping material. Cheon et al. (2011) established general damage level criteria through laboratory bending and shear tests on a model that comprised a waveguide and surrounding grout of increased brittleness before installation at a field site. The proposed system was installed in a weathered andesite slope in southern Korea which had previously failed during a typhoon and was reprofiled. AE analysed is from the summer of 2008 and 2009, which is the critical rainy season. Based on the criteria developed in the laboratory (Figure 2.18),

the authors suggested that the slope was in the early stages of shear failure. However, they warn that this method only indirectly evaluates the stability of a rock slope. In fact, the framework compares the damage in the waveguide-grout system measured in the lab to the AE measured in the rock slope, without considering the AE activity that is generated by the unstable slope itself.

AE parameters					Damage level	Failure type and feature	Applied force (kN)
Cumulative counts	Cumulative amplitude (mV)	Whether considering trends of summed parameter		b-value			
		Counts	Amp.	<60 dB	>60 dB		
$<3.5 \times 10^4$	–	Yes	No	$<1.54$	–	T I or S I <sup>a</sup>	10
$3.5 \times 10^4$ – $8.5 \times 10^4$	–	Yes	No	1.54–1.64	–	T II or S I	20
$8.5 \times 10^4$ – $<$	–	Yes	No	$<1.64$	–	T III or S I	25
$<2.3 \times 10^6$	$<6 \times 10^4$	Yes	Yes	0.72–	1.34–	S I	50–100
$2.3 \times 10^6$ – $5.4 \times 10^6$	$6 \times 10^4$ – $1.1 \times 10^5$	Yes	Yes	0.52–0.72	1.26–1.34	S II	200
$5.4 \times 10^6$ – $<$	$1.1 \times 10^5$ – $<$	Yes	Yes	0.40–	0.78–	S III	250

<sup>a</sup> T: tensile, S: shear.

**Figure 2.18:** Criteria for evaluation of damage level in unstable slopes based on shear and bending laboratory tests. After Cheon et al. (2011)

The monitoring system proposed by Dixon et al. (2003) makes use of an active waveguide (see Section 2.4.1) and a unitary battery-operated sensor Dixon and Spriggs (2010) known as the Slope ALARMS (Assessment of Landslides using Acoustic Real-time Monitoring Systems) to monitor displacement of fine-grained soil slopes. Laboratory tests and field trials have proved (Dixon et al., 2012; Dixon et al., 2014; Smith et al., 2014a; Smith et al., 2014b; Smith and Dixon, 2014) that detected AE trends are proportional to the rate of deformation (velocity) of the unstable slope. The acoustic emission rate ( $AE_{rate}$ ) of a slope is function of the displacement velocity ( $v$ ) and coefficient of proportionality ( $C_p$ ) (Smith, 2015):

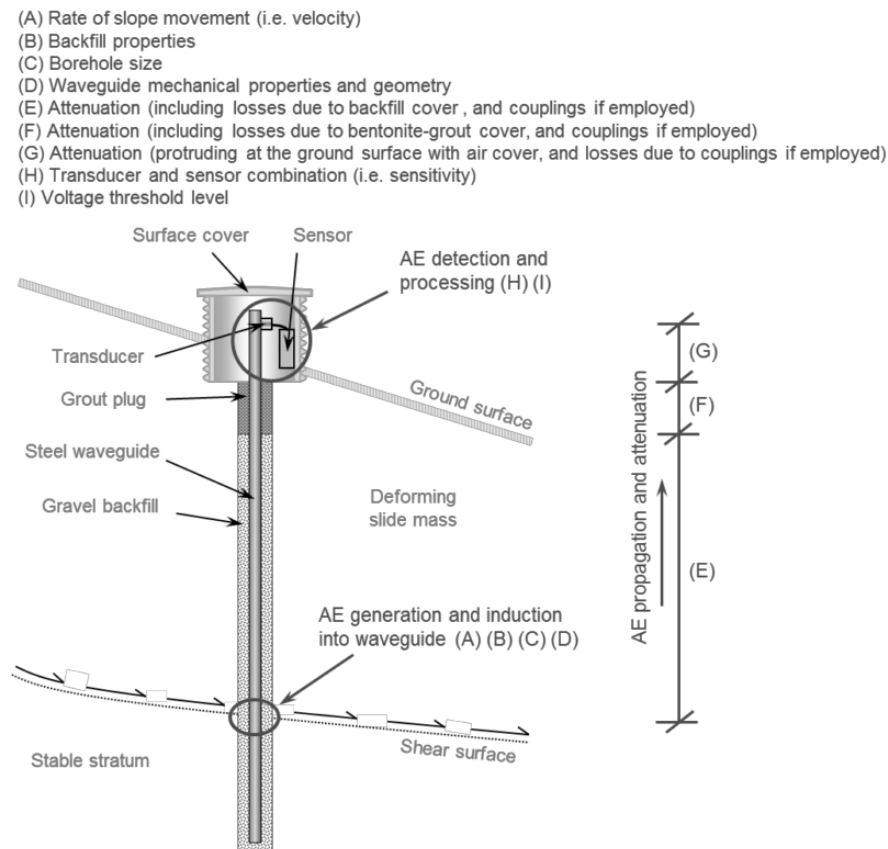
$$AE_{rate} = (C_p, v) \quad (2.9)$$

$$C_p = f(B, C, D, E, F, G, H, I) \quad (2.10)$$

where:

$B, C, D, E, F, G, H, I$  are the parameters that have influence on the system as the acoustic emission waves propagate from the shear surface to the sensor; the parameters are detailed in Figure 2.19. Smith (2015) studied these factors separately and proposed a series of charts defining empirical relationships for each of them.

Although specifically devised for the monitoring of fine-grained soil slopes, the Slope ALARMS system represents an advance in technology as it works continuously and in near real-time using reduced power consumption, thus not requiring to be plugged into the mains. Moreover, the system is able to send warning text messages through the mobile phone network to named users when a system of thresholds is exceeded. The system is explained in more detail in the methodology at Chapter 3.



**Figure 2.19:** Parameters that have an influence on the acoustic emission detected by the Slope ALARMS system. The schematic considers the use of an active waveguide installed in a fine-grained soil and placed across one (or more) shear surface(s). After Smith (2015)

## **2.5 Summary**

This chapter has outlined pertinent studies in the field of acoustic emission applied to monitoring of rock slopes.

It is well established that AE is generated by the nucleation and growth of cracks in the rock at the microscopic level (Section 2.3.1), therefore monitoring of AE can provide early information of developing phenomena. In fact, it is demonstrated through laboratory experiments (e.g. Evans, 1978) that the acoustic emission is proportional to damage and accelerating AE trends prior to collapse have been also observed in natural slope failure (e.g. Amitrano et al., 2005).

Acoustic emission is not a new monitoring technique, it has been employed for the monitoring of rock structures in the mining and tunnelling industry for decades. However, the application to natural rock slopes has so far hindered by attenuation-related issues.

Attenuation in rock is much lower than in other geotechnical materials, such as soils (see Figure 2.5 in Section 2.3), however in a rock mass attenuation is highly influenced by the presence of discontinuities and their characteristics (e.g. opening, spacing, filling, etc.). Therefore, only small portions of rock can be investigated and the location of transducer is crucial in order to detect emission generated from instability processes. Such a problem does not exist in tunnelling or mining where the source of acoustic emission is generally expected to be restricted to recently excavated areas (Hardy, 1992). However, in natural rock slopes there is generally more uncertainty about the location of possible shear zones or critical discontinuities, which could be situated much deeper into the rock mass. These may be difficult to identify due to lack of clear forerunners, as deformation preceding a failure can be of very small magnitude.

As attenuation is highly frequency dependent (i.e. low frequency waves attenuate much less than high frequency ones) some authors used low frequency waves

(i.e.  $<10,000$  Hz) in order to monitor larger portions of rock, but signals in this range of frequencies can be contaminated by noise generated from anthropic activities or external electronic interference. Therefore this approach seems to be appropriate for use in sites located at a distance from possible sources of noise. The application in areas where there is infrastructure, which are those where the monitoring is much needed, would pose more challenges requiring extensive signal filtering. Hence, the monitoring of signals  $>20,000$  Hz is advisable.

To improve the attenuation and noise problems some authors (e.g. Amitrano et al., 2005) have decided to grout the sensors within boreholes formed in the unstable rock mass at the desired depth and orientation. This approach allows to place a sensor closer to the location of interest and also to be placed further away from sources of noise. However, this method does not permit an easy maintenance of sensors; if a sensor does not work, it cannot be repaired or replaced.

A different approach adopted to, at least partially, overcome attenuation issues being able to use higher frequencies is to create a preferential path for stress waves to reach the transducer(s) by means of waveguides installed within the rock mass. The most notable contributions in this field were provided by Hardy (1992), with underground applications to mine and tunnel roofs, and Shiotani and Ohtsu (1999) with applications to rock slopes. They assessed the practicality of acoustic emission systems that make use of waveguides in the monitoring of rock structures. Significant contribution to the development of systems that use waveguides has been provided also by Dixon et al. (2003) in the application to soil slopes.

Dixon et al. (2010) proposed a battery-operated unitary sensor which uses reduced power to detect and process acoustic emission. Moreover, the system has also the capability to set thresholds and send short text messages (SMSs) for warning of ongoing increases in AE activity. This system represents a considerable advance in technology as it is robust, low maintenance, low power-demanding and portable thus suitable for the monitoring at remote locations where mains are not available



or access is restricted.

Practitioners agree (Michoud et al., 2013) that there is an evident need for development of sensors that are robust, have high life expectancy, are reliable, low maintenance, automatic, near-real time and are affordable, still providing high sensitivity characteristics.

Moreover, in the literature there is a lack of monitoring instruments directly able to raise warning of impending phenomena, that is that they don't have built-in communication modules and rely on integration within wider system with communication capability to be used for warning purposes. The cost of this additional segment must also be considered.

Although specifically conceived for the monitoring of soil slopes, the system developed by Dixon et al. (2010) provide the sought-after specifications discussed above. Hence, the extension to rock slope applications, with appropriate modifications, could be advantageous.

AE monitoring using active waveguides is becoming an established approach to monitor the stability of soil slopes, however, the very different behaviour of deforming rock slopes compared to soil slopes means that different acoustic emission rates and trends are detected and that correlation between acoustic emission rate and displacement velocity (i.e. Smith, 2015) is not applicable. Hence, the challenge is to firstly identify the mechanisms that generate the acoustic trends and secondly develop strategies to be able to interpret deformation from the detected AE rates. This constitutes the aim of this research project as defined in Section 1.2.

# Chapter 3

## Methodology

This chapter defines the research approach used to conduct the study and to address the research objectives stated in Section 1.2. Justification for the research design and the research instruments employed is given, explaining how the necessary data and information were collected. The main method used for data collection is field monitoring, supported by focused laboratory testing to address key variables influencing the performance of the system and eliminate associated uncertainties.

The methodology chapter is organised in five sections. Section 3.1 explains the methodological approach to the work used to address each objective. In Section 3.2 specifications of the AE monitoring system employed in this work is given, the reasons for choosing this apparatus are discussed along with the system limitations. A description of the two trial sites at which data were collected is provided in Section 3.3, detailing also the AE monitoring instruments installed at each site and the traditional monitoring instruments available. Section 3.4 gives details of the laboratory and field tests performed describing the equipment used and procedure. Section 3.5 summarises the methodology and research methods used in this work.

## 3.1 Research methods

The research methods applied to address each objective and the associated outputs can be summarised as follows:

- (1) Objective 1 was addressed by field data collection. As a wide number of variables are involved in the generation of AE in rock slopes, it was necessary to observe AE trends from real sites and compare these to conventional instrumentation (e.g. Shiotani et al., 2001a, see Section 2.4.4). The monitoring sites needed to be distinct cases to add value to the scientific development, as the use of a single case-study to generalise from is highly discouraged (Flyvbjerg, 2006). Two trial sites which could provide valuable information were set-up, they are characterised by different type of rock masses, different failure mechanisms and are monitored with a number of traditional geotechnical instruments;
- (2) Objective 2 was addressed by means of laboratory experiments in order to try eliminate uncertainties due to modifications made to the original monitoring system. As an AE wave travels through these components, it has an influence on RDC response. Therefore, these elements need to be validated to establish whether they are suitable for acoustic emission monitoring or not. This was done by designing experiments similar to those carried out on the system used for soils by Smith (2015), which allows performance comparison with the original system. Also experiments designed to achieve a better understanding of how the system performs when installed within a rock medium were carried out. These tests were performed on site, although this was not ideal due to health and safety reasons and the scale of the problem. However, given the complexity of the rock masses and their scale-dependant behaviour (Hoek, 1983, as seen in Section 2.1), it would be extremely difficult to replicate the rock mass or to take large-size samples to be tested in the laboratory.

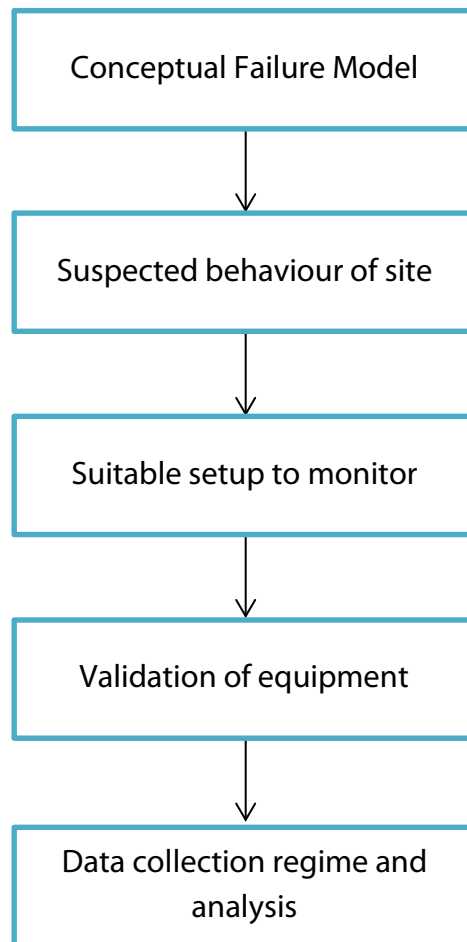
Experiments designed to address this objective are discussed in Section 3.4;

- (3) Objective 3 was addressed by developing a framework for the use of the system within rock slopes and to define strategies to interpret AE trends. This makes use of all information and experience gathered from AE data collection at the field trials, experiments conducted at the sites and testing of the impact of specific system elements in the laboratory.

The overall approach used to achieve the aim and objectives of this research is summarised in five key points in Figure 3.1.

Conceptual failure models for the two available trial sites were developed. Conceptual models allowed to formulate the most likely behaviour for each site and to make hypothesis on the possible locations where displacements would take place, and hence where acoustic emission is likely to be generated. The most suitable installation set-up for monitoring was then determined on the basis of the most probable locations where deformation, and hence AE, can occur.

Validation of the monitoring equipment was needed to establish whether all the system elements (in particular the modifications made to the system) were appropriate for acoustic emission monitoring.



**Figure 3.1:** Methodological approach

## 3.2 Measurement system

Rock slopes, in particular brittle rock masses, often show very small displacement magnitude prior to large scale and rapid collapses. There is therefore a need for systems that enable detection of ongoing processes as early as possible and allow action to be taken. As seen in Section 2.4.4, AE trends have been observed being emitted before collapse and patterns of ongoing accelerating damage could be recognised as long as two hours before collapse (e.g. Amitrano, 2004). This clearly demonstrates that recognising AE patterns in advance of slope failure is possible.

However, this technology has not been widespread as traditional AE monitoring is generally affected by attenuation-issues (which implies extremely localised monitoring, Section 2.3.2), the monitoring equipment is very demanding in terms of power, very expensive and often heavy and bulky (Section 2.3).

The AE sensor chosen and used throughout this work for collecting data is the unitary battery-operated Slope ALARMS sensor, acronym for "Slope Assessment of Landslides using Acoustic Real-time Monitoring Systems". The sensor was originally developed by Dixon and Spriggs (2010) and used in conjunction with a granular active waveguide (Dixon et al. (2014), see also Section 2.4.1) to assess the stability of fine-grained soil slopes by means of measuring the AE generated by the granular backfill installed in the moving slope. The concept was developed at Loughborough University and the sensor was designed in collaboration with the British Geological Survey.

The Slope ALARMS system was selected, among other AE and non-AE systems (Section 2.2), for its characteristics of:

- (i) *sensitivity*, in applications to soil slopes the system was able to detect AE trends linked to changes in displacement at very slow rate, e.g. 0.0018 mm/-day (Dixon and Spriggs, 2007), 0.075 mm/day (Smith, 2015, p. 257). A relationship that quantifies soil slope deformation using AE monitoring was also developed (see Section 2.4.4). In rock slopes, as AE is generated by development of new fractures and displacement along existing discontinuities (Section 2.3.1), the monitoring of the acoustic emission has the potential to give information useful to identify patterns of accelerating sub-mm displacements or even patterns linked to the formation of cracks (i.e. pre-displacement) and thus recognise the very early stages of a macroscopic failure process. As seen in Section 2.2 the most sensitive surface and subsurface monitoring instruments available today (e.g. extensometers, inclinometers) only have resolution of about 0.01 mm;

- (ii) *extended reach*, thanks to the use of a waveguide the reach of the sensor is increased, as opposed to placing an instrument on the rock mass surface, as traditional AE or seismic sensors, or across a singular specific discontinuity, as it happens for example with tiltmeters and wire extensometers;
- (iii) *high temporal resolution*, the capability of providing information continuously and in near real-time (i.e. up to 1 min) makes the sensor suitable to be used as an early warning device;
- (iv) *built-in warning system*, the sensor is capable of computing and communicating warnings of increasing acoustic trends (which in soil slopes are linked to increasing velocity of deformation) through the standard phone network sending SMSs to a pre-set list of phone numbers. None of the other AE monitoring systems found in the literature (see Section 2.4.4) is equipped with an integrated warning system which has the ability to send warnings, they were all used as monitoring systems rather than warning systems;
- (v) *reliability, robustness and low maintenance*, which make the system appropriate for long-term monitoring in the field environment and are characteristics highly sought after by practitioners (see Section 2.2). Sensors had been working for more than 5 years at some trial sites before major maintenance was carried out (e.g. see Section 3.3.1). Long-term robustness is a key area of existing traditional instrumentation that most practitioners agree need improvement (Michoud et al., 2013);
- (vi) *easy maintenance*, the sensor unit is placed at the ground level thus being very easy to access. Moreover, the transducer is tied to the free end of the waveguide and can easily be accessed or replaced. Many AE systems found in literature have their sensors grouted into the rock mass (e.g. see Section 2.4.4), which makes it impossible to get them repaired or replaced if malfunctioning occurs;

- (vii) *low power consumption*, the sensor architecture is optimised for minimal consumption, i.e. two 9.0 V/120 Ah air alkaline batteries are sufficient to power a sensor for up to 1.5 years, thus suitable for use at remote sites cutting work, costs and problems related to setting up a mains/solar panel connection which most of the traditional equipment require;
- (viii) *power back-up*, the dual battery system guarantees continuity of operation should the primary battery fail or discharge. Most geotechnical monitoring instruments do not feature an integrated power back-up; power back-up is often separately predisposed as part of the power wiring of extended monitoring network systems (i.e. multiple instruments networks), but often this essential feature is neglected (Michoud et al., 2013);
- (ix) *small dimensions*, the transducer, sensor and batteries assembly is easy to transport and requires a small space to be installed on site. Traditional AE equipment able to be left on site for prolonged periods of time (i.e. not portable hand-held units) is still very large in size.

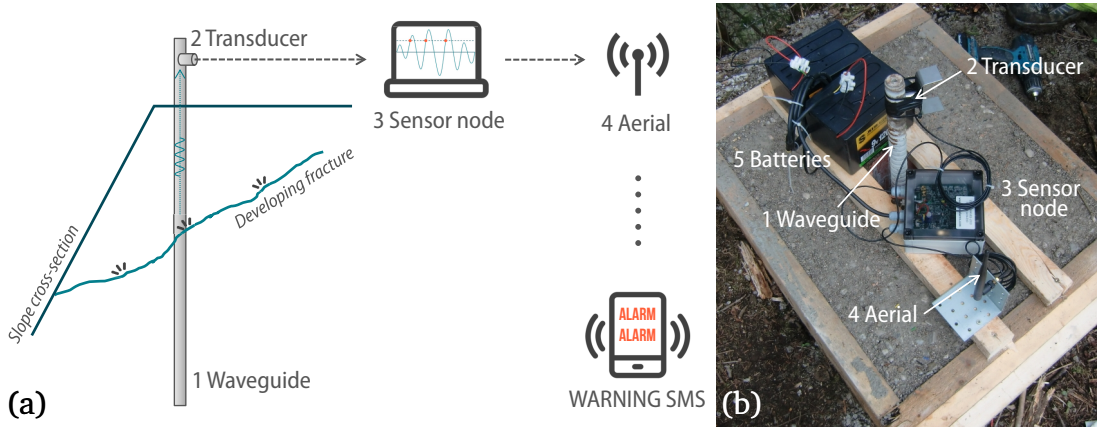
The Slope ALARMS sensor has so far been used in conjunction with the active waveguide developed by Dixon et al. (2003) for the monitoring of fine-grained soil slopes. However, the use of granular active waveguides is not appropriate for the monitoring of rock slopes. The principle of operation of the Slope ALARMS system is explained in the following Section 3.2.1. The main differences between the original system used for soils and the modified system used in this work for the monitoring of rock slopes are also described.

### 3.2.1 The Slope ALARMS system

The working principle of the system is based on the concept of using a steel pipe installed in a borehole, called a *waveguide* Section 2.4.1, to direct acoustic stress waves produced by a deforming body (i.e. soil or rock slope) to a piezoelectric



transducer (Section 2.4.2) mounted at the free end of the pipe. Figure 3.2 illustrates the working principle of the system installed within a rock slope.



**Figure 3.2:** (a) Simplified concept schematic of the Slope ALARMS acoustic emission monitoring system installed within a rock slope; (b) installation at one of the sites. As AE travels along the passive waveguide grouted into the rock mass (1), it is measured by a piezoelectric transducer placed at the free end of the waveguide (2) and subsequently processed by a sensor node (3). In case an alarm is triggered, a warning SMS is sent through the aerial (4). The system is battery operated (5). All the equipment is protected with a weatherproof cover

The system, as it was originally devised by Dixon et al. (2003), uses an active waveguide to generate an enhanced acoustic signal. The active waveguide (see also Section 2.4.1) consists of a steel tube placed in the centre of a pre-formed borehole then backfilled with a granular material (i.e. gravel) which is the primary source of acoustic emission as the soil mass moves. Ideally, the active waveguide should be installed through any shear surfaces or zone of deformation in order for the gravel to generate the stress waves.

When the acoustic signal travelling along the waveguide reaches the transducer mounted at the free end of the bar, the piezoelectric element continuously transforms the mechanical vibration of the pipe into an electric voltage. The voltage signal is then transferred via cable connection to a computing and data storage device called a *sensor node*.

The sensor node, which operates in continuous monitoring mode, processes the

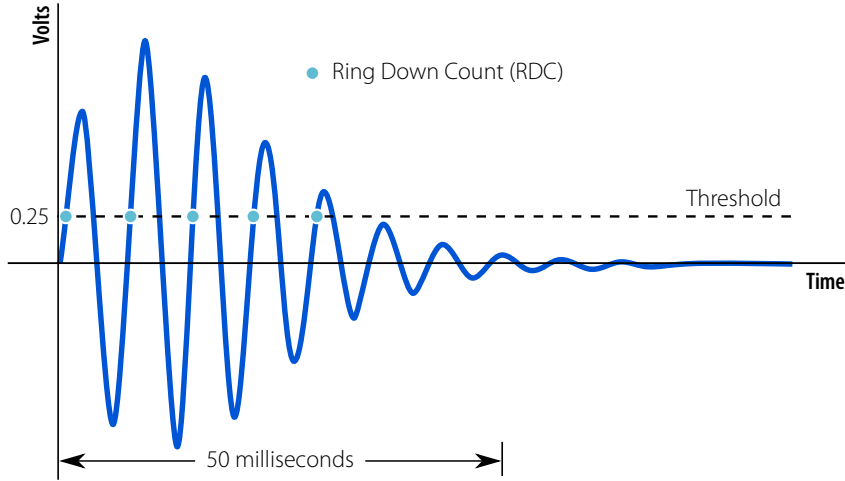
signal applying two pre-amplifiers for a total gain of 70 dB (Section 2.4.3.1).

Subsequently, a band-pass filter (Section 2.4.3.2) attenuates frequencies lower than 20 kHz and higher than 30 kHz so that only the frequencies in the range of interest are retained. The lower limit is set to remove background noise and the upper to restrict AE to a range that can be readily processed in this battery-powered device (i.e. higher processing rates would require increased power). AE in deforming rocks is commonly measured between 20 kHz–1 MHz (e.g. Manthei, 2005).

An analog-to-digital (A/D) converter (Section 2.4.3.3) samples the continuous voltage signal to a discrete digital number representing the voltage amplitude. Every A/D sampled voltage value is then compared to a user-selected threshold voltage, which can range from 0.05 V to 0.49 V. The threshold voltage is used to completely remove the effect of lower amplitude background electronic and spurious noise, hence it needs to be set sufficiently high so that no RDC is recorded during periods of time when there are no rock deformations occurring (e.g. during periods of good weather when no deformation is expected to take place, see for example Section 5.3.1) for the studies reported in this work it was set at 0.25 V. When a number of devices are installed at one site it is advisable to set the same voltage value for each device, so that the output is comparable. The comparator (Section 2.4.3.4) determines the number of times the threshold voltage is exceeded within one monitoring period, returning a number that takes the name of Ring Down Count (RDC). The concept of RDC counting is illustrated in Figure 3.3. For each monitoring interval, RDC is time-stamped and recorded in the sensor node memory.

The monitoring interval (also monitoring period or sampling frequency) can range from 1 to 60 minutes. It is possible to monitor the RDC every 5 seconds during installation or test purposes (i.e. they are not time-stamped and recorded). Typically, time periods of 15 minutes are a good compromise in order to maximise memory storage capacity and yet provide the benefit of high temporal resolution

monitoring.



**Figure 3.3:** Generalised concept of Ring Down Count. RDC is computed counting the number of times the signal exceeds a voltage threshold (e.g. 0.25 V) in a set period of time (e.g. 15 min). In the figure an example rate equal to 5 RDC/50 milliseconds is given

At the end of every monitoring period, the sensor compares the number of RDC counts with four user-selected alarm thresholds of increasing RDC magnitude. The sensor node is capable of sending an alert SMS with the corresponding warning status to a list of assigned responsible persons when one of the thresholds is exceeded. For soil slopes an empirical relationship (see Section 2.4.4) that links increasing RDC rates to increasing rate of deformation (i.e. velocity) have been found, therefore the thresholds can be set so that the four warning statuses available correspond to *Very slow*, *Slow*, *Moderate* and *Rapid* displacement rates (i.e.  $> 0.001$  mm/h,  $> 0.1$  mm/h,  $> 10$  mm/h,  $> 100$  mm/h respectively, Smith, 2015, p. 244).

### 3.2.2 System modifications

The system modifications made to the system for the applications within this work, compared to its previous applications to soil slopes (e.g. as used by Dixon et al., 2012), are essentially three:

- Use of passive waveguides (see Section 2.4.1 for active/passive waveguides);

- Use of threaded self-drilling rods as waveguides;
- Use of an improved version of the sensor nodes (i.e. the signal conditioning section of the system, Section 2.4.3).

The following three sections give a detail explanation of each one of the above items.

### **3.2.2.1 Grouted waveguides**

The installation of active waveguides in rock slopes is impractical as boreholes may be formed horizontally, hence the granular backfill would be arduous to place. It is also uncertain whether this method would provide benefits at all over grouting the waveguide within the rock mass. Acoustic emission generated within rock is effectively much less attenuated than in soil (Section 2.3.2), thus able to travel further along unbroken portions of rock. Therefore, in rock it is important to ensure continuity for the stress waves travelling within the rock to reach the waveguide (i.e. in particular stress waves that are not generated across the waveguide but in the rock surrounding it) and this can be achieved by grouting the waveguides within the rock mass. The grout is not expected to be the primary source of AE and the waveguide is therefore considered to be passive (see Section 2.4.1 for active/passive waveguides).

It could be objected that any material undergoing deformation generates acoustic emission and the grout is no exception, therefore generating AE of its own. This is correct when displacement or deformation involve the waveguide system (i.e. movement across the waveguide + grout). However, acoustic emission can be measured that is not generated across the waveguide as it will be assessed through testing at the field sites (Section 4.2.3). This means that AE is able to travel from the rock, through the grout and finally through the waveguide, and it is not generated by the grout. Hence, the grout is a mere medium for waves to be transferred

from the rock to the waveguide and cannot be considered as the primary generator of AE. Acoustic emission generated by grout cracking can only occur when the displacement involves the grout itself and therefore this has to be considered as a secondary effect.

Waveguides installed within rock slopes at the sites in this work were grouted with cement mortar to ensure continuity.

### 3.2.2.2 Waveguides

As said, passive waveguides were used in this work as opposed to the active waveguides utilised for the monitoring of fine-grained soil slopes (e.g. see Section 2.4.4).

In this work also two different types of steel pipes that serve as waveguides were used: standard smooth pipes (SW) and threaded pipes (TW). Table 3.1 reports specifications for both waveguide types including dimensions, material and type of cement used to grout the waveguides into rock masses.

The standard waveguides are composed of smooth pipes in 3 m lengths. The lengths are connected using screw threaded couplings to reach the required total length. These waveguides were inserted in a 101 mm diameter pre-formed borehole and grouted with a mixture of cement and water (see Table 3.1 for further details). The bottom end and the couplings of the pipe were sealed so the grout is present only on the outside and the centre is hollow (filled with air). This type of waveguides are referred to as standard because this is the type of pipes used in most Slope ALARMS applications (e.g. see Dixon et al., 2015a).

The threaded waveguides (see Figure 3.4) are self-drilling hollow bars commonly used in slope surface stabilisation (e.g. as anchor rock bolts, soil nails, etc.) for their ease of installation. Their use as waveguides is innovative: there is no need to pre-drill a borehole of bigger diameter, no need to use temporary drill casting, thus the time for installation is greatly reduced, as well as the overall cost. Moreover the use of Slope ALARMS in combination to this type of bars would al-

low thousands of existing installations to be monitored, reducing the costs even more and providing the added benefit of near real-time monitoring. The threaded waveguide technical sheet is reported Appendix A.

**Table 3.1:** Specifications of smooth and threaded waveguide types used in this work and and type of cement used to grout the waveguides

Waveguide	Smooth (SW)	Threaded (TW)
Manufacturer	Arvedi	DYWIDAG-SYSTEMS INT.
Product	EN10255 Heavy	DYWI <sup>®</sup> Drill R32-280
Material	S195T Steel	Steel
Finish	Galvanised	Plain
Length	300 mm	300 mm
Nominal Outer Diameter	50 mm	32 mm
Inner Diameter	35 mm	18 mm
Thread size	30 mm	(whole bar) 300 mm
Thread standard	UNI ISO 7-1	ISO 10208
Coupling dimensions	66 x 60 mm	52 x 140 mm
<b>Cement</b>		
Manufacturer	Buzzi Unicem	LEUBE Baustoffe
Product	Tipo I 52,5 R	CEM II/A-S 42,5 R WT38 'SPEZIAL'
Additives	No	No
Water/cement ratio	0.40	0.40



**Figure 3.4:** 32 mm outer diameter self-drilling threaded pipes

To install the self-drilling (hollow) bars a drill bit is attached on the first bar

and drilled into the rock using a standard rotary percussive drilling machine; when almost all the bar is drilled into the rock, a second bar is attached to the first one using a coupler with internal thread-stop. The process is repeated until the desired depth is reached. The annulus between the rod and borehole wall is filled by pumping cement mortar through the hollow stem to the drill bit thus backfilling towards the slope surface. The drill bit forms a hole that is 75 mm in diameter, which means that the grout around the bar is about 21 mm in thickness.

The downside of this installation approach is that in hard rock it is not possible to reach a great depth. Bars are quite thin for the stress they undergo and after about 10 m they struggle to transmit to the drill bit the power needed for progression into the rock mass. The suitability of this type of threaded bars to be used as waveguides was tested before installation. It was found that there is little difference in terms of signal propagation when compared to smooth pipes for use with the Slope ALARMS sensor node (Section 4.1.3). However, care must be taken when installing the piezoelectric transducers. The mounting configuration can greatly affect the transmission of stress waves from the bar to the transducer; the best mounting configuration was established with lab tests (Section 4.1.2).

Standard smooth waveguides were used at the Passo della Morte site (Chapter 5) and threaded self-drilling rods were used for the very first time as waveguides at the Grossreifling site (Chapter 6); the trial sites are introduced in Section 3.3.

#### **3.2.2.3 Sensor node versions MK1 and MK2**

Two versions of the Slope ALARMS (here intended as coupled transducer-sensor node) exist, the original first-built version MK1 and the upgraded version MK2. The version mostly used for this research work is the MK2, however at one of the sites (Passo della Morte, Section 3.3.1) the MK1 was installed prior to commencement of this work and then upgraded to MK2.

The principle of operation is the same for both MK1 and MK2, but hardware

and software were updated in the MK2. Slight differences in the components mean that the input signal is interpreted and processed in a different way, giving different RDC rates. Therefore data from the two series are not directly comparable. Testing of the two versions (Section 3.4) allowed to establish how different the response is. The main components leading to different RDC response are:

- (i) *Transducer* (Section 2.4.2), the Slope ALARMS MK1 mounted the Physical Acoustics R6 $\alpha$  transducer with a resonant frequency of 60 kHz, which have been substituted in the MK2 version by the R3 $\alpha$  transducer. Specifications of the two piezoelectric transducers are reported in Table 3.2 and calibration sheets are available in Appendix A. The transducers show significantly different operating frequency range and resonance frequencies, which translates into different sensitivities to the same input signal. The 30 kHz resonant frequency makes R3 $\alpha$  more suitable for monitoring of frequencies in the range 20–30 kHz. The frequency range of R6 $\alpha$  is higher compared to the 20–30 kHz range of interest; frequencies in this range are still recorded but the instrument sensitivity to them is expected to be lower;
- (ii) *Comparator* (Section 2.4.3.4), although both versions had the same voltage range (0.05 V to 0.49 V), version MK1 featured a manual setting switch which was not precise and didn't allow to know the voltage it was set at. The newer MK2 version of the sensors features a digital voltage setting, allowing precise control of threshold setting.



**Table 3.2:** Technical specifications of piezoelectric transducers. R3 $\alpha$  is used in the Slope ALARMS MK2 version while R3 $\alpha$  was used in the previous MK1 version of the system

Transducer	R6 $\alpha$	R3 $\alpha$
Manufacturer	Physical Acoustics	Physical Acoustics
Product	R6 $\alpha$	R3 $\alpha$
Type	Piezoelectric	Piezoelectric
Resonance	60 kHz	30 kHz
Peak sensitivity V/(m/s); [V/ $\mu$ bar]	75 [−64] dB	80 [−63] dB
Operating frequency range	35–100 kHz	25–70 kHz
Resonant freq V/(m/s); [V/ $\mu$ bar]	55 [90] kHz	29 [140] kHz
Directionality	$\pm 1.5$ dB	$\pm 1.5$ dB
Dimensions	19×22.4 mm	19×22.4 mm
Case material	Stainless steel	Stainless steel
Face material	Ceramic	Ceramic

#### 3.2.2.4 Monitoring periods and downsampling

The Slope ALARMS system allows to choose monitoring periods (also referred to as sampling frequency) as little as 1 min and up to 60 min in duration. 1 min monitoring periods are suggested when the system is purely used as a near-real time warning system, however, the memory storage would be quickly filled up. Therefore when RDC recording is relevant (e.g. in monitoring applications where trends need to be subsequently analysed) it is advisable to increase the duration of monitoring periods to maximise memory storage.

In this work the sampling frequency was set to 15 min to maximise node memory still providing a high temporal resolution. However, data discussed in this thesis are downsampled to 60 min periods. This is useful to match other instruments sampling frequency (i.e. rain gauge, snow gauge, piezometer, crackmeters) which is normally set to 60 min, allowing easier comparison of the outputs.

The criteria for downsampling follow the principle that data are recorded at the end of a monitoring period (e.g. data recorded at 07:00:00 refers to the interval 06:45:01 to 07:00:00). In the same way, values recorded at 15, 30, 45 minutes are

summed up to the next rounded-up hour, that is the following 00 minute (see an example in Table 3.3).

**Table 3.3:** Example of downsampling RDC/15min to RDC/hour

Date and Time	RDC/15min	RDC/h
16/02/2016 06:15:00	1	
16/02/2016 06:30:00	5	
16/02/2016 06:45:00	10	
16/02/2016 07:00:00	0	16

### 3.2.3 Limitations of the Slope ALARMS

The Slope ALARMS ability to minimise power consumption (i.e. 2 x 120 Ah/9 V air alkaline batteries are sufficient to power a sensor for up to 1.5 years) and maximise memory storage is due to the use of a simple signal processing approach, that is counting of the number of times the signal amplitude exceeds a single static threshold in a monitoring period (ring down count). Clearly such simple approach limits analysis capabilities as the waveform parameters are unknown. The use of an event-triggered recording of the whole waveform such as the Short Time Average/Long Time Average (STA/LTA), which is the most broadly used algorithm in weak-motion seismology, could provide increased information, e.g. the possibility to locate the AE source along the waveguide using the difference in arrival time of different wave modes (Maji et al., 1997). The STA/LTA algorithm continuously calculates the average values of absolute amplitude in two moving time windows. STA provides information about seismic events and LTA provides information about the temporal amplitude of seismic noise at the site. The system starts recording when the STA/LTA ratio exceeds a certain trigger value, which has to be user-selected. Successful recording of seismic events depends on adequate settings of the trigger parameters (Trnkoczy, 2012). However, the use of STA/LTA algorithms would not add benefits to the system. An algorithm that continuously calculates the ra-

tio between moving windows not only would require increased power use but also significantly increased sensor processing capacity and a memory capable of storing the enormous amount of data recorded. This translates into more expensive components, wiring to a mains power supply and much bulkier equipment, which is often impracticable when working at remote sites.

### 3.3 Trial sites

In order to achieve the research objectives (Section 1.2), to test system performance and suitability to be used as a rock slope monitoring and early warning system, it was essential to obtain real acoustic emission response from deforming/degrading rock slopes.

Two sites that could provide valuable information were instrumented and maintained during the course of this project. The sites, located at Passo della Morte in the Italian Alps and Grossreifling in the Austrian Alps, are characterised by different types of rock masses and different failure mechanisms.

A crucial aspect for monitoring these sites is that traditional instrumentation exist on site and weather data are available. Comparison with these data is an essential requirement to identify the origin of AE measured by the system (Objective 1).

Prior to deployment to the sites, the author performed testing and checks of the (then new-built) Slope ALARMS MK2 to test proper functioning, as the new version of the system was not installed at other sites, which included liaising with the electronic engineers to fix the software bugs that arose from equipment testing. The author also collected, sorted and analysed all weather, deformation and other data made available from project partners.

### 3.3.1 Passo della Morte (PdM)

This site located on the flank of the narrow Tagliamento River valley in the Italian Alps consists of a limestone layered rock mass (Figure 3.5) which is considered to be unstable for its structural layout with thin layers steeply laying parallel to the slope. The dip direction of the layers coincides with the slope, with layers inclined at  $73^\circ$  towards the valley. The rock mass has the potential to mobilise approximately  $650,000 \text{ m}^3$  of material in case of collapse of the whole unit (Codeglia et al., 2017). The site threatens the downstream villages for the potential of valley damming and consequent sudden discharge of the water accumulated at its back by the river, if dam outburst occurs (Codeglia, 2013).



**Figure 3.5:** Photograph of Passo della Morte (Italy) taken towards north-east, along the Tagliamento River valley. Modified after Codeglia et al., 2017

The failure mechanism expected for this site is of the translational sliding type (Table 2.1). The sliding is expected to occur along the major joint system (bedding) subsequent to the formation of a shear zone transverse to the bedding system at the base of the slope. This condition is needed because the bedding is parallel to the

slope (not daylighting) and thus the toe needs to be freed for the sliding to develop. A particularly stressed and fragmented zone was identified at the base of the slope, which leads to believe that this process is ongoing.

For the high threat that this portion of the slope represents, a large monitoring system was set up at Passo della Morte in various stages since the Summer of 2010. This monitoring project was undertaken by the Research Institute for Geo-Hydrological Protection of the Italian National Research Council (CNR-IRPI) on behalf of the Civil Protection Department to assess the state of activity of the unstable rock mass and risk associated. A plan of the site with instruments locations is provided in Figure 3.6. Table 3.4 details the existing instruments for which data were made available along with their location, sampling frequency, resolution and temporal range. Boreholes that accommodate instrumentation (including waveguides) were drilled from within the road tunnel that goes through the rock mass for its entire length. The tunnel ceased to be operational on 20/06/2016 and therefore it is no longer considered an element at risk.

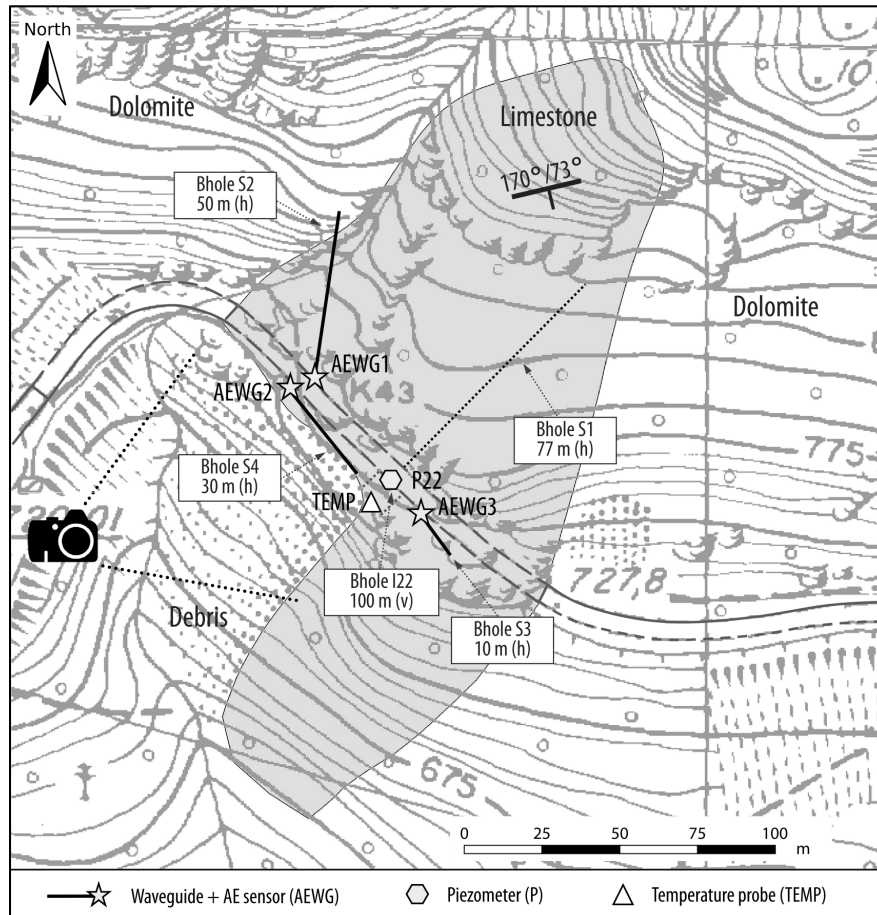
As part of this project, the site was instrumented with three Slope ALARMS MK1 sensors in three phases commencing in December 2010 (Series 1 in Table 3.5), prior to the start of this PhD project. In October 2014 the sensors were all replaced by the author with the newer MK2 sensors (Series 2 in Table 3.5).

The author has been involved with the study of this site since 2010. The author identified possible evolution scenarios and contributed to installation of monitoring instrumentation as reported in her dissertation (Codeglia, 2011). The author later continued to contribute to the study of this site by producing a 3D run-out model of the potential landslide which was discussed in her Master's thesis (Codeglia, 2013); parts of this work were published in Codeglia et al. (2017).

Passo della Morte is located in an area of high seismicity, the expected peak ground acceleration (PGA) at site is in the order of 0.225-0.250 g with 10% probability of exceedance (occurring probability) in 50 years. Therefore earthquakes of

$M_L \geq 2.5$  occurred within 20 km from PdM were taken into consideration as possible source of AE. The earthquakes database was obtained from the Italian National Institute of Oceanography and Experimental Geophysics (CRS-OGS, 2016) and refers to the period 17/12/2010–10/01/2016.

The site and acoustic emission trends associated are discussed in Chapter 5.



**Figure 3.6:** Schematic of the unstable limestone rock mass outcrop and position of waveguides (AEWG1, AEWG2, AEWG3), along with piezometer (P22), temperature probe (TEMP). The camera icon indicates the approximate camera position used to photograph the west rock mass face; (h) and (v) indicate horizontal or vertical borehole orientations

**Table 3.4:** Specifications of instruments installed at Passo della Morte site. For each instrument are reported: identification code (ID), device type, location, near real-time data (Near-RT), sampling frequency and resolution

ID	Device	Location	Sampling frequency	Resolution	Data start	Data end
P22	Piezometer	Bhole I22	60 min	1 mm	20/04/2011	31/12/2016
AEWG1	50 m steel waveguide + AE sensor	Bhole S2	15 min		16/12/2010	31/12/2016
AEWG3	10 m steel waveguide + AE sensor	Bhole S3	15 min		27/09/2011	31/12/2016
AEWG2	10 m steel waveguide + AE sensor	Bhole S4	15 min		12/10/2012	31/12/2016
EXT4	Crackmeter	West face	60 min	0.01 mm	20/04/2011	03/09/2014
EXT5	Crackmeter	West face	60 min	0.01 mm	20/04/2011	03/09/2014
EXT6	Crackmeter	West face	60 min	0.01 mm	20/04/2011	03/09/2014
TEMP	Thermometer	Opening	60 min	0.01°C	20/04/2011	31/12/2016
PLUVIO	Rain-gauge	Lat 46.3921, Lon 12.7149	60 min	0.1 mm	01/10/2010	31/12/2016
SNOW	Snow-gauge	Lat 46.3505, Lon 12.6790	60 min	10 mm	01/01/2012	12/05/2016

\*From top of borehole

**Table 3.5:** Specifications of AE monitoring installation at Passo della Morte site. Series 1 and Series 2 refer to data collected using Slope ALARMS MK1 and MK2 respectively

	<b>AEWG1</b>	<b>AEWG2</b>	<b>AEWG3</b>
Wg length	50 m	30 m	10 m
Wg type	Smooth*	Smooth*	Smooth*
Wg orientation	Horizontal	Horizontal	Horizontal
<b>Series 1</b>			
Data start	16/12/2010	27/09/2011	12/10/2012
Data end	07/08/2014	13/10/2014	13/10/2014
Sensor version	MK1	MK1	MK1
Firmware	V0.0 Build 0	V0.0 Build 0	V0.0 Build 0
Transducer	R6 $\alpha$	R6 $\alpha$	R6 $\alpha$
Voltage threshold	Medium	Medium	Medium
Log frequency	15min (until 27/09/2011)	30min (until 04/11/2013)	30min (until 04/11/2013)
	30min (until 07/08/2014)	15min (until 13/10/2014)	15min (until 13/10/2014)
Data time zone	UTC+1 (no Summer Time)	UTC+1 (no Summer Time)	UTC+1 (no Summer Time)
File format	.rdc	.rdc	.rdc
Conversion script	RDC2XLSG2.exe v. 10/02/2012	RDC2XLSG2.exe v. 10/02/2012	RDC2XLSG2.exe v. 10/02/2012
<b>Series 2</b>			
Data start	13/10/2014	13/10/2014	13/10/2014
Data end**	31/12/2016	31/12/2016	31/12/2016
Sensor version	MKII.1	MKII.1	MKII.1
Firmware	V1.1 Build 1221	V1.1 Build 1221	V1.1 Build 1221
Transducer	R3 $\alpha$	R3 $\alpha$	R3 $\alpha$
Voltage threshold	0.25 V	0.25 V	0.25 V
Log frequency	15min	15min	15min
Data time zone	UTC+1 (no Summer Time)	UTC+1 (no Summer Time)	UTC+1 (no Summer Time)
File format	.sart	.sart	.sart
Conversion scripts	SART2XLS.exe v. 20/12/2013	SART2XLS.exe v. 20/12/2013	SART2XLS.exe v. 20/12/2013

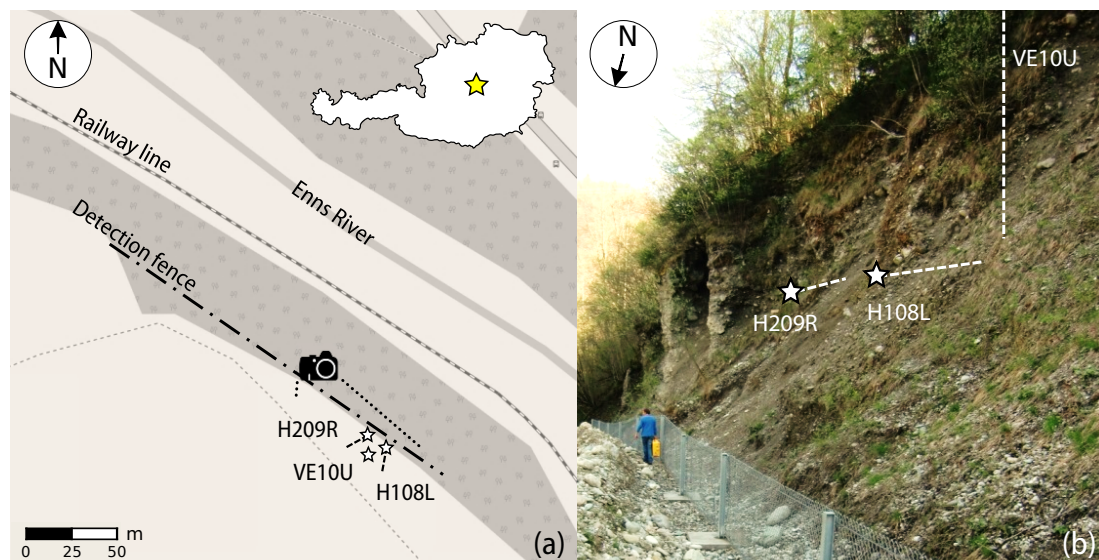
\*see Table 3.1 for waveguide specs; \*\*End of data considered in this work, monitoring is still ongoing



### 3.3.2 Grossreifling (SART)

Situated in the Austrian Alps, this site concerns a conglomerate slope which endangers a section of the local freight train line. A map of the site is provided in Figure 3.7. The site has a history of rock falls detaching from the slope and landing on the rail track. The most recent rockfall of large volume occurred in April 2013 can be seen in Figure 3.8.

According to the Varnes' landslide classification (Table 2.1, Section 2.1) the phenomena affecting this slope are of the rockfall type. Detachment of elements that constitute the conglomerate, mainly due to weathering processes such as freeze-thaw, rainfall washout, etc. are expected to affect this slope. The size of rockfalls is variable as the conglomerate includes particles of a range of sizes, from pebbles to large boulders. In general volumes up to  $1 \text{ m}^3$  are expected for single elements, however, depending on local conditions, larger portions of conglomerate can be destabilised up to  $10 \text{ m}^3$ .



**Figure 3.7:** Grossreifling (Austria) site location: **(a)** schematic map of the site with waveguides and detection fence location, note the railway line at the base of the slope; **(b)** image of the conglomerate slope with location of the sensor nodes and projection of the steel bars



**Figure 3.8:** April 2013. Rockfall occurred at the Grossreifling site landing on the rail track. The boulder of about  $0.8 \text{ m}^3$  is broken in two pieces

The AE monitoring system at Grossreifling trial site was installed in April 2014 as a complementary component of the Sentinel for Alpine Railway Traffic (SART) project. The project was undertaken by INGLAS GmbH with Loughborough University as partner, on behalf of the Austrian Federal Railways (OeBB) and Austrian Research Promotion Agency (FFG).

SART is a pilot project which aims to increase the safety of mountain railways reducing the risk of track and train damage due to rock falls occurring along the rail line, providing also a cost saving alternative to expensive dynamic rock fall barriers.

The SART system takes advantage of a dual approach: early warning of imminent rockfalls, provided by the Slope ALARMS through monitoring of the acoustic emission generated within the rock forming the slope; and detection of occurrence, provided by a light static catch fence instrumented with movement sensors and cameras (Detection Fence) that give information about impacts occurring on the fence. The two subsystems share a common control centre able to issue warnings and alarms to the rail traffic operator, providing information in time to take action, specifically slow down or stop the railway traffic (although this control function

was not implemented in the pilot phase).

The slope was selected by OeBB for the pilot project. The main reason for the selection is the occurrence of the rock fall in April 2013 (Figure 3.8) which reached the rail track. Hence, it is considered likely that other instabilities would affect the same slope in the near future.

Three Slope ALARMS sensors were installed by the author at this site in April 2014. The piezoelectric transducers were mounted on two 3 m horizontal waveguides (Sensors H108L and H209R) and one 12 m vertical waveguide (Sensor VE10U). Table 3.6 summarises all the specifications and settings relative to the three sensors.

At the SART site weather data (temperature and rainfall) measured at a nearby weather station are available. Also records of impacts on the Detection Fence are available and were compared to the RDC trends measured on site. Table 3.7 reports the location, sampling frequency and data temporal range available for these instruments.

Grossreifling site and data are discussed in detail in Chapter 6.

**Table 3.6:** Parameters and specifications of Grossreifling site installation, including: waveguides lengths and types, sensor and firmware version, type of transducer, timezone used for data recording, start and end of data recording, log frequency, file format and conversion script version used to convert the .sart files into readable .xls files

	H108L	H209R	VE10U
Wg length	3 m	3 m	12 m
Wg type	Threaded*	Threaded*	Threaded*
Wg orientation	Horizontal	Horizontal	Vertical
Data start	01/04/2014	01/04/2014	01/04/2014
Data end**	31/12/2016	24/06/2016	17/12/2016
Sensor version	MK2	MK2	MK2
Firmware	V1.1 Build 1221	V1.1 Build 1221	V1.1 Build 1221
Transducer	R3 $\alpha$	R3 $\alpha$	R3 $\alpha$
Voltage threshold	0.25 V	0.25 V	0.25 V
Log frequency	15 min	15 min	15 min
Data time zone	UTC+1 (no Summer Time)	UTC+1 (no Summer Time)	UTC+1 (no Summer Time)
File format	.sart	.sart	.sart
Conversion script	SART2XLS.exe v. 20/12/2013	SART2XLS.exe v. 20/12/2013	SART2XLS.exe v. 20/12/2013

\*see Table 3.1 for waveguide specs; \*\*End of data considered in this work, monitoring is still ongoing

**Table 3.7:** Range of instruments available for comparison at SART

Device	Location	Sampling frequency	Data start	Data end
Rain gauge	Lat 47.6469, Lon 14.7611	60 min	01/04/2014	31/12/2016
Thermometer	Lat 47.6469, Lon 14.7611	60 min	01/04/2014	31/12/2016
Detection fence	Interception ditch	Trigger	01/04/2014	31/12/2016

## **3.4 Laboratory testing of system elements and field experiments**

RDC measured by the system depends on a number of factors. Different versions of the sensor nodes and transducers, transducer mounting configurations and different types of waveguides, can all have an impact on the number of counts that are ultimately measured by the system. This is because AE travelling through different types of components result in slightly different RDC rates.

Laboratory tests were designed to assess in what capacity the RDC response is affected. Testing of each equipment component with reference to a standard (i.e. in this case is the use of a MK2 sensor node combined to a smooth waveguide) is important to quantify these differences and to enable generalised rules to be drawn for a wider usage of the system.

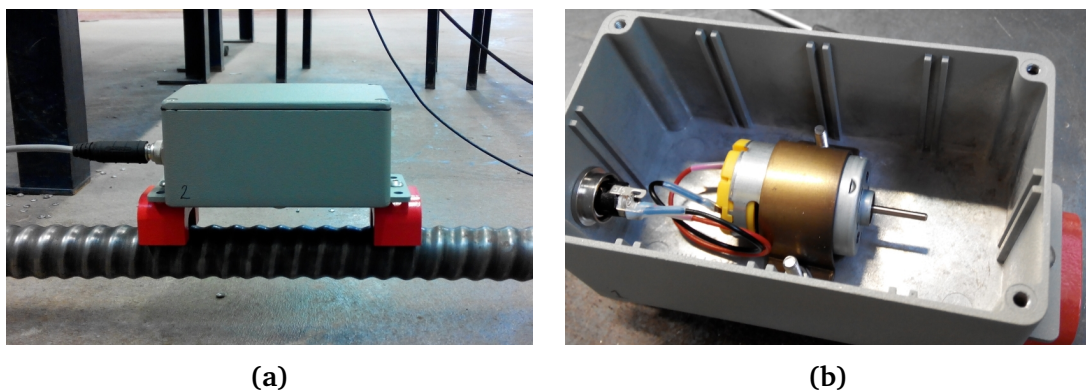
Laboratory experiments were carried out to try eliminate uncertainties due to modifications made to the original monitoring system. This allows performance comparison with the original system. Field experiments were designed to achieve a better understanding of how the system performs when installed within a rock medium, trying to assess the extent of rock that the system is able to monitor in the field and find possible sources of unwanted AE activity which could interfere with the system and trigger false alarms.

In this section the controlled AE source generator used for laboratory experiments is described in Subsection 3.4.1. Laboratory tests and field experiments design and procedures are detailed in Subsection 3.4.2 and Subsection 3.4.3 respectively. Laboratory and field testing results are discussed in Chapter 4.

### 3.4.1 Controlled AE generator

Laboratory experiments required a repeatable and consistent source of acoustic emission to test system components. The portable controlled AE source generator developed by Smith (2015, p. 195) was chosen. This generator was developed to generate AE waveforms that replicate those generated by deforming soil, however, the apparatus generally emits characteristic acoustic emission waves in the range of interest (20–30 kHz) and the output is repeatable and consistent. In this work the AE generator will not be used to specifically replicate acoustic waveforms comparable to those emitted by rock slopes; it will be used to test and compare specific system components. For these tests the crucial aspects of the AE source are repeatability and consistency. Another reason for choosing this apparatus was that the laboratory tests on system components can be compared with those obtained by Smith (2015) who used the generator for similar experiments.

The AE generator features a 26,000 RPM DC motor encased in a waterproof case which connects to the waveguide using magnets (Figure 3.9). The motor is wired to a control box which houses the battery and allows 1 second, 10 seconds, and 100 seconds bursts of vibration to be induced. After the selected time elapses, the power is cut automatically to ensure repeatability.



**Figure 3.9:** The controlled AE source generator developed by Smith (2015); **(a)** exterior, magnets are used to connect the encased motor to a waveguide; **(b)** interior, the DC motor is fastened to the waterproof case

### 3.4.2 Laboratory testing

For consistency, all laboratory tests were performed using the following set-up:

- (i) a Slope ALARMS MK2 version (for specifications see Section 3.2.2.3) coupled with the R3 $\alpha$  transducer (detailed in Table 3.2) was used;
- (ii) a threshold voltage of 0.25 V was used;
- (iii) waveguides were placed on a series wood stands and sponges to elevate the bars from the working surface and remove any mechanical contact. Sponges were used because of their low stiffness and density characteristics which ensure a high acoustic impedance contrast at the interface waveguide-sponge, thus signal losses into the sponge are minimal and can be assumed to be negligible (Smith, 2015, p. 192);
- (iv) a film of gel-based ultrasonic couplant (commonly referred to as silicone gel) was spread at the interface pipe-transducer to facilitate the transmission of AE energy. This works by removing any air pockets introduced by material microstructure (i.e. materials at the interface are not perfectly in contact). The reason is that air acoustic impedance is much lower than that of the ceramic sensor face or the steel pipe and would cause significant loss in transmission.

#### 3.4.2.1 Comparison of versions MK1 and MK2 (Test A)

This test was carried out in order to assess the difference in terms of RDC response between the old Slope ALARMS version MK1 and the newer MK2 (sensor node and transducer couples). This experiment was aimed in particular to assess whether Series 1 and Series 2 measured at PdM with the two versions of the system were comparable.

Differences of the two system versions are discussed in Section 3.2.2.3 and essentially can be summarised in: different transducers, version MK1 was paired with

R6 $\alpha$  transducer whereas version MK2 was paired with R3 $\alpha$  transducer, and different voltage threshold setting apparatus, MK1 featured a manual switch whereas MK2 features an electronic setting. The manual switch does not allow an accurate control of the threshold voltage setting, which means that there can also be differences in terms of RDC response among different MK1 sensor nodes. A different voltage setting would produce a different RDC response as assessed by Smith (2015).

The devices tested were three MK1 devices that were installed at PdM site (AEWG1, AEWG2, AEWG3 of Series 1 in Table 3.5), which voltage setting was set to "medium" on site (i.e. value in the region of 0.2 – 0.3 V), and one MK2 sensor node with 0.25 V voltage threshold for comparison.

A standard smooth waveguide (specifications in Table 3.1) placed on sponge stands was used for this test. For each one of the sensors the relative transducer was placed at 0.15 m from one end of the waveguide at one time and fastened to the waveguide with elastic bands. A film of silicone gel was used to ensure optimal coupling between the steel tube and the transducer face. The AE generator (Section 3.4.1) was placed at a constant centre-to-centre distance of 0.5 m from the transducer. For each sensor, the test comprised 45 x 1 second and 15 x 10 seconds bursts of vibration from the wave-generator.

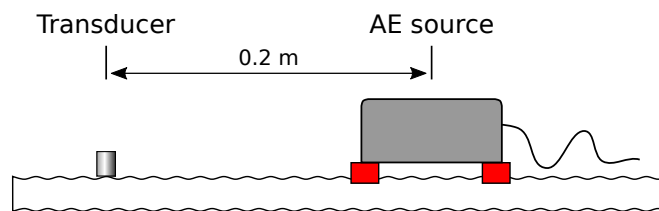
#### **3.4.2.2 Transducer mounting on threaded waveguide (Test B)**

The test was designed to assess the influence of different transducer mounting configurations on a threaded waveguide of the type detailed in Table 3.1. The aim of this series of tests was to determine the best possible transducer mounting configuration that allows the greatest transmission of the induced signal at the threaded pipe–transducer interface, with minimal losses. The best configuration is considered to be the one which results are the closest to those obtained performing the same experiment on a smooth pipe, which was considered as reference.

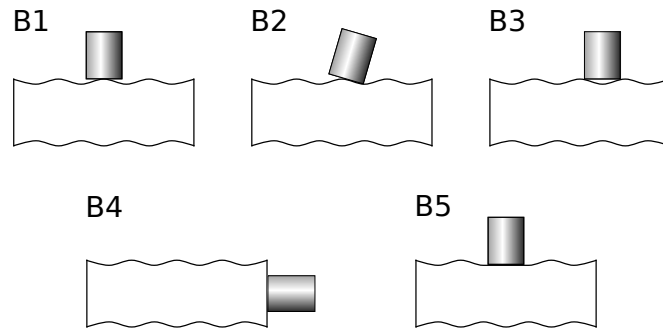


This experiment comprises a controlled AE generator (see specifications in Section 3.4.1) and a piezoelectric transducer mounted over a threaded hollow waveguide of the type reported in Table 3.1. A centre-to-centre distance of 0.2 m between the transducer and the AE generator machine was maintained throughout the tests so that effects of attenuation (Section 2.3.2) were consistent. A schematic of the test setting is reproduced in Figure 3.10.

The first test was conducted on a smooth waveguide for reference, the position of the transducer was upright on the tube (B0). The subsequent tests were conducted on a threaded waveguide; five different transducer mounting configurations were considered: upright on a thread (B1), at an angle to the side of a thread (B2), upright over two threads with additional silicone gel filling the gap in between the two threads (B3), horizontal at the end of the pipe (B4) and upright on a flat area formed by filing consecutive threads (B5) as can be seen in Figure 3.12. The configurations are depicted in Figure 3.11. The transducer was secured to the waveguide using a cable tie, except B4 where the transducer was held in place by pinching it between the pipe and a heavy plastic box. Each test comprised of 10 x 1 second bursts and 10 x 10 seconds bursts of vibration from the AE generator. The results were compared to those obtained from the test conducted on a standard smooth steel pipe (B0).



**Figure 3.10:** Test B set-up. The transducer and AE source were installed at a constant centre-to-centre distance of 0.2 m



**Figure 3.11:** The five transducer mounting configurations considered in Test B



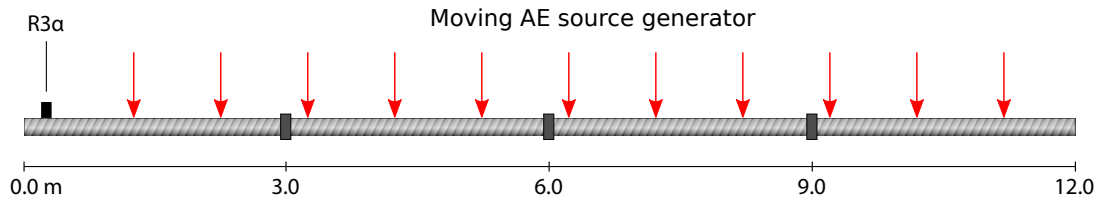
**Figure 3.12:** Transducer mounting on flattened threads obtained by filing (B5)

### 3.4.2.3 Attenuation in threaded waveguides (Test C)

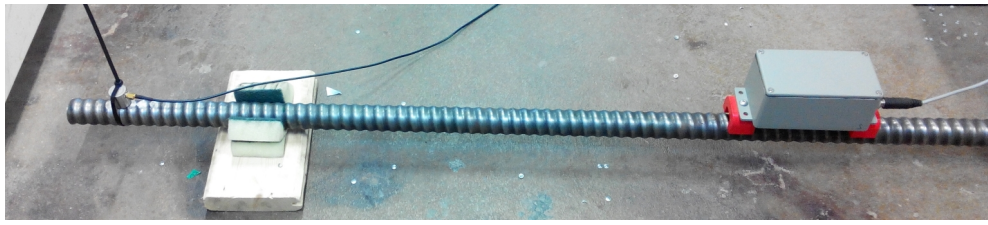
This test was designed to assess the attenuation in threaded waveguides including the effect of couplings that connect rod lengths and it compares to the attenuation in smooth waveguides. The results of this test were compared to those obtained by Smith (2015, pp. 198–200), who performed the same experiment with the same equipment on a 16.5 m long smooth waveguide.

The test was performed on 4 lengths of threaded hollow rods (see Table 3.1 for details) screwed together for a total length of 12 m. As the tightness of couplings can affect the wave transmission as demonstrated by Smith (2015), the bars were tightened with the aid of chain wrenches; silicone gel was spread on the bars ends and inside the couplers to ensure that no air gaps were left. The transducer was mounted on a flat surface obtained by filing some threads and secured with a cable

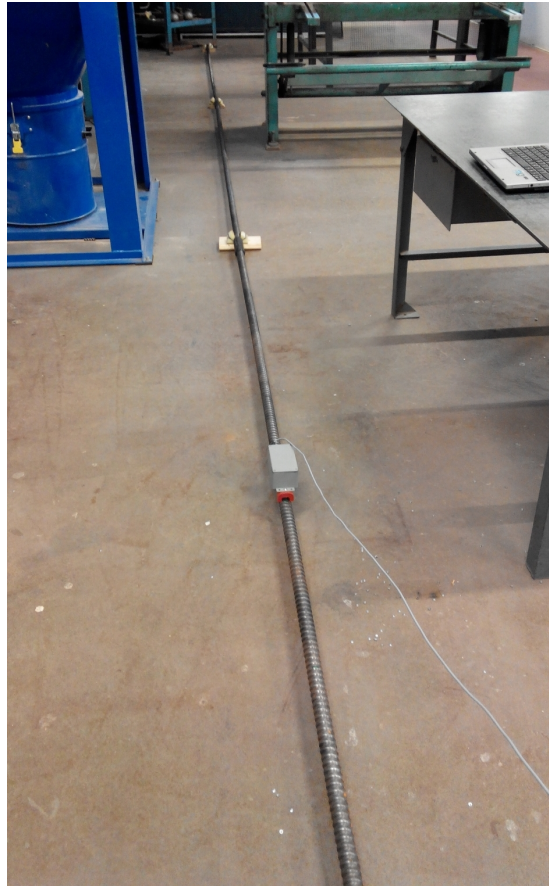
tie. A film of silicone gel was spread on the transducer face to ensure optimal coupling. The AE source generator was placed initially at a centre-to-centre distance of 1 m from the transducer (Figure 3.14 shows the initial test set-up) and then the distance was increased of 1 m at a time as reported in the schematic in Figure 3.13.



**Figure 3.13:** Schematic representing Test C set-up



**Figure 3.14:** Test C. A threaded waveguide is positioned on a stand made of sponges, the transducer is placed on a flat surface and tied to the waveguide



**Figure 3.15:** The 12 m waveguide employed in Test C

### **3.4.3 Field experiments**

All field experiments were carried out according to the following prescriptions:

- (i) AE was measured using the sensor nodes already present on site;
- (ii) At the time of testing all sensors were of the MK2 version and the threshold voltage was set to 0.25 V, see Series 2 in Table 3.5 for sensors installed at PdM and Table 3.6 for sensors installed at SART.

#### 3.4.3.1 Attenuation along waveguides on site (Test D)

A factor that affects attenuation in waveguides (Section 2.4.1) is the type of external environment (material) that surrounds the waveguide. This is in fact responsible for losses of signal at the interface. As it would be impractical to replicate the rock mass properties in the laboratory, this test was carried out on site.

This experiment was designed to assess the attenuation along a waveguide installed on site, which external environment is the rock mass. This is necessary in order to assess whether a signal generated several metres (as long as 50 m) away would propagate all the way to the transducer, or it would be damped along the path.

This experiment was carried out at PdM as waveguides at this site are hollow and thus a wave-generator can be inserted within them (waveguides installed at SART are completely grouted). A small artificial source was used to generate AE in the range of interest. The AE generator was a 10,000 RPM motor (equivalent to a rotational frequency of 167 Hz) with a power input of 6 V (this is different from the motor in the AE generator described in 3.4.1). The 10,000 RPM motor was chosen for the small body diameter ( $\varnothing$  28 mm), required to fit it into the inner  $\varnothing$  35 mm diameter of the waveguide, and the relatively high rotational frequency. The restricted space available between the motor and the tube did not make possible to encase the motor in a water-tight protective shell, however the holes in the motor body were filled with grease for protection from moisture ingress. The motor was attached to a 50 m power cable to be able to test the whole length of the waveguides. The control box used for this experiment was the same as for the wave-generator used in the lab (see Section 3.4.1). The control box allows regular sets of 1, 10 or 100 seconds of continuous vibration to be induced. The equipment is shown in Figure 3.16. The AE generator was secured to a  $\varnothing$  4 mm galvanised steel wire rope to aid insertion into the tube Figure 3.17. The equipment was tested in the lab and this configuration was found to give repeatable and consistent RDC

rates.

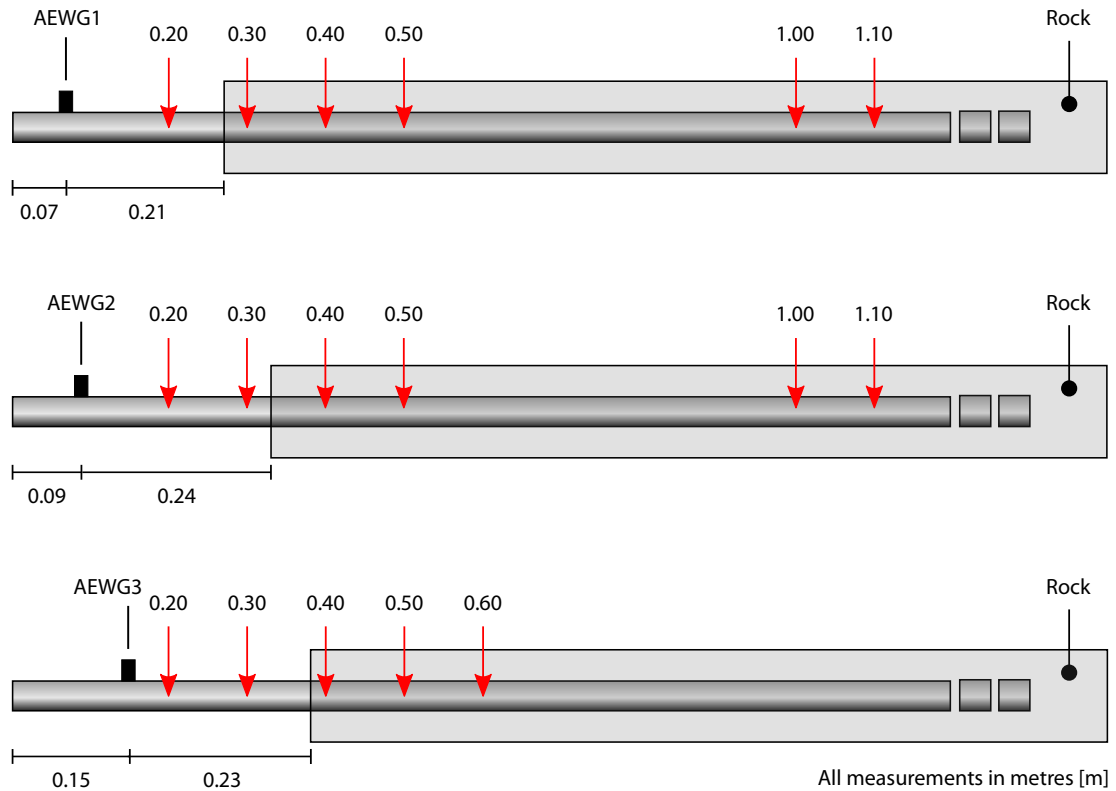


**Figure 3.16:** 10,000 RPM DC motor connected to the control box through a 50 m cable

The small AE generator was inserted in each waveguide at PdM site (see Figure 3.17) and placed at various lengths. The schematic in Figure 3.18 shows the positions where the source was triggered and the position of the transducer for each waveguide (AEWG1, AEWG2 and AEWG3). For every position 10 x 1 s bursts of vibration were induced. The AE transported along the waveguide was measured with the equipment already in place at Passo della Morte (see Series 2 in Table 3.4).



**Figure 3.17:** Test D. The small AE wave-generator being inserted in one of the waveguides at Passo della Morte



**Figure 3.18:** Schematic of Test D. For each waveguide (AEWG1, AEWG2, AEWG3) the positions where the wave-generator was triggered are detailed. The schematic also shows at which distance from the end the waveguide enters the rock mass

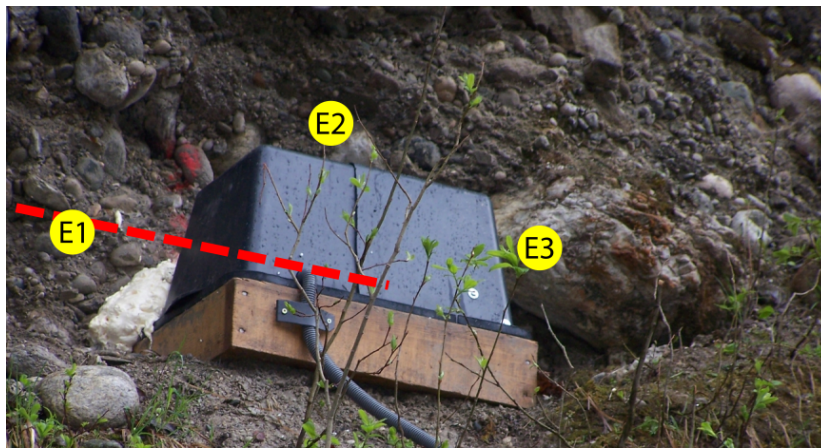
### 3.4.3.2 Extent of monitoring (Test E)

This experiment was designed to assess the component of attenuation due to the rock mass surrounding the waveguide. This would determine whether the source of AE must be located across the waveguide to be measured by the system or it can be generated within a certain distance from the waveguide and still be measured by the sensor. The experiment was carried at SART site.

The experiment was performed at SART site and consisted in generating AE on the rock surrounding a waveguide. Waveguide H108L was chosen for this experiment because it is entirely grouted in rock. The AE source was a standard 0.5 kg hammer. The rock was hit trying to maintain the same intensity each time. The locations (E1,E2,E3) where the rock was hit are shown in Figure 3.19. The three



locations are all about 0.5 m from the sensors which is placed at the end of the waveguide in the cover. However, due to the waveguide entering the rock mass at an angle, the minimum distances to the grouted waveguide are approximately 0.30 m for E1, 0.60 m for E2 and 1.10 m for E3. 5 repetitions were executed for each location. It was not possible to extend this experiment to a larger area surrounding the sensor for health and safety reasons.



**Figure 3.19:** Sensor H108L cover. The locations where the rock was hit to perform Test E are indicated with a circle (E1,E2,E3). The waveguide (red dashed line) enters the rock mass at an angle to the left-hand side

### 3.4.3.3 External sources of AE (Test F)

It is important to understand whether common activity that might take place around the sensors on site can generate AE trends high enough to interfere with the correct operation of the system and generate false alarms. This includes for example people or animals passing by, debris falling onto system covers, rain tapping on top of covers, etc. This series of experiments were designed in order to assess possible sources of AE due to environmental or anthropic causes that could generate AE trends considered to be noise and their levels.

Test F was carried out at SART site and was subdivided in three distinct experiments:



- (i) Test F1, was carried out on all sensor covers (H108L, H209R, VE10U) to simulate the tapping of rainfall and test if this generates AE trends; this was achieved by pouring 4 l of water from a common plastic watering can with rose diffuser, an approximate rate of 2 l/min was maintained throughout the experiments. RDC was logged every 5 seconds;
- (ii) Test F2, was performed to test whether an object hitting the covers, both for a prolonged period of time and instantaneously, can generate AE trends; this was achieved by drumming continuously for 5 seconds on top of covers with hands (3 repetitions) and hitting the covers with the shank of a screwdriver for 3 times. This experiments involved all three sensors (H108L, H209R and VE10U);
- (iii) Test F3, was carried out on sensor VE10U to test whether the top stratum of soil at SART site is able to transmit AE and therefore to test whether, for example, people or animals moving around the sensor can induce AE noise; this was achieved by releasing three masses of 10, 60 and 80 kg for 5 times in an area surrounding (0.30–0.50 m) the system.

## 3.5 Summary

A justification for the selection of the Slope ALARMS system used in this research work was provided along with a description of the working principle. This system was chosen primarily for its characteristics of: high sensitivity (potentially sub-millimetre in terms of displacement), high temporal resolution (i.e. up to 1 min), built-in warning system, reliability, robustness, low and easy maintenance, low power consumption, power back-up and small size of the equipment.

Field monitoring at two trial sites was used to collect the field data necessary to test system performance. The two selected slopes are characterised by different types of rock and different failure mechanisms, thus different acoustic trends are

expected. In order to define the processes that led to generation of the acoustic trends (Objective 1) the AE data collected were compared to conventional geotechnical instrumentation available at the sites. AE data were compared to a range of traditional instrumentations installed at the sites. As uniformity and consistency are key in order to establish general rules that allow the widest use of the system, a description of the components that differ among installations at the sites was provided (i.e. Slope ALARMS version MK1 and version MK2, smooth waveguides, threaded waveguides). As an AE wave travels through these components, it has an influence on RDC response. Therefore these elements needed to be validated in the laboratory to establish whether they were suitable for acoustic emission monitoring (Objective 2).

All the information obtained from the monitoring at the two trial sites and from field and laboratory tests was used to produce a framework for the use of the system within rock slope and to define strategies to interpret AE trends (Objective 3).

# **Chapter 4**

## **Laboratory testing of system elements and field experiments**

This Chapter discusses the analysis of test results designed to validate the system used in this work (Objective 2, Section 1.2). The system uses modified components that have not been previously used in traditional soil applications and therefore needs to be validated to assess whether the system still performs in the same way. Component differences with the original Slope ALARMS system are discussed in Section 3.4.1.

Laboratory tests results (Test A, B, C) are discussed in Section 4.1 and field experiments (Test D, E, F) results in Section 4.2. The tests design and procedures were described in detail in Section 3.4.

Test A, was design to assess the difference in terms of RDC response between the Slope ALARMS system version MK1 and MK2 to a standardised AE input. This is aimed at quantifying the difference between the two versions of the system and aid comparison of data series recorded at the same site with the two sensor node versions.

Test B, was designed to assess the best method for mounting a piezoelectric transducer on a threaded waveguide allowing AE wave transmission comparable

to that of a transducer mounted on a smooth waveguide.

Test C, was designed to assess attenuation of an AE signal travelling along a threaded waveguide and compare this result to a smooth waveguide for which the attenuation behaviour is known.

In general, Test B and Test C were aimed at assessing how the threaded waveguide system compares to a standard smooth waveguide system in terms of RDC response. Assessment of variables that influences AE response is useful to generalise the findings and the system behaviour so that rules that apply to both smooth and threaded waveguides can be developed.

Test D was intended to assess the attenuation of a waveguide installed into a rock mass and Test E was intended to assess the attenuation due to the rock mass. These two experiments combined are aimed to assess the reach of the system, i.e. whether the source of AE must be located across the waveguide (and how far along it) to be able to travel to the piezoelectric transducer or if it can be generated at a radial distance in the rock surrounding the waveguide and still be detected by the transducer.

Test F was intended as a check for possible sources of unwanted AE activity which could interfere with the system and trigger false alarms. These sources of AE could be for example rainfall impacting on top of sensor nodes covers, objects (such as debris, tree branches, etc.) hitting the covers and people or animals moving in the proximity of sensors.

## **4.1 Laboratory testing**

### **4.1.1 Comparison of versions MK1 and MK2 (Test A)**

The aim of this test was to quantify the difference in terms of measured RDC between the first-built MK1 and the newer MK2 version of the Slope ALARMS system.

This is of particular interest because at PdM (Section 3.3.1) site almost 4 years of data were collected with the MK1 version and additional 2 years of data were collected using the MK2 version (respectively Series 1 and Series 2 in Table 3.5). A quantification of the difference between the two Slope ALARMS versions could allow comparison of the two data series collected at PdM site.

In this test the response of a MK2 sensor to a standardised input is compared to the response of three MK1 sensors to the same input. The three MK1 sensors are those that were installed at PdM from initial installation until October 2014 (Series 1 in Table 3.5): AEWG1, AEWG2, AEWG3 and in this test their IDs are respectively MK1-WG1, MK1-WG2 and MK1-WG3. Only one MK2 sensor was used in the experiment, as opposed to testing all three MK2 sensors that are installed on site. This is due to the comparable sensitivity across the MK2 batch of sensors, which were tested prior to commencement of this PhD project, therefore testing all the MK2 sensors would be redundant. Test A1 comprised 45 x 1 s bursts of vibration from the wave-generator (Section 3.4.1) for each sensor and Test A2 comprised 15 x 10 s bursts of vibration from each sensor.

The test design was discussed in Section 3.4.2.1. The main differences between version MK1 and MK2 of the Slope ALARMS system were discussed in Section 3.2.2.3.

##### 4.1.1.1 Results

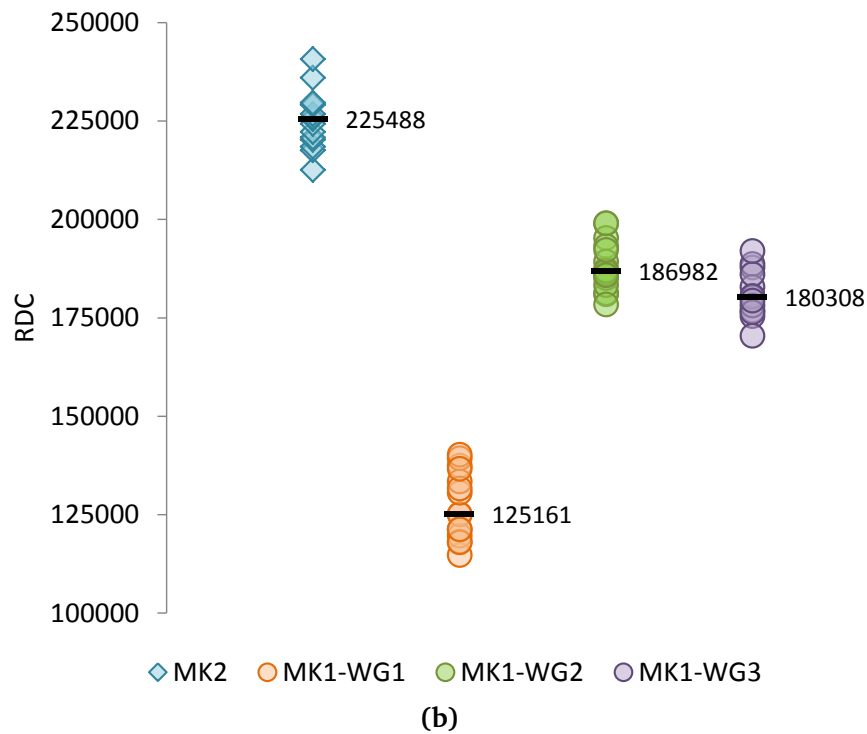
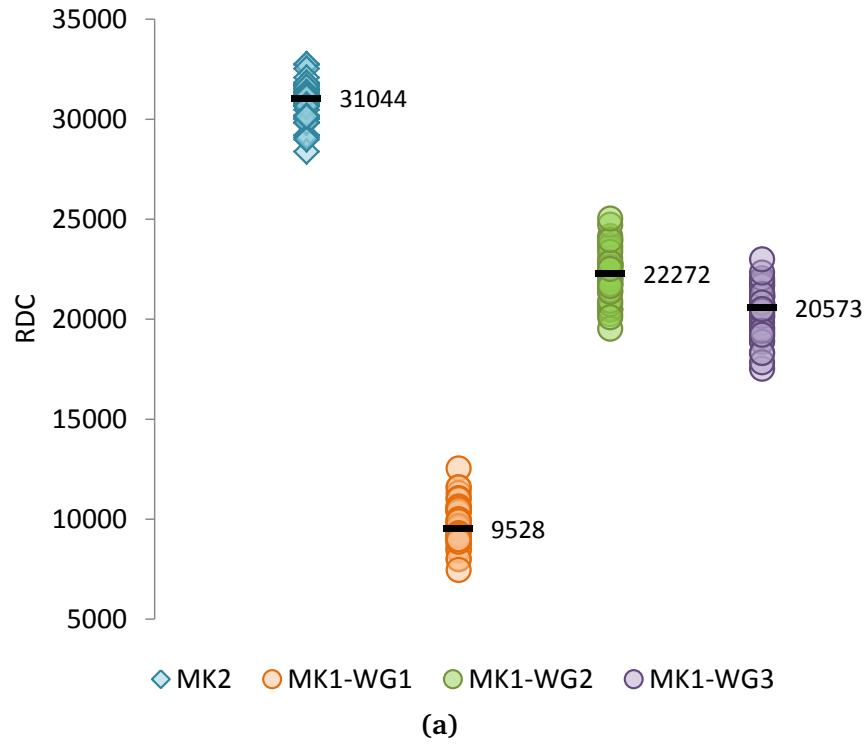
Results of Test A1 obtained by inducing 45 x 1 second bursts of vibration for each sensor can be seen in Figure 4.1a and results of Test A2 obtained by inducing 15 x 10 seconds burst of vibration are shown in Figure 4.1b.

In general, the results of both tests show that the MK1 version of the system is less sensitive to the same input and registered fewer RDC counts. MK1-WG1 consistently recorded the least counts whereas MK1-WG2 and MK1-WG3 recorded similar counts between them but significantly higher than MK1-WG1.

The statistical dispersion (or standard deviation) is consistent for all the devices within the same test duration: about 1,000 RDC for all sensors in the 1 s test (Test A1) and about 7,000 RDC for all sensors in the 10 s test (Test A2). However, it is clear that the dispersion increases with the duration of the vibration.

Considering the median RDC values for each sensor, which are identified by black markers in Figure 4.1a and b, in Test A1 sensor MK1-WG1 measured about 70% less RDC counts than MK2, MK1-WG2 about 28% less and MK1-WG3 about 34% less. In Test A2 sensor MK1-WG1 measured 45% less RDC compared to MK2, MK1-WG2 measured about 17% less RDC and MK1-WG3 about 20% less than MK2. The results show that the difference in measured RDC becomes smaller for longer durations of vibration. For example, sensor MK1-WG1 went from 70% less measured RDC than MK2 in Test A1 to 45% less RDC in Test A2, an increase of 25%. However, this increase is not consistent among the three sensors: MK1-WG1 underwent an increase of 25%, MK1-WG2 increased by only 11% and MK1-WG3 increased by 14% in Test A2 compared to Test A1.

The variability observed in the results demonstrates that there is no linear relation between rates measured with the MK1 version and rates measured with the MK2 version of the system. It was observed that in percentage the difference in terms of measured RDC is larger for short (1 s) bursts of vibration and becomes smaller for larger (10 s) bursts of vibration. This is due to the fact that sensors with different sensitivities were used for the two versions of the system (Section 3.2.2.3).



**Figure 4.1:** Results of Test A. Comparison of RDC responses given by the Slope ALARMS MK1 and MK2; **(a)** Test A1, 1 second burst of vibration; **(b)** Test A2, 10 seconds burst of vibration

### 4.1.2 Transducer mounting on threaded waveguide (Test B)

Test B design is reported in Section 3.4.2.2. This test was designed to assess the influence of different transducer mounting configurations on a threaded waveguide of the type explained in Section 3.2.2.2 and used at Grossreifling site (Chapter 6). The aim of this series of tests was to determine the best possible transducer mounting configuration that allows the greatest transmission of the induced signal at the threaded pipe–transducer interface, with minimal losses. The best configuration is considered to be the one which results are the closest to those obtained performing the same experiment on a standard non-threaded pipe. A standard non-threaded waveguide was considered as reference.

The experiment setting comprises an acoustic emission generator (source) and a piezoelectric transducer mounted over a threaded waveguide (see schematic in Figure 3.10).

The series of tests were carried out on five different transducer mounting configurations, which are B1 to B5 described in Table 4.1. The transducer was secured to the waveguide using elastic bands, except B4 where the transducer was held in place by pinching it between the pipe and a heavy plastic box to keep it in place.

Configuration B4 is expected to give the best result as the sensor is placed on the section of the waveguide. As the body of the waveguide carries most of the acoustic energy as opposed to the surface (see Section 2.4.1), this configuration is expected to give the highest results in terms of RDC. However, in the field it would be very impractical to clamp the transducer to the end of the tube.

Each test comprised 10 x 1 second bursts and 10 x 10 seconds bursts of vibration from the AE generator to the waveguide. The results were compared to those obtained from the same tests conducted on a standard smooth steel pipe (B0).



**Table 4.1:** The five mounting configurations tested (B1 – B5). B0 represents the reference test conducted on a smooth waveguide. Figure 3.11 shows a diagram of the configurations

Test	Transducer mounting configuration
B0	On a standard non-threaded pipe
B1	Upright over one thread
B2	At an angle, to the side of a thread
B3	Upright over two threads, with additional silicon gel filling the gap in between the two threads
B4	Horizontal at the end of the pipe
B5	Upright on a flat area formed by hand-filing some threads

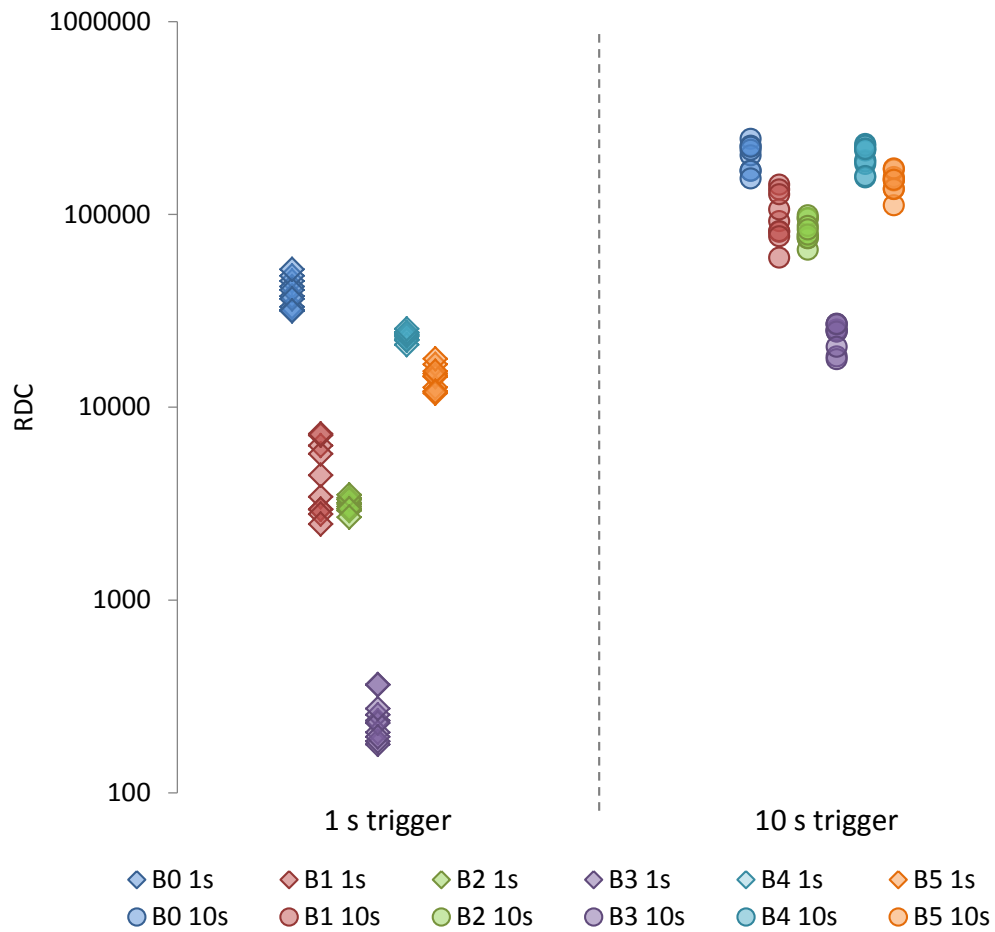
#### 4.1.2.1 Results

Figure 4.2 reports the results from the five different mounting configurations (B1 to B5) compared to the RDC produced from a transducer–standard pipe system (B0). Note that RDC is plotted on a logarithmic scale to separate the RDC response by orders of magnitude.

The transducer–threaded hollow bar mounting configuration that produced the greatest response was B4 (transducer mounted at the end of the threaded bar), with results in the same region of those produced from the standard pipe system (B0) for both 1 and 10 seconds experiments. Mounting configuration B5 produced results that were similar to B4, although slightly lower for the 1 second experiment. Mounting configuration B1 (transducer held vertically over one thread) produced RDC lower of about one order of magnitude compared to B0 and configuration B2 (at an angle) produced slightly lower magnitude RDC than configuration B1. B3 (mounting over two threads) produced the weakest response and this mounting should therefore always be avoided.

Although B4 gave the closest results to the standard pipe (B0), it would be very difficult in practice to hold the transducer in place at the end of the bar when installing the system on a waveguide placed horizontally at a field site (i.e. a special mounting bracket should be designed for this purpose to ensure that the transducer

would not move from its position over time). It is therefore advisable to choose configuration B5 which performed well in the experiment and allows to keep the transducer in place more easily fastening it around the pipe with the aid of elastic bands and cable ties.



**Figure 4.2:** Results of Test B. RDC responses of five different mounting configurations (B1 to B5) compared to the response of a standard steel pipe (B0). 1 second burst of vibration to the left and 10 seconds to the right

### 4.1.3 Attenuation in threaded waveguides (Test C)

This experiment was performed in order to quantify the attenuation of an AE signal travelling through a threaded waveguide. This would be useful to assess if a signal generated several metres away from the transducer is able to travel along

the threaded steel bar and be recorded by the system and how it would be attenuated along the path.

The threaded waveguide tested is of the type reported in Table 3.1. Four 3 m lengths of threaded rod were screwed and tightened together for a total length of 12 m. A transducer was secured on a file flattened area near one of the ends of the waveguide and a wave-generator (Section 3.4.1) was placed at regular intervals along the length. The test design was discussed in detail in Section 3.4.2.3.

The results of the experiment performed on a threaded waveguide are here analysed. The results are also compared to those obtained by Smith (2015). Smith performed the same laboratory experiment (using same equipment and set-up) on a smooth standard waveguide. This comparison will be used to assess whether the propagation of AE through threaded waveguides differs significantly from the propagation through smooth pipes. Smooth hollow pipes have become a standard in the application of Slope ALARMS therefore it is important to assess whether there are any significant changes in the propagation of waves through waveguides with a different external interface shape (threads in this case). The threaded interface might determine additional reflection and this could increase or decrease the number of RDC ultimately registered, compared to a standard waveguide with same experiment set-up.

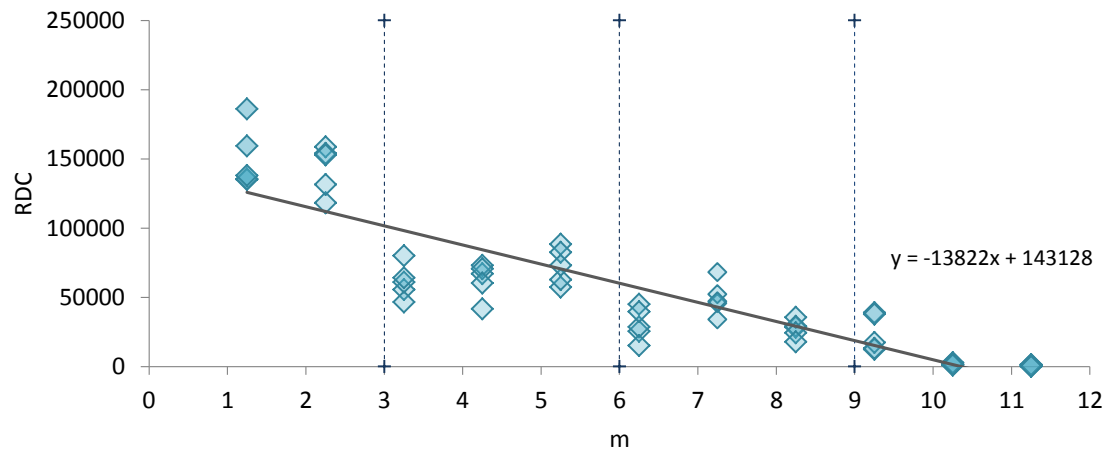
#### **4.1.3.1 Results**

In Figure 4.3 the results of Test C can be observed. It is immediately clear that the general trend of AE reduces linearly with the distance thus a linear regression was calculated considering the average values for each position and plotted on the graph.

In the graph can also be noted that AE is significantly attenuated after the 10 m mark and there seem also to be quite a conspicuous loss moving from one 3 m length to another. This loss effect is observed when lengths are connected with

loose couplings (see for example Figure 4.4a). In this experiment the couplings were tightened and spread with acoustic couplant but still the signal seems to be attenuated significantly at the couplings. This could be explained by the type of couplings and bars. The threads of the self-drilling bars are quite wide (as they are also used by the drilling machine to grasp onto the bars and transmit the power for drilling) and it is more difficult to hand-tighten them in the lab (even with wrenches). As a result the bar ends are not clamped as tight as they are in smooth pipes, which threads are much narrower and allow the bars to be screwed together much tighter. However, a significant loss is only registered for lengths greater than 10 m.

It is worth noting that when installed on site using a drilling machine, the couplings would be tighter and AE travelling through them could be less attenuated. Table 4.2 reports the threaded waveguide attenuation in RDC/m, Np/m and the more commonly used units of decibel per metre (dB/m) calculated along the whole waveguide, including losses due to couplings using Equation 2.5 and 2.6.



**Figure 4.3:** Results of Test C. The trendline is calculated on the average of the RDC results for each wave-generator position. Each 3 m rod length is identified by a dashed line

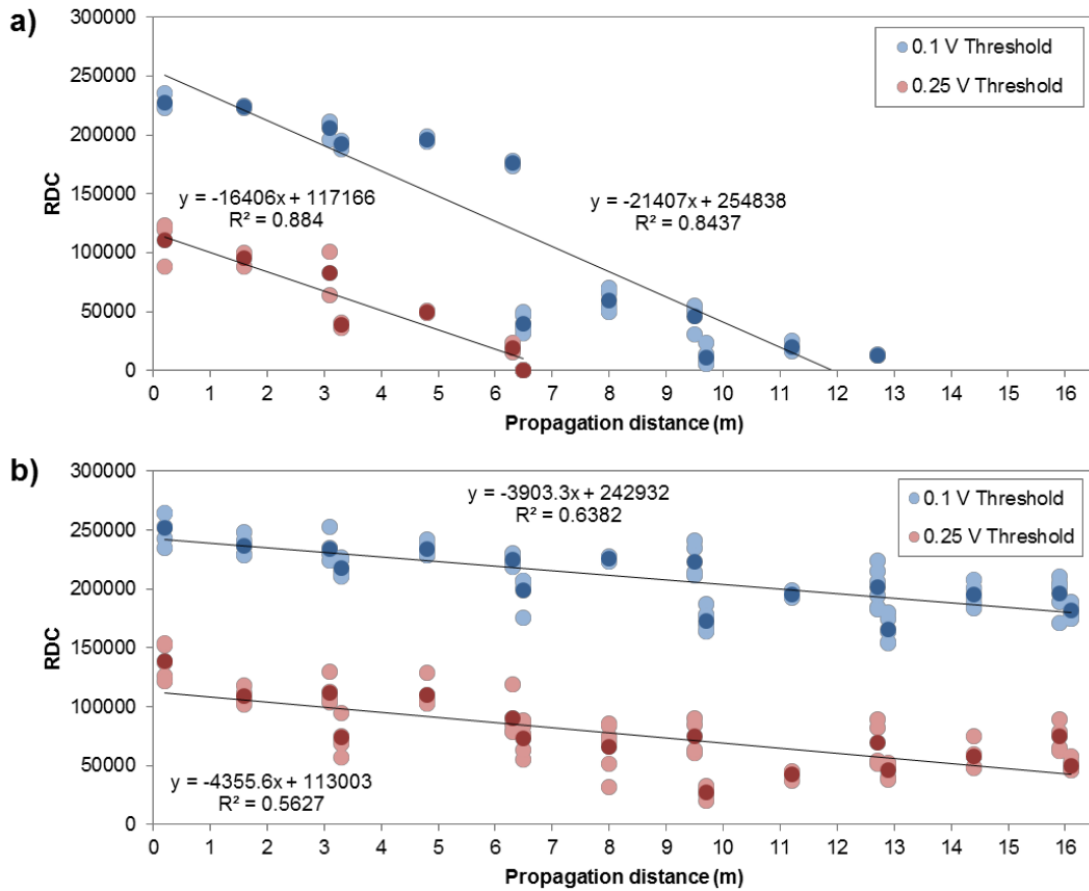
**Table 4.2:** Attenuation along waveguide obtained from Test C

<b>Np/m</b>	<b>dB/m</b>
0.22	1.91

Figure 4.4 and Table 4.3 report the results obtained by Smith (2015) who performed the experiment on a standard smooth waveguide composed of 5 x 3.2 m pipe lengths and an additional 0.5 m length for a total of 16.5 m. Figure 4.4a is relative to the experiment conducted with loose couplings and Figure 4.4b is relative to the experiment carried out after tightening the couplings with the aid of chain wrenches. The experiment was carried out using a Slope ALARMS MK2 to record the RDC generated on a smooth waveguide by the wave-generator described in Section 3.4.1. The vibration was induced by the source generator over 10 second durations. The results of interest in this discussion are those relative to a threshold voltage of 0.25 V (in red in Figure 4.4).

Comparing the results obtained by Smith (2015) using a smooth waveguide (0.25 V threshold) to the results obtained using a threaded waveguide (Figure 4.3) can be observed that they are comparable. The threaded waveguide attenuates 0.12 dB/m less than a smooth waveguide with loose couplings but 1.75 dB/m more than a smooth waveguide with tight couplings. The state of couplings seem to affect significantly the AE transmission both within smooth and threaded pipes.

However, considering one single length of 3 m (i.e. the first 3 m of each the experiment) the results of smooth and threaded are similar (i.e. in the region of 150,000 RDC).



**Figure 4.4:** Results of the test performed by Smith (2015) on smooth waveguides. RDC induced by 10 s vibration vs propagation distance. **(a)** loose couplings; **(b)** tight couplings. The values referring to the 0.1 voltage threshold test (light blue) are here not considered

**Table 4.3:** Attenuation along waveguide obtained by Smith (2015)

	Np/m	dB/m
Loose	0.02	0.16
Tight	0.23	2.03

Figure 4.5 reports the percentage of signal loss after each of the tree couplings along the waveguide calculated from the results of Test C. It is noticeable that the attenuation actually decreases after the last coupling. The same phenomenon was observed by Smith (2015) on smooth waveguides with tight couplings. However, the percentage of signal loss after couplings averaging around 60% is more similar to Smith's experiment using loose couplings (see Figure 4.6).

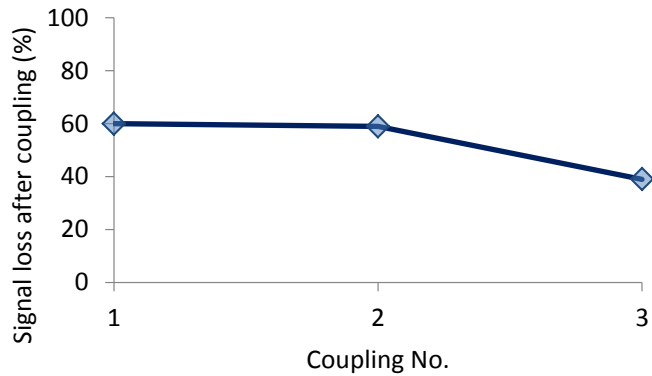


Figure 4.5: Percentage of signal loss after couplings: (a) for Test C; (b)

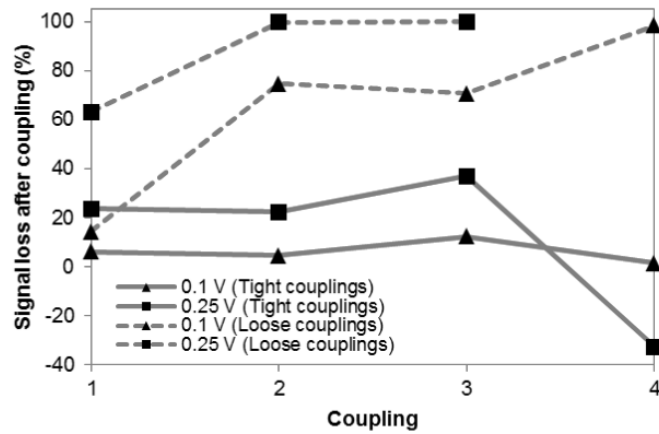


Figure 4.6: Percentage of signal loss after couplings. After Smith (2015)

## 4.2 Field experiments

### 4.2.1 Attenuation along waveguides on site (Test D)

This test was designed to assess the attenuation of smooth waveguides grouted into a rock mass. This is useful in order to assess whether a signal generated several metres (up to as long as 50 m) away would propagate all the way to the transducer, or it would be attenuated along the path.

Test D was carried out at Passo della Morte as at this site the waveguides are grouted on the outside and the centre is hollow. A small AE generator was inserted

into the hollow smooth waveguides at different lengths (see Figure 3.18) and 10 x 1 s bursts of vibration where induced per each position. This experiment was designed to run for the whole length of the three waveguides (50, 30 and 10 m respectively for AEWG1, AEWG2 and AEWG3) at intervals of 0.5 m. The AE generator used in this test is detailed in Test D design description in Section 3.4.3.1. The AE transmitted along the waveguide was measured with the equipment already in place at the PdM site (Section 3.3.1).

The test design was detailed in Section 3.4.3.1.

#### 4.2.1.1 Results

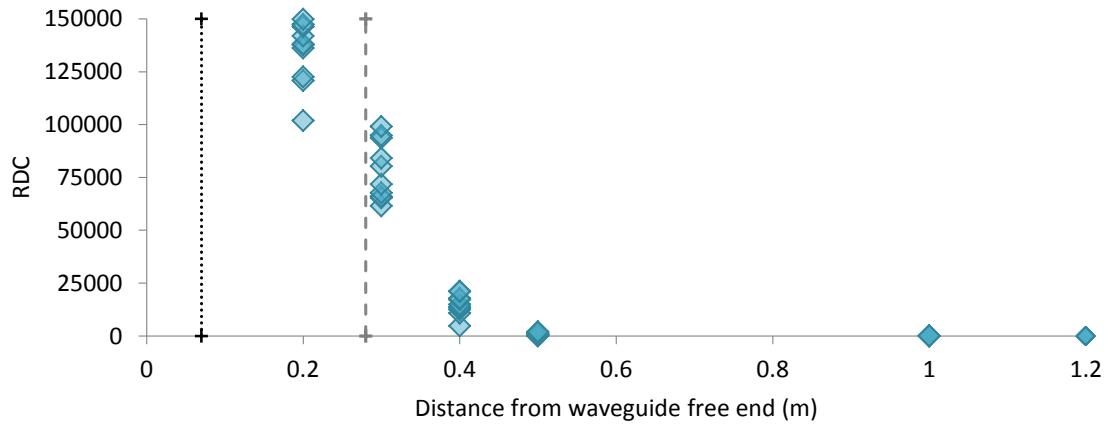
Figure 4.7 reports the results of the experiment relative to the first 1.2 m of waveguides AEWG1, AEWG2 and AEWG3 installed at the PdM site. Beyond the 1.2 m length, the RDC recorded resulted null for all waveguides. Therefore, the experiment was restricted to the beginning section of the pipe, up to the point where no RDC was longer recorded.

The general trend of RDC detected appears to reduce with the distance from the transducer. In particular the RDC drops soon after the point where the waveguide enters the rock mass (in particular for AEWG1 and AEWG3). The dispersion is high when AE is generated in the section of waveguide that is free (i.e. out of the rock mass). The dispersion of RDC values for each location reduces as the waveguide enters the rock mass, however this is not true for AEWG2. Signals generated at 1.2 m from the free end of waveguides AEWG1 and AEWG2 and 0.6 m of waveguide AEWG3 are completely damped along the path to the transducer and no RDC is measured.

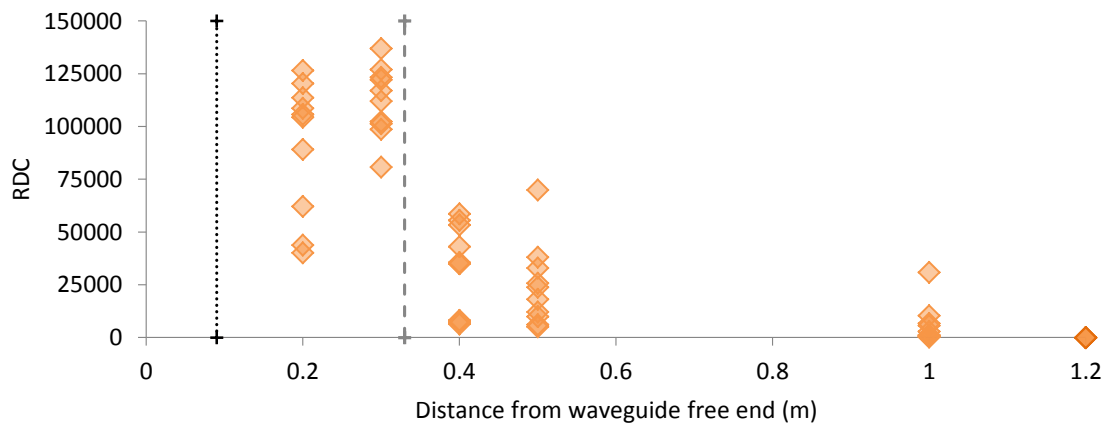
Although RDC was recorded only in the initial section of waveguides installed on site, it cannot be concluded that the waveguide is not capable of transferring acoustic energy. In fact very high RDC/h activity, in the region of 100,000s RDC, is recorded at this site (see Chapter 5) from the same waveguides. It is very unlikely



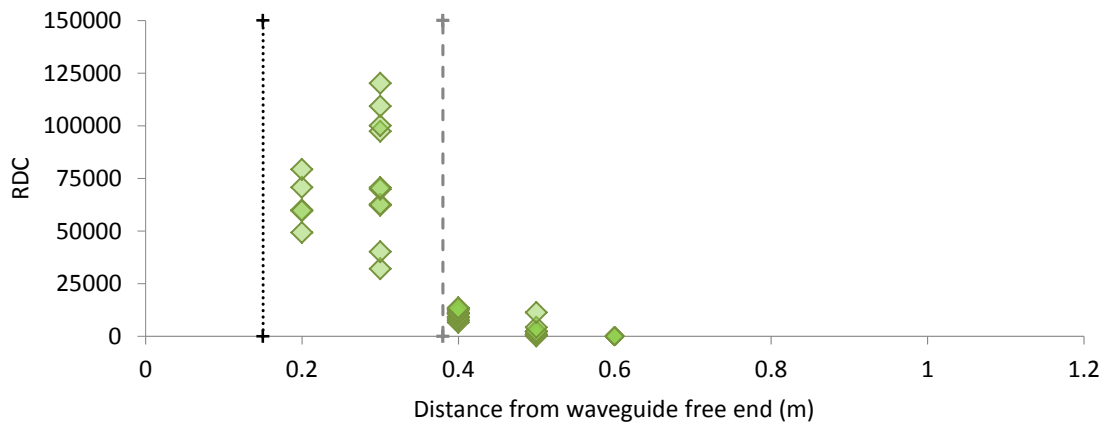
that this activity is generated only in the first 0.6 – 1 m. An hypothesis is therefore that the artificial AE source employed in this test is not powerful enough. It is clearly not comparable to the energy generated by processes actually acting within the rock mass.



(a)



(b)



(c)

**Figure 4.7:** Results of Test D. RDC vs distance from free end of waveguide. The black dotted line represents the location of the transducer along the waveguide and the grey dashed line represents the point where the waveguide enters the rock mass, both refer to the x-axis. (a) AEWG1; (b) AEWG2; (c) AEWG3

### 4.2.2 Monitoring extent (Test E)

This experiment was designed to assess the component of attenuation due to the rock mass surrounding the waveguide. This would determine whether the source of AE must be located across the waveguide to be measured by the system or it can be located within a certain distance from the waveguide and still be measured by the sensor. The experiment was performed at SART site and consisted in generating AE at increasing distances on the rock surrounding a waveguide. Waveguide H108L was chosen for this experiment because it is entirely grouted in rock. The AE source was a standard 0.5 kg hammer. The rock was hit trying to maintain the same intensity each time. The locations where the rock mass was hit can be seen in Figure 3.19: the left of the sensor (E1), on a cobble above the sensor (E2) and on a large boulder to the right of the sensor (E3); the minimum distances to the grouted waveguide are approximately 0.30 m, 0.60 m and 1.10 m, respectively. 5 repetitions were executed for each location.

Test design was detailed in Section 3.4.3.2.

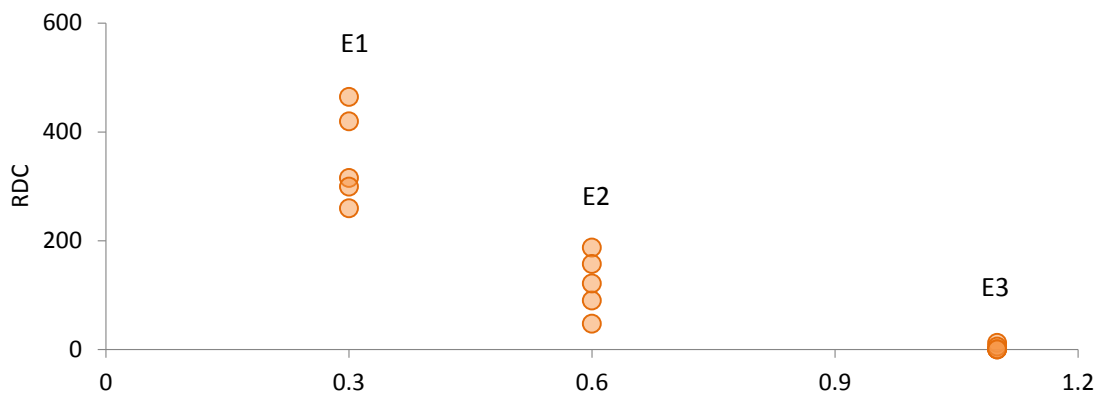
#### 4.2.2.1 Results

Figure 4.8 shows the results of Test E. In the interpretation it must be considered that this is a more qualitative assessment as the source cannot be controlled exactly.

Location E1 gave the highest counts between 200–500 RDC, location E2 between 50–200 RDC and the response from location E3 was almost null. The results can be explained by the fact that the waveguide enters the rock mass at an angle, going to the left. Therefore, there is less distance to travel for waves generated in E1 than there is for the other two locations (E2, E3). It must also be taken into account that waves in the three locations are generated onto different-sized conglomerate particles and this has an effect on signal propagation in the rock mass, with losses as the stress waves propagate across weakly cemented particle boundaries.

However, the most important result is that AE was measured in general as a results of this test and it demonstrates that not only AE generated across the waveguide can be measured by the system but also AE generated at a distance from the waveguide.

Unfortunately, due to safety reasons, the experiment was not repeated at increasing distances from the sensor, as the experiment was thought in a first phase. This would have made possible an estimation of the attenuation in the conglomerate rock mass.



**Figure 4.8:** Results of Test E. Refer to Figure 3.19 for E1, E2, E3 locations. E1 is approximately 0.30 m from the grouted part of the waveguide, E2 about 0.60 m and E3 about 1.10 m

### 4.2.3 External sources of AE (Test F)

A simple series of tests was conducted at SART site to establish whether the AE signal could be contaminated by impacts on the sensors covers or people and animals moving around them and generate counts high enough to be able to interfere with the operation of the sensors, specifically trigger false alarms. For this to happen the RDC produced should be at least of some thousand RDC counts.

Test F was carried out at SART site and is subdivided in three distinct experiments which aim is to simulate:

- the tapping of rainfall onto covers (Test F1), this was achieved by pouring 4 l of water from a watering can with rose diffuser at a constant rate of 2 l/min, approximately, onto the three sensors covers (H108L, H209R and VE10U);
- debris detaching from the slope and falling onto the protective covers (Test F2), the test consisted in drumming onto the covers (H108L, H209R and VE10U) with hands for 5 sec for 3 times and hitting the covers with a screwdriver for 3 times;
- people or animals moving around covers (Test F3), this was achieved by releasing three masses of 10, 60 and 80 kg in the area surrounding sensor VE10U (within 0.5 m from the sensor).

The tests design details were discussed in Section 3.4.3.3.

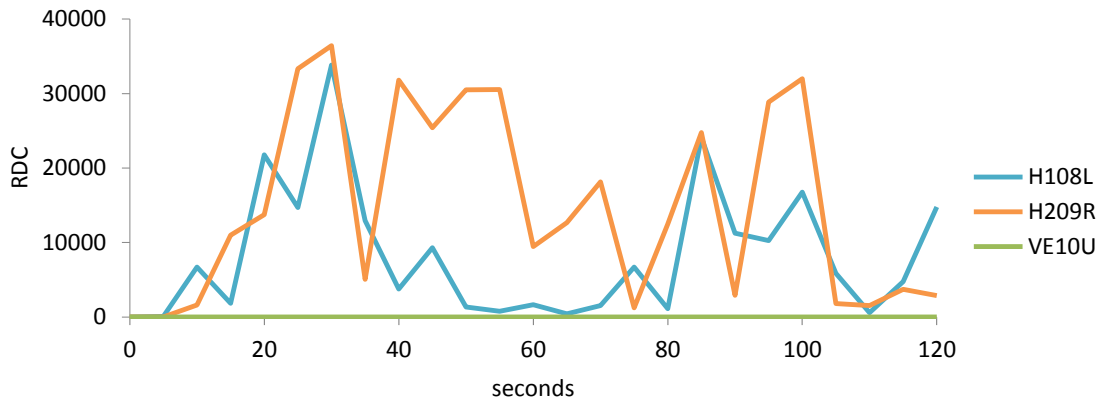
##### 4.2.3.1 Results

The results of Test F1 are reported in Figure 4.9. The water poured on the covers protecting sensors H108L and H209R clearly generated some RDC trends. The RDC counts generated are particularly high (up to about 40,000 RDC) and could definitely interfere with the system operation. However, as assessed after inspecting the covers, they were made of two overlapping parts leaving a gap in between them. The gap so formed allowed water to seep through and drip directly onto the waveguides thus generating AE trends almost immediately. The covers were sealed and the test repeated to ensure that they were watertight. Both sensors measured no RDC trends after the covers were repaired. It is therefore advisable not to use the data collected up to the day the covers were sealed (28/08/2014) as they cannot be considered representative of deformation occurring within the rock mass.

Sensor VE10U cover was made of one single piece only and thus watertight. It measured 0 RDC trends already during the first test.

The 0 RDC results obtained (on VE10U and after H108L and H209R covers were

sealed) show that rain water droplets tapping on the covers as they fall are not responsible for RDC trends being generated. Moreover, it has been demonstrated that, after being repaired, all covers are watertight and thus RDC rates are not generated by water dripping onto the equipment.



**Figure 4.9:** Results of Test F1. The test consisted in pouring water from a watering can onto sensors covers at SART site

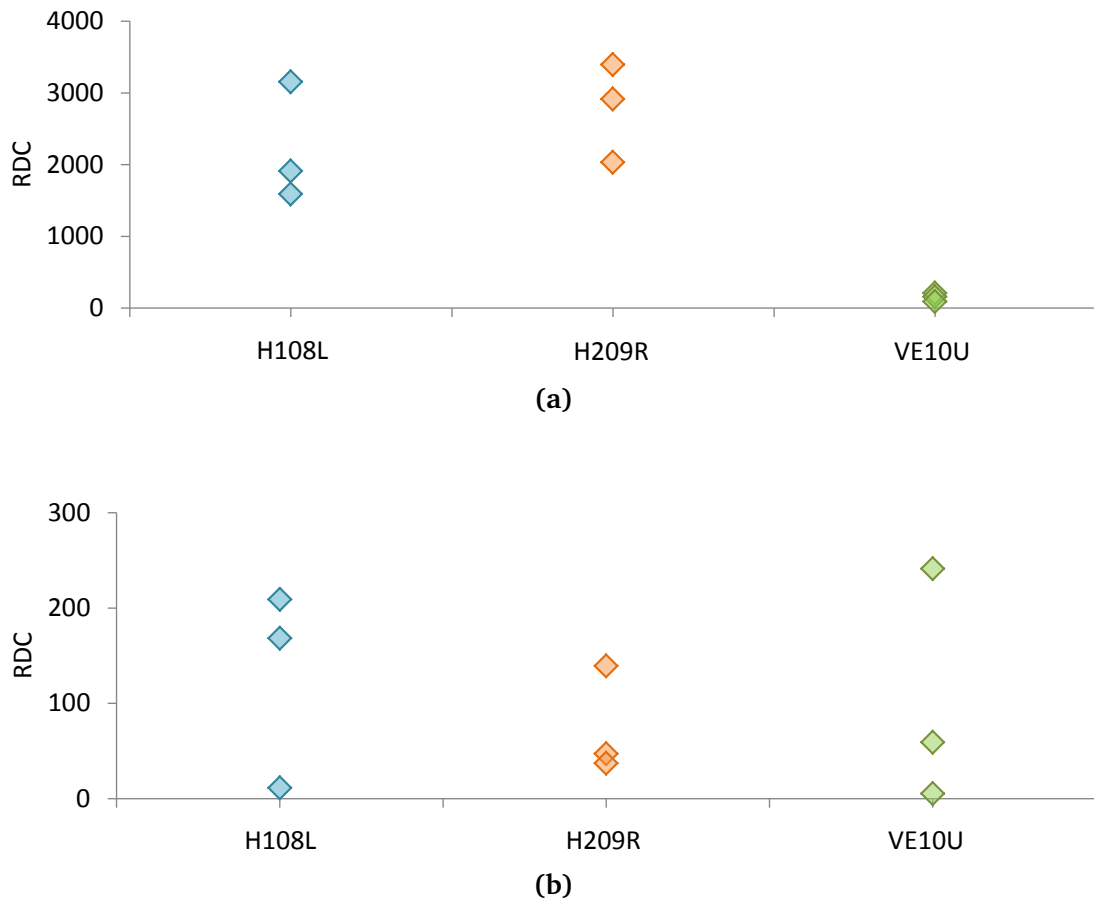
Figure 4.10a shows the results of the first part of Test F2 which was performed by drumming for on top of the covers with hands for 5 seconds and repeated 3 times. Sensors H108L and H209R gave similar RDC responses, both between 1500–3500 RDC, whereas sensor VE10U measured much lower RDC, between 89–206 RDC.

The results of the second part of Test F2 are reported in Figure 4.10b. The test was performed by hitting the covers with a screwdriver shank and repeated for three times.

In the second part of the test, all three sensors measured counts lower than 250 RDC and some as little as 5 RDC (VE10U). The amount of RDC generated was probably due to the location where the covers were hit, i.e. when hit at the corners resulted in higher RDC; this could be due to the fact that corners generate higher frequency waves as their stiffness is higher.

The result of this experiment shows that an object hitting the covers is able to generate RDC counts, however, it is unlikely that these RDC would interfere with

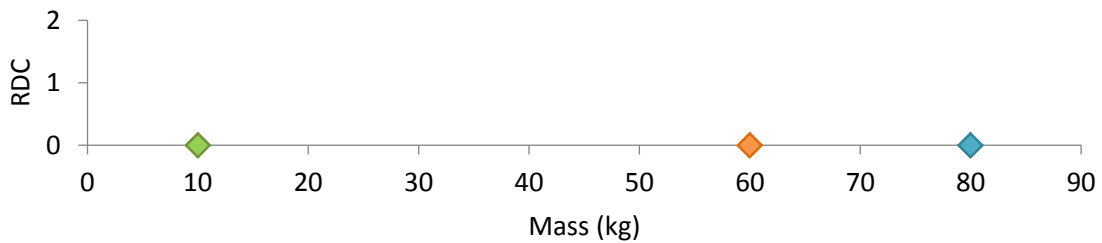
the correct operation of the system (i.e. would not trigger thresholds). In fact single hits, which could be compared to cobbles or tree branches falling onto the covers for example, only generated few counts. Even considering multiple events taking place in the same monitoring period (i.e. 15 min on the devices at SART site) it is unlikely that the sum of these events would alone trigger an alarm. The test also showed that to generate rates that could potentially interfere with the system (i.e. higher than some thousand counts), the event should have a duration prolonged in time as in the first part of the test, however, this is unlikely to happen in a real situation.



**Figure 4.10:** Results of Test F2. (a) drumming onto sensors covers for 5 seconds (3 repetitions); (b) hitting the cover with the shank of a screwdriver (3 repetitions)

The results of Test F3 are reported in Figure 4.11. This test was performed by releasing three different masses of 80 kg, 60 kg and 10 kg on the ground surrounding sensor VE10U, within 0.5 m. The test was repeated for 5 times per each mass.

As shown in Figure 4.11 there is clearly no AE recorded by the system. Therefore, the first stratum of about 0.8 m of soil can be considered as very highly damping and the presence of people or animals moving around the sensor or object falling on the ground would not generate any RDC trends.



**Figure 4.11:** Results of Test F3. Three masses of 80 kg, 60 kg and 10 kg were dropped 5 times each on the ground surrounding sensor VE10U

### 4.3 Summary

Tests in this chapter were aimed at validation of the monitoring equipment used at the trial sites in this work (Objective 2, Section 1.2). In the first part of this chapter the results of laboratory experiments were discussed.

In Test A differences in terms of RDC response to the same input between the two versions of Slope ALARMS MK1 and MK2 were assessed. It was demonstrated that MK1 measured considerable less counts than MK2 but the relationship was found not linear. In fact, the difference appears to reduce for higher RDC counts generated by a prolonged duration of the induced vibration (10 s). This test was used for interpretation of PdM data, specifically to assess whether the two series of data (Series 1 and Series 2) collected at PdM with the two versions of the system (MK1 and MK2, respectively) were comparable (Section 5.3.1).



The best mounting configuration of a piezoelectric transducer on a threaded waveguide was assessed in Test B. It demonstrated that the best configuration for the transducer is upright on a flat surface produced by filing some of the threads. This method produces RDC results that are comparable to a transducer mounted on a smooth waveguide. This ensures a good coupling at the interface that allows AE waves to be transmitted to the transducer while still providing an easy and practical method of installation, compared to other methods considered in the test. This method was used to install the transducer on threaded waveguides at the Grossreifling site (Section 6.2).

In Test C the attenuation in a threaded waveguide made of multiple rod lengths joined together by means of screw thread couplers was assessed and compared to the attenuation of a smooth waveguide. This test was performed to assess the attenuation of the waveguide component only (i.e. surrounded by air). It was found that the attenuation of a threaded waveguide is comparable to a smooth waveguide (i.e. attenuation of 1.91 dB/m). This experiment was performed to design the monitoring system at Grossreifling (Section 6.2), assessing suitability of threaded rods to be used as waveguides.

The second part of this chapter was dedicated to the results of field experiments. Test D and Test E were designed to assess the component of attenuation due to a waveguide grouted into the rock mass (Test D) and the component of attenuation due to the rock mass itself (Test E). The aim of the two combined tests was also to assess the extent of influence of the transducer, that is the volume surrounding the waveguide within which the source of AE must be located for its waves to travel to and be detected by the transducer.

Test D was carried out at PdM site. The signal produced by a small wave-generator inserted into the waveguides installed at the site was measured and found to be damped soon after the waveguide enters the rock mass. This does not mean that the waveguide installed into the rock mass attenuates all signals. In fact, very

high RDC activity (100,000s RDC) was recorded at this site and this activity is unlikely to be entirely generated in the first metre of the waveguide. In conclusion, the wave-generator was probably not appropriate for this experiment (i.e. not powerful enough to induce a vibration similar to that generated within the rock mass).

Test E was carried out at SART site. The rock surrounding one of the sensors installed on site was repeatedly hit. Some hundreds of counts were measured as a result. This is important because demonstrates that not only AE generated across the waveguide but also AE generated within a distance of approximately 1 m from the waveguide can be measured by the system. However, the experiment was not repeated at increasing distances from the sensor, as the experiment was initially designed, because of safety reasons. This did not allow the rock mass attenuation of AE to be investigated in more detail.

The last field experiment, Test F, was carried out to assess possible sources of noise in the surroundings of a sensor node at Grossreifling in order to aid interpretation of data (Section 6.3) excluding spurious counts. Sources of noise could also interfere with the correct functioning of the system, specifically trigger false alarms. The test showed that rain falling on top of sensor covers is not responsible for generating acoustic emission trends. An object hitting the covers can produce few hundreds RDC, although the level is low and unlikely to interfere with the system. Prolonged drumming on the covers produced some thousand counts, however an action similar to this is unlikely to happen on site. Finally, the presence of people or animal moving around or passing by a sensor was tested by releasing different masses onto the ground. No RDC was measured as a result, which shows that the soil is very highly damping and this was excluded from possible sources of noise.

# **Chapter 5**

## **The Passo della Morte site**

Instrumentation at the Passo della Morte site was funded by project partner CNR-IRPI (the Research Institute for Geo-Hydrological Protection of the Italian National Research Council). The project was intended to assess the state of activity of the unstable rock mass and risk associated. The site was introduced in Section 3.3.1.

This chapter is subdivided in four sections. Section 5.1 introduces the geology of the site and defines the failure mechanism. Section 5.2 provides details of the AE sensors and the monitoring network available at the site. These first two sections will provide the reader with the essential information needed to understand the AE trends analysis and the comparison with traditional established instrumentation that follows in Section 5.3. Section 5.4 summarises the findings of this chapter.

### **5.1 Site description**

The Passo della Morte (PdM) site is situated on the left flank of a narrow Alpine valley in north-eastern Italy (Figure 5.1), about 3 km to the east of the village of Forni di Sotto [Lon 12.7026, Lat 46.3978]. The Tagliamento River flows at the bottom of the valley along a west to east direction.

The site consists of an unstable rock mass, as indicated by the history of failures,

that occupies elevations between 900 m a.s.l. and the toe of the slope at 620 m a.s.l. Between 650 m of elevation and the toe of the slope the rock is hidden by coarse loose deposits accumulated by rockfalls of small dimensions. The rock spur is about 130 m wide.

At the site a road tunnel (*Passo della Morte tunnel* in Figure 5.1) crosses the unstable rock mass for its entire width at a constant elevation of 720 m a.s.l. with only shallow cover (0–15 m) on the side towards the slope. The tunnel ceased to be operational in June 2016 and therefore it is no longer considered an element at risk.

The rock mass has the potential to mobilise some 650,000 m<sup>3</sup> (Codeglia, 2013) of material in case of collapse of the whole unit. The phenomenon threatens the downstream settlements and strategic infrastructures for the potential of valley damming and consequent sudden discharge of the water accumulated at its back by the river, if dam outburst occurs.

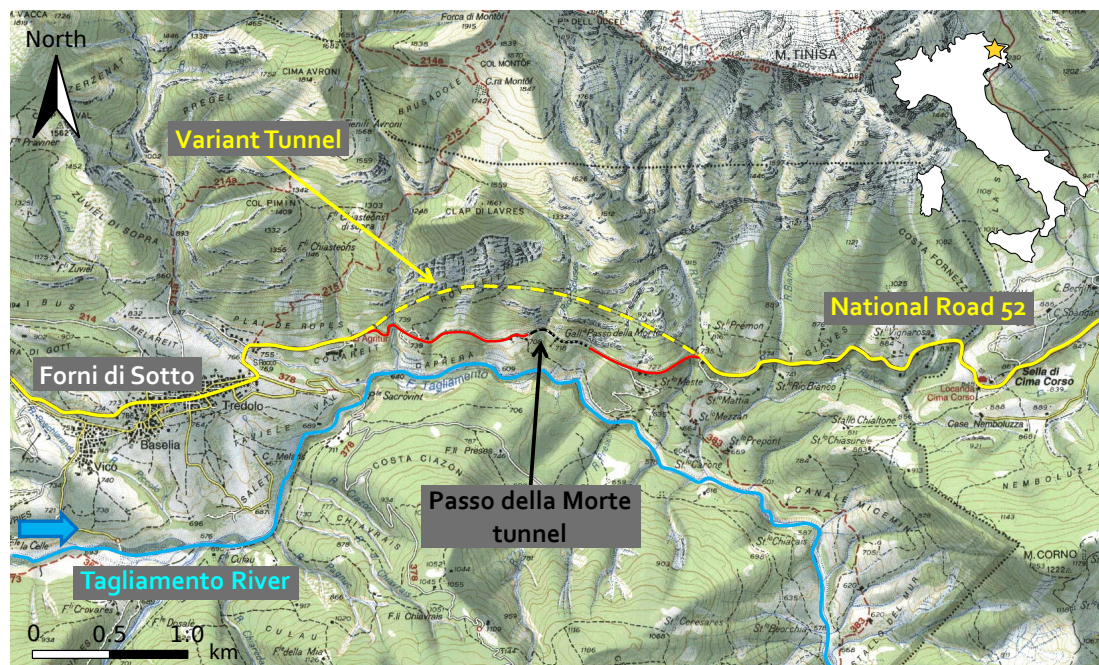
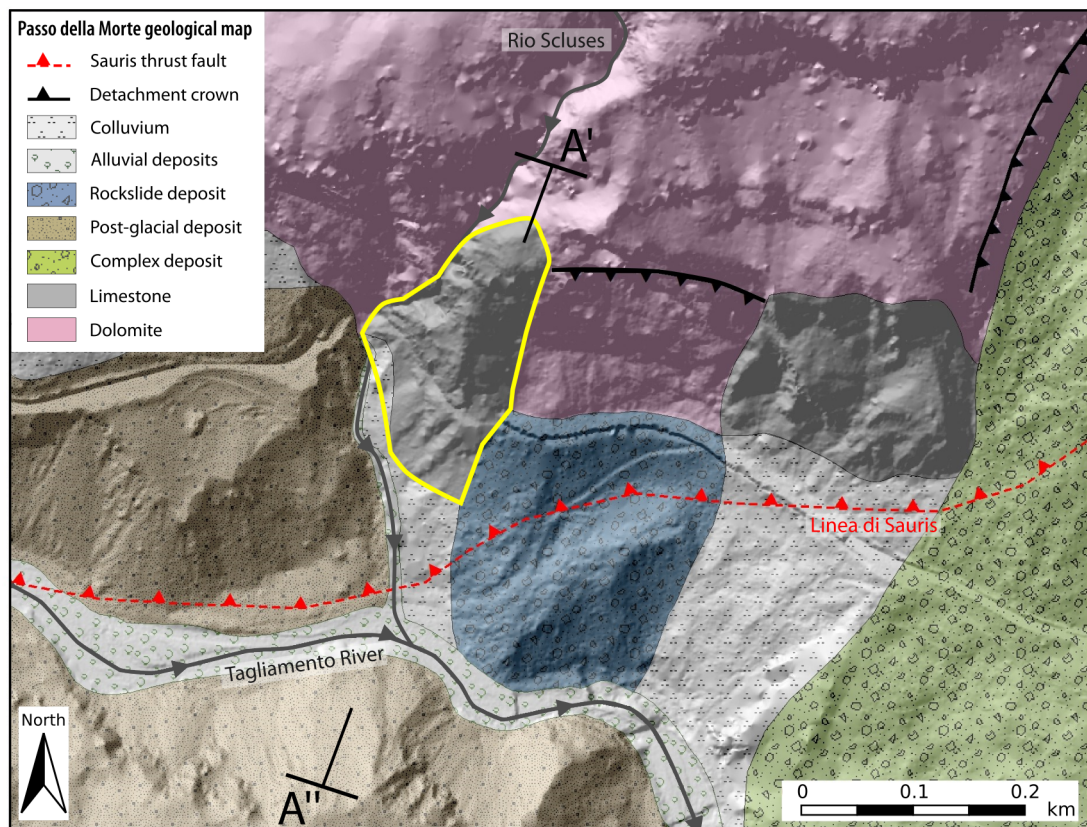


Figure 5.1: Passo della Morte (Italy) site location (Tabacco Maps, 2008, mod.)

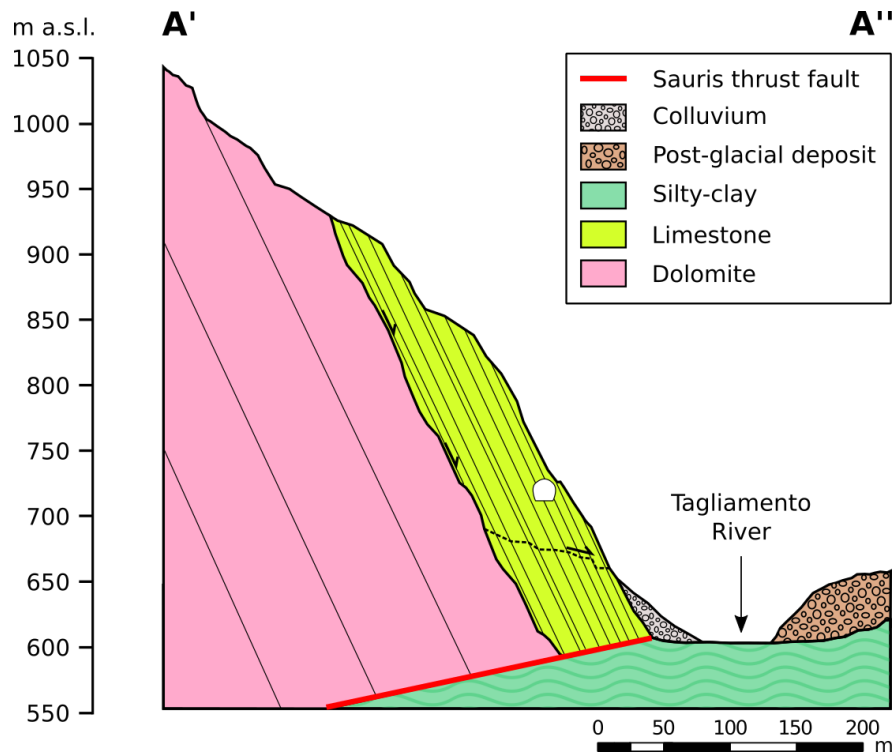
### 5.1.1 Geologic overview

As can be observed in the geological map of the area in Figure 5.2 and in the cross-section on Figure 5.3, at the Passo della Morte the outcropping formations are thick-bedded dolomite (Dolomia dello Schlern – Ladinian), which constitutes the bedrock, and thinly stratified limestone (Calcari scuri stratificati – Carnian) which steeply lies on the dolomite. Dolomite and limestone sit on top of silty-clays (Argille siltose varicolori – Middle Carnian) which are present at the base of the slope and covered by loose debris that detaches from the upper slopes (*Colluvium* in Figure 5.2).



**Figure 5.2:** Bedrock geology and superficial deposits map of Passo della Morte. The unstable limestone outcrop is highlighted in yellow. The camera icon indicates the approximate position and orientation used to photograph the west rock mass face (e.g. Figure 5.4 and 5.9). A'-A'' indicates approximately the cross-section in Figure 5.3. Modified after Codeglia (2013)





**Figure 5.3:** Indicative cross-section of Passo della Morte

The *Linea di Sauris* (Figure 5.2 and 5.2), a regional over-thrust fault, was responsible for pushing the dolomite and limestone to a south-facing near-vertical aspect during the Alpine orogeny (Podda and Ponton, 1997), placing them on top of the more recent silty-clays. The thrust fault runs along the Tagliamento River bed to the west and elevates its position up the slope in the PdM area (Codeglia et al., 2017). The structural setting predisposes the rocks to slide along planes of weakness such as faults, or bedding strata or between two different rock formations.

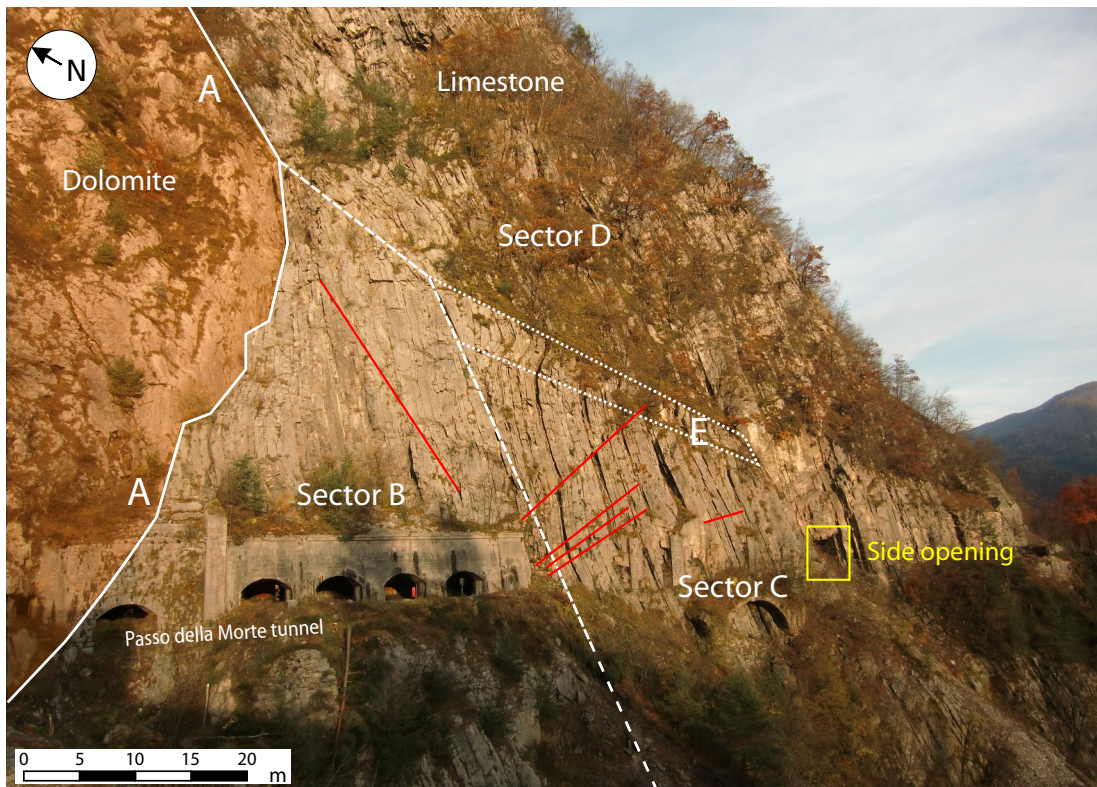
The valley in this section is particularly narrow, thus collapses of large volumes of rock represent a considerable threat of valley damming and consequent sudden release of the water accumulated by the river at the back of the obstruction. Examples of landslides that caused damming of the Tagliamento river bed since the last glacial period are found in the literature (e.g. Cavallin and Martinis, 1974; Codeglia et al., 2017; Martinis, 1985).

Martinis (1985) for example describes a rockslide that occurred during the last post-glacial era caused by de-buttressing due to a retreating glacier. Radiocarbon dating confirmed an age of about 10,000 years Before Present (BP). The rockslide of about 50,000,000 m<sup>3</sup> generated a barrier lake about 6.5 km long that lasted for at least 100 years, as assessed by analysing the clay deposits found in the area (Martinis, 1985). The post-glacial landslide deposit have been partly eroded by the river but is still visible on both flanks of the valley in the area of Passo della Morte (*Post-glacial deposit* in Figure 5.2).

Another ancient rockslide, *Rockslide deposit* in Figure 5.2, was recognised in the area of Passo della Morte and described by Codeglia et al. (2017). The landslide has not been dated but geomorphological evidence show that it is successive to the post-glacial deposit above described. This rockslide is of particular interest because it affected the slope immediately to the east of the rock mass studied in this work, involving the same rock formations. The triggering factor was determined in the erosion at the toe of the slope, which indented the rock formations at the base (silty-clay), particularly stressed by the presence of the Sauris over-thrust fault. The steep dolomite, deprived of support at the toe, was free to slide down peeling along the bedding planes and leaving bare dolomite on the slope.

#### 5.1.2 Rock mass description

The outcrop (highlighted in yellow in Figure 5.2) studied in this work consists of stratified limestone (10–40 cm) that steeply lie on thick-bedded dolomite (1–3 m). A photograph of the rock mass can be seen in Figure 5.4. The limestone outcrop is unconfined both to the east, by the detachment zone of an ancient landslide that involved part of the slope (described above in Section 5.1.1), and to the west, by a fault line incision which hosts a seasonal stream called the Rio Scluses.



**Figure 5.4:** The limestone rock mass face photographed from the west. The structural elements described in the text are outlined: A is the contact between dolomite and limestone; B the sector characterised by tight bedding; C the sector with open bedding and marl infill; D the sector with shallower dip angle and E are small folds. The dolomite bedrock is coloured in light orange and the small faults are marked in red. The Rio Scuses flows along A during rainfall events. Some openings in the Passo della Morte tunnel are visible

The limestone strata dip  $73^\circ$  to the south-west, in the direction of the Tagliamento River valley. The bedding joint surfaces are undulated, appear to be altered and can have varying thickness of weathered marlstone infill, from few millimetres to a maximum thickness of 25 cm. The sub-vertical attitude of the strata, combined with common openings between layers and the weak properties of the infill material, allows easy infiltration of water into the rock mass during rainfall.

The rock mass is throughout its volume sub-divided by other three joint sets, which aspect and properties description are reported in Table 5.1. Other discontinuities that lead to subdivision of the rock mass are small faults (red lines in Figure 5.4) which are non-continuous and involve only some strata. These structural



features are the result of intense tectonic activity that acted in this area during the orogeny. Further evidence of tectonic activity that acted at an earlier stage, during the sedimentary phase, are the small folds that can be noticed in the central part of the west rock mass face, which make the strata aspect shallower in the upper slope (see Figure 5.4).

**Table 5.1:** Rock mass joint sets, after Codeglia (2011)

Name	Dip dir °	Dip °	Properties
Bedding	170	73	0.1–0.5 m spacing, undulated altered opened joints with 0–25 cm marl infilling
Joint Set 1	065	60	0.5–1.5 m spacing, planar and smooth or slightly rough joints, no filling
Joint Set 2	255	45	0.5–1.5 m spacing, planar and smooth or slightly rough joints, no filling
Joint Set 3	250	85	0.5–0.8 m spacing, slightly altered, tight, smooth joints, no filling

The limestone rock mass can be subdivided in three regions within which structural features are approximately uniform (i.e. Sector B, Sector C, Sector D in Figure 5.4). (A) represents the limestone–dolomite boundary. Sector B is the closest to dolomite, here the limestone bedding is tight, substantially closed, infill material is almost absent and layers are planar and slightly irregular (Sector B). Progressing towards the frontal part of the rock mass, openings between bedding layers become larger, up to several centimetres, with various thickness of weathered marl infill (Sector C). The same opening characteristic is observed in the upper part, above the small folds (E), although the bedding dip angle appears to be shallower (Sector D). Additional features that indicate an area of weakness between Sector B and C is the presence of a particularly fractured zone in which the small faults converge (Figure 5.4).

Further down the slope, about 50 m below tunnel level, at elevations between 670–680 m a.s.l. the limestone outcrop is more fractured. The same discontinuity

sets as in the main outcrop are present, the frequency of the discontinuities is so high that the rock is divided into small elements.

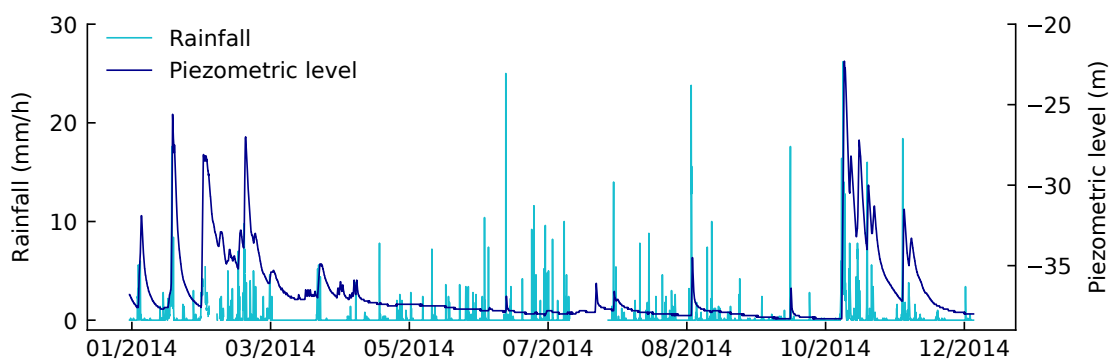
### 5.1.3 Hydrogeology

The hydrogeology of the slope is strongly dependent on the types of rock (i.e. dolomite and limestone), the complexity of the structural setting and the high degree of fracturing of the rock mass. Dolomite and limestone are characterised by very low primary permeability, i.e. low primary porosity, compared to the permeability along zones of high fracturing, such as faults and discontinuities, i.e. secondary porosity (Marcato, 2006). The high degree of pervasive fracturing in the limestone and the very steep orientation of the bedding planes strongly condition the permeability and direction of flow of the underground water that, in general, is directed towards the toe of the slope and replenish the Tagliamento River waters.

The piezometer available on site (see Section 5.2), located within the road tunnel just meters away from the slope (about 5 m from well head at tunnel level, as Figure 5.5 shows), continuously measures the groundwater level by means of a piezometric transducer. Figure 5.6 shows the comparison between the groundwater level measured by P22 and the precipitation. The rise in groundwater level follows the start of rainfall events after few hours, generally in the order of 12–15 hours. The base level is around  $-39$  m from tunnel level, which corresponds to an elevation of about 678 m a.s.l., as can be seen in the example graph reported in Figure 5.6.



**Figure 5.5:** Side tunnel, also referred to as opening on the side of Passo della Morte tunnel. The red arrow indicate the location of piezometer P22 (in this photo it was not yet installed)



**Figure 5.6:** Typical yearly rainfall and piezometric level for the site. To note the variations of groundwater level which can be greater than 15 m

The groundwater level position is considerably high considering the vicinity to the slope (i.e. base level is about 60 m above the river level in the tunnel area). This can be explained in part with the abundant yearly precipitation in the area and in part with the structure of the aquifer.

The yearly average precipitation is about 2,000 mm of rainfall and some 2 m

of snow, which determine a high recharge of the aquifer, able to maintain the level at such elevation. On the surface, common openings between layers aid water infiltration into the rock mass. A preferential water infiltration zone is also located at the dolomite–limestone contact (A in Figure 5.4). It is characterised by a deep incision which hosts the so-called Rio Scluses, a seasonal stream that originates from the rainfall run off occurring onto a 0.55 km<sup>2</sup> basin (Proto, 2014). During intense rainfall events the Rio Scluses waters can be seen falling from this almost vertical channel and during normal rainfall events, the stream waters seep quickly into the very permeable rock. It is interesting to note the presence of karst pools and small caves in the limestone, close to the contact with the dolomite, where the water gather before seeping into the rock. Also the mountains at the back of PdM, which are characterised by karst aquifers, are likely to feed waters into the groundwater at PdM.

In Figure 5.6 it is noticeable how reactive the groundwater system is to rainfall events. It is not rare that the groundwater level rises 15 m or more after an intense or prolonged rainfall event. Rainfall events that last for days are typical during autumn in the area. Events that make the groundwater table rise considerably are usually recorded during autumn time, which is the typical rainy season for the area, and during winter time (generally January to March), caused by simultaneous rainfall and snowmelt that often occurs between consequent snow fall events as well as at the end of winter.

From the graph is also clear that often the amount of rainfall, or its intensity, are not proportional to the variation of groundwater level. As noted above this could be due to snowmelt over winter time but can also be due to the type of aquifer. Waters flowing in a karst aquifer follow preferential channels which are generally related to the rock structure and fractures, which means that they are not confined by watersheds into a certain basin. Waters can travel long distances in a very short period of time compared to granular porous media aquifers. The rock massif at the back of PdM is characterised by this type of aquifer. The structure and asset of rocks

are such that waters tend to travel to the south of the mountain range, where Passo della Morte is located. This means that variations in groundwater level are not always a product of the rain fallen locally but there might be a large contribution by the waters coming from the rock massif at the back of PdM.

#### 5.1.4 Conceptual failure model

The expected failure mechanism for the Passo della Morte limestone rock mass could be described as translational rock sliding, based on the classification of landslides by Varnes (1978), reported in Section 2.1. A typical translational rock sliding would assume that the dip direction of the major discontinuity set is approximately the same as that of the slope (condition one), and the dip angle of the major discontinuity set is shallower than the slope angle, hence daylighting from the slope (condition two). If the dip of the rock blocks is the same as the slope, thus not daylighting from it, a secondary basal release surface with shallower dip must form for the movement to be possible (Stead and Wolter, 2015). A breakout at the toe of steep rock blocks can be generated by development of inter block shear surfaces allowing the toe to be released (e.g. Havaej et al., 2014). When this happens for each steep block forming a rock mass, a stepped release surface can be formed at the toe of the slope.

At PdM the major discontinuity set of the rock mass is the bedding, which persistence and small spacing is predominant with respect to the other discontinuity sets (Section 5.1.2). The bedding orientation is the same as the slope, which makes the rock mass potentially favourable to sliding (condition one above is verified). However, the movement is hindered by the bedding dip of  $73^\circ$  which coincides with the slope dip (see Figure 5.3). The bedding does not daylight from the slope (condition two is not verified). Therefore, additional conditions need to exist for sliding to occur. The development of a release shear surface at the base of the slope would allow the sliding to occur. A potential developing shear zone was identified in the

highly fractured level observed towards the toe of the slope.

It is therefore anticipated that the main sliding surface expected to be at the limestone formation boundary with the dolomite. This is supported by evidence from other landslides occurred in the area (Section 5.1.1), which detached on the formation boundary. A secondary stepped release shear surface will develop towards the toe of the slope to enable translational sliding to occur.

Displacements are expected to occur at the limestone-dolomite surface and at the developing stepped shear surface, but also differential displacements internal to the rock mass, between the limestone strata, are expected to take place. As AE is generated by fracture development and motion along discontinuities (Section 2.3.1), also AE are expected to be generated at these key locations.

Small and impulsive displacements in the order of millimetres at a time are anticipated to occur between layers/boundary limestone dolomite. The interlocking asperities on the bedding surfaces need to be overcome for failure to occur (Section 2.1.1), but this is not entirely possible until the shear zone at the toe of the slope is developed. Therefore the sliding along these vertical features is thought to be stick-slip like (Section 2.1.1.1) until the release conditions are favourable for the asperities to be fully overridden and failure can occur. The frequency and magnitude of stick-slip events are expected to increase as the available resisting forces degrade, until a collapse can occur. The acceleration over time of these events would not be a linear process, which means that, as the critical conditions approach, the events frequency would accelerate towards the failure.

## 5.2 Measurement system

### 5.2.1 Acoustic Emission

At this site three horizontal waveguides, named AEWG1, AEWG2, and AEWG3, were installed in boreholes drilled through the steep limestone layers from within the road tunnel (Figure 5.7). The type of waveguides installed, sensors and parameter settings were previously discussed in Section 3.3.1 and summarised in Table 3.5. It is important to remind that data from this site are subdivided into Series 1 and Series 2 as two versions of the Slope ALARM system, version MK1 and MK2 respectively, were installed at this site at different times.

Each Slope Alarm sensor is housed in a niche created in the tunnel lining around the waveguide end and protected by a plastic enclosure, see an example from the site in Figure 5.8.



**Figure 5.7:** Location of sensors AEWG1 and AEWG2 within the PdM tunnel (yellow circles). The dashed line represents the projection of waveguide AEWG2; waveguide AEWG1 enters the rock mass approximately perpendicular to the photograph, which makes not possible to indicate the waveguide



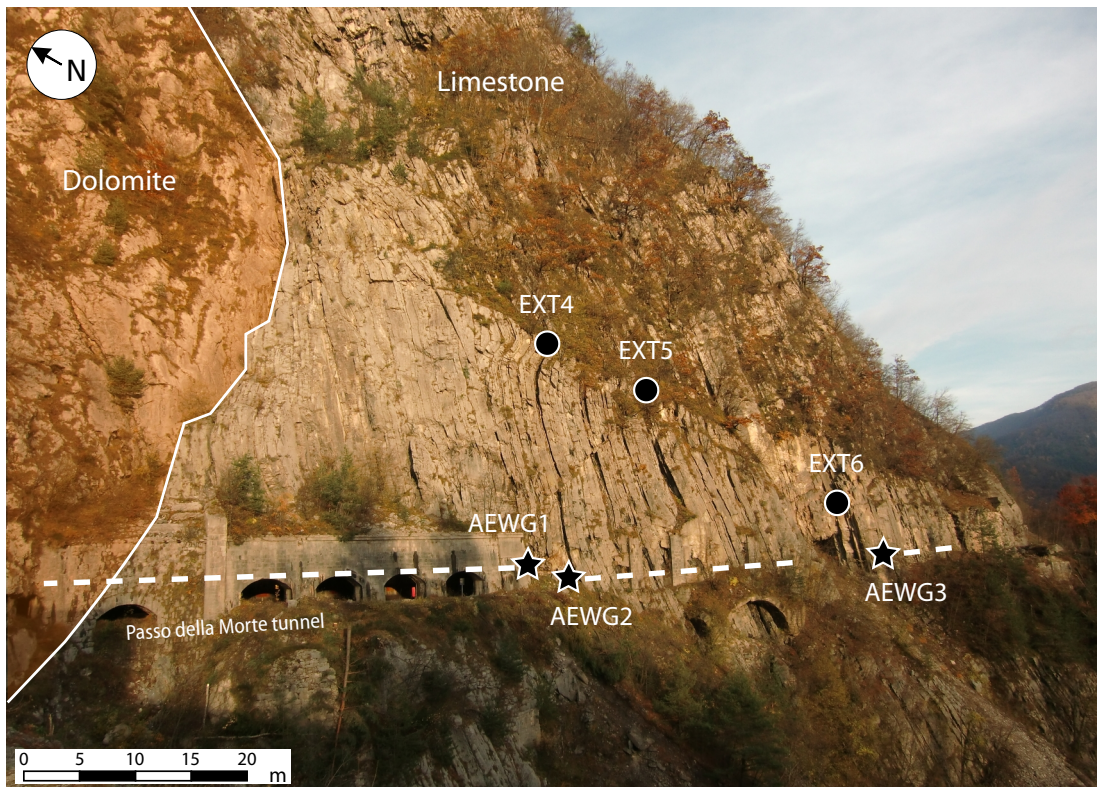
**Figure 5.8:** Plastic enclosure protecting AE equipment at Passo della Morte site placed in a niche formed within the road tunnel lining



The three waveguides are grouted within boreholes that were designed to monitor critical zones of the rock mass that were identified through geological and geomorphological surveys. The waveguides, therefore, monitor specific features of the rock mass, referring to Figure 5.4 and Figure 5.9:

- AEWG1 (50 m) is placed across the limestone-dolomite boundary. It penetrates the rock mass away from the slope, reaching the stable stratum of dolomite in the last 12 m thus monitoring the behaviour of the rock mass at the contact limestone–dolomite (A);
- AEWG2 (30 m) is placed within Sector C, it penetrates the limestone slabs between the tunnel lining and the slope surface, to monitor activity of those openings filled with marl that can be observed daylighting on the slope face;
- AEWG3 (10 m) penetrates the limestone layers between the tunnel lining and the slope face in the front part of the rock mass.

The waveguides are smooth steel pipes in singular lengths of 3 m joined together with connectors to reach the desired total length. The waveguides were equipped with three MK1 sensors at different times (see Series 1 in Table 3.5). After AEWG1 ceased to operate during the Autumn of 2014, after about 5 years of continuous operation, all the devices were replaced with sensors and transducers of the newer version MK2 on 13/10/2014 (see Series 2 in Table 3.5). Data collected with the two Slope ALARMS versions are not directly comparable because of the different sensitivity of the sensors, as it will be discussed in Section 5.3.1.



**Figure 5.9:** West rock mass face with projection of waveguides (dashed lines) and position of the Slope ALARMS sensors (stars, AEWG1,2,3) and locations of crackmeters (EXT4,5,6)

## 5.2.2 Other available instruments

Several conventional monitoring instruments are installed at the Passo della Morte site. The monitoring network was set up in various stages since the Summer of 2010. This monitoring project was undertaken by the Research Institute for Geo-Hydrological Protection of the Italian National Research Council (CNR-IRPI) on behalf of the Civil Protection Department to assess the state of activity of the unstable rock mass and risk associated. CNR-IRPI has made data available for comparison with RDC trends throughout this research project.

In this work, acoustic emission data are compared to displacement data from three crackmeters, groundwater table level from a piezometric sensor, rainfall, snowfall and temperature data.

A summary of the instruments available at site and used for comparison is provided in Table 3.4. Below a brief description of their location and main characteristics is provided.

#### **5.2.2.1 Temperature probe**

The temperature sensor is located on the west rock mass face, in an opening between the tunnel and the slope and shaded by the surrounding rock to measure the air temperature. The location is shown in Figure 5.11.

#### **5.2.2.2 Rain gauge**

The rain gauge is located 1 km South-East from the PdM site along the same valley, see Figure 5.10, therefore rainfall data are fully representative of the conditions at site. Continuous rainfall data are available since December 2010.

#### **5.2.2.3 Snow gauge**

The snow fall data used for comparison were measured at the closest available snow gauge which is located on the opposite side of the valley, about 5 km South-West from the PdM site at an elevation of 1710 m a.s.l. (Figure 5.10). Data are available since January 2012.

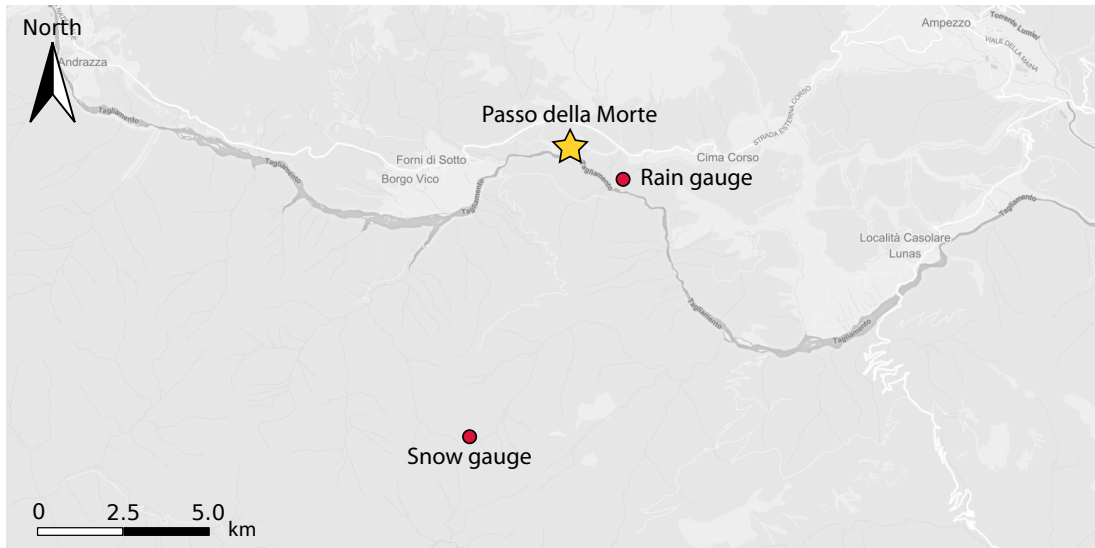


Figure 5.10: Location of rain gauge and snow gauge with respect to Passo della Morte

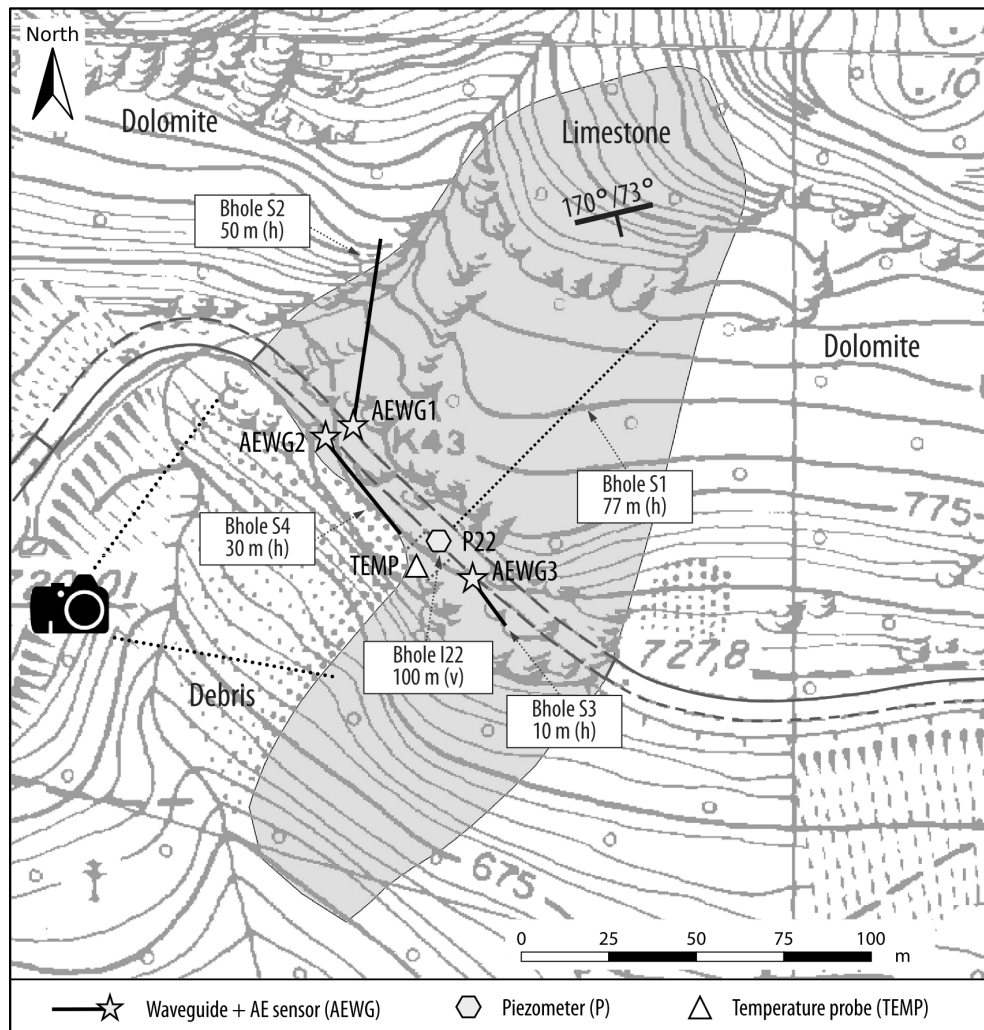
#### 5.2.2.4 Crackmeters

Three crackmeters (EXT4, EXT5, EXT6) were installed to monitor activity across critical bedding planes within Sector C. The bedding planes daylight on the west rock mass face and are filled with particularly thick levels of marl, which has lower strength than limestone and therefore are considered as weakness features that need monitoring. The location of crackmeters EXT4, EXT5 and EXT6 on the west rock mass face can be seen in Figure 5.9. The crackmeters were in operation from April 2011 until failure in September 2014.

#### 5.2.2.5 Piezometer

The piezometric transducer is placed at the bottom of a 100 m deep vertical borehole that contains an inclinometer case permeable to water. The borehole was drilled from within the road tunnel, therefore its head and reference for the piezometric measurements is located at an elevation of 720 m a.s.l. From a plan view, the borehole is about 5–10 m from the edge of the slope at the tunnel elevation. The piezometer location can be seen in the map of the site in Figure 5.11. Data are

available since April 2011.



**Figure 5.11:** Schematic of the unstable limestone rock mass outcrop and position of waveguides (AEWG1, AEWG2, AEWG3), along with piezometer (P22), temperature probe (TEMP). The camera icon indicates the approximate camera position and orientation used to photograph the west rock mass face (e.g. Figure 5.9); (h) and (v) indicate horizontal or vertical borehole orientations respectively

### 5.3 Analysis of field monitoring results

In order to identify significant trends, acoustic data were firstly analysed to understand their range and distribution and to locate patterns that repeat over time. Secondly, acoustic data were compared to data from other traditional instrumen-

tation available at the site. AE data were therefore compared to the variation of groundwater level measured by the piezometer (P22), to the displacement of discontinuities measured by crackmeters (EXT4, EXT5, EXT6) and the snowfall data measured at the closest available snow-gauge. Additionally, possible correlations with earthquakes occurred in the area were considered.

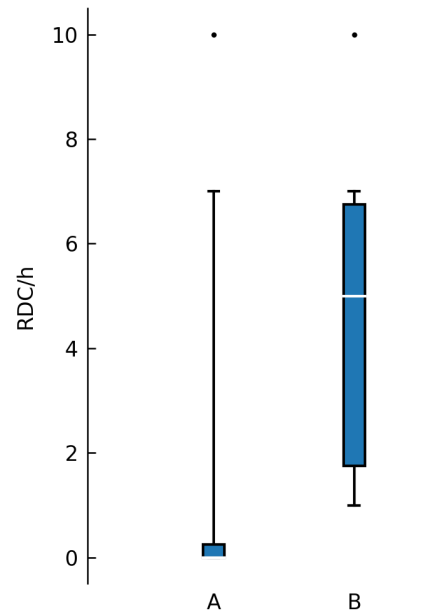
### 5.3.1 Acoustic Emission

Figure 5.13 shows RDC/h data distribution represented with boxplots. Two boxplots, which represent Series 1 and Series 2, were generated for each one of the sensors installed at the site (AEWG1, AEWG2, AEWG3). Series 1 is represented in blue (AEWG1), red (AEWG2) and green (AEWG3) boxplots placed to the left-hand side of the pair. Series 2 is represented with lighter shades of the same colours placed to the right of each pair. In each boxplot the white middle line represents the median (or 50<sup>th</sup> percentile), the top line of the box is the 75<sup>th</sup> percentile, the bottom line of the box is the 25<sup>th</sup> percentile, the top whisker represent the 99<sup>th</sup> percentile and the lower whisker represents the 1<sup>st</sup> percentile. Data higher than the 99<sup>th</sup> percentile and lower than the 1<sup>st</sup> percentile are represented with dot markers. The outlier values (i.e. the black dots) are infrequent as they represent the extreme 1% of each side of the represented data range, which means that it is rare for them to occur. Data equal to zero RDC/h are excluded from the boxplot representation.

Data equal to zero RDC/h signifies that no acoustic emission was recorded for that time period as a consequence of no AE being generated at the site. Therefore, time periods in which data are zero mean that nothing is happening. This is essential in the validation of AE data that are higher than zero RDC/h as it demonstrates that these latter can be linked to discrete (i.e. individual and non continuous) events.

Data equal to zero RDC/h are excluded from the boxplots in Figure 5.13 for the sole purpose of showing the spread in AE data recorded that represent events

happening at the site (i.e.  $>0$  RDC/h). Data equal to zero RDC/h mean that nothing is happening at the site and are therefore excluded from this representation. However, it is important to clarify that data equal to zero RDC/h are considered in the data analysis throughout this thesis and are also used as an important control in the comparison with other instruments data. As boxplots show the frequency of data, not excluding data equal to zero in the representation, would partially mask data greater than zero RDC/h not showing their actual distribution, as in the example on Figure 5.12. As Table 5.2 shows, largely over 50% of data are equal to zero RDC/h.



**Figure 5.12:** Example. (A) represents a population of data with 75% zero values; (B) represents the same data with zeroes removed to show distribution of data greater than zero

Table 5.2 shows the percentage of measurements that were equal to zero RDC/h per each sensor and per each Series (algorithm for calculation of the percentages is available in Appendix D). It is noticeable that Series 1 measured considerably less events than Series 2, but this is expected as the sensors were less sensitive (i.e. see Test A in Section 4.1.1). Series 2 shows more balance between measurements and

periods of nothing happening, 65% of zero RDC/h data on average, than Series 1. The fact that over 50% of data is actually equal to 0 RDC/h provides evidence of the stability of the measurement system but also that the system does not record rates all the time, which encourages to think that it does not measure activity that is to be considered noise.

**Table 5.2:** Percentage of monitoring periods equal to 0 RDC/h for every sensor and each series

	AEWG1	AEWG2	AEWG3
Series 1	63%	91%	92%
Series 2	50%	61%	83%

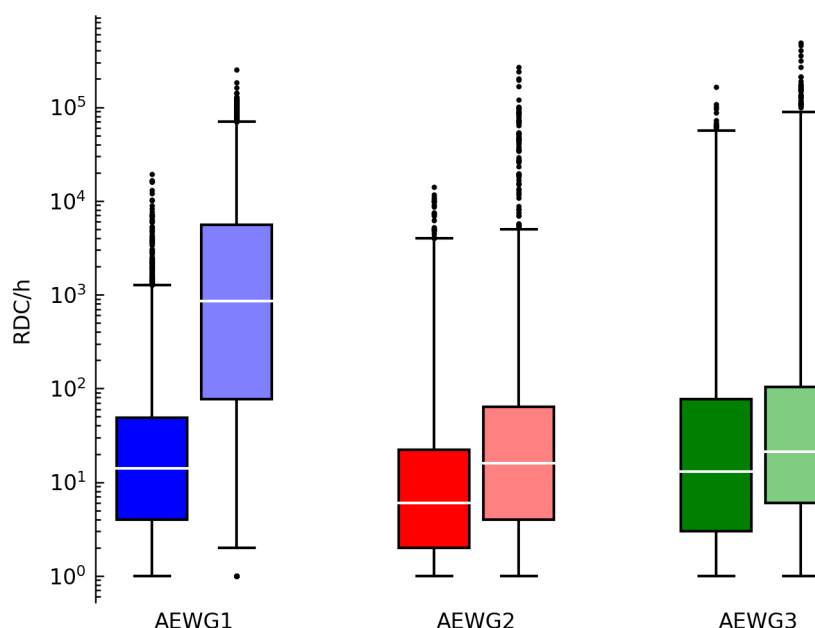
Data higher than 0 RDC/h are plotted in Figure 5.13 on a logarithmic scale to be able to visualise the whole data range, which spans several orders of magnitude. The logarithmic plot is also the reason for the outliers to appear so densely located, they would be much more scattered if plotted on a normal scale.

All boxplots are positively skewed, which means that most of the observations are concentrated on the low end of the scale, although this does not appear obvious from the graph as boxplots are plotted on a logarithmic scale.

In the comparison it has to be considered also that the two series were recorded at different times and the rock mass behaviour changes over time (i.e. it is not a regular signal), hence it is to be taken into account that the series would never match even if they were recorded with the same sensors.

The boxplots relative to Series 1, which are represented with darker shades to the left of the pairs in Figure 5.13, show quite low RDC/h values for all sensors. The 50<sup>th</sup> percentiles are lower than 14 RDC/h and the 75<sup>th</sup> percentiles lower than 77 RDC/h. The 99<sup>th</sup> percentiles are below 4,000 RDC/h for AEWG1 and AEWG2 whereas AEWG3 shows completely different rates in the upper part of the range, being its 99<sup>th</sup> percentile more than one order of magnitude higher than the other two sensors, about 56,000 RDC/h.





**Figure 5.13:** Distribution of RDC/h values higher than zero: top whisker = 99% of data, box top = 75%, white middle line = median (50%), box bottom = 25%, low whisker = 1%. Dots are outliers. Series 1 to the left of the pair and Series 2 to the right of the pair

It might seem that there is consistency among the three sensors as the range of measured AE data is quite similar. However, this is not the case as the sensors voltage threshold was not set to the same level due to manual switches, as explained in Section 3.2.2.3. This leads to differences in the measured RDC counts. A laboratory test was designed to assess the difference in measured RDC when a standard signal input is given (Test A, Section 4.1.1). It was found that, on average, AEWG1 measured 45% less RDC counts than AEWG2 and 42% less than AEWG3 and AEWG2 measured 6% more than AEWG3.

The boxplots representing Series 2, which are those in lighter shades to the right of the pair in Figure 5.13, show similar distribution and data ranges, except for sensor AEWG1. In fact this sensor measured much higher RDC/h being its 50<sup>th</sup> percentile about 850 RDC/h and its 75<sup>th</sup> percentile around 5,500 RDC/h which is much higher compared to AEWG2 and AEWG3, which 75% of data does not exceed 104 RDC/h. However, AEWG1 outliers are between about 70,000 RDC/h and

250,000 RDC/h, which are not higher than the other two sensors, being their maximum counts around 270,000 RDC/h for AEWG2 and 490,000 RDC/h for AEWG3.

Comparing the two series, the AEWG1 median value appears higher of about two orders of magnitude in Series 2 compared to Series 1 and the same can be noticed for the 25<sup>th</sup> and 75<sup>th</sup> percentile. Also values lower than 3 RDC/h are much less frequent, being in fact less than 1% of the total number of values. AEWG2 is more consistent across the two series with the 1<sup>st</sup> and the 25<sup>th</sup> percentile higher of just few RDC/h, the median and the 75<sup>th</sup> percentile shifted higher of some tens of RDC/h. The 99<sup>th</sup> percentile is noticeably similar between the two series. The most significant difference is that the outliers reach two orders of magnitude higher in Series 2. AEWG3 is the sensor that shows most consistency across the two series, with a difference of only a few RDC/h in the distribution, and a few higher RDC/h outliers.

Although there are similarities in the distribution and data range between the two series (for AEWG2 and AEWG3 at least), Series 1 and Series 2 cannot be directly compared. When tested in the laboratory (Test A, Section 4.1.1) the MKI sensors used in Series 1 recorded fewer counts than the MK2 sensor used in Series 2. On average, AEWG1 recorded 57% less counts than a MK2 sensor, AEWG2 23% less and AEWG3 27% less.

For consistency Series 2 will be used throughout this work, unless otherwise explicitly stated, as the three sensors were set up with the same settings (i.e. voltage threshold set to 0.25 V) and comparison among them is therefore meaningful. This assures that a difference in data range and distribution is exclusively due to different rock mass behaviour at different locations and is not due to differences in the sensitivity of the equipment.

#### 5.3.1.1 Daily and weekly trends

As the waveguides at Passo della Morte are installed through the road tunnel, which was open to traffic circulation until 20/06/2016, a preliminary analysis was carried out in order to assess whether the database is affected by events recurring on a daily or weekly basis. Events with such frequency could be linked to noise generated by human recurring activities (e.g. road traffic) or interference.

The road tunnel has not been used as the main road since the opening of a new by-pass tunnel in 2008 (see Figure 5.1) but it remained in operation for local residents traffic until June 2016. Therefore, vibration induced by cars and vans passing through the tunnel has to be taken into account as a potential source of AE recorded by the sensors. It is reasonable to assume, for example, that traffic circulation would be higher during the morning and afternoon rather than the evening and night and during weekdays rather than weekends.

To look for such trends, the number of monitoring periods (hours) in which RDC resulted higher than zero was taken into account and grouped by hour of the day in Figure 5.14a and day of the week in Figure 5.14b. In this analysis the number of hours with  $RDC > 0$  are used as opposed to adding together the RDC for every hour of the day or day of the week. Doing so gives an indication of whether there was activity or not during that hour or day and therefore can be used as an estimation of the frequency of events occurring within certain time periods. If data (i.e. RDC) were added up the resultant would take into account the intensity of the events, which might not be relevant in this case (i.e. we are interested to see if AE is recorded more often at a certain time rather than how strong this AE is).

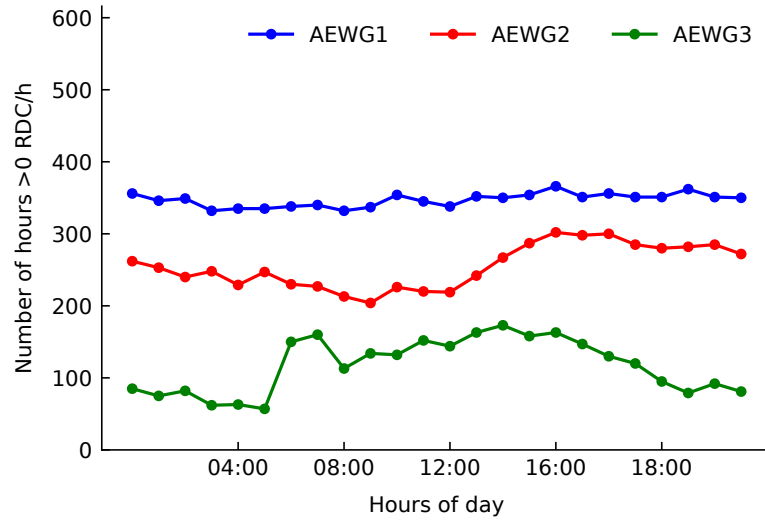
For consistency, only data from Series 2 were used (Table 3.5, recorded after 13/10/2014 20:00), until the tunnel closure (20/06/2016 12:00); it is important to remind that all three sensors were working correctly during this time frame. The functions used for data selection are fully available in Appendix D.

Figure 5.14a shows the daily graph on which the number of hours with RD-

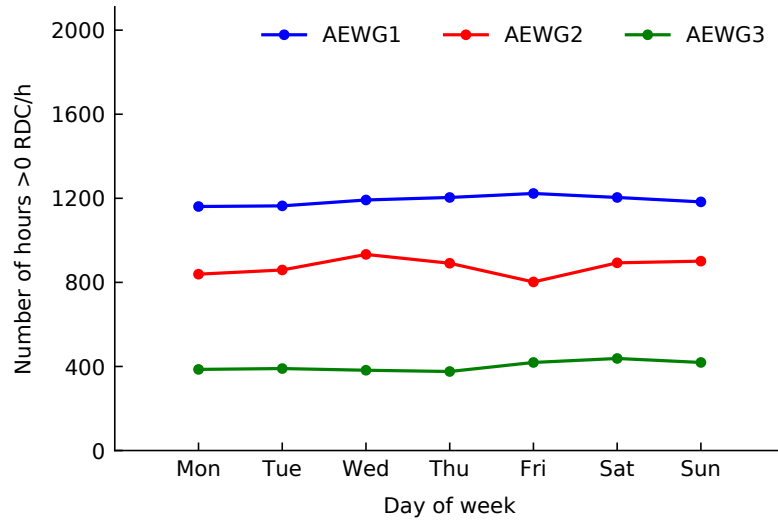
$C/h > 0$  where plotted for each hour of the day (00:00–23:00). All sensors show trends that are relatively flat, with no significant higher activity at particular times. The trend for AEWG1 is completely flat, AEWG2 shows a slightly increasing number of activity hours during late afternoon/evening and AEWG3 shows higher numbers during the day, increasing during the morning and decreasing during the afternoon, with the lowest value at 05:00 and the highest around 14:00–15:00. This might resemble daily temperature cycles, although a more gradual increase would be expected in the early morning (06:00–07:00). In fact AEWG3 shows a sharp increase in the number of times there was AE activity in the early hours of the day. However, considering the absolute number, this is still much lower than the average number of hours with  $RDC/h > 0$  for sensors AEWG1 and AEWG2, which observation takes to the conclusion that this increase is not significant.

Figure 5.14b reports the weekly plot which show rather flat trends for all sensors, with no differences between weekdays and weekends. It is reasonable to conclude that the dataset is not affected by traffic-induced acoustic emission.

It is also interesting to note that the number of hours in which acoustic activity is recorded is generally higher for AEWG1 and lower for AEWG3. In general AEWG1 records acoustic emission more frequently than AEWG2 and AEWG3 and sensor AEWG3 records AE the least frequently compared to the other two sensors.



(a)

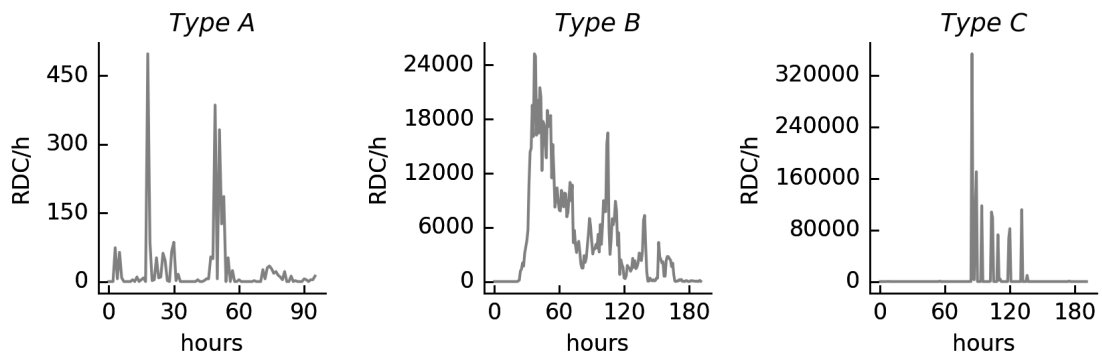


(b)

**Figure 5.14:** Number of hourly AE monitoring periods above zero (a) by hour of the day; (b) by day of the week, for each sensor. The y axis upper limit is set to the actual total number of monitoring periods (hours) existing per each hour of the day and day of the week, respectively, for the time interval considered (13/10/2014 20:00:00 to 20/06/2016 12:00:00)

### 5.3.1.2 Recurring patterns

Recurring types of AE events can be observed in the data measured at the Passo della Morte site. The events can be visually subdivided in three categories based on different patterns (Type A, Type B, Type C) which are characterised by specific RDC/h ranges: Type A is generally in the order of hundreds of RDC/h, Type B is in the order of tens of thousands RDC/h and Type C is in the order of hundreds of thousands RDC/h, as can be seen in Figure 5.15. Events are defined as periods of measured AE activity that can be one or more monitoring periods bounded by periods of zero or RDC/h  $< 10$  within one monitoring period.



**Figure 5.15:** Type A, Type B and Type C acoustic emission patterns at Passo della Morte. Generally, Type A is in the order of hundreds RDC/h, Type B in the order of tens of thousands RDC/h and Type C in the order of hundreds of thousands RDC/h

*Type A* pattern events are common throughout the data series, occurring during both dry and rainfall periods. AEWG1 typically has measured counts in the range 100–400 RDC/h, which last for one or very few 1-hour monitoring periods. AEWG2 *Type A* events are in the same order of count rate as AEWG1 but they can last for several consecutive 1-hour monitoring periods. AEWG3 event rates are higher, about 300–1000 RDC/h and generally last for a single 1-hour monitoring period and are more frequent than AEWG1 events. Rarely these events are recorded by all the waveguides simultaneously, which leads to the hypothesis that such events are generated by local mechanisms (e.g. deformation on a discontinu-

ity or local rockfall) generating low energy AE that cannot propagate to more than one waveguide.

*Type B* pattern events usually last for a few days and are recorded primarily by AEWG1. These types of events can show a sharp increase in RDC/h rate at the beginning, or they can gently rise to a peak RDC/h rate, but in both cases the rates typically decrease gradually. AEWG2 occasionally shows the same pattern, simultaneously with AEWG1 but with much lower RDC/h. AEWG3 never shows this type of events. Type B events seem to be mainly associated with changes in the groundwater level. A thorough discussion is provided in Section 5.3.2.

*Type C* pattern events are in the order of hundreds of thousands RDC/h within a single 1-hour monitoring period, giving them a very sharp peak shape. These events reached 260,000 RDC/h on waveguide AEWG1 and AEWG2 and almost 500,000 RDC/h on AEWG3. The peculiarity of this type of events is that they in general last for short periods of time, normally one to three monitoring periods (i.e. hours) and the number of counts recorded per monitoring period is extremely high. The spikes can be grouped in clusters over periods of some days or be more sporadic. AEWG1 and AEWG2 show the same event pattern in the same time periods. However, AEWG3 appears to be particularly sensitive to the generation of this type of events showing RDC rates that are approximately double of those recorded from AEWG1 and AEWG2 in the same monitoring period. Comparison with snowfall data suggest that they could be generated by snow loading on the surface of the slope. Acoustic emission rates due to snow load are discussed in Section 5.3.3.

It is important to consider also that Type A pattern can be masked by Type B and Type C events, thus it might not be possible to recognise them when the other two types are present. In some cases Type C pattern can be superimposed on Type B, thus acquiring the shape of spikes rising from a Type B event.

Some patterns above described are often lost from the graph representation when analysing data at a higher-order scale, because they might be too small to

be represented (i.e. a 100 RDC/h event might not be visualised when the y-axis is set to 100,000 RDC/h because too small). To overcome this problem during the analysis, data were plotted on dynamic graphs that allowed zooming/panning, thus updating live the x and y-axis range displayed. The Python programming language was used and the code to achieve this is available in Appendix D.

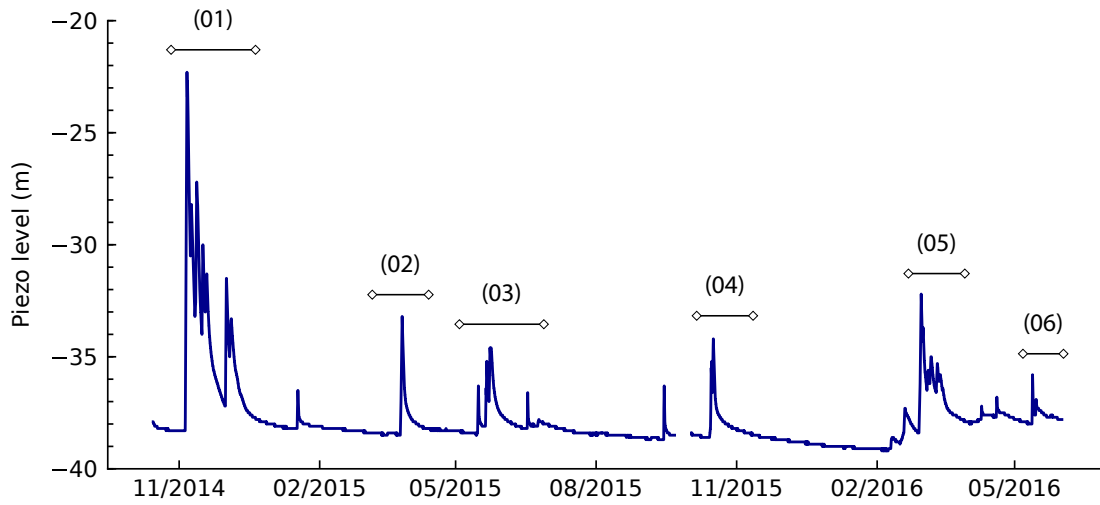
To be able to reach a better understanding of the acoustic trends recorded, all the possible causes that can generate acoustic emission have to be taken into account, therefore, earthquakes have been considered as a possible source as Passo della Morte is located in an active seismic zone. As a rock mass shakes under the effect of the peak ground acceleration (PGA) cracks can grow or small displacements can take place, hence releasing energy in the form of high frequency waves (AE). Further discussion is reported in Section 5.3.5.

### **5.3.2 Variation of groundwater level**

Periods of intense and prolonged rainfall, which are common in particular during autumn time in the area, induce very large variations in the piezometric level, in the order of tens of meters. AE trends are recorded in response to these changes in water pressure within the rock mass. It was observed that these AE trends correspond to the Type B recurring pattern (Section 5.3.1.2).

In order to quantify the acoustic emission rates recorded in response to varied conditions in groundwater level, six groundwater variation events were analysed. The events were recorded between October 2014 and June 2016 and the time frames considered are indicated in Figure 5.16, which shows the piezometric level graph for this period of time.





**Figure 5.16:** Groundwater level variation events analysed

Event 1 is reported in Figure 5.17. This is the event with the biggest variation in the groundwater level. A group of five overlapped events can be observed in Figure 5.17a, the first of which shows a rise in groundwater level of 17 m. In the example, the first rainfall event starts at 00:00 on 04/11/2014 after a quiet and dry period; the piezometric level is initially  $-39$  m from tunnel level, which elevation is 720 m a.s.l. As the groundwater table response begins at 00:00 on 05/11/2014, RDC/h increasing trends are recorded by waveguide AEWG1. The sensor records AE trends for the whole duration of the event, which appear to be somehow proportional, except for some peaks. Figure 5.17b, which shows AE versus variation in the groundwater level (referred to the initial level), confirms that there is correlation between the acoustic emission measured by AEWG1 and the variation in groundwater level.

During the 24 hours preceding the event no AE activity is recorded by any of the sensors, although it was raining intensely, up to a maximum intensity of 28 mm/hour. This observation is of great importance because it excludes the possibility that the AE recorded is generated by rainfall seepage through discontinuities or by water flowing onto the waveguides. If that was the case AE would have been recorded earlier, in conjunction with the start of the rainfall or shortly after. This is

confirmed by the graphs in Figure 5.17c, which plots the AE data for each sensor versus the rainfall. The graphs clearly show that there is no correlation between the two quantities.

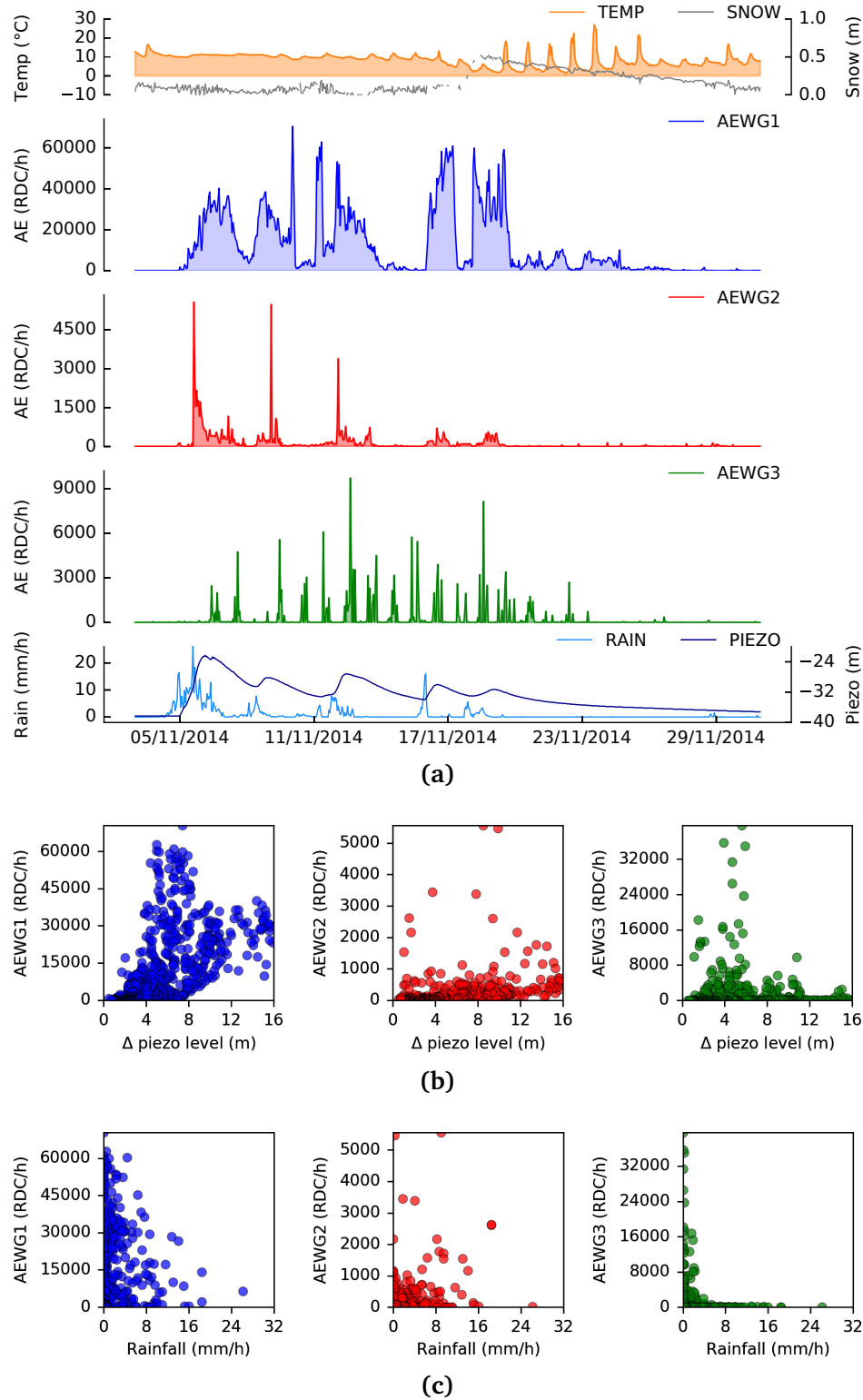
The same behaviour can be observed for the consecutive rainfall events, although RDC/h does not start from zero as there is an overlapping effect from previous events. The groundwater level reaches its maximum (−22 m) at 03:00 on 06/11/2014 and after a few hours it starts to decrease. Finally, AE rates decrease, but do not reach zero because a new rainfall event again takes place.

AEWG2 do not seem to respond instantly to the rise of groundwater level. Looking at the first event, AEWG2 has a delay of several hours with the start of the variation. Considering the respective graph in Figure 5.17b, the sensor seem to show proportionality with the groundwater only for variations larger than 10 m.

AEWG3 response is completely different, it appears spiky throughout and does not show any proportionality to the groundwater variation events. AE trends measured by AEWG2 and AEWG3 do not correlate with rainfall data (Figure 5.17c). To summarise, only AEWG1 shows a clear proportionality with the variation in groundwater level, although with occasional higher AE spikes. There is also proportionality in terms of distribution with time, that is a sharp increase at the beginning of an event followed by a gentle decrease as the water level equilibrates to the long-term level. The proportionality is also confirmed by the AE rates versus piezometric (absolute) variation graph (Figure 5.17b) where it can also be observed that:

- a water level increase of 1 to 2 m induce 1,000–5,000 RDC/h;
- an increase bigger than 5 m induce AE rates in the order of 5,000-30,000 RDC/h.

### 5.3. Analysis of field monitoring results

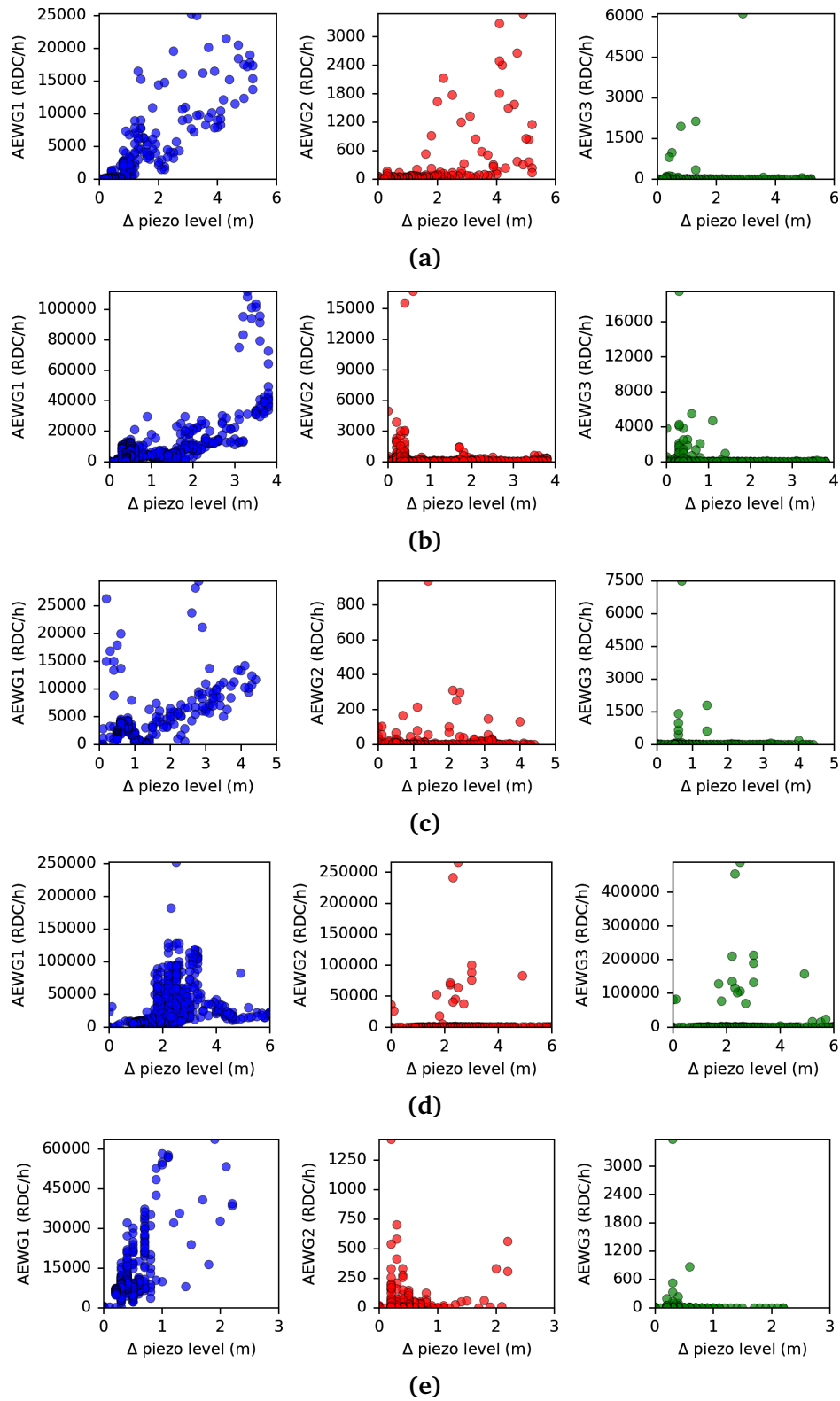


**Figure 5.17:** Event 1. (a) full graph (representing temperature, snowfall, AEWG1, AEWG2, AEWG3, rainfall and piezometric level) vs time; (b) acoustic emission (RDC/h) vs variation of groundwater level (m); (c) acoustic emission (RDC/h) vs rainfall (mm/h)

Figure 5.18 reports the AE versus GWL variation graphs for Events 2 to 6. The variation is calculated from the groundwater base level, which is  $-39$  m from tunnel level (720 m a.s.l.) and equals to 681 m above sea level. Considering all six events, including Event 1, the following recurring patterns can be consistently recognised:

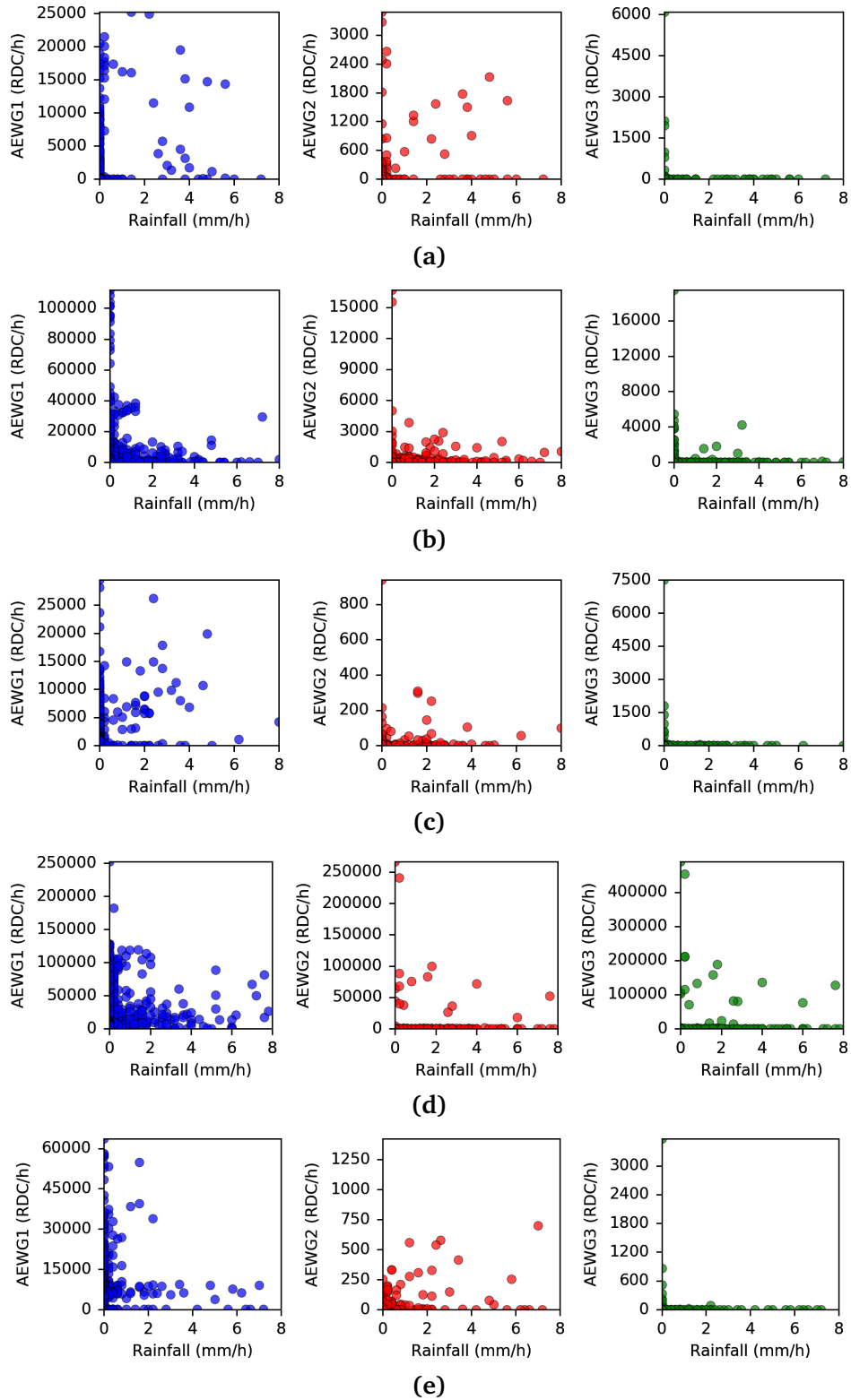
- A delay of 12–24 hours occurs between the start of a rainfall event and the rise of water level and no RDC is generally recorded during this period of time, which implies that seepage through fractures between the rock slope surface and groundwater is not responsible for generation of AE trends;
- RDC/h vs rainfall graphs confirm that there is no relationship between these two quantities for any of the sensors as it appears clear in Figure 5.19. This demonstrates that AE is not generated by rainfall directly seeping on sensors components or on the waveguides, which would be considered spurious noise;
- AEWG1 shows a relationship with the variation in groundwater level. The response is simultaneous with a rise in groundwater level. AE rates tend to accelerate when the water table rises and to decelerate, more or less sharply, when it returns to the base level. Hence, the AE follows the stress changes within the rock structure;
- Figure 5.18 confirms that there is proportionality for all the Events with the acoustic emission measured by AEWG1;
- AEWG2 shows a similar response, although not as pronounced: only increases in water level  $>10$  m (from the groundwater base level that is around  $-39$  m) correlate with increased AE activity. Counts are in the order of 1,000–2,000 RDC/h;
- None of the events represented in Figure 5.18 shows proportionality with AEWG2, however none of the events exceeds 6 m of groundwater level variation;

- AEWG3 shows sporadic activity that appears sharp and spiky (i.e. RDC is generated over a small number of monitoring periods) and does not show any proportionality with the variation of groundwater level, which is confirmed by the graphs in Figure 5.18.



**Figure 5.18:** Acoustic emission (RDC/h) vs variation of groundwater level (m) graphs for: (a) Event 2; (b) Event 3; (c) Event 4; (d) Event 5; (e) Event 6

### 5.3. Analysis of field monitoring results



**Figure 5.19:** Acoustic emission (RDC/h) vs rainfall (mm/h) graphs for: (a) Event 2; (b) Event 3; (c) Event 4; (d) Event 5; (e) Event 6

Given these observations, the hypothesis for this type of events is that changes in water pressures due to an increase/decrease of water level induce micro-deformation and consequent AE stress release (Section 2.3.1).

Increased water pressure in cracks due to rising groundwater level (approx. 681 m a.s.l.) can determine a small decrease of the available resisting forces along the bedding planes by applying pressure in a direction normal to the sides of the discontinuities. This way the discontinuity is able to move due to gravity and its own weight, even if just fractions of mm.

The deformation is a non-linear process and develops in steps of instant energy release. This can relate to slip-stick behaviour along the main discontinuity set, the bedding. Build-up of water pressure helps slightly decrease the strength of discontinuities and thus micro-asperities can be overcome (i.e. stick-slip, Section 2.1.1.1).

The micro-displacements generate AE that is measured by the Slope ALARMS sensors. However, the AE is unlikely to be linearly related to the displacement. Rather, the release intensity depends on the energy previously accumulated and hence it is expected that the relationship between piezometric level change and AE rates will not always be proportional (referring mainly to AEWG1).

This process is transient, lasting until the increased water pressure is dissipated by the natural system drainage (i.e. water flows out of the slope to the river and the groundwater level decreases to the normal base level).

The different response for sensor AEWG1 compared to AEWG2 and AEWG3 to the same generating mechanism is explained by their location: AEWG1 penetrates deep into the rock mass crossing multiple bedding planes and the contact between the limestone and dolomite, whereas AEWG2 and AEWG3 are located near to the slope face and thus monitor a portion of the rock mass close to the surface.

This suggests that the release of acoustic emission happens predominantly at the back of the pack of limestone strata, towards the dolomite-limestone boundary (A in Figure 5.4) and that the front part of the rock mass Sector B, C, D probably



act as a block, with little deformation within it. This well reflects the hypothesis set out in the failure model (Section 5.1.4).

It is expected that the groundwater level rises much more at the back towards the dolomite than it does at the front of the rock mass towards the valley (where the piezometric transducer P22 is placed) due to the high recharge input from the massif at the back. Hence the water pressure would be higher at the back towards the dolomite and cause micro-displacements in this area.

### 5.3.3 Snowfall

Events of the Type C that were defined in Section 5.3.1.2 are observed during winter time. For this reason they were compared with temperature and snow data. Snow data are acquired at the the closest available snow-gauge which is located in the vicinity of Malga Cjampiuiz [Lat 46.3505, Lon 12.6790]. When interpreting snow data versus other parameters such as temperature it is important to take into account that the snow-gauge is located 5.5 km SW from Passo della Morte at an elevation of 1710 m a.s.l., which is about 1000 m higher than Passo della Morte at tunnel level, where the temperature sensor (TEMP) is located. Therefore, snow events recorded by the gauge might have not taken place at PdM site. For this reason, only events that meet the following two conditions are considered as actual snowfall events occurring at Passo della Morte:

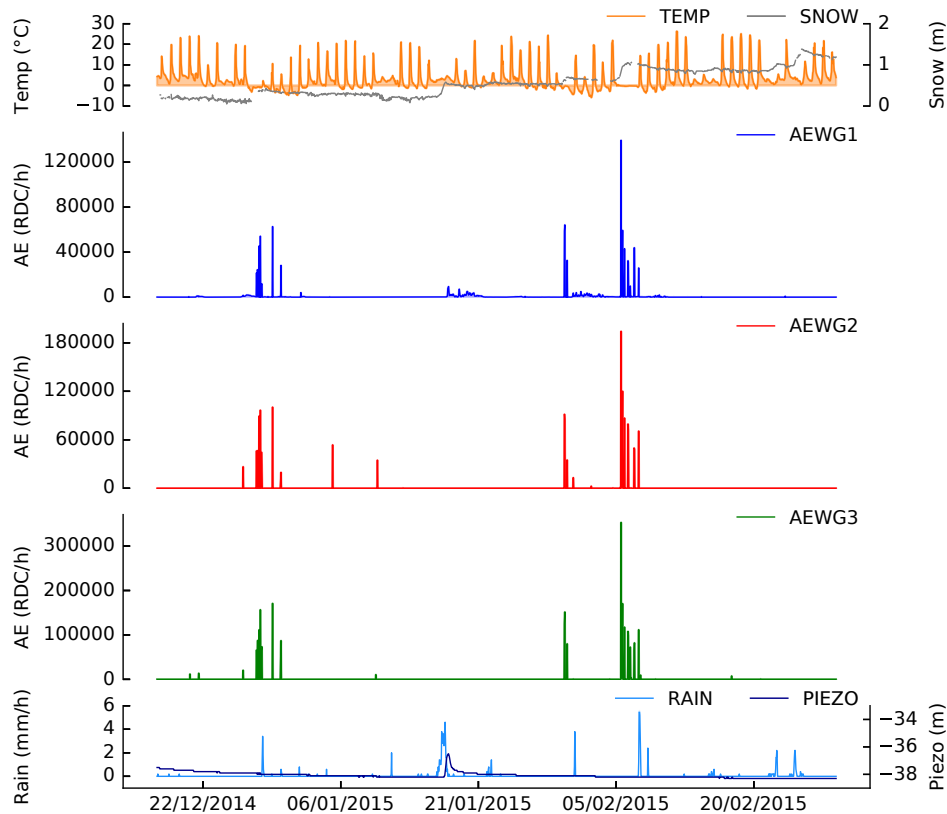
- (1) an increase in the snow-gauge plot can be observed;
- (2) the temperature is ranging around zero.

At higher elevations temperatures are generally lower, if condition (1) is verified but condition (2) is not, a snowfall event has probably taken place at the snow-gauge elevation, but not at PdM where temperatures are higher and hence precipitation is expected as rainfall. Also a period of constant temperature is considered as an indicator of thick cloud cover, which could indicate favourable conditions

for snow precipitations, provided that temperature is low enough. It is generally accepted (e.g. Rossow and Lacis, 1990; Rossow and Zhang, 1995) that cloud cover reflects part of the sun light spectrum determining lesser earth's heating during the day, and retaining earth's warmth from escaping into space at night, hence influencing the fluctuation of air temperature. Fluctuation will thus be minimal in case of clouds cover during winter time as temperatures are already generally low.

The snow would determine an additional load on top of the rock mass. To give an approximate order of magnitude, typical snow density values were researched. Paterson (1994) suggests snow density values between about  $100 \text{ kg/m}^3$  for light new snow immediately after falling and  $400 \text{ kg/m}^3$  for wind packed snow, in this range are included intermediate values which refer to damp and settled snow. Taking an average snow density value of  $200 \text{ kg/m}^3$ , the stress increase for every 0.1 m of snow depth would be in the order of  $20 \text{ kg/m}^2$ . Multiplying this value for the extension of the upper slope, approximately  $5000 \text{ m}^2$ , would mean 100 tonne across the whole surface per every 0.1 m of snow depth. It is not rare that a single snow fall event in the area reaches 0.5–1 m, which would mean that 500–1000 tonnes can be applied to the top of the slope in a few hours.

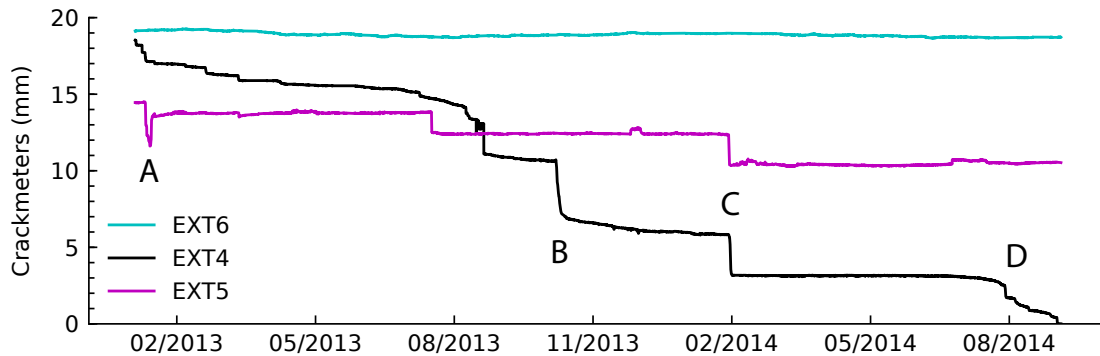
This increased load could lead the rock mass to vertical movement as a block. The main movement would probably concentrate on a single discontinuity at the back of the rock mass, likely along the dolomite–limestone transition. As such complex structure moves, however, it would also generate differential micro-displacements within the rock mass itself, generating the acoustic emission behaviour recorded by all sensors simultaneously.



**Figure 5.20:** Examples of AE rates (RDC/h) in response to snow load. The high count events last for short time. They are clustered around the times when the snowfall occurs and are clearly not correlated with piezometric level changes or rainfall events

### 5.3.4 Displacement on discontinuities

Crackmeters installed to monitor activity along critical bedding planes daylighting on the slope (EXT4, EXT5, EXT6 in Figure 5.9) were able to identify displacements of different entities. The instrument that was able to measure the biggest deformation is EXT4. As can be observed in Figure 5.21, the cumulative displacement measured by EXT4 is about 18 mm in 21 months (January 2013 to September 2014), EXT5 recorded 4 mm cumulatively in the same period of time and EXT6 did not measure any significant displacement, which means that it is installed in an area that is not subject to deformation. Considering the brittle nature of the rock mass, a displacement of 18 mm is highly significant.



**Figure 5.21:** Crackmeters measurements. A, B C, D correspond to the events analysed in this Section

The deformation has strong correlation with intense rainfall events. The delay with respect to the precipitation peak is normally less than 24 hours. However, some deformation events do not seem to be related to rainfall.

In the graph it is clear that crackmeters EXT4 and EXT5 work in compression rather than in extension, which means that one side of the crack moves towards the other. This could be due to differential movements along bedding strata as the crackmeters are installed in an area where the limestone layers are folded. The nature of EXT4 and EXT5 movement is impulsive. Step changes in measured displacements are most probably related to stick-slip behaviour (Section 2.1.1.1) of the monitored joints. A trend to note in the deformation impulses is that the bedding planes tend to close every time of a greater quantity.

Note that all crackmeters stopped working in September 2014, before the new MK2 sensors were installed. Therefore, AE data used in this section refer to Series 1 which was measured with the MK1 version of the Slope ALARMS (see Table 3.5) and therefore the results are not directly comparable to the rest of AE measured at the site as assessed comparing the two versions of the system in the laboratory (Test A in Section 4.1.1). In particular in Series 1 groundwater variation events are not visible on sensor AEWG1 as its sensitivity was too low; on the contrary spiky AE events related to snowfall are visible on all three sensors, although with slightly lower rates compared to Series 2.

The relationships between the crackmeters and the AE waveguides can be described as follows:

- EXT4 and EXT5 are installed across bedding planes that are intersected by waveguide AEWG2, therefore if a differential displacement along these planes of weakness occurs, the AE so produced should be measured by AEWG2;
- EXT6 is located just 1–2 m to the right of AEWG3 but the waveguide does not go through the same bedding planes, it is therefore unlikely that AE so produced will be measured by AEWG3.

In order to assess possible correlation between displacement of the bedding planes and acoustic emission, four events were analysed. For each event the respective graph is provided in Figures 5.22 to 5.25.

Event A in Figure 5.22 shows AE activity preceding the movement of the crackmeter but little or no AE during the actual displacement. Just before the displacement takes place there is a snowfall event of about 1 m. AE is probably related to the snow rather than an actual movement on the discontinuities. In fact (although we are looking at Series 1) the shape of the AE events is very similar to that seen in Section 5.3.3 for events generated by snow load. As the crackmeters show a compressional behaviour, it is unlikely that their movement is generated by snow accumulating on them as in this case they would extend. As the rock mass seem to respond to the snow falling and accumulating on the slope, the displacement measured by the crackmeters might be a product of this increased load with a slight delay. However, the absence of acoustic emission during the movement recorded by the crackmeters, reveals that they probably monitor a local condition and AE is not propagated to the sensors (i.e. the movement does not propagate along the rock beds across the waveguide).

The same observations are valid for Event B in Figure 5.23. In fact snowfall events (cumulative snow for the period showed in the graph is over 3 m) seem to

be the cause for AE being generated and measured by all three sensors, although with different RDC/rates. The fact that all the sensors recorded the same events forms is an indicator that the generating mechanism is diffuse and not local to one or few discontinuities. Variations in the groundwater level are rather pronounced in this time frame. Part of the water replenishing the aquifer comes from the snowmelt that occurs between successive snow fall events as the temperature at site fluctuates between 0 and 10 °C. AE events in the graph, however, do not seem to be correlated to the variation in the piezometric level. This is likely due to the fact that the sensors used in Series 1, AEWG1 in particular, were less sensitive than those used in Series 2, which clearly shows correlation with variations of groundwater level (Section 5.3.2).

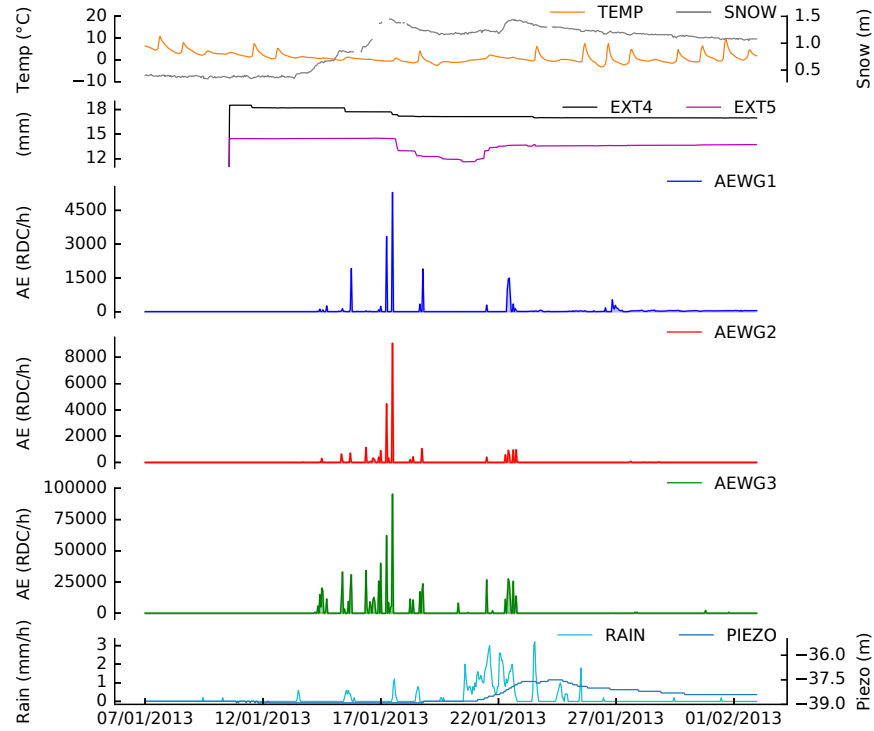
Figure 5.24 shows Event C which is a substantial displacement on EXT 4 of about 2 mm. The movement seems to be initiated when the groundwater table starts to raise, with a delay of few hours from the start of the rainfall event. Snow here is absent. In this case the three acoustic sensors recorded AE activity at the beginning of the displacement, but the fact that all three sensors have a peak at the same time and then the AE gradually goes back to zero after a few monitoring periods, reveals that this AE is probably due to the changing conditions in the piezometric level. The fact that the trends do not follow the whole water table variation but return quickly to zero RDC/h is again due to the decreased sensitivity of the Slope ALARMS MK1 used to measure AE activity during this period of time. If the AE was due to displacements taking place across waveguide AEWG2, the trends this sensor recorded would have been much higher (the peak is only about 60 RDC/h) and would have lasted until the movement stopped. Therefore again it seems that the crackmeter measures a local condition that is not propagated along the discontinuity.

Event D in Figure 5.25 shows a main displacement on EXT 4 of 0.8 mm on 30/07/2014. This seems to be initiated in response to a rainfall event. In this case there is no acoustic emission that is related to the displacement nor the variation in the groundwater level, although this is only about 1 m. A minor event of 0.2 mm

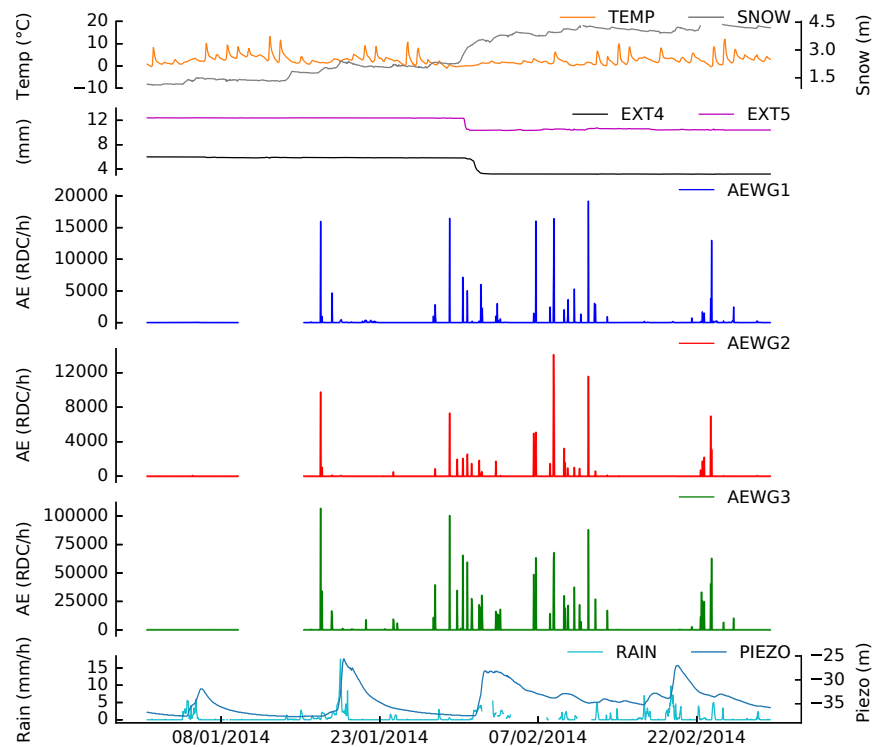
takes place around 05/08/2014 and does not seem related to a particular rainfall event. However, both AEWG2 and AEWG3 show a peak at the beginning of the displacement. AEWG1 shows throughout RDC/h rates that do not seem related to the measurements available, therefore the hypothesis is that are generated locally.

The outcome of the comparison of acoustic emission data with displacements measures by EXT4 and EXT5 is that:

- Crackmeters EXT4 and EXT5 show that the discontinuities are clearly deforming;
- AE was measured at the time of crackmeter deformation measurement. Given the shape of the acoustic events, AE appear to be caused by effects of snow load and groundwater level variation. Thus, AE trends are not directly related to the displacement of the discontinuities but are generated by snow load and variation of groundwater level;
- Therefore, the displacement measured by EXT4 and EXT5 is also likely to be generated by the same processes due to snow load on the slope and groundwater level variation;
- The deformation measured by the crackmeters is indicative of differential displacement occurring within the moving rock mass, between the limestone strata (as explained in the failure model in Section 5.1.4.)



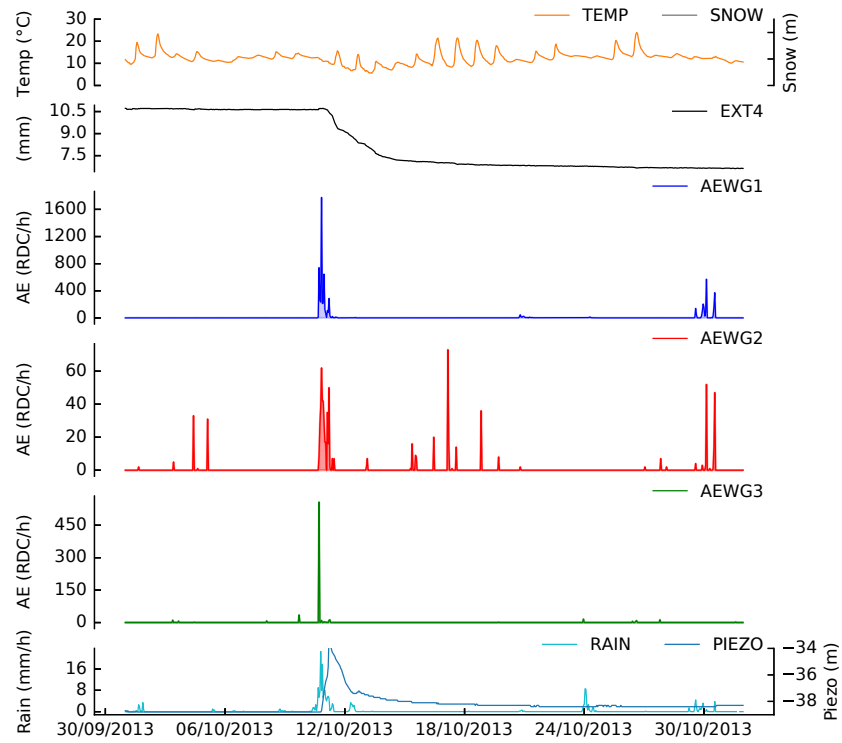
**Figure 5.22:** Event A – EXT4 cumulative displacement 1 mm; EXT5 cumulative displacement 1.5 mm



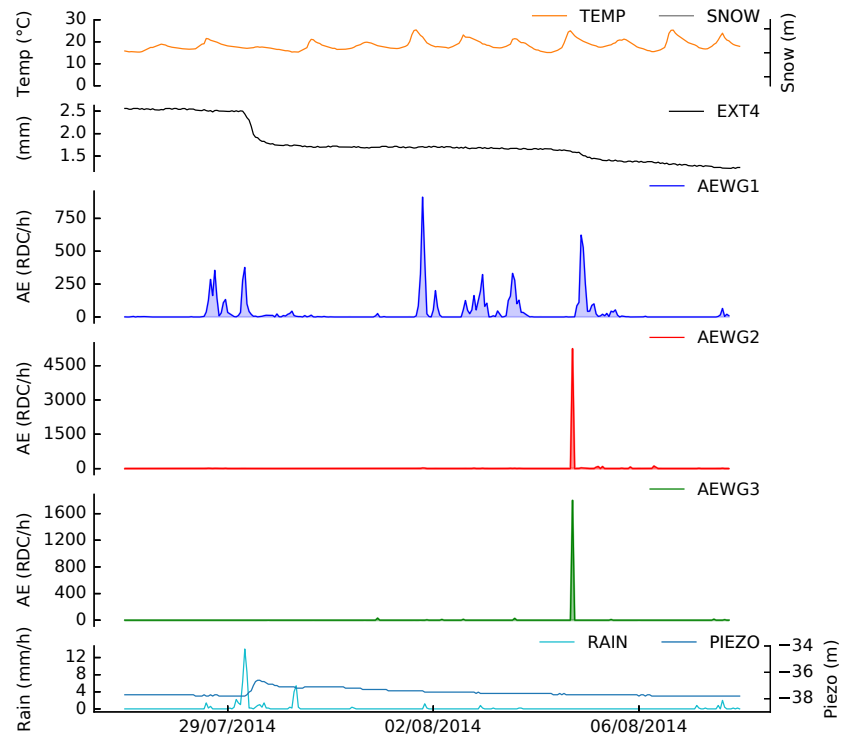
**Figure 5.23:** Event B – EXT4 displacement 3 mm; EXT5 displacement 2 mm



### 5.3. Analysis of field monitoring results



**Figure 5.24:** Event C – EXT4 displacement 2 mm

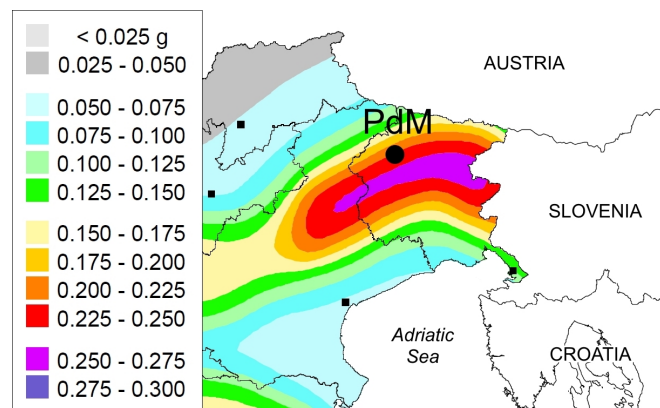


**Figure 5.25:** Event D – EXT4 displacement 0.8 mm main event; 0.2 mm minor event

### 5.3.5 Earthquakes

Ground shaking during an earthquake is one of the major causes for slope instability. This potential trigger for landslides must be considered for instabilities in north-eastern Italy as this area is seismically active. The "Seismic Hazard Map of the Italian territory" (Ordinanza PCM 3519, 2006) developed by the Italian National Institute for Geophysics and Volcanology reports expected peak ground acceleration (PGA) values for the area in the order of 0.225–0.250 g with 10% probability of exceedance in 50 years (red in Figure 5.26). Generally, PGA of 0.1 g is the minimum for damage on structures and many authors (e.g. Xu et al., 2015) observed that  $\text{PGA} \geq 0.2 \text{ g}$  was able to cause landsliding in many parts of the world.

From the point of view of the magnitude, that is the size of an earthquake at its source, Keefer (1984) developed a generic hazard model that outlines the relationship between earthquake magnitude and landsliding. Table 5.3 reports minimum local magnitude ( $M_L$ ) values for triggering of various landslides types, stating that 4.0  $M_L$  is the minimum for any types of landslides to occur.



**Figure 5.26:** Extract of the Seismic Hazard Map of Italy with 10% probability of exceedance in 50 years, modified after Opcm 3519 (2006). Passo della Morte site (PdM), which is indicated with a black dot marker, falls on an area with an assigned PGA range between 0.225 and 0.250 g

**Table 5.3:** Minimum local magnitude values for triggering of different landslide types based on the terminology of Varnes (1978), after Keefer (1984)

Landslide type	Magnitude $M_L$
Rock falls, rock slides, soil falls and disrupted soil slides	4.0
Soil slumps and soil block slides	4.5
Rock slumps, rock block slides, slow earth flows, soil lateral spreads, rapid soil flows and sub-aqueous landslides	5.0
Rock avalanches	6.0
Soil avalanches	6.5

Both the magnitude and/or the PGA values above mentioned (magnitude is a quantity related to the seismic source, whereas PGA is influenced by wave propagation effects, seismic source and local effects at the measuring site) give only an indication that a generic landslide could be initiated by an earthquake of certain intensity and/or certain acceleration of the ground, respectively. Moreover, the magnitude by itself is not an effective descriptor of the landslide potential at a specific site as it is related exclusively to the seismic source. Therefore, it must be taken into consideration that if a failure is incipient before an earthquake occurs, the collapse could be initiated even by weak shaking and/or smaller magnitudes. Also, other conditions at the time of earthquake occurrence that could affect slope stability should be taken into consideration, e.g. water pressure within the slope.

When the ground motion is not strong enough to induce a collapse, the shaking can still result in internal deformation of the rock mass (Moore et al., 2012). The ground motion can be responsible for systematic fracturing and damage to the rock mass creating amplified shaking (i.e. site effects) in the next earthquake(s) and likely contributing to failure.

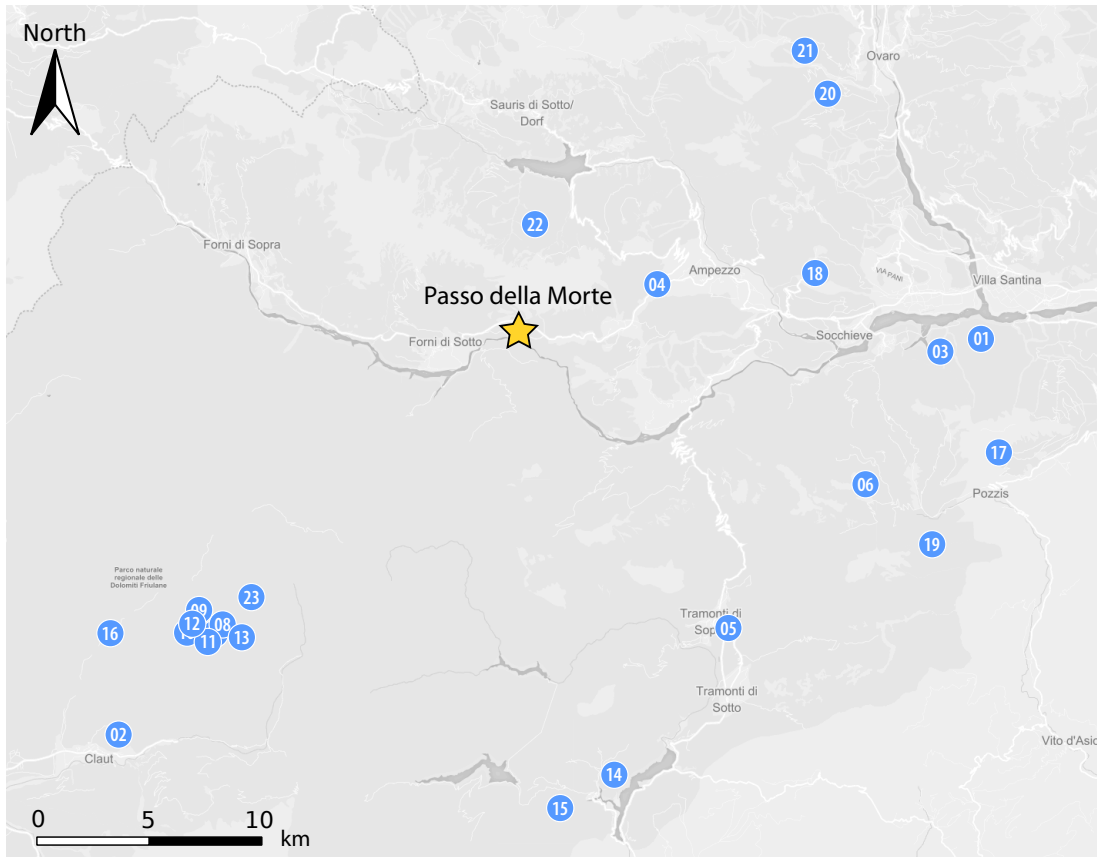
The database was searched for acoustic emission rates generated by cracking induced during earthquake occurrences. Earthquake records were obtained from the Italian National Institute of Oceanography and Experimental Geophysics seismic network (CRS-OGS, 2016) for the period 17/12/2010–10/01/2016. Data were fil-

tered (see Appendix D) to exclude duplicate events on the basis of matching date, time and magnitude values. As an initial analysis, only earthquakes that occurred within a radius of 20 km from Passo della Morte (epicentral distance) and with local magnitude  $M_L \geq 2.5$  are considered as those representing the highest energy events that occurred in the surroundings of Passo della Morte since the first AE sensor was installed (December 2010). As RDC values are recorded at the end of one-hour monitoring periods, RDC values taken into account for every earthquake refer to the following rounded up hour (e.g. earthquake time 16:05:01 corresponds to RDC recorded at 17:00:00). It would be best to use the hypocentral distance rather than the epicentral distance but the earthquake database (CRS-OGS, 2016) does not include depth of the source.

Twenty-three earthquakes were found in the earthquake database that match the criteria discussed. The epicentres locations are shown on a map of the area in Figure 5.27. Table 5.4 reports the twenty-three earthquakes, for every event the table reports information relative to the earthquake event itself (date and time of occurrence, latitude and longitude of epicentre), distance from the Passo della Morte site, the rounded-up time used to extract acoustic emission data and the AE data relative to the three sensors available on site (AEWG1, AEWG2, AEWG3).

The local magnitude ( $M_L$ ) values of the twenty-three earthquakes identified are in range 2.5–3.8  $M_L$ , with five events exceeding  $M_L=3$ . The minimum epicentre distance from the site is 3.8 km and the maximum is 19.5 km. The general response from the three waveguides is  $RDC=0$ , in very few cases RDC is greater than 0 RDC/h but this is not registered by all three sensors. One single case (No. 18) exceeds 240 RDC/h reaching 3,813 RDC/h, 77 RDC/h and 1,798 RDC/h on sensors AEWG1, AEWG2 and AEWG3 respectively. As RDC counts could be generated not by shaking of the ground but originating from other processes taking place at the same time, the AE data relative to events No. 18 were compared to environmental (temperature and rainfall) and groundwater level data measured in the 24 hours before and after the earthquake time. This further comparison allowed to conclude

that the counts are due to rock mass response to fluctuations of the groundwater level and not the concurrent seismic event. The graph relative to event No. 18 is available in Appendix B.



**Figure 5.27:** Map showing the location of the earthquakes considered in the analysis. The numbers refer to Table 5.4

**Table 5.4:** Earthquakes considered and acoustic emission trends (RDC/h) at the round up time

No.	ID	Date	Time UTC+1	Time round*	Lat	Lon	Mag M <sub>L</sub>	Dist km**	AEWG1 RDC/h	AEWG2 RDC/h	AEWG3 RDC/h
01	01132	04/07/2011	05:44	06:00	46.396	12.909	3.1	15.8	1	n/a	n/a
02	01569	16/09/2011	15:15	16:00	46.274	12.523	2.5	19.5	0	n/a	n/a
03	01684	06/10/2011	12:59	13:00	46.392	12.890	2.7	14.4	0	0	n/a
04	02039	08/12/2011	21:19	22:00	46.412	12.764	2.6	5.0	n/a	0	n/a
05	02149	29/12/2011	20:22	21:00	46.307	12.796	2.5	12.4	0	0	n/a
06	01896	08/12/2012	06:37	07:00	46.351	12.858	2.6	13.0	0	0	0
07	00124	10/02/2013	13:15	14:00	46.306	12.568	2.6	14.5	0	0	0
08	00125	10/02/2013	15:28	16:00	46.307	12.570	2.5	14.3	0	0	0
09	00148	12/02/2013	14:19	15:00	46.312	12.560	2.6	14.5	0	0	240
10	00156	12/02/2013	15:27	16:00	46.307	12.557	2.7	15.1	0	0	26
11	00169	12/02/2013	19:12	20:00	46.309	12.559	3.8	14.8	0	0	0
12	00168	12/02/2013	19:12	20:00	46.303	12.564	2.8	15.0	0	0	0
13	00829	03/07/2013	11:21	12:00	46.304	12.578	2.8	14.2	0	0	0
14	00188	15/03/2014	23:19	00:00	46.261	12.745	2.7	15.6	0	0	0
15	00219	21/03/2014	14:37	15:00	46.251	12.720	2.6	16.4	0	0	0
16	00632	06/07/2014	21:17	22:00	46.305	12.520	2.7	17.4	0	0	0
17	00729	08/08/2014	13:14	14:00	46.361	12.917	2.7	17.0	n/a	n/a	n/a
18	85052	05/12/2014	10:11	11:00	46.416	12.834	2.8	10.3	7626	154	3596
19	85846	18/01/2015	15:42	16:00	46.333	12.887	2.9	15.9	80	2	0
20	91256	11/11/2015	20:46	21:00	46.472	12.840	3.2	13.4	0	0	0
21	91266	11/11/2015	22:20	23:00	46.484	12.829	2.6	13.7	0	0	0
22	91583	21/11/2015	12:52	13:00	46.431	12.710	3.5	3.8	0	6	0
23	91909	08/12/2015	16:05	17:00	46.316	12.584	3.4	12.9	0	0	94

Earthquakes data source: [rtscrs.inogs.it/en](https://rtscrs.inogs.it/en), does not include info on depth of the source

\*Distance from PdM [Lat 46.398, Lon 12.703]; n/a denotes data not available.

The analysis clearly concludes that there is no acoustic emission response to the earthquakes recorded to date. The result is in line with Zoppè (2015) who calculates the theoretical peak ground acceleration (PGA) at Passo della Morte based on the strongest earthquakes ( $M_L > 4.5$ ) recorded in the last 30 years within 100 km from the site: the eight earthquakes identified by Zoppè (2015) ( $M_L$  in range 5.4–6.3, distances between 32–77 km) which are reported in Table 5.5, give PGA values between 0.005–0.050 g, which are too low to induce fracturing and hence generate acoustic emission (note that they all occurred before the monitoring system at Passo della Morte was installed, therefore AE data from site cannot be analysed).

**Table 5.5:** Theoretical acceleration calculated for Passo della Morte as a consequence of earthquakes with local magnitude  $M_L$  greater than 4.5 occurred in the last thirty years in the South-Eastern Alps. Modified after Zoppè (2015)

Date and Time UTC	Lat °	Lon °	Depth km	Distance* km	Mag $M_L$	PGA g
06/05/1976 20:00	46.29	13.25	7.0	43.6	6.3	0.045
11/09/1976 16:31	46.29	13.16	3.0	37	5.4	0.016
11/09/1976 16:35	46.28	13.18	12.0	39	5.7	0.023
15/09/1976 03:15	46.29	13.15	5.0	36.5	6.2	0.049
15/09/1976 09:21	46.32	13.12	8.0	32.6	6.1	0.050
12/04/1998 10:55	46.32	13.68	15.2	75.8	5.7	0.008
14/02/2002 03:17	46.38	13.16	10.0	35.4	4.9	0.007
12/07/2004 13:04	46.30	13.69	6.0	76.8	5.4	0.005

\*Distance from Passo della Morte

## 5.4 Summary

At the Passo della Morte site three Slope ALARMS MK1 sensors were installed in various phases since 2010 (Series 1). In 2014 all sensors were replaced with the newer MK2 sensor version (Series 2). In this work the Series 2 acoustic emission data were analysed, unless explicitly stated. Series 2 refer to the time interval October 2014 to December 2016.

In this chapter AE data were compared to rainfall, groundwater level, snowfall, displacement measured by extensometers and time of earthquake occurrence to identify possible rock deformations due to ground shaking.

At this site no collapse of considerable dimensions occurred during the time frame considered in this work, for this reason the acoustic emission pattern of approaching failure is still undetermined. However, AE trends were identified as being generated by changed conditions in the water pressure within the slope and by snow load, which are processes that cause destabilising forces to grow.

AE trends are generated simultaneously with variation of groundwater level. The AE sharply increase at the beginning of the event and slowly decrease, almost following the groundwater level variation trend. AE stops when the water returns to its base level. AE rates are in the order of tens of thousands RDC/h.

Snow load generates rates in the region of tens of thousands to hundreds of thousands RDC/h which last for just one or two monitoring periods, imparting a typical spike-like shape.

Interesting negative results were also obtained from the comparison with rainfall, extensometers and earthquake occurrence.

It was determined that rainfall does not generate RDC/h and also seepage of water through discontinuities was excluded as a source of acoustic trends.

RDC/h rates were recorded simultaneously to the displacement of extensometers, however, AE trends are not directly related to the displacement of the discon-



tinuities but are generated by the same processes (i.e. snow load or variation of groundwater level).

No acoustic emission was recorded in response to the earthquakes analysed ( $M_L$  in range 2.5–3.8 between 3.8–19.5 km from site), but this does not exclude that in the future the occurrence of earthquakes (perhaps closer to site and/or stronger in magnitude) could not determine deformation of the limestone rock mass and generate AE rates.

# Chapter 6

## The Grossreifling site

The acoustic monitoring system was installed at the Grossreifling trial site in April 2014 as a complementary component of the Sentinel for Alpine Railway Traffic (SART) project. The project was undertaken in collaboration with INGLAS GmbH and funded by the Austrian Federal Railways (OeBB) and Austrian Research Promotion Agency (FFG). SART is a pilot project which aims to increase the safety of mountain railways reducing the risk of track and train damage due to rock falls occurring along the rail line, providing also a cost saving alternative to expensive dynamic rockfall barriers. The SART system makes use of a dual approach:

- (1) early warning of imminent rockfalls, through monitoring of the acoustic emission generated within the rock forming the slope (using the Slope ALARMS);
- (2) detection of occurrence, provided by a light static catch fence instrumented with movement sensors that give information about impacts.

The two subsystems share a common control centre able to issue warnings and alarms to the rail traffic operator, providing information in time to take action, specifically slow down or stop the railway traffic (although this control function was not implemented in the pilot phase). The SART project and the site were introduced in Section 3.3.2.

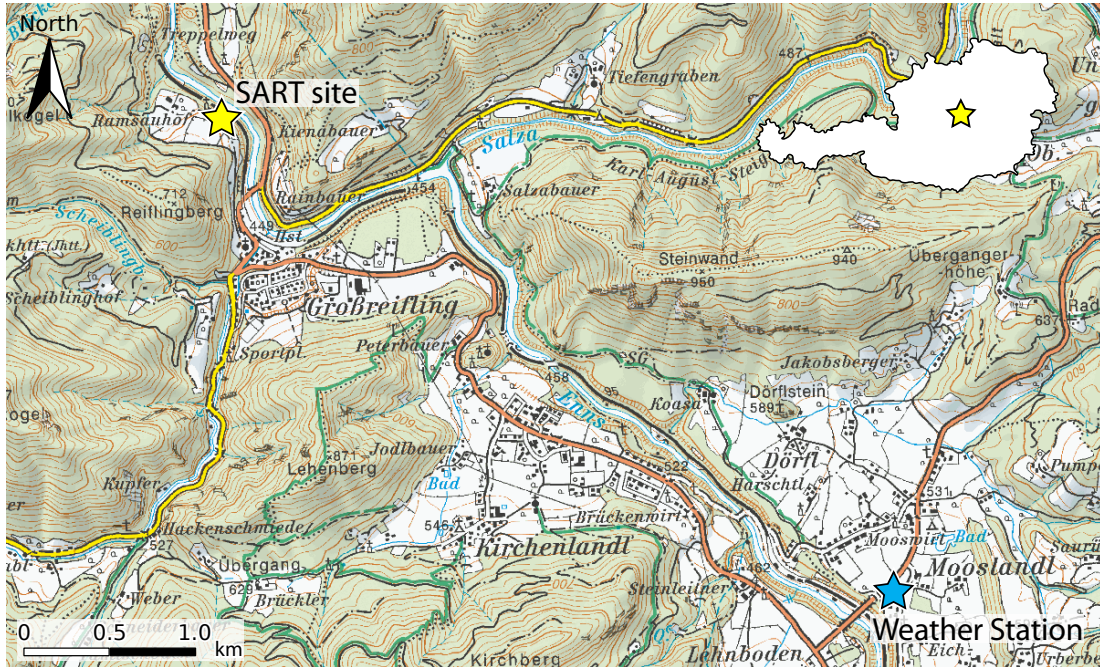
The slope was selected by OeBB for the pilot project following the occurrence of a rock fall of about 1 m<sup>3</sup> in April 2013 which reached the rail track. It is considered likely that other instabilities would affect the same slope in the near future.

This chapter is subdivided into four sections. A description of the SART site is provided in Section 6.1. Section 6.2 reports the monitoring instruments available, giving details of the AE sensors installed at site and other instruments which data were used for comparison (detection fence and weather station). In Section 6.3 AE data collected at the site over a period of 2.5 years are analysed and compared to rainfall, temperature and hits measured by the detection fence; a discussion of trends generated by water seepage and the mechanisms that generate the AE trends recorded is provided. Section 6.4 summarises the key findings and the lessons learnt by monitoring this site.

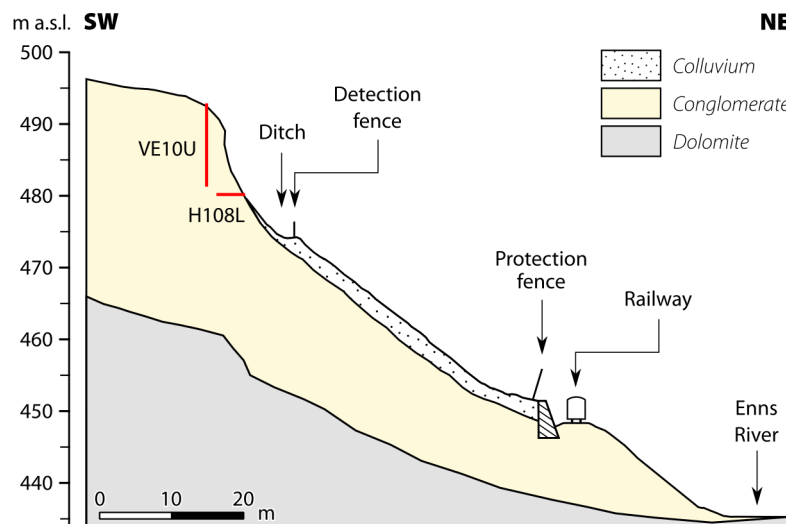
## 6.1 Site description

The site is situated in Styria, Austria about 1.5 km north of the town of Grossreifling [Lon 14.7099, Lat 47.6739] on the left bank of the Enns River (Figure 6.1), which is one of the largest Austrian tributaries of the Danube River. The site consists of a steep conglomerate slope that threatens a section of the freight rail line St. Valentin (Austria)–Tarvisio (Italy) at km 91.400.

The study slope is about 60 m high, the lowest point being the river bed at 435 m a.s.l. and the highest being the top of the slope at 495 m a.s.l. (Figure 6.2). The section of interest is the conglomerate that outcrops in the upper 15 m of the slope, which appears sub-vertical with local overhangs. Below this elevation the rock is hidden by debris falling from the top of the slope (colluvium), accumulating with an angle of about 40°.



**Figure 6.1:** Map of the Grossreifling, Styria (Austria) area. The SART site (yellow star) is located about 1.0 km NW of Grossreifling. Weather data are collected at Mooslandl weather station (blue star), about 4.5 km SE of the SART site along the Enns River valley



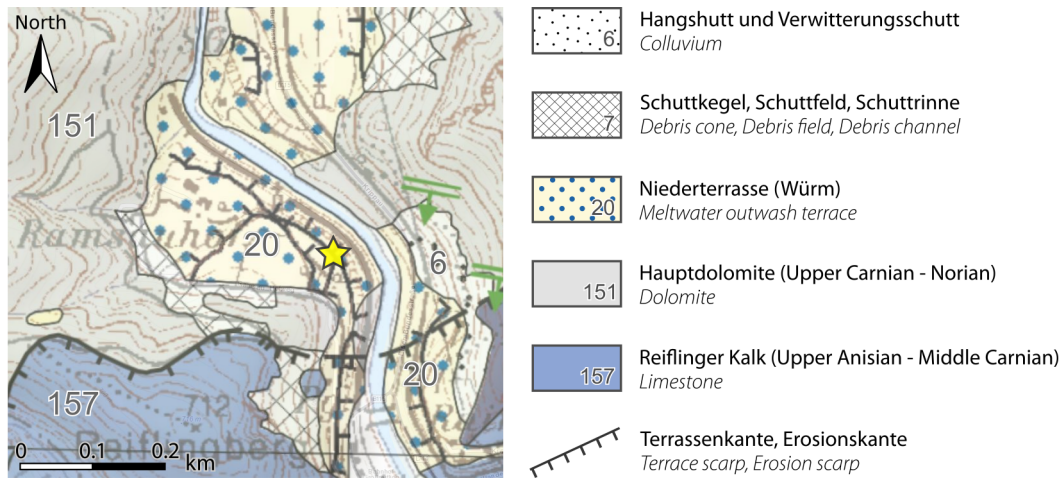
**Figure 6.2:** Indicative SW-NE cross-section of the study slope with elements mentioned in the text and geological setting

A rockfall interception ditch was formed at the toe of the outcropping section about 475 m a.s.l. The ditch served also as an access pathway for both pedestrians and machinery from the Ramsauhof farm (located to the NW of site). A light static fence instrumented with movement sensors, identified as *Detection fence* in Figure 6.2, was erected along the ditch in order to detect ongoing detachments of rocks from the slope (principle of operation explained in Section 6.2.2).

At the toe of the slope, the railway track is protected by a dynamic 4 m high 1000 kJ rockfall barrier, identified as *Protection fence* in Figure 6.2, installed by OeBB after the occurrence of a 1 m<sup>3</sup> rockfall in April 2013 (a photography of the rockfall is provided in Figure 3.8).

### 6.1.1 Geologic overview

The Enns River valley developed during the Riss alpine glaciation between 300,000 and 130,000 years BP (Ehlers et al., 2011). During this ice age the area was covered with hundreds of meters of ice, causing excavation of the valley bedrock (Limestone and Dolomite in the geological map in Figure 6.3). At the glacier terminus during the last glacial cycle (Würm) around 20,000 years BP, the copious waters of the river enriched with the outwash from the melting glacier, transported and deposited huge amounts of sediment filling the valley and forming the conglomerate deposit (Keil and Neubauer, 2011; Husen and Reitner, 2011). When the depositional phase ended, the conglomerate previously formed was eroded by the river and terraces were formed (Niederterrasse in Figure 6.3), as it can also be deduced from the morphology. These steep terraces are today in the process of re-equilibrating, thus rockfalls of various volumes are extremely frequent. The Grossreifling trial site concerns the top section of one of these terraces.



**Figure 6.3:** Geological map of Austria 1:50,000 – Nr. 100 Hieflau. The Grossreifling site is indicated with a yellow star

### 6.1.2 Ground model and material characterisation

The Niederterrasse (conglomerate) lies on top of the Hauptdolomite (dolomite), which constitute the bedrock in this area (Figure 6.1.1). The conglomerate thickness is estimated to be in the order of 25-30 m at its thickest point at the top of the slope, thinning towards the Enns River, where the bedrock outcrops.

The conglomerate consists of well rounded boulders (up to 1 m<sup>3</sup>), cobbles and coarse gravel in a matrix of fine to coarse sand. The majority of the components are carbonate, mainly limestone and dolomite, with a small proportion of crystalline particles. The grade of cementation is variable; well cemented zones are interposed to very poorly cemented ones that can be easily be removed with a hammer.

The location of the groundwater within the slope is unknown as there is no information available (i.e. there are no standpipes or groundwater monitoring). However, from observation of the site, the zone of interest in this work (i.e. the top 15 m of the conglomerate terrace) should not be interested by groundwater.

### 6.1.3 Expected failure mechanisms

According to Varnes's landslide classification (Varnes (1978), provided in Table 2.1) the phenomena affecting this slope can be grouped under the "rockfall" category. The processes leading to failure are due to weathering of the slope and local conditions of the conglomerate. Based on observations at the site, two failure mechanisms can be expected:

- (1) *Detachment of conglomerate constituents*, by deterioration of the matrix that bonds conglomerate constituents together. The matrix is weathered by processes such as freeze-thaw and rainfall washout acting on the slope face. As the weathering weakens the bonds between particles over time, these detach due to gravity and fall from the slope face. The size of rockfalls is variable as the conglomerate includes particles of a range of sizes, from pebbles to large boulders. This failure mode is local to the slope surface and volumes up to 1 m<sup>3</sup> are expected, such as the rockfall occurred in April 2013;
- (2) *Development of local shear zones within the conglomerate*, where the outcrop is overhanging. Triggering mechanisms include differential weathering (freeze/thaw) which leads to undercutting and hence lack of support at the toe of the overhanging section. A built up of pore water pressure caused by particularly intense rainfall or snowmelt, or a combination of both, could also initiate the movement. Volumes are expected to be up to 10 m<sup>3</sup>.

## 6.2 Measurement system

### 6.2.1 Acoustic Emission

At the Grossreifling site a total of three Slope ALARMS sensors were installed in April 2014. The piezoelectric transducers were mounted on two horizontal waveguides (Sensors H108L and H209R) and one vertical waveguide (Sensor VE10U).

Details of the sensors, parameter settings, sampling frequency, waveguide types were previously discussed in Section 3.3.2 and are summarised in Table 3.6.

Threaded bars were used at this sites. Suitability of these type of bars to be used as waveguide was assessed in the lab, see Section 4.1.3. Waveguides H108L and H209R were installed within the outcropping conglomerate section at elevations of about 487 m a.s.l. and 486 m a.s.l., respectively, and penetrate into the rock mass for about 2.7 m. They were installed 5 m apart from one another diverging of an angle of about 45°. It is important to note that H209R was installed into loose debris for about 0.8 to 1 m.

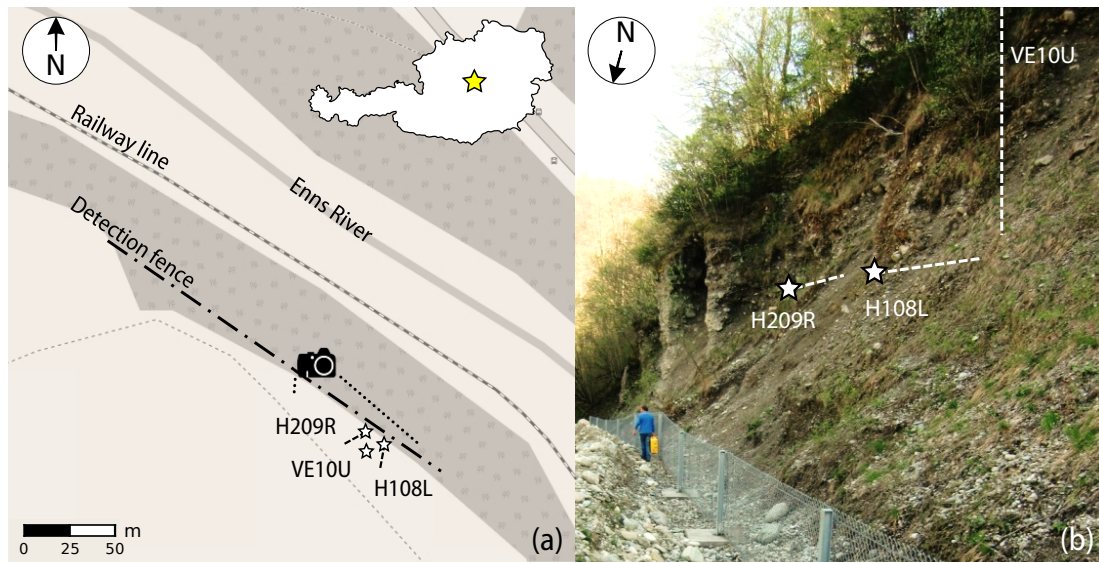
Waveguide VE10U is composed of four 3 m length bars screwed together. It penetrates the conglomerate for about 11.60 m from the top of the terrace (495 m a.s.l.). Its bottom end is therefore about 1 to 2 m higher in terms of elevation than the two horizontal waveguides. From a plan perspective waveguide VE10U is located in between H108L and H209R. A schematic of the layout is provided in Figure 6.5.

The waveguides are installed in the area where the April 2013 rockfall detached. From visual inspection this area seemed particularly prone to collapse due to vicinity of a overhanging section of the conglomerate sustained by two conglomerate pillars, forming a sort of small cave which can be observed in Figure 6.4. Wearing at the base of the two pillars by detachment of elements forming the conglomerate is foreseeable in the near future, thus enabling for a bigger-size collapse of the structure. An evidence of this is the rockfall occurred in April 2013, which detached from this area. The three waveguides are installed just to the right of the cave.





**Figure 6.4:** The small cave formed by localised washout of conglomerate material; sensor H108L is indicated with a yellow star



**Figure 6.5:** Grossreifling (Austria) site location: **(a)** schematic map of the site with waveguides and detection fence location, note the railway line at the base of the slope; **(b)** image of the conglomerate slope with location of the sensor nodes and projection of the steel bars

Threaded self-drilling rods (detailed in Section 3.2.2.2) were used as waveguides at this site. These differ from the 50 mm smooth pipes usually installed at other sites (see Section 3.2.2.2). The annulus between the rod and borehole wall is filled by pumping grout through the hollow stem to the drill bit thus backfilling towards the slope surface.

As assessed through laboratory experiments conducted on smooth and threaded waveguides (Section 4.1.3) there is little difference, for slope monitoring purposes, in AE propagation along a singular 3 m rod lengths between the two types of bars. The difference increases when rod lengths are coupled to increase the total length of the waveguide and the loss is due to energy leakage at the couplings. However, the loss in threaded waveguides with couplings has been found comparable to the loss in smooth waveguides with couplings. This gives confidence that threaded waveguides are appropriate to use for AE monitoring.

Attention should be paid when mounting the piezoelectric transducer on a threaded waveguide. As assessed through laboratory experiments in Section 4.1.2, signal loss can occur if the transducer is not mounted correctly. The test clearly showed that the area of contact between the transducer and the waveguide should be maximised. The best coupling method resulted to be with the transducer mounted on a flattened thread (i.e. produced by filing).

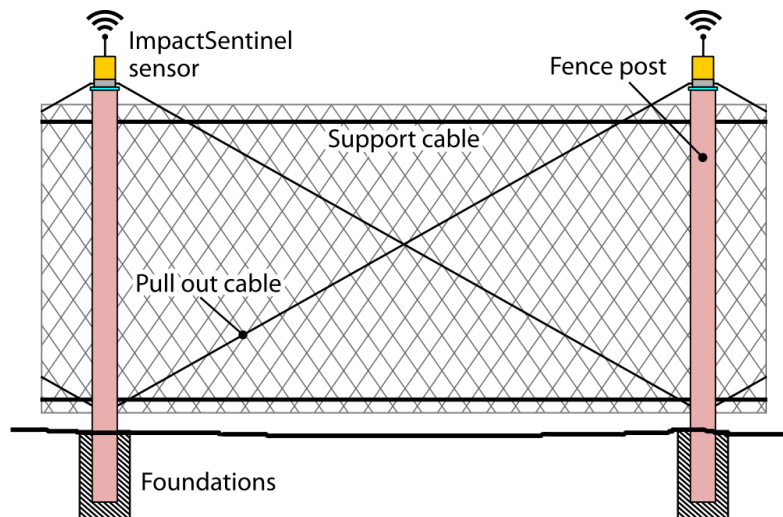
### **6.2.2 Detection fence**

The debris detection subsystem is composed of an 80 m long, 1.5 m tall light static fence. The fence is erected in a 1.5 m wide rockfall catchment ditch formed at the base of the outcropping conglomerate. It is composed of a net supported by 15 posts connected by an upper and a lower steel wire ropes, called support cables, which run from post to post (Figure 6.6). The fence is equipped with one movement sensor (ImpactSentinel, developed by INGLAS GmbH) per every post and two sensors on the upper support cable, for a total of 17 sensors. Two cameras were installed at

both ends of the fence for remote visual inspection. The sensors are able to detect movements, shocks and deformation of the posts and the net caused by impacting material.

The movement sensors are wirelessly connected to a logger (Data Relay) which records a number of parameters, such as the static acceleration ( $t_x$ ,  $t_y$ ,  $t_z$ ) which defines the tilt direction of the sensor with respect to the Earth gravity vector, and the maximum dynamic acceleration ( $a_x$ ,  $a_y$ ,  $a_z$ ) which gives information about the actual movement of the sensor (i.e. when the sensor is not moving  $a_x$ ,  $a_y$ ,  $a_z = 0$ ).

When an object impacts on the fence, the vibration that this causes is measured by the movement sensors. If any component of the dynamic acceleration exceeds the 30 mg threshold, an initial warning is triggered and the parameters are recorded in the Data Relay log 10 seconds after the occurrence (SW1), and subsequently after about 30 seconds (SW2) and 60 seconds (SW3) of the initial warning. An example of impact log is provided in Table 6.1. The system is set to wake up the cameras and take a photo when a warning is issued.

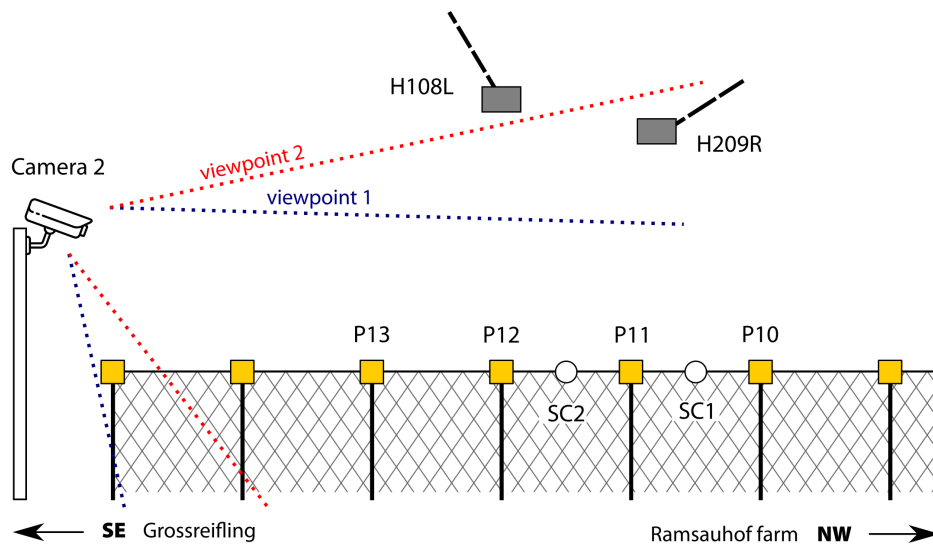


**Figure 6.6:** Schematic of the Detection Fence design. Modified after Hendricks et al. (2014)

**Table 6.1:** Example of impact detected by sensor No.12. Each impact record consist of a sequence of three warning messages, namely SW1, SW2, SW3, for which the static and dynamic acceleration parameters are recorded

Timestamp	Type	Domain	Device	ax mg	ay mg	az mg	tx mg	ty mg	tz mg
2016-05-28 17:48:19	SW1	1	12	31	31	62	46	0	984
2016-05-28 17:48:44	SW2	1	12	281	218	734	62	0	953
2016-05-28 17:49:18	SW3	1	12	109	109	93	46	15	953

A schematic of the southernmost part of the detection fence is provided in Figure 6.7. The figure also shows the position of acoustic sensors H108L and H209R in relation to the fence and the closest camera location. It is important to note that sensors at locations P10, P11, P12, P13, SC1 and SC2 are positioned right below the acoustic sensors H108L and H209R and therefore only the sensors installed at these locations will be considered in the analysis of data. Due to improvement requirements the sensors were reconfigured in many occasions resulting in changes of the device codes in the records relative to the same location. Table 6.2 reports the reconfiguration dates and the sensor number relative to the locations of interest.



**Figure 6.7:** Schematic of the southernmost part of the detection fence below acoustic sensors H108L and H209R. The schematic includes the movement sensors locations, (P) = post, (SC) = support cable

**Table 6.2:** Detection fence sensors in the vicinity of Slope ALARM sensors H108L and H209R. Per every location are reported the date of reconfiguration and the devices codes. The location codes are related to the schematic in Figure 6.7

Date	P10	P11	P12	P13	SC1	SC2
2014-04-10	11	13	12	15	14	—
2014-06-04	10	12	14	15	11	13
2014-11-12	—	12	—	15	11	01
2015-01-22	07	09	—	12	11	01
2015-11-08	07	09	107	12	106	01

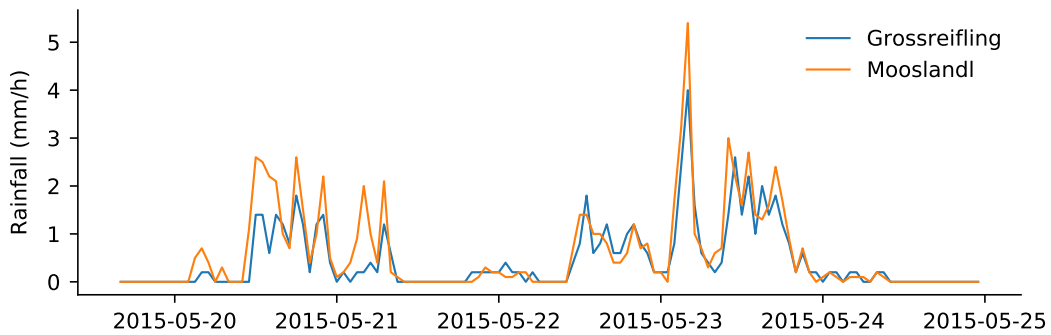


The debris detection fence is aimed at giving information about rockfalls detaching from the slope. However, this might not always be the case as the sensors can detect any variation in their position. To give a few examples, the sensors may be triggered by material already detached and just moving on the slope surface, or by an animal passing close to the fence, etc. Photos from the cameras can help to identify the type of impact and potentially the size of rockfall detached.

### **6.2.3 Weather station**

At the Grossreifling site a rain gauge and temperature sensor were installed at the top of the slope beside sensor VE10U at the beginning of the project. However, they had been subject to power faults and other problems (i.e. irregular sampling, inconsistent data, missing data) for prolonged periods of time, hence did not provide continuous reliable time series. Thus, the decision was made to acquire hourly data from the closest weather station located in Mooslandl (Figure 6.1) about 4.5 km SE from the site in a straight line, along the Enns River valley.

A preliminary comparison of selected parts of the two rainfall data sets was useful to determine that the rainfall measured in Mooslandl is representative of the weather in Grossreifling and suitable for comparison with AE recorded at the site. The example provided in Figure 6.8 shows that there is a general correspondence of the two data sets as dry and rainy periods match consistently. However, as it can be expected, the rainfall intensity may vary slightly. This must be taken into account when comparing data recorded at Grossreifling with rainfall measured at Mooslandl weather station, for example in the analysis of AE trends due to rainfall in Section 6.3.2.



**Figure 6.8:** Comparison of rainfall data measured at Grossreifling and Mooslandl

### 6.3 Analysis of field monitoring results

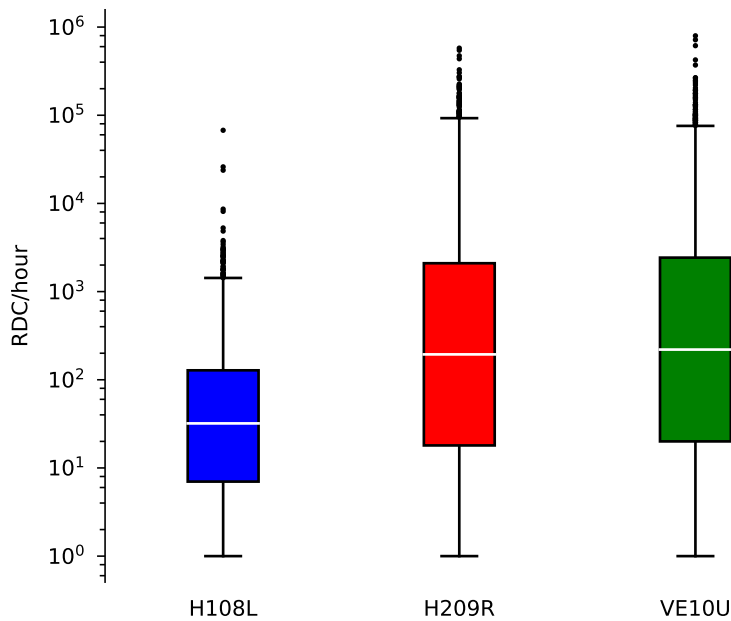
As previously detailed in Table 3.6 acoustic emission records started in April 2014. Gaps in H108L and H209R covers allowed water to leak and drip onto the free end of the respective waveguides, generating spurious RDC trends, as it was unexpectedly found during Test F1 (Section 4.2.3). The covers were made water tight on 28/08/2014 and the data collected before this date were not considered in the analyses. Therefore the period of time considered for data analysis in this work is from 29/08/2014 to 30/12/2016.

In Figure 6.9 the distribution of AE data is represented with a boxplot for each of the three sensors. Data equal to zero RDC/h are excluded from the boxplot representation of as doing so means that the spread in values associated with events is highlighted. For a more detailed explanation about excluding zero RDC/h from the boxplot representation refer to Section 5.3.1. It is important to bear in mind that data equal to zero RDC/h are still considered in the data analysis in the following sections of the thesis and are used as an essential control in the comparison with data from different instruments.

As can be observed in Figure 6.9 AE data distributions are asymmetrical with a positive skew, that is the tail in the positive direction extends further than the tail in



the negative direction, which in general means that the upper 50% of the data range is very spread out compared to the lower 50%. However, the logarithmic scale is used for this representation to be able to give visibility to the low RDC/h, hence the boxplots appear symmetrical. In this representation also the lower whisker represents the 1<sup>st</sup> percentile and the higher whisker represents the 99<sup>th</sup> percentile, thus the outliers in Figure 6.9 represent the upper 1% of the data range.



**Figure 6.9:** Boxplots representing sensors H108L, H209R and VE10U AE data distribution. The lowest whisker represents the 1% mark and the highest whisker represents the 99% mark, thus outliers are the highest 1% of the data range. RDC/h = 0 is not considered

From the boxplot data representation of Figure 6.9 can be observed that:

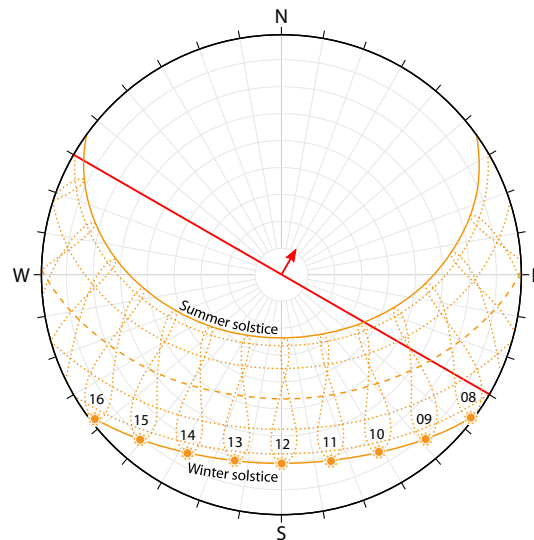
- The 1<sup>st</sup> percentile is equal to 1 RDC/h for all three sensors;
- H209R and VE10U data distributions are very similar, comparing all percentile markers;
- Comparing the 50<sup>th</sup> marker, H108L (32 RDC/h) is one order of magnitude lower than H209R and VE10U (respectively 194 and 220 RDC/h);

- The difference of one order of magnitude is observed when comparing the 75<sup>th</sup> percentiles as well, being H108L (126 RDC/h) about one order of magnitude lower than H209R and VE10U (respectively 2097 and 2406 RDC/h);
- The difference increases considerably when considering the 99<sup>nd</sup> percentiles, being H108L (1431 RDC/h) nearly two orders of magnitude lower than H209R and VE10U (93440 and 76194 RDC/h respectively);
- The RDC/h exceeding the 99<sup>th</sup> percentile (outliers in Figure 6.9) represents less than 1% of the entire data series. These values are also disproportionately high compared to the rest of the data series (e.g. 99% of H108L data is less or equal to about 1,500 RDC/h but the maximum value recorded by the same sensor is about 68,000 RDC/h);
- The outliers cannot be considered representative of the data series. When analysing trends (i.e. due to seepage), such disproportion can be misleading. The decision was therefore made to not include the upper outliers in the analysis of trends, which means AE above 1,500 RDC/h for H108L and above 100,000 RDC/h for H209R and 80,000 VE10U (however outliers were analysed separately as they might be related to other physical processes);
- The maximum number of counts measured within a 1-hour monitoring interval (during the period of time considered in this work) is about 68,000 RDC/h for H108L, 600,000 RDC/h for H209R and 800,000 RDC/h for VE10U.

Although rates are significantly different for the three waveguides, it has been possible to identify two patterns of events that are, with different response rates (RDC/h), present in all three datasets: events related to water seepage, discussed in Section 6.3.2, and events related to freeze-thaw cycles, discussed in Section 6.3.4.

### 6.3.1 Solar exposure

The sun path diagram in Figure 6.10 represents the position of the sun in the sky at any point in time throughout the year at site latitude and longitude, from the point of view of an observer positioned in the sky looking down at the ground. The sun path is superimposed to the study slope strike and dip direction, indicated with a red line and red arrow respectively. The diagram shows that the slope (i.e. the out-cropping conglomerate) does not get lit by direct sunlight as it faces north-east. This excludes differential thermal dilation processes that would induce thermal stress in the rock. Thus direct sunlight-related AE trends can be excluded from the acoustic generating mechanisms for what concerns sensors H108L and H209R. In this condition also overheating of the covers and of the measuring equipment contained within would not be possible as range of air temperature changes is small and the change slow. Therefore acoustic artefacts, such as AE trends generated by dilation and contraction of covers and equipment, can be removed from consideration.



**Figure 6.10:** Equidistant stereographic Sun Path chart at Grossreifling site coordinates. The diagram is superimposed to the study slope strike and dip direction (in red)

The flat top of the slope, on the contrary, can be lit by direct sunlight. As there are no elements in the immediate vicinity to shade this area, it can certainly be lit

in summer and during central hours of the day in winter, when the sun is at its top position in the sky. As VE10U is positioned in this area, attention must be paid to recurring daily trends, in particular during summer when the diurnal temperature variation on a black object, such as the sensor cover, placed in direct sunlight can be considerable.

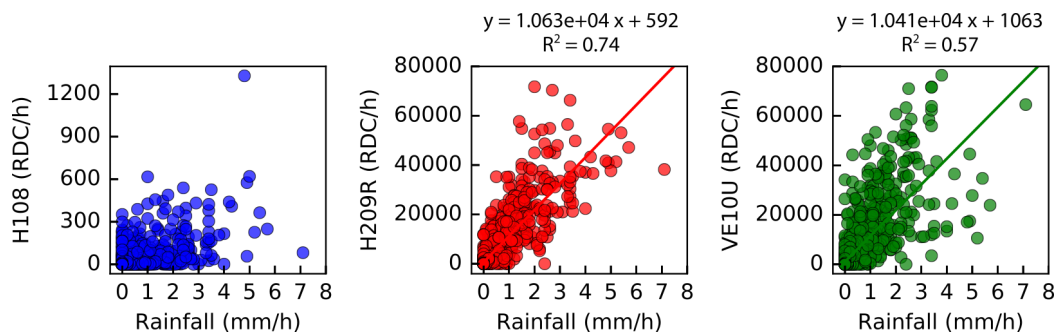
### 6.3.2 Water seepage

Comparing AE trends with rainfall data, it is evident that acoustic trends are recorded when precipitation occurs. The response is particularly clear for sensors H209R and VE10U and less obvious for sensor H108L. In order to look for dependencies, 79 days (1896 one-hour monitoring periods) during which rain occurred, were selected from the database. The dates considered are reported in Appendix C. The selected time periods are representative of most rain conditions at the site (i.e. no rain to 9.1 mm/h and hour to day-long rainfall periods). Rates above 1,500 RDC/h for sensor H108L and rates above 100,000 RDC/h for H209R and higher than 80,000 RDC/h for VE10U (values corresponding to the 99<sup>th</sup> percentile) were excluded from this analysis as they are considered to be values that are not representative of the general behaviour, as previously explained in Section 6.3.

Figure 6.11 illustrates three graphs detailing relationship between acoustic emission and rainfall over 1896 one-hour monitoring periods:

- H108L acoustic trends do not appear to have proportionality with rainfall, although weak acoustic rates are often recorded and major rainfall events (greater than 4.0 mm/h) generate increased AE levels; rates are about 1 to 1.5 orders of magnitude lower than the other two sensors;
- H209R and VE10U clearly show that there is some form of dependency between rainfall and the generation of acoustic emission. The relationship that connects an increase in RDC to an increase in rainfall rates seem to be linear.

- The graph relative to H209R shows that there is clearly a dependency between rainfall and the generation of AE activity. The linear model well describes the increase in AE with the rainfall intensity;
- H209R and VE10U trendlines are very similar, although waveguide VE10U is characterised by a higher dispersion.



**Figure 6.11:** Acoustic emission vs rainfall for the three sensors H108L, H209R and VE10U. The number of monitoring periods considered (same for each sensors) is 1896 one-hour monitoring periods

In this discussion it is important to take into consideration the following factors:

- *Rain precipitation data is collected about 4.5 km away from site.* As seen in Section 6.2.3 the rainfall intensity might not always be an accurate representation of the precipitation at the site or there might be a delay in the precipitation between the two locations (i.e. precipitation might start at Grossreifling first or at Mooslandl first);
- *The AE recording equipment is protected by watertight covers.* This means that acoustic trends are not directly generated by precipitation. Both H209R and VE10U, which are installed through a permeable stratum (respectively loose colluvium and organic soil), show rainfall-related trends. It is therefore reasonable to assume that the acoustic emission is rather generated by seepage through the permeable strata during rainfall events. This explains why the relationship is not linear and there is such high dispersion;

- *AE is generated as long as there is water flowing through the permeable stratum regardless of the duration of the rainfall. As AE is generated by seepage, this may continue after the rainfall has stopped. Water could also be canalised from higher elevations increasing the amount that needs to be drained and the time needed for this to happen. This could reflect into higher RDC/h at low or zero mm/h of rainfall.*

The example of rainfall dependency reported in Figure 6.12(a) represents events characterised by particularly high AE rates. The events depicted in this figure include rates that belong to the 99<sup>th</sup> percentile, hence considered a rare occurrence. In fact, events which RDC/h rates fall into the 99<sup>th</sup> percentile are normally spike-type (such as the spike around 14/05/2015 to the left of the graph; see also Section 6.3.3), which means that their duration is one or very few monitoring periods. The events represented in Figure 6.12 are instead prolonged in time and simultaneous with rainfall.

In Figure 6.12(a) H209R and VE10U acoustic emission response is instantaneous with the rainfall and no AE trends are recorded when it does not rain. AE rates with time are similar in shape to rainfall trends. AE and rainfall rates are proportional as can be seen in the AE vs rainfall graphs in Figure 6.12(b), although the relationship is not always consistent.

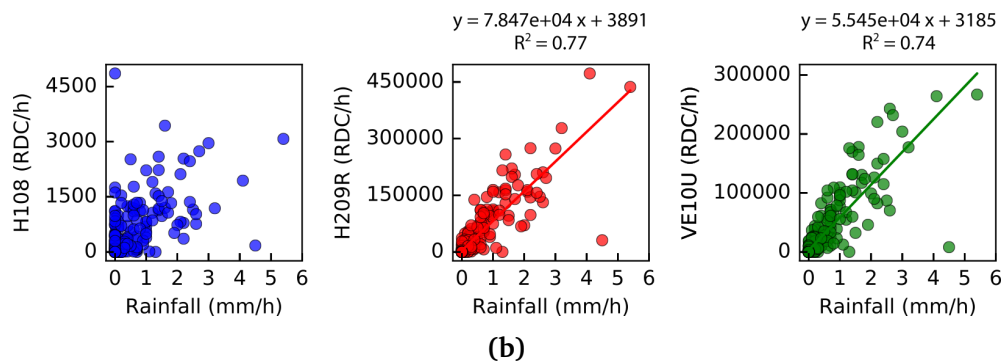
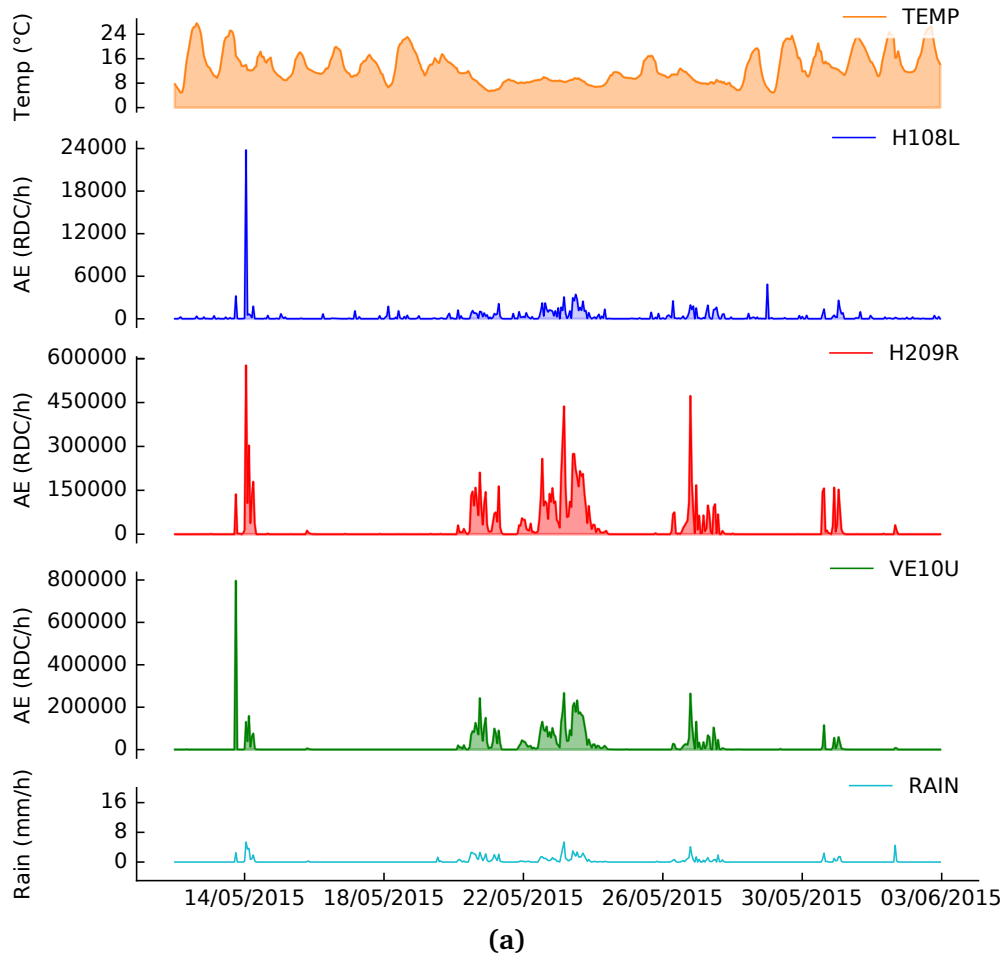
As expected, H108L rates are not dependent on rainfall rates. This is in accordance to the generalised observations above, although the graph in Figure 6.12(a) shows a slight increase in AE activity during a rainfall event.

The graph shows also that there is no delay between rainfall and generated AE, or at least the delay is restricted to the 1 hour time resolution of measurements. This suggests that the AE is generated by almost immediate infiltration into the near surface high permeable stratum, which is slope talus for H209R and vegetated soil for VE10U.

In Figure 6.12 a major spike-type event is reported, showing very high sustained

counts well above 100,000 RDC/hour. The occasional high count events last for a single monitoring period conferring the spike shape.

It is interesting to observe that all waveguides show, throughout the dataset, some AE rate peaks that are relatively higher (i.e. a larger ratio of rainfall rate to AE response of slope). An example is shown in Figure 6.12.



**Figure 6.12:** (a) AE rates (RDC/h) in response to major rainfall events. The highest AE peaks recorded are a stronger response to the rainfall and could be generated with processes triggered by the rainfall; (b) graphs showing the relationship between rainfall rates (mm/h) and AE rates (RDC/h) for each waveguide. The time window considered is 17/05/2015 to 02/06/2015, cutting out the very high event shown in (a) occurred around 14/05/2015 to give emphasis to the rainfall–AE proportionality



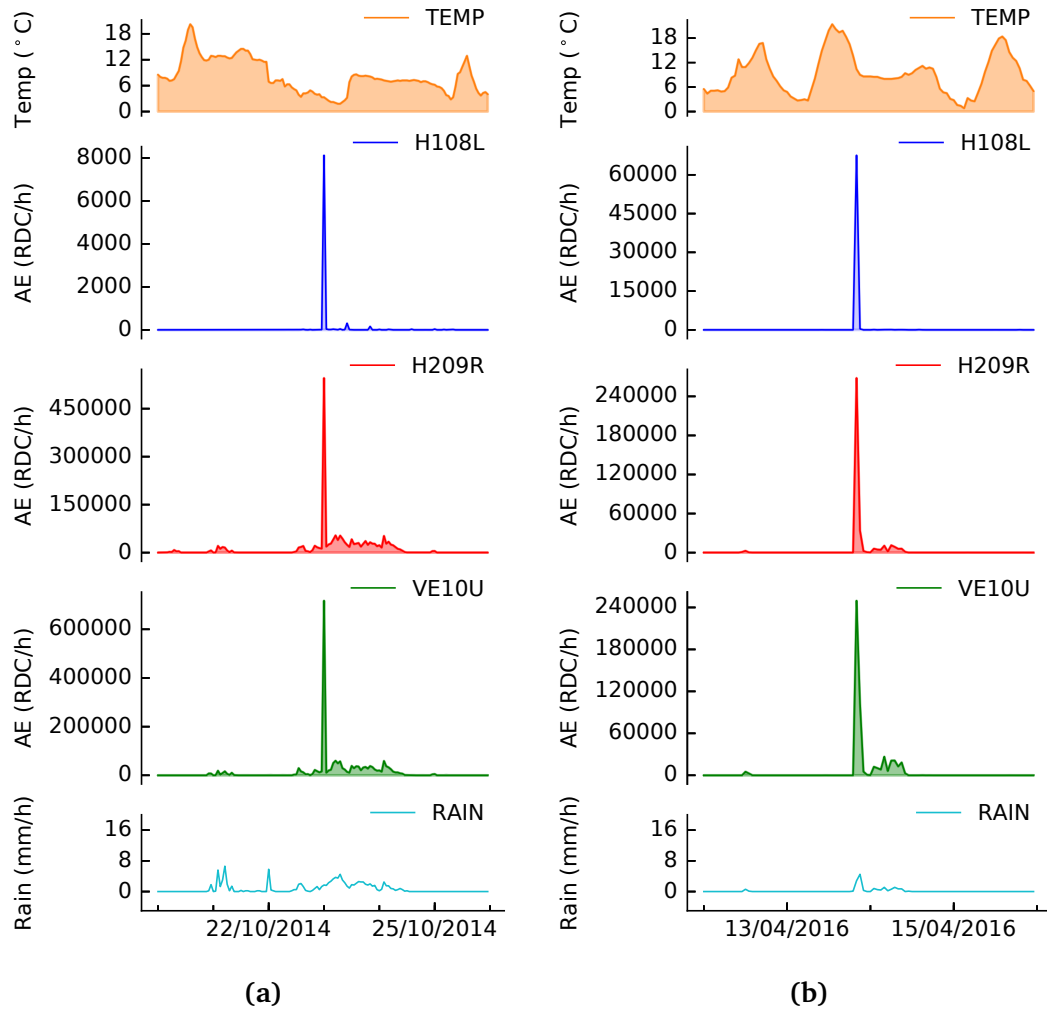
### 6.3.3 High RDC/h peaks

A handful of events recorded at this site can be described as very high RDC/h with rates well above the 99<sup>th</sup> percentile:

- $5,000 \leq H108L \leq 68,000$  RDC/h
- $200,000 \leq H209R \leq 580,000$  RDC/h
- $200,000 \leq VE10U \leq 800,000$  RDC/h

Two of events are reported in Figure 6.13 as examples. The high rate events are simultaneously recorded by all three sensors, with different rates amongst them. They last for one single monitoring period, thus acquiring the form of a peak or a spike. It is unclear what is the mechanism that generates these rates as they cannot be linked to any of the measured parameters. Although rain is normally recorded when these AE events appear, they are clearly not generated by seepage. The evidence is that the abnormal higher acoustic rates are recorded by all three waveguides, not only H208L and VE10U which are mostly linked to seepage-generated rates as seen in Section 6.3.2, and there is no particular increase in the rainfall rate at the time either.

As environmental sources or noise are excluded, it can be interpreted that AE is generated by one or more other mechanisms occurring within the slope and superimposed on top of the AE activity generated by the flow of water. Rainfall-triggered deformation of the slope material would be a potential mechanism generating AE, such as movement along a shear zone, which might be triggered by rainfall after a quiet period during which the strength properties were degrading. However, this cannot be proven as there is no visible evidence of major discontinuities in the conglomerate at the site.



**Figure 6.13:** High RDC/h rates events. The spike shape is due to the one-monitoring period duration. Note that RDC/h ranges differ amongst the sensors and between event (a) and event (b)

### 6.3.4 Freeze-thaw weathering

AE rates are recorded daily during winter time when there is a distinct temperature variation between day and night and the temperature fluctuates above and below zero degrees Celsius. H108L and H209R acoustic records show peaks of activity during the warmest hours of the day and lower activity during the cold hours at night. VE10U shows some RDC/h peaks during cold hours. The mechanism that generates these acoustic trends is clearly cyclical. This suggests that the trends

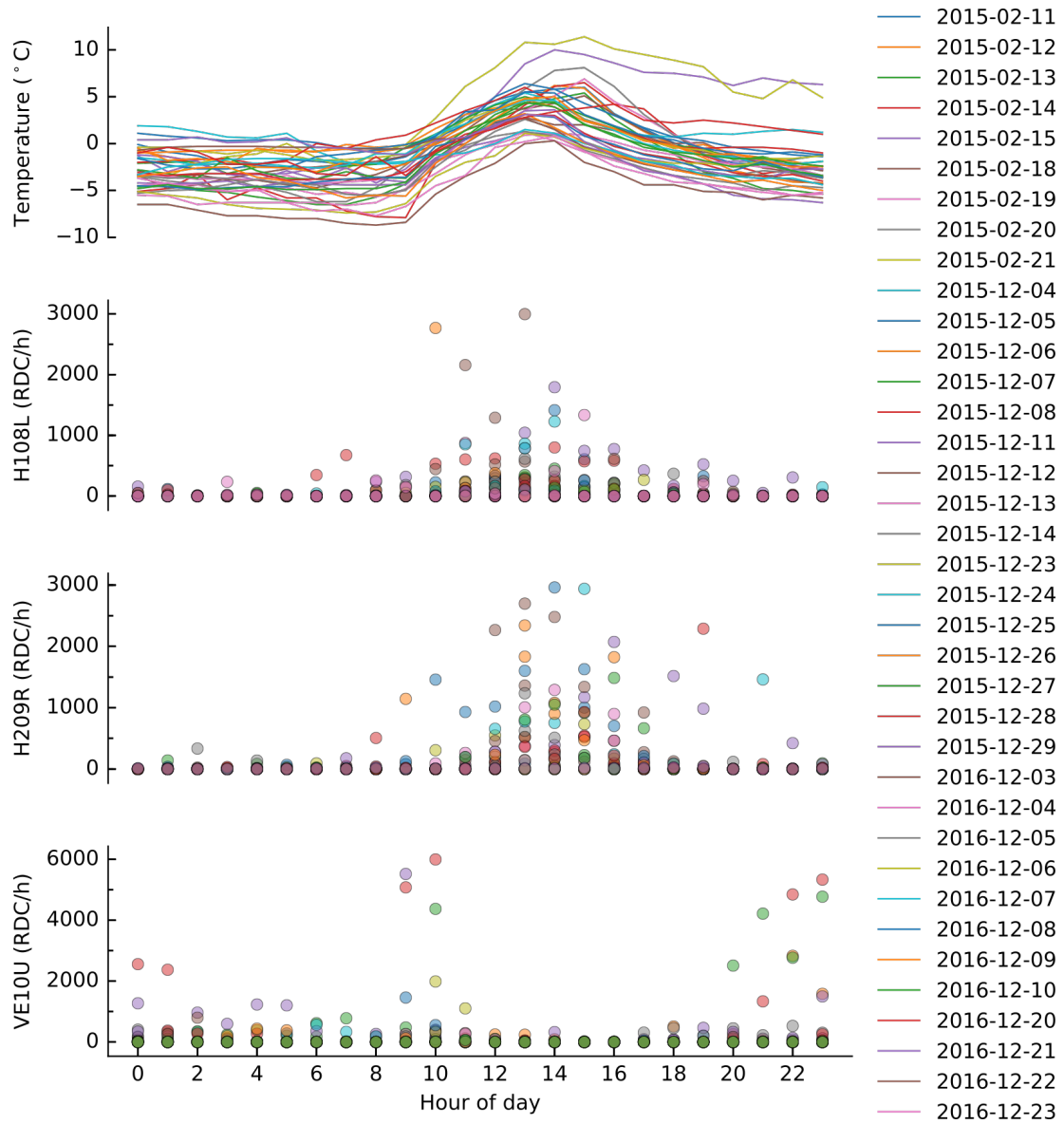
could be generated by processes connected to temperature fluctuation and in particular to freezing and thawing of water or moisture contained within the materials the waveguides are installed through.

To test whether the acoustic activity is influenced by temperature fluctuation, 37 days representative of freeze-thaw conditions were selected. The criteria for the selection were:

- Temperature must be below 0 °C for part of the day, typically night-time;
- Temperature must rise above 0 °C for part of the day, typically day-time;
- No rain must be recorded during the whole 24-hour periods analysed, to exclude rain-generated acoustic trends.

Acoustic trends related to freeze-thaw are recorded also in different conditions, for example when the temperature rises after a prolonged period of sub-zero temperatures, e.g. more than one day of temperatures continuously below zero Celsius. The above criteria were selected as they give the advantage of (daily) repeatable conditions and the comparison among them is therefore meaningful.

Figure 6.14 shows the hourly temperature and acoustic emission plots for the 37 sampled days. The hourly data for each day are overlapped so that they can be easily compared and trends can be identified. A general temperature trend can be recognised in the temperature top plot. The minimum daily temperature is generally recorded at around 09:00 in the morning. The temperature increases approaching the central hours of the day, reaching its maximum at around 14:00. The temperature then shows a sharp decrease until 18:00, and later it decreases at more steady rates throughout the night. A marked nocturnal–diurnal temperature variation is observed in the graph, with minimum of  $-7.9\text{ °C}$  and maximum of  $11.4\text{ °C}$  (minimum mean  $-3.0\text{ °C}$ , maximum mean  $4.6\text{ °C}$ , therefore with an average  $\Delta T = 7.6\text{ °C}$ ).

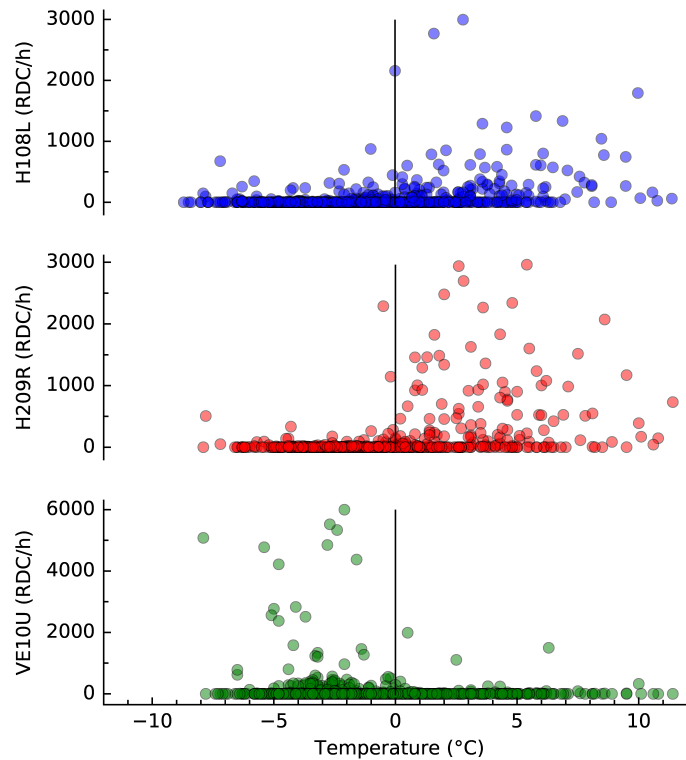


**Figure 6.14:** Hourly temperature and acoustic emission observations for 37 representative days. The legend explains the match between colour and date. No rainfall was registered during the days analysed

The other three graphs in Figure 6.14 represent the hourly acoustic emission rates for the three sensors H108L, H209R and VE10U. It can be observed that:

- H108L shows a basic acoustic activity between 0–100 RDC/h common to all hours of the day. Much greater is the variability during day-time (08:00–16:00) as higher values up to about 1000 RDC/h are often recorded. Occasional rates exceed these levels up to a maximum of 3,000 RDC/h;
- H209R rates are similar to the sensor previously described, with basic activity between 0–100 RDC/h common to all hours of the day. Higher rates up to about 2,000 RDC/h are concentrated between 10:00–18:00. Occasional rates exceed these levels, rates up to 3,000 RDC/h are registered during day-time;
- VE10U rates show different trends compared to the previous two sensors. The basic acoustic activity common to most of the 24 hours is between 0–600 RDC/h, considerably higher than the other two. Few rates are above this level and they mainly happen overnight or at the beginning of the day (09:00–10:00). Noticeable is that all records for 15:00 and 16:00 do not exceed 20 RDC/h.

Figure 6.15 shows the same acoustic data plotted against temperature. The graph confirms that the increased RDC/h rates are recorded at temperatures above zero Celsius for H108L and H209R and at temperatures below zero Celsius in the case of sensor VE10U.



**Figure 6.15:** Acoustic emission (RDC/h) versus Temperature (°C) graphs for the three sensors H108L, H209R and VE10U. Data represented are same as Figure 6.14. H108L and H209R higher acoustic rates are concentrated at temperatures greater than 0 °C whereas VE10U shows higher rates at temperatures lower than 0 °C. The red line represents the 0 °C

The hypothesis is that temperatures below zero degrees Celsius at night freeze the water contained within discontinuities in the ground, here intended as pores and cracks in rock or soil structure. When water freezes, it expands by approximately 9% in volume, forcing the pores to widen as the frost heave force is considerably greater than the cohesive force between particles (Zhou et al., 2014; Li et al., 2016). Temperatures rising above the melting point of water during the day cause the ice to thaw and the meltwater is free to migrate deeper into the opened structure. The cycle repeats as long as the environmental conditions allow temperatures to fluctuate below and above zero Celsius.

In this case it would be reasonable however to expect that all the acoustic emission would be generated during night time, when the temperature drops below

zero and the water expands inducing crack growth. So why two sensors (H108L and H209R) show higher activity at temperatures above zero and one (VE10U) at temperatures below zero. The different behaviour could be explained considering the different waveguides locations. Waveguides H108L and H209R are installed on the terrace slope, through the outcropping conglomerate of the rock mass face. Waveguide VE10U is located at the top of the terrace, away from the outcropping conglomerate face, and installed through about 1 m of organic soil. Therefore two different hypothesis have to be formulated for the generation of acoustic trends, depending on the location and the material involved:

- (1) *Terrace slope*, freeze–thaw cycles affecting the outcropping conglomerate exposed to weather agents. Conglomerate at Grossreifling is composed essentially of two types of material: the clasts, fragments of rocks that underwent lithification processes (primarily limestone and dolomite, Section 6.1.1) thus expected to have low primary porosity, and the matrix that holds them together, composed of relatively finer particles poorly cemented by calcium carbonate, with much higher primary porosity. The freeze-thaw weathering acts much faster on the porous medium than the clast elements for the process explained above, thus causing the matrix to degrade quicker than clasts and consequently allowing detachment of clasts and boulders from the slope. The detachment of boulders typically occurs when the ice within the discontinuities melts and the clast is no longer retained. Therefore the hypothesis is that the peaks of AE are actually generated by clasts detaching and falling/rolling on the slope rather than being produced by the propagation of fractures in the rock mass (i.e. Section 2.3.1);
- (2) *Top of terrace*, freezing of water contained within the top soil layer. Ice needles commonly form in moist soils when temperatures drop below freezing overnight (this process is also called ice segregation). It requires temperatures of the soil above zero and temperatures of the air below zero. This way

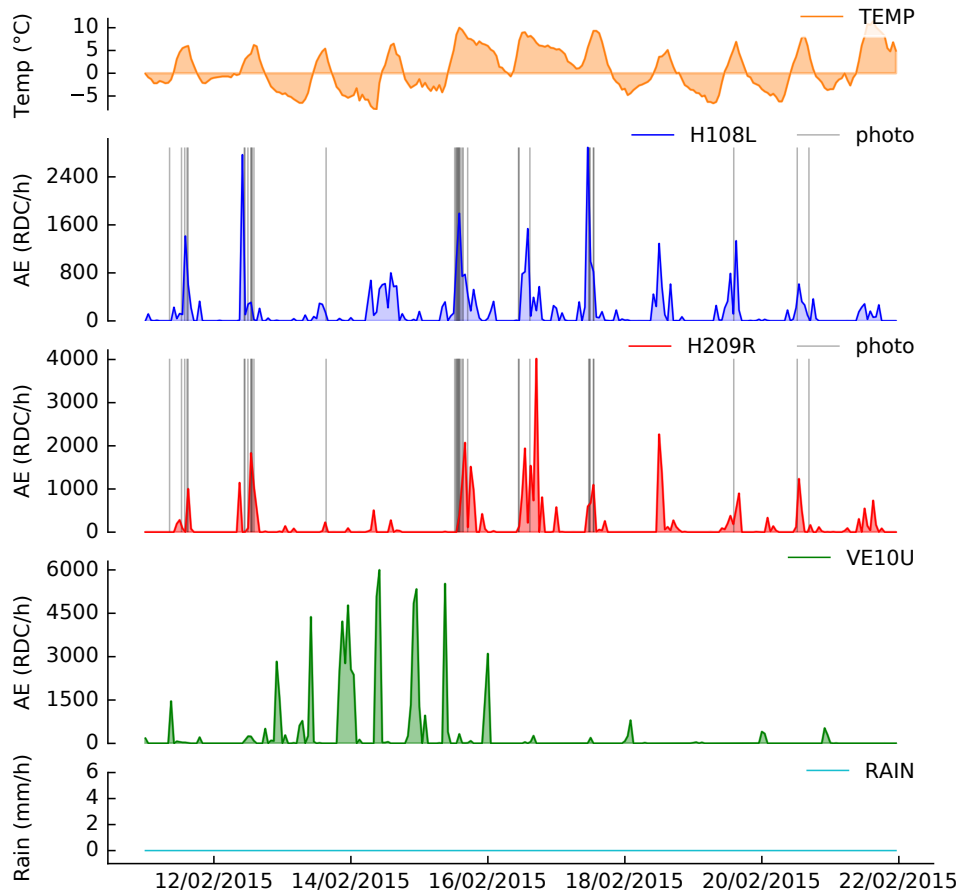
the water contained into the soil is moved towards the surface via capillary action and freezes, growing into needles shaped formations. The acoustic trends are generated by the moving particles and discontinuities widening within the soil layer. Ice segregation in soil is a process that contributes to slope degradation, however in this case it affects only the flat top of the slope and it does not contribute to overall instability processes, for this reason the hypothesis will not be further discussed.

In Figure 6.16 an example of the daily occurrence of this type of AE events over an eleven-day period is reported. The period shown in the graph is characterised by absolute absence of rainfall precipitations, which excludes rainfall-generated trends.

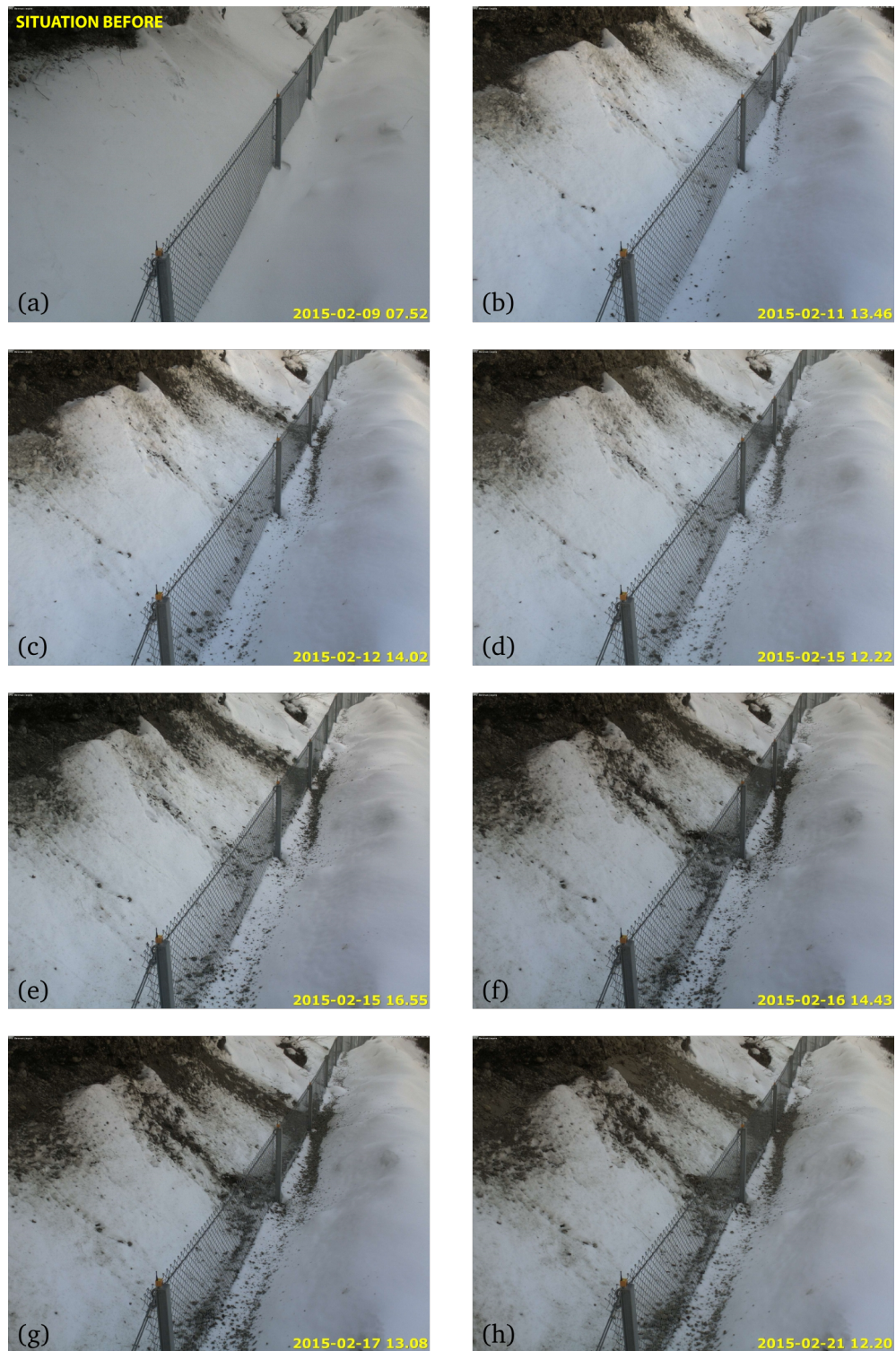
H108L and H209R peaks of acoustic activity are consistently recorded when temperature is above zero degrees Celsius and lower RDC/h are recorded when the temperature drops below zero. VE10U shows peaks of activity during sub-zero temperature periods but these very high events are limited to some of the days shown in the graph, lower RDC/h rates ( $<500$  RDC/h) are recorded although these are hardly identifiable due to the scale of the graph.

In order to establish whether the trends recorded by sensors H108L and H209R are generated by detachment of material from the slope and test the hypothesis formulated above, a vertical line was plotted in the graph for every photo triggered by the Detection Fence system (Section 6.2.2) which automatically triggers a camera when debris impact the fence. It appears clear from the graph that clusters of photos are concentrated around acoustic emission peaks. In the time frame represented in the graph at Figure 6.16, 36 photos were triggered and some samples are reported in Figure 6.17. The photos show that the material detached is predominantly fine and no major blocks detached on this occasion. Times of the photographs confirm that detachments are concentrated mainly during the day, although a few photos were triggered at night as well.





**Figure 6.16:** AE rates due to freeze-thaw cycles for the period 11/02/2015 to 21/02/2015. H108L and H209R show rates during warm hours, VE10U shows rates during cold hours. Lines represent photos triggered by detection fence sensors and taken by Camera 2 (does not apply to sensor VE10U due to its location)



**Figure 6.17:** Material detached as consequence of freeze-thaw weathering. Samples of photos taken by Camera 2 (viewpoint 1) in the period 10–21/02/2015. For camera location reference to Figure 6.7

In Section 6.3.1 the possibility of rates generated by overheating of the equipment was excluded for sensors H108L and H209R as their location is shaded by the northeast-facing slope. The point was raised that acoustic rates might be generated by direct sunlight on the VE10U sensor cover as this is positioned at the top of the slope, thus being exposed to solar radiation. In the analysis of data concerned with freeze-thawing, as can be deduced from the graph relative to sensor VE10U in Figure 6.14, no significant increase in the VE10U AE records is observed during daytime. In fact, RDC/h trends are actually lower during day-time than during night-time, which proves that trends are not artificially generated by overheating of the equipment.

Freeze-thaw weathering is clearly a process very local to the slope surface, involving a shallow depth of the rock mass, but it has the potential to weaken the bonds that keep large boulders attached to the slope. Over time this can determine the disengagement of large rockfalls. As detachment of fine material was recorded by the system, detachment of larger conglomerate constituents has the potential to be recorded too.

## 6.4 Summary

At SART site three Slope ALARMS sensors were installed in 2014. In this chapter acoustic emission recorded over a period of about two years is analysed and compared to rainfall data and photos triggered from the detection fence provided evidence of material actually detached from the slope.

This site has a history of rocks detaching during spring time due to washout caused by snowmelt (e.g. see Section 3.3.2). However, no significant event (i.e. rockfall of considerable dimensions) occurred during the time frame analysed in this work, therefore the acoustic behaviour of the conglomerate approaching failure is still unknown. During the exceptionally mild winters of 2014, 2015 and 2016

only few centimetres of snow fell and the conditions for detachments of large dimensions were not satisfied. Nonetheless, the analysis of AE trends measured at site gave some interesting results related to seepage in permeable materials and freeze–thaw processes.

Permeable material should always be avoided when installing waveguides as RDC/h rates are easily generated by seepage. Seepage-generated rates are considered to be noise as they do not provide any useful information about the stability of the slope. Moreover, they could mask trends that are, instead, indicative of an ongoing instability process caused by washout. As said, washout is one of the main triggering factors (in particular when combined to snowmelt). Very high spikes recorded by all three sensors (H108L, H209R and VE10U) during rainfall events actually show that there might be some underlying trends generated by instability processes triggered by rainfall. However, it is still unclear what generates these spikes.

Higher RDC counts correlated to freeze–thaw processes were measured during winter days when the temperature rises above zero Celsius during the warm hours. As shown by photos taken by cameras triggered by impacts occurring on the Detection fence, these acoustic trends are caused by the detachment of material from the slope. The counts measured are in the order of few hundred to few thousands RDC/h. The material detached from the slope during monitoring was predominantly fine (i.e. pebbles, cobbles) and yet clear counts were measured. This clearly shows that there is potential for detachment of large boulders to be recorded.

# Chapter 7

## Framework

This chapter is subdivided in two sections. In Section 7.1 a discussion of the findings of this research project is provided. This will lead to strategies for interpretation of AE trends, which addresses Objective 3 (Section 1.2). Based on this discussion, recommendations for future work are provided in Section 7.2.

### 7.1 Interpretation of AE trends

The different AE rates and trends shown in Chapter 5 and Chapter 6 clearly demonstrate that it is possible to detect and differentiate a range of rock slope deformation mechanisms by analysing measured AE trends. The results also show that the acoustic emission measured within rock slopes is highly site dependant.

AE trends are influenced by the type of rock mass (i.e. structured or unstructured, with high or low primary porosity, etc.) and by the type of failure mechanism that the rock mass is subject to. AE activity is generated by the deformation occurring within the rock mass in response to varied conditions (e.g. water pressure, external load, etc.). For this reason, AE can be seen as an analogy of displacement.

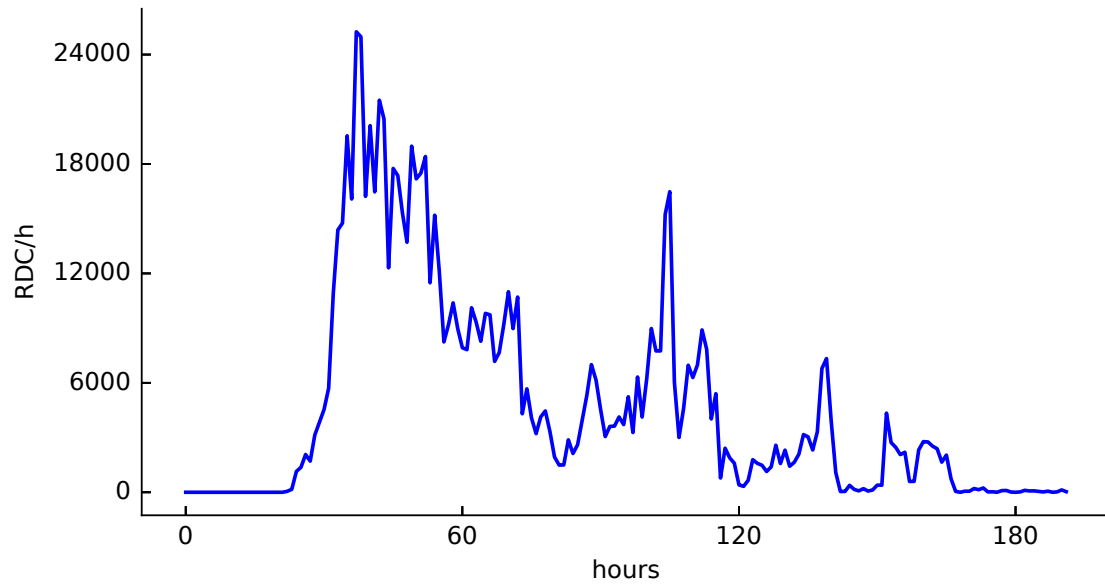
Examples from Passo della Morte rock mass of mechanisms generating displacement that are, in turn, the source of measured acoustic emission, are:

(1) **increase in water pressure** within rock mass (i.e. groundwater level).

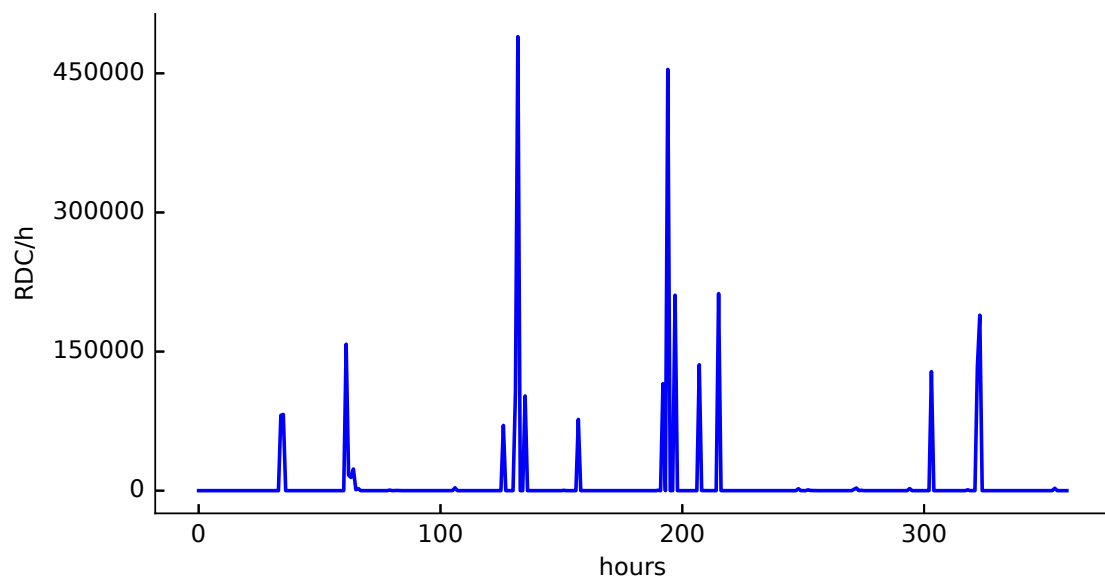
The increase in pore water pressure decreases effective stresses and hence strength, which leads to deformations. This is identifiable because the trend generally increases sharply within few hourly monitoring periods compared to the decrease, which can last several hourly monitoring periods (i.e. it can last up to several days), until the groundwater level goes back to its base-level. The trend (i.e. the shape of the AE event) is proportional to the increase and decrease of the groundwater level but the acoustic rate level RDC/h is variable (i.e. as seen in Section 5.3.2 variation of 1 m on average corresponds to about 5,000 RDC/h but also 20,000 RDC/h were measured for the same variation magnitude). Figure 7.1 illustrates a typical acoustic emission trend due to variations in groundwater level (i.e. water pressure);

(2) **external loading** on top of rock mass (i.e. snow load). This is recognisable as the RDC/h generally rises from 0 RDC/h to a value greater than 20,000 RDC/h within one hourly monitoring period and in the successive monitoring period decreases to 0 RDC/h again. A peak ( $>20,000$  RDC/h) repeats after several monitoring periods in which 0 RDC/h is measured. Figure 7.2 shows typical acoustic emission trends due to snow load.

From their description, it is clear that the key method to identify these generating mechanisms is to evaluate at the same time their magnitude, that is the AE rate (RDC/h), and their shape, that is the AE trend (variation of RDC/h through time).



**Figure 7.1:** Typical AE trend due to variation of water pressure conditions (sharp increase and slow decrease)



**Figure 7.2:** Typical AE trends due to snow load (sharp spikes)

Although such a close relationship exists between AE generation and displacement events, this work does not provide a correlation between AE rates and displacement rates. This results from the unavailability of data from the field sites suitable to quantify displacements occurring across the waveguides or in their vicinity. In addition, it must also be considered that AE has the potential to be much more sensitive (e.g. in soil slopes the technique was able to monitor displacement rates as little as 0.0018 mm/day, Section 2.4.4) than other traditional monitoring techniques (i.e. extensometers, crackmeters, etc.) and, as a consequence, deformation detected through AE might not be detected by traditional instruments, hence not allowing for comparison.

A slope deforming as a result of an applied stress smaller than the instantaneous strength will eventually fail, after a time that is dependant on the applied stress (Saito, 1965). Therefore, if a slope is deforming it can be assumed that the deformation is time-dependant and it is expected that the displacement will accelerate towards the time to failure, according to the most established inverse velocity methods (e.g. Saito, 1965; Fukuzono, 1985). Evidence of power-law acceleration of AE events in a natural slope starting two hours before collapse is reported by Amitrano et al. (2005), as seen in Section 2.4.4.

As AE can be seen as an analogy of displacement, it is expected that it will accelerate towards the time-to-failure. For the Slope ALARMS system this translates into increased RDC rates (i.e. RDC/h). However, the single hourly rate is meaningless if not put into context. As seen at the monitoring sites, rates can span several orders of magnitude (e.g. see Section 5.4), hence, taken singularly, AE rates cannot be descriptive of any process taking place within a slope. Rather, what we need to look for is a pattern of increasing event magnitudes over time (i.e. RDC trends). Taking as an example the trends generated by internal stress changes due to varied groundwater levels at Passo della Morte, a considerable increase of RDC per unity of variation (i.e. RDC/m) throughout time could be symptomatic of an acceleration in AE events, thus meaning that the slope stability could be degrading and



ultimately approaching failure. This would qualitatively translate in events that still have the same shape of a “groundwater variation” event seen in Figure 7.1 but characterised by considerably higher RDC/h rates, and these would increase again for subsequent events.

It is the opinion of the author that the system has a good potential for being used to monitor degrading stability conditions, however, further work is required to be used as an early warning of impending collapse because of the difficulty of setting meaningful AE rate thresholds values on which to make decisions.

## **7.2 Recommendations for future work**

The discussion provided forms the basis for recommending further work. The aim of this research was the development of reliable instrumentation for the monitoring of AE generated by the deformation and fracture propagation occurring within rock slopes prior to collapse. The investigation reported in this thesis represents a considerable contribution towards this goal, however, further work is needed to enable the system to automatically provide warning of failure in time to be of use to take action. The following areas have been identified for future work:

- The development of an approach for the quantification of slope deformation using measured acoustic emission rates (i.e. quantifying displacement rate occurring across waveguides and developing a relationship with measured AE rates);
- To quantify the attenuation along a waveguide installed through a rock mass in order to be able to locate the zone of deformation within it and prescribe the maximum length that is practicable for stress waves to reach the sensor (avoiding unnecessarily long waveguides will also keep the associated costs low);

- Further investigation to connect measured AE trends, magnitude and deformation mechanisms to accomplish a time-to-failure model based on RDC and hence enabling development of rules for setting thresholds;
- The development of an emergency protocol to be implemented when a threshold is reached and a warning/alarm is issued; without a clear plan of action to be put into effect, the development of any warning system would be meaningless.

# Chapter 8

## Conclusions

The aim of this research was the development a system able to monitor acoustic emission generated in rock slopes by deformation mechanisms preceding a collapse. The investigation clearly shows that it is possible to detect and differentiate a range of rock slope deformation mechanisms that have the potential to lead to failure of the monitored slopes. The aim of this research project has therefore been achieved.

Monitoring at two trial sites characterised by different types of rock masses, distinct failure mechanisms and monitored with a number of traditional geotechnical instruments provided valuable real data to be analysed. Potential drivers of rock mass deformation mechanisms were considered systematically (i.e. rainfall, snow, temperature fluctuations and seismic activity). Clear and repeatable AE trends were measured and associated with changes in external slope loading and internal stress changes (Objective 1).

At Passo della Morte (PdM), Italy, a steeply bedded limestone slope was monitored for over 6 years. Clear and consistent AE trends were measured at this site as the rock mass responds to variations in the groundwater level, which alters stress conditions in the steeply bedded limestone. In addition, AE is also generated in response to snow loading on the slope and the hypothesis is that the vertical stress increase results in differential micro-displacements between the limestone layers.

The distribution and magnitude of AE rates from these two mechanisms can be differentiated. Confidence in the interpretation of the links between destabilising factors (e.g. snow loading and ground water level) is provided by the multiple events recorded, consistent behaviour and simultaneous measurement of AE on multiple waveguides. It has been shown that to date there is no link between seismic activity from local events up to magnitude  $M_L = 3.8$  and AE recorded by the system, although generation of AE linked to shaking of the rock mass cannot be discounted for future earthquake events.

At Grossreifling (SART), Austria, a conglomerate terrace was monitored for about 2.5 years. At this site rain seepage into the near surface slope talus and top soil has been found to generate high rates of AE. However, the correlation between rainfall and AE rates is not always consistent and it is hypothesised that rain-triggered mechanisms of slope instability could be indicated by elevated AE (i.e. higher RDC spikes were recorded a handful of times during rainfall events). AE rates linked to observed detachment of small boulders from the slope surface were detected following freeze-thaw temperature cycles.

Large scale failure events have not occurred at either site during the monitoring periods considered in this work. Therefore, the ability of AE measurements to detect deterioration of rock slope stability towards failure, and hence be used to provide an early warning, is not yet proven. However, the sensitivity of measured AE to relatively small scale changes to rock mass loading and stress state, which could yield displacements in the order of fractions of millimetre, give confidence that a large scale event can be detected using acoustic emission as stability deteriorates.

The system was validated (Objective 2) through laboratory experiments and comparison of the results to better-understood behaviour of components used in the original Slope ALARMS system (i.e. Section 3.2.1). Laboratory tests proved that threaded waveguides attenuate in a similar way to smooth waveguides therefore

---

making them suitable for AE monitoring, provided that the transducer is mounted on a flattened surface obtained by filing one or more threads. This mounting method ensures optimal coupling of the transducer-waveguide allowing AE waves to be efficiently transmitted through this interface.

Field tests qualitatively proved that the source of AE does not necessarily need to be located across the waveguide to be measured by the sensor. AE generated at a radial distance from the waveguide (up to about 1 m in this work) was able to be transmitted through the rock to the waveguide and through the waveguide to the transducer. Also AE activity detected by multiple waveguides at the same time is good evidence of this (such as at PdM site). This also means that passive waveguides are suitable for the monitoring of rock masses as opposed to active waveguides. Nonetheless, AE generated across the waveguide will always be detected much more clearly, as waves decay with the distance (attenuation). Another important aspect that was tried to be addressed was, actually, the attenuation (Section 2.3.2) along a waveguide installed within a rock mass. Due to technical issues was not possible to quantify the attenuation of the waveguide installed on site, however it is highly recommended to quantify this aspect in future work.

A discussion has been provided about identification and interpretation of AE trends (Objective 3), however, further work is necessary link measured AE trends, magnitude and deformation mechanisms to achieve a time-to-failure model based on RDC and hence enabling development of rules for setting thresholds.

# References

- Amitrano, D. (2004). “Emerging complexity in a simple model of the mechanical behaviour of rocks”. In: *Geoscience* 336.6, pp. 505–512.
- Amitrano, D. (2006). “Rupture by damage accumulation in rocks”. In: *International Journal of Fracture* 139.3-4, pp. 369–381. arXiv: [0709.2647](#).
- Amitrano, D., J. Grasso, and G Senfaute (2005). “Seismic precursory patterns before a cliff collapse and critical point phenomena”. In: *Geophysical Research Letters* 32.8, pp. 1–5. arXiv: [0709.2651](#).
- Amitrano, D., M Arattano, M Chiarle, G Mortara, C Occhiena, M Pirulli, and C Scavia (2010). “Microseismic activity analysis for the study of the rupture mechanisms in unstable rock masses”. In: *Natural Hazards and Earth System Science* 10, pp. 831–841.
- Anastasopoulos, A., D. Kourousis, and K. Bollas (2009). “Acoustic Emission Leak Detection Of Liquid Filled Buried Pipeline”. In: *Journal of Acoustic Emission* 27, pp. 27–39.
- Angeli, M. G., A. Pasuto, and S. Silvano (2000). “A critical review of landslide monitoring experiences”. In: *Engineering Geology* 55.3, pp. 133–147.
- Arosio, D, L Longoni, M Papini, M Scaioni, L Zanzi, and M Alba (2009). “Towards rockfall forecasting through observing deformations and listening to microseismic emissions”. In: *Natural Hazards and Earth System Sciences* 9.4, pp. 1119–1131.
- Aster, R (2005). *Fundamentals of Seismic Wave Propagation*. Vol. 86, p. 105.
- ASTM Standard E1316 (2016). *Terminology for nondestructive examinations standard*. Tech. rep.
- Barton, N. (2007). *Rock quality, seismic velocity, attenuation and anisotropy*. Cambridge: Balkema, p. 756.
- Cai, M, P Kaiser, and C. Martin (2001). “Quantification of rock mass damage in underground excavations from microseismic event monitoring”. In: *International Journal of Rock Mechanics and Mining Sciences* 38.8, pp. 1135–1145.

- Cavallin, A and B Martinis (1974). “Studio geologico della grande frana di Borta (Ampezzo)”. In: *In Alto* 58, pp. 297–319.
- Cheon, D., Y. Jung, E. Park, W. Song, and H. Jang (2011). “Evaluation of damage level for rock slopes using acoustic emission technique with waveguides”. In: *Engineering Geology* 121.1-2, pp. 75–88.
- Chichibu, A, K Jo, M Nakamura, T Goto, and M Kamata (1989). “Acoustic Emission Characteristics of Unstable Slopes”. In: *Journal of Acoustic Emission* 8.4, pp. 107–112.
- Codeglia, D. (2011). “Analisi geomeccanica e predisposizione di un sistema di monitoraggio lungo la galleria del Passo della Morte”. PhD thesis. University of Trieste, Italy, p. 43.
- Codeglia, D. (2013). “Analisi numerica tridimensionale tramite modello SPH della frana di Passo della Morte (UD)”. Unpublished Master’s Thesis. University of Bologna, Italy, p. 56.
- Codeglia, D., N. Dixon, G. Bossi, and G. Marcato (2017). “Alpine landslide risk scenario: run-out modelling using a 3D approach”. In: *Rend. Online Soc. Geol. It.* 42, pp. 14–17.
- Construction and Design (2017). *Earthquake Waves*. (Visited on 08/31/2017).
- Corsini, A. (2008). “Monitoring Methods - systems behind a safer environment”. In: *Results of the International Conference Monitor/08, 21-22 February 2008*. Research and Education Centre Raumberg-Gumpenstein, Austria, pp. 47–54.
- Crozier, M. (2010). “Deciphering the effect of climate change on landslide activity: A review”. In: *Geomorphology* 124.3-4, pp. 260–267. URL: <http://dx.doi.org/10.1016/j.geomorph.2010.04.009>.
- CRS-OGS (2016). *Real Time Seismology of the OGS Seismological Research Centre website*.
- Cruden, D. and D. Varnes (1996). “Landslide types and processes”. In: *Landslides: investigation and mitigation. National Research Council, Transportation and Research Board Special Report 247*. Ed. by A. Turner and R. Schuster. Washington, DC, USA, pp. 36–75.
- Dijkstra, T. and N. Dixon (2010). “Climate change and slope stability in the UK: challenges and approaches”. In: *Quarterly Journal of Engineering Geology and Hydrogeology* 43.4, pp. 371–385. URL: <http://qjgeh.lyellcollection.org/cgi/doi/10.1144/1470-9236/09-036>.
- Dixon, N. and M. P. Spriggs (2007). “Quantification of slope displacement rates using acoustic emission monitoring”. In: *Canadian Geotechnical Journal* 44.8, pp. 966–976. URL: <http://www.nrcresearchpress.com/doi/abs/10.1139/T07-046>.

- Dixon, N. and M. P. Spriggs (2010). *Apparatus and method for monitoring soil slope displacement rate by detecting acoustic emissions*. UK Patent Application.
- Dixon, N., R Hill, and J Kavanagh (2003). "Acoustic emission monitoring of slope instability: development of an active waveguide system". In: *Proceedings of the ICE - Geotechnical Engineering* 156.2, pp. 83–95.
- Dixon, N., M. P. Spriggs, P Meldrum, and R Ogilvy (2010). "Development of a low cost acoustic emission early warning system for slope instability". In: *Geologically Active: Proceedings of the 11th IAEG Congress*, pp. 1803–1810.
- Dixon, N., M. P. Spriggs, P Meldrum, and E. Haslam (2012). "Field trial of an acoustic emission early warning system for slope instability". In: *Landslides and Engineered Slopes: Protecting Society through Improved Understanding. Proceedings of the 11th International Symposium on Landslides and 2nd North American Symposium on Landslides (Banff, Alberta, Canada, 2-8 June 2012)*, pp. 1399–1404.
- Dixon, N., M. P. Spriggs, A. Smith, P Meldrum, and E. Haslam (2014). "Quantification of reactivated landslide behaviour using acoustic emission monitoring". In: *Landslides* October 2013.
- Dixon, N., D. Codeglia, A. Smith, G. J. Fowmes, and P. Meldrum (2015a). "An acoustic emission slope displacement rate sensor — case studies". en. In: *Proceedings of the Ninth International Symposium on Field Measurements in Geomechanics*. Ed. by P. Digh. Perth, Australia: Australian Centre for Geomechanics, pp. 743–756.
- Dixon, N., R Moore, M. P. Spriggs, A. Smith, P Meldrum, and R Siddle (2015b). "Performance of an Acoustic Emission Monitoring System to Detect Subsurface Ground Movement at Flat Cliffs, North Yorkshire, UK". In: *Engineering Geology for Society and Territory - Volume 2: Landslide Processes*. Ed. by G. Lollino, D. Giordan, G. B. Crosta, J. Corominas, R. Azzam, J. Wasowski, and N. Sciarra. Vol. 2. Springer International Publishing, pp. 117–120.
- Dixon, N., A. Smith, M. P. Spriggs, A Ridley, P Meldrum, and E. Haslam (2015c). "Stability monitoring of a rail slope using acoustic emission". In: *Proceedings of Institution of Civil Engineers – Geotechnical Engineering Journal*.
- Dunnicliff, J (1988). *Geotechnical Instrumentation for Monitoring Field Performance*. New York: John Wiley & Sons.
- Ehlers, J., P L.P L. Gibbard, and P D. Hughes (2011). *Quaternary glaciations - extent and chronology : a closer look*. Elsevier, p. 1108.
- Evans, A. (1978). "Acoustic emission sources in brittle solids". In: *Conference on Acoustic Emissions by the Acoustical Society of America and the Acoustical Society of Japan, November 27-December 1, 1978*. Honolulu, Hawaii, pp. 209–227.



- Farrar, C. and K Worden (2007). "An introduction to structural health monitoring". In: *Philosophical transactions of the Royal Society* 365.1851, pp. 303–15. arXiv: [B](#).
- Flyvbjerg, B. (2006). "Five Misunderstandings About Case-Study Research". In: *Qualitative Inquiry* 12.2, pp. 219–245. arXiv: [1304.1186](#).
- Fukuzono, T (1985). "A new method for predicting the failure time of a slope". In: *Proceedings of the 4th International Conference and Field Workshop on Landslides*. Tokyo, pp. 145–150.
- Ghosh, A, S.-M. Hsiung, and A. Chowdhury (1996). *Seismic response of rock joints and jointed rock mass*. Tech. rep. Oak Ridge, TN: Office of Scientific and Technical Information, p. 116.
- Gili, J., J. Corominas, and J. Rius (2000). "Using global positioning system techniques in landslide monitoring". In: *Engineering Geology* 55, pp. 167–192.
- Hardy, H. (1992). "Laboratory Studies Relative to the Development of Mechanical Waveguides for Acoustic Emission Monitoring of Geologic Structures". In: *Italian Journal Nondestructive Testing and Diagnostics* XIII.2, pp. 32–38.
- Hardy, H. (1994). "Geotechnical field applications of AE/MS techniques at the Pennsylvania State University: a historical review". In: *NDT & E International* 27.4, pp. 191–200.
- Hardy, H. (2003). *Acoustic Emission/Microseismic Activity: Volume 1: Principles, Techniques and Geotechnical Applications*. Lisse, The Netherlands: Balkema Publishers, p. 297.
- Havaej, M., D. Stead, E. Eberhardt, and B. R. Fisher (2014). "Characterization of bi-planar and ploughing failure mechanisms in footwall slopes using numerical modelling". In: *Engineering Geology* 178, pp. 109–120. URL: <http://dx.doi.org/10.1016/j.enggeo.2014.06.003>.
- Helmstetter, A and S Garambois (2010). "Seismic monitoring of Schilienne rock-slide (French Alps): Analysis of seismic signals and their correlation with rain-falls". In: *Journal of Geophysical Research: Earth Surface* 115.3, pp. 1–15.
- Hendricks, R, N. Dixon, and T Meisel (2014). *Requirements and Design Specification for the SART Pilot Installation SART-IPS-SP-0002*. Tech. rep., pp. 1–68.
- Hoek, E. (1983). "Strength of jointed rock masses". In: *Geotechnique* 23.3, pp. 187–223.
- Hungr, O. (2001). "A Review of the Classification of Landslides of the Flow Type". In: *Environmental & Engineering Geoscience* VII.3, pp. 221–238.
- Hungr, O., S. Leroueil, and L. Picarelli (2014). "The Varnes classification of landslide types, an update". In: *Landslides* 11.2, pp. 167–194.

- Husen, D. van and J. M. Reitner (2011). “An outline of the Quaternary stratigraphy of Austria”. In: *Quaternary Science Journal* 60, pp. 17–24.
- Hutchinson, J. (1988). “Morphological and geotechnical parameters of landslides in relation to geology and hydrogeology”. In: *Proceedings of the 5th International Symposium on Landslides*. Lausanne, pp. 3–35.
- Keefer, D. K. (1984). “Landslides caused by earthquakes”. In: *Geological Society of America Bulletin* 95.4, pp. 406–421. arXiv: ??.
- Keil, M. and F Neubauer (2011). “Neotectonics, drainage pattern and geomorphology of the orogen-parallel Upper Enns Valley (Eastern Alps)”. In: *Geologica Carpathica* 62.3, pp. 279–295.
- Koerner, R. M., W. M. McCabe, and A. Lord (1981). “Acoustic Emission Behavior and Monitoring of Soils”. In: *Acoustic Emissions in Geotechnical Engineering Practice, ASTM STP 750*. Ed. by V. Drnevich and R. Gray. American Society for Testing and Materials, pp. 93–141.
- Kranz, R. (1983). “Microcracks in rocks: a review”. In: *Tectonophysics* 100.1-3, pp. 449–480.
- Li, J.-l., K.-p. Zhou, W.-j. Liu, and H.-w. Deng (2016). “NMR research on deterioration characteristics of microscopic structure of sandstones in freeze–thaw cycles”. In: *Transactions of Nonferrous Metals Society of China* 26.11, pp. 2997–3003.
- Long, R, M Lowe, and P Cawley (2003). “Attenuation characteristics of the fundamental modes that propagate in buried iron water pipes”. In: *Ultrasonics* 41.7, pp. 509–519.
- Lord, A., C. Fisk, and R. M. Koerner (1982). “UTILIZATION OF STEEL RODS AS AE WAVEGUIDES”. In: *Journal of Geotechnical and Geoenvironmental Engineering* 108.GT2.
- Maji, A., D Satpathi, and T Kratochvil (1997). “Acoustic Emission Source Location Using Lamb Wave Modes”. In: *Journal of Engineering Mechanic* 123.2, pp. 154–161.
- Mandl, G. (2000). *Faulting in Brittle Rocks*. Berlin, Heidelberg: Springer, p. 434.
- Manthei, G. (2005). “Characterization of Acoustic Emission Sources in a Rock Salt Specimen Under Triaxial Load”. In: *Bulletin of the Seismological Society of America* 95.October, pp. 1674–1700.
- Marcato, G. (2006). “Valutazione della pericolosità da frana in località Passo della Morte”. Unpublished PhD Thesis. University of Modena and Reggio Emilia, Italy, p. 129.
- Marks, R., A. Clarke, C. Featherston, C. Paget, and R. Pullin (2016). “Lamb Wave Interaction with Adhesively Bonded Stiffeners and Disbonds Using 3D Vibrom-

- etry". In: *Applied Sciences* 6.1, p. 12. URL: <http://www.mdpi.com/2076-3417/6/1/12>.
- Martinis, B (1985). *Il lago quaternario di Forni di Sotto (Alpi Carniche)*.
- Matcharashvili, T, T Chelidze, N Zhukova, and E Mepharidze (2011). "Investigation of acoustic emission accompanying stick-slip movement of rock samples at different stiffnesses of springblock system". In: *Tribology International* 44.7-8, pp. 811–819.
- Mathiyaparanam, J (2006). "Analysis of acoustic emission in cohesionless soil". MSc Thesis. University of South Florida.
- McCauley, M. (1976). "Microsonic detection of landslides". en. In: *Transportation research record* 581, pp. 25–30.
- Michlmayr, G. and D. Or (2014). "Mechanisms for acoustic emissions generation during granular shearing". In: *Granular Matter* 16.5, pp. 627–640.
- Michlmayr, G., D Cohen, and D. Or (2012). "Sources and characteristics of acoustic emissions from mechanically stressed geologic granular media - A review". In: *Earth-Science Reviews* 112.3-4, pp. 97–114.
- Michoud, C, S Bazin, L. Blikra, M. Derron, and M Jaboyedoff (2013). "Experiences from site-specific landslide early warning systems". In: *Natural Hazards and Earth System Sciences* 13.10, pp. 2659–2673.
- Moore, J, V Gischig, J Burjanek, F Amann, and M Hunziker (2012). "Earthquake-triggered rock slope failures: Damage and site effects". In: *COGEAR: COupled seismogenic GEohazards in Alpine Regions* 3b.2.7.1, pp. 1–11.
- Moradian, Z., H. H. Einstein, and G. Ballivy (2016). "Detection of Cracking Levels in Brittle Rocks by Parametric Analysis of the Acoustic Emission Signals". In: *Rock Mechanics and Rock Engineering* 49.3, pp. 785–800.
- Nakajima, I, M Negishi, M Ujihira, and T Tanabe (1995). "Application of the Acoustic Emission Monitoring Rod to Landslide Measurements". In: *5th Conf. on Acoustic/Microseismic Activity in Geologic Structures and Materials*. Pennsylvania State University, pp. 505–519.
- Nakajima, L, J Sato, N Taira, and N Kubota (1988). "The observation of landslide by the acoustic emission monitoring rod". In: *Progress in Acoustic Emission IV*, pp. 273–281.
- Noorsuhada, M. (2016). "An overview on fatigue damage assessment of reinforced concrete structures with the aid of acoustic emission technique". In: *Construction and Building Materials* 112, pp. 424–439.
- Opcm 3519 (2006). *Ordinanza PCM 3519 del 28 aprile 2006*.

- Ordinanza PCM 3519 (2006). *Mappa di pericolosità sismica del territorio nazionale - Allegato 1b*.
- Ozevin, D, D. W. Greve, I. J. Oppenheim, and S. P. Pessiki (2006). "Resonant capacitive MEMS acoustic emission transducers". In: *Smart Materials and Structures* 15.6, pp. 1863–1871.
- Paipetis, A. S., T. E. Matikas, D. G. Aggelis, and D Van Hemelrijck, eds. (2012). *Emerging Technologies in Non-Destructive Testing V*, p. 526.
- Palmström, A. (2001). "Measurement and characterizations of rock mass jointing". In: *In-Situ Characterization of Rocks - Chapter 2*, pp. 1–40.
- Paterson, W. (1994). *The Physics of Glaciers*. Elsevier, p. 480.
- Petley, D (2012). "Global patterns of loss of life from landslides". In: *Geology* 40.10, pp. 927–930.
- Plona, T., K Winkler, R D'Angelo, B Sinha, P Papanastasiou, and J. Cook (1997). "Acoustic detection of stress-induced effects around a borehole". In: *International Journal of Rock Mechanics & Mining Science* 34.290, pp. 3–4.
- Podda, F and M Ponton (1997). "Paleogeographic and paleostructural evolution during the upper Triassic-lower Jurassic in the northern Carnian Prealps". In: *Atti Ticinensi di Scienze della Terra* 39, pp. 269–270.
- Proto, L. (2014). "No Title". Master's thesis. University of Padova (Italy), p. 100.
- Romana, M (1993). *A Geomechanical Classification for Slopes: Slope Mass Rating*, pp. 575–600.
- Rossow, W. B. and A. A. A. Lacis (1990). "Global, Seasonal Cloud Variations from Satellite Radiance Measurements. Part II. Cloud Properties and Radiative Effects". In: *Journal of Climate* 3.11, pp. 1204–1253.
- Rossow, W. B. and Y. C. Zhang (1995). "Calculation of surface and top of atmosphere radiative fluxes from physical quantities based on ISCPP date sets. 2. Validation and first results". In: *Journal of Geophysical Research-Atmospheres* 100.D1, pp. 1167–1197.
- Saito, M (1965). "Forecasting the time of occurrence of a slope failure". In: *Proceedings, Sixth International Conference on Soil Mechanics and Foundation Engineering*, pp. 537–541.
- Savvaidis, P. (2003). "Existing landslide monitoring systems and techniques". In: pp. 242–258.
- Schuster, R. and R. Krizek (1978). *Landslides Analysis and Control. Transportation Research Board Special Report 176*. Ed. by R. Schuster and R. Krizek. Washington, DC, USA: National Academy of Science.

- Scruby, C. (1987). "An introduction to acoustic emission". In: *Journal of Physics E: Scientific Instruments* 20.8, pp. 946–953.
- Senfaute, G, a Duperret, and J. a. Lawrence (2009). "Micro-seismic precursory cracks prior to rock-fall on coastal chalk cliffs: a case study at Mesnil-Val, Normandie, NW France". In: *Natural Hazards And Earth System Science* 9.5, pp. 1625–1641. URL: <http://www.nat-hazards-earth-syst-sci.net/9/1625/2009/>.
- Shehadeh, M., W Abdou, J. Steel, and R. Reuben (2008). "Aspects of acoustic emission attenuation in steel pipes subject to different internal and external environments". In: *Proceedings of the Institution of Mechanical Engineers, Part E: Journal of Process Mechanical Engineering* 222.1, pp. 41–54. URL: <http://pie.sagepub.com/lookup/doi/10.1243/09544089JPME143>.
- Shiotani, T (2004). *WEAD - Waveguide for AE waves due to rock Deformation*. Tech. rep., p. 2.
- Shiotani, T (2006). "Evaluation of long-term stability for rock slope by means of acoustic emission technique". In: *NDT & E International* 39.3, pp. 217–228.
- Shiotani, T and M Ohtsu (1999). "Prediction of slope failure based on AE activity". In: *Acoustic Emission: Standards and Technology Update, ASTM STP 1353*. Ed. by S. Vahaviolos. West Conshohocken, PA: American Society for Testing and Materials, pp. 156–172.
- Shiotani, T, S Yuyama, M. Carlos, and S. Vahaviolos (2001a). "Continuous monitoring of rock failure by a remote AE system". In: *Journal of Acoustic Emission* 19, pp. 248–257.
- Shiotani, T, M Ohtsu, and K Ikeda (2001b). "Detection and evaluation of AE waves due to rock deformation". In: *Construction and Building Materials* 15.5-6, pp. 235–246.
- Sikorska, J and J Pan (2004). "The effect of waveguide material and shape on acoustic emission transmission characteristics part 1: Traditional Features". In: *Journal of Acoustic Emission* 22, pp. 264–273.
- Smith, A. (2015). "Quantification of slope deformation behaviour using acoustic emission monitoring". PhD Thesis. Loughborough University, p. 330.
- Smith, A. and N. Dixon (2014). "Quantification of landslide velocity from active waveguide-generated acoustic emission". In: *Canadian Geotechnical Journal*.
- Smith, A., N. Dixon, P Meldrum, E. Haslam, and J Chambers (2014a). "Acoustic emission monitoring of a soil slope: Comparisons with continuous deformation measurements". In: *Géotechnique Letters* 255, pp. 255–261.

- Smith, A., N. Dixon, P. Meldrum, and E. Haslam (2014b). "Inclinometer casings retrofitted with acoustic real-time monitoring systems". In: *Ground Engineering* October, pp. 24–29.
- Sonmez, H., R. Ulusay, and C. Gokceoglu (1998). "A practical procedure for the back analysis of slope failures in closely jointed rock masses". In: *International Journal of Rock Mechanics and Mining Sciences* 35.2, pp. 219–233.
- Spillmann, T., H. Maurer, A. G. Green, B. Heincke, H. Willenberg, and S. Husen (2007). "Microseismic investigation of an unstable mountain slope in the Swiss Alps". In: *Journal of Geophysical Research: Solid Earth* 112.7, pp. 1–25.
- Stead, D. and A. Wolter (2015). "A critical review of rock slope failure mechanisms: The importance of structural geology". In: *Journal of Structural Geology* 74, pp. 1–23. URL: <http://dx.doi.org/10.1016/j.jsg.2015.02.002>.
- Stierle, E., V Vavryčuk, G. Kwiątek, E. M. Charalampidou, and M. Bohnhoff (2016). "Seismic moment tensors of acoustic emissions recorded during laboratory rock deformation experiments: Sensitivity to attenuation and anisotropy". In: *Geophysical Journal International* 205.1, pp. 38–50.
- Tabacco Maps (2008). *No.02 Forni di Sopra - Ampezzo - Sauris - Alta Val Tagliamento*. Tavagnacco (UD).
- Thompson, B. D., R. P. Young, and D. Lockner (2009). "Premonitory acoustic emissions and stick-slip in natural and smooth-faulted Westerly granite". In: *Journal of Geophysical Research: Solid Earth* 114.2, pp. 1–14.
- Tonnellier, A., A. Helmstetter, J. P. Malet, J. Schmittbuhl, A. Corsini, and M. Joswig (2013). "Seismic monitoring of soft-rock landslides: The Super-Sauze and Valoria case studies". In: *Geophysical Journal International* 193.3, pp. 1515–1536.
- Trnkoczy, A. (2012). "Understanding and parameter setting of STA/LTA trigger algorithm". In: *New Manual of Seismological Observatory Practice 2 (NMSOP-2)*, pp. 1–80. URL: [http://gfzpublic.gfz-potsdam.de/pubman/item/escidoc:43337:3/component/escidoc:56122/IS{\\\_}8.1{\\\_}rev1.pdf](http://gfzpublic.gfz-potsdam.de/pubman/item/escidoc:43337:3/component/escidoc:56122/IS{\_}8.1{\_}rev1.pdf).
- Uhlemann, S., A. Smith, J. Chambers, N. Dixon, T. A. Dijkstra, E. Haslam, P. Meldrum, A. Merritt, D. Gunn, and J. Mackay (2016). "Assessment of ground-based monitoring techniques applied to landslide investigations". In: *Geomorphology* 253, pp. 438–451.
- Varnes, D. (1978). "Slope movement types and processes". In: *Landslides—Analysis and control: National Academy of Sciences Transportation Research Board Special Report 176*. Ed. by R. Schuster and R. Krizek, pp. 12–33.
- Xu, C., X. Xu, and J. B. H. Shyu (2015). "Database and spatial distribution of landslides triggered by the Lushan, China Mw 6.6 earthquake of 20 April 2013". In: *Geomorphology* 248, pp. 77–92. URL: <http://dx.doi.org/10.1016/j.geomorph.2015.07.002>.

- Zelenyak, A., M Hamstad, and M Sause (2015). “Modeling of Acoustic Emission Signal Propagation in Waveguides”. In: *Sensors* 15.5, pp. 11805–11822. URL: <http://www.mdpi.com/1424-8220/15/5/11805/>.
- Zhang, J., W. Peng, F. Liu, H. Zhang, and Z. Li (2016). “Monitoring Rock Failure Processes Using the Hilbert - Huang Transform of Acoustic Emission Signals”. In: *Rock Mechanics and Rock Engineering* 49, pp. 427–442.
- Zhou, J, X. Yang, H Xing, Y Xue, and G He (2014). “Assessment of the Excavation-Damaged Zone in a Tall Rock Slope Using Acoustic Testing Method”. In: *Geotechnical and Geological Engineering* 32.4, pp. 1149–1158.
- Zoppè, G. (2015). “Seismological contribution to Passo della Morte landslide characterization (North Eastern Italy)”. Unpublished PhD Thesis. University of Trieste, Italy, p. 141.





# **Appendix A**

## **Instruments specifications**



# R3α Sensor

## General Purpose, 30 kHz Resonant Frequency Acoustic Emission Sensor

### Description and Features

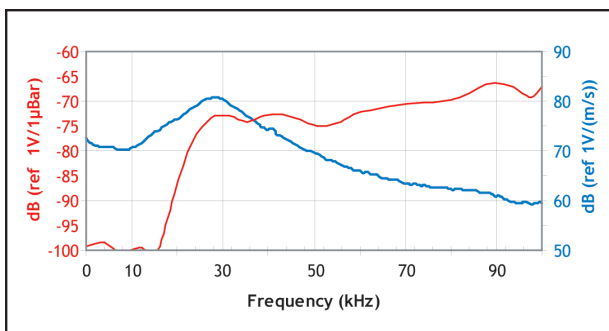
The R3α sensor cavity is machined from a solid stainless steel rod, making the sensor extremely rugged and reliable. The ceramic face electrically isolates the sensor from the structure to assure a low noise operation.

Most low frequency AE sensors are relatively large. However, the R3α sensor has the same compact size as our other Alpha series sensors and boasts a low frequency, 30 kHz resonant response. This feature makes it extremely useful in tight areas that require a low frequency sensor for testing.

The Alpha series family of sensors features SMA connectors versus the Microdot connectors found on PAC's RXX series of passive sensors. The Alpha series includes R3α, R6α, R15α, R30α, R50α, R80α and WSα sensors.

### Application

This sensor is normally selected for structural health monitoring of small to medium concrete and geologic structures and for concrete and metal pipeline leak detection applications where there needs to be high acoustic background noise rejection and distances between sensors can be relatively close (tens of feet).



Frequency response of the R3α. Calibration based on ASTM E1106; Calibration based on ASTM E976.

### Operating Specifications

#### Dynamic

Peak Sensitivity  $V/(m/s)$ ;  $[V/\mu\text{bar}]$  ..... 80 [-63] dB  
 Operating Frequency Range ..... 25 - 70 kHz  
 Resonant Freq.  $V/(m/s)$ ;  $[V/\mu\text{bar}]$  ..... 29 [140] kHz  
 Directionality.....  $\pm 1.5$  dB

#### Environmental

Temperature Range ..... -65 to 175°C  
 Shock Limit ..... 500 g  
 Completely enclosed crystal for RFI/EMI immunity

#### Physical

Dimensions..... 0.75" dia. x 0.88" h (19 x 22.4 mm)  
 Weight..... 41 grams  
 Case Material..... Stainless Steel  
 Face Material..... Ceramic  
 Connector..... SMA  
 Connector Locations ..... Side  
 Seal ..... Epoxy  
 Sensor to Preamp Cable (1 or 2 meters)..... 1232-X-SMA

### Ordering Information and Accessories

R3α ..... R3α or R3a  
 Magnetic Hold-Down ..... MHR15A  
 Preamplifier..... 0/2/4, 2/4/6  
 Preamp to System Cable (specify length in meters) ..... 1234 - X

#### Sensors include

NIST Calibration Certificate & Warranty



Products & Systems  
Division

195 Clarksville Road, Princeton Junction, NJ 08550

Phone: 609-716-4000 • Fax: 609-716-0706 •

Email: sales.systems@mistrasgroup.com • www.mistrasgroup.com



Due to continuing improvement, MISTRAS Group, Inc. reserves the right to amend specifications without notice.  
 Copyright © 2010 MISTRAS Group Inc. All Rights Reserved.

#201-04



# R6α Sensor

## General Purpose, 60 kHz Resonant Frequency Acoustic Emission Sensor

### Description and Features

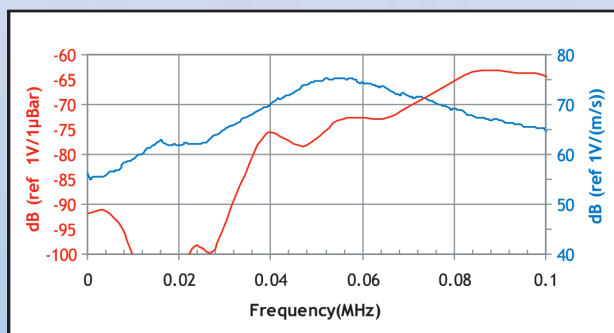
The Alpha series family of sensors features SMA connectors versus the Microdot connectors found on PAC's RXX series of passive sensors. The Alpha series includes R3α, R6α, R15α, R30α, R50α, R80α and WSα sensors. The major improvements in Alpha series over the RXX series include:

- Use of the more popular SMA type of connector.
- Cavity is machined from a solid stainless steel rod making for a simpler and more robust design.
- Dramatically increased thickness of the ceramic shoe for better mechanical stability.
- Distance from the bottom of the ceramic shoe to the bottom edge of sensor cavity increased for better insulation resistance and ground avoidance.
- Introduced a 30-degree angle at the bottom edge of the sensor cavity.

All these improvements make the Alpha series sensors more robust, reliable and greatly reduce the possible grounding of the cavity to the structure caused by wet environment.

### Application

This sensor can be used on metal and FRP structures such as pipelines or storage tanks in petroleum, refineries, chemical plants, and offshore platforms, due to its high sensitivity and low resonance frequency properties.



Frequency response of the R6α. Calibration based on ASTM E1106;  
Calibration based on ASTM E976.

### Operating Specifications

#### Dynamic

Peak Sensitivity  $V/(m/s)$ ;  $[V/\mu\text{bar}]$  ..... 75 [-64] dB  
 Operating Frequency Range ..... 35 - 100 kHz  
 Resonant Freq.  $V/(m/s)$ ;  $[V/\mu\text{bar}]$  ..... 55 [90] kHz  
 Directionality.....  $\pm 1.5$  dB

#### Environmental

Temperature Range ..... -65 to 175°C  
 Shock Limit ..... 500 g  
 Completely enclosed crystal for RFI/EMI immunity

#### Physical

Dimensions..... 0.75" dia. x 0.88" h (19 x 22.4 mm)  
 Weight ..... 38 grams  
 Case Material ..... Stainless Steel  
 Face Material ..... Ceramic  
 Connector ..... SMA  
 Connector Locations ..... Side  
 Seal ..... Epoxy  
 Sensor to Preamp Cable (1 or 2 meters) ..... 1232-X-SMA

### Ordering Information and Accessories

R6α ..... R6α or R6α  
 Magnetic Hold-Down ..... MHR15A  
 Preamplifier ..... 0/2/4, 2/4/6  
 Preamp to System Cable (specify length in meters) ..... 1234 - X

#### Sensors include

NIST Calibration Certificate & Warranty



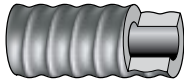
195 Clarksville Road, Princeton Junction, NJ 08550 • Phone: 609-716-4000

Fax: 609-716-0706 • Email: sales.systems@mistrasgroup.com • Internet: www.mistrasgroup.com

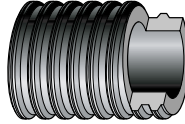


## DYWI® Drill Technical Data

### DYWI® Drill Rope Thread (R)



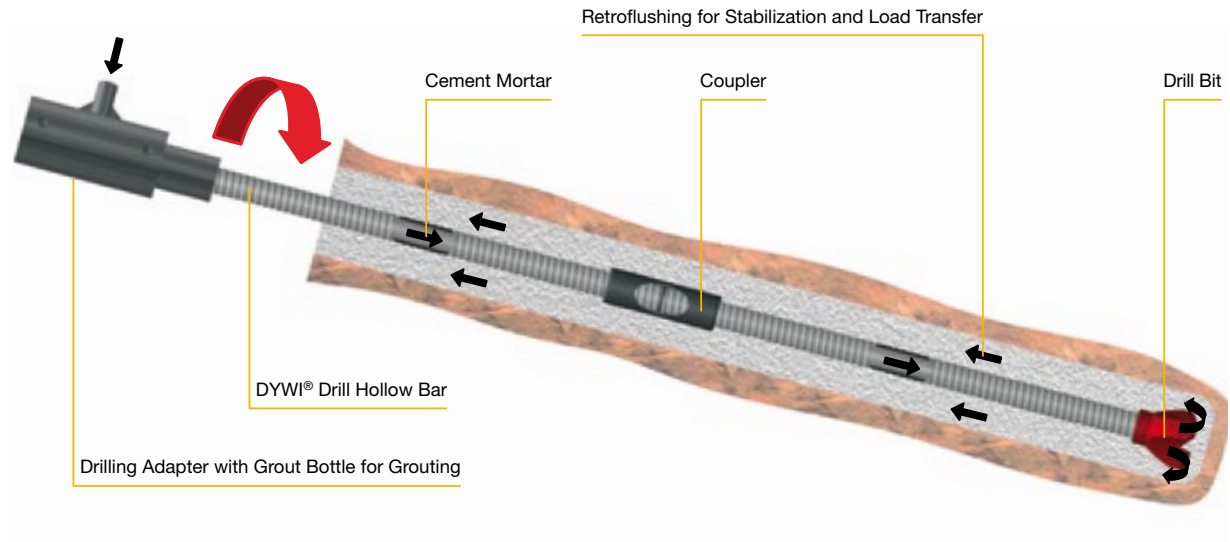
### DYWI® Drill "T" Thread



- Bar Finishes: Plain or Galvanized to EN 1461

E Value:

- Strain at Ultimate Load
- Fractile Value of Strain



### Technical Data

Type	Cross-sectional area A [mm <sup>2</sup> ]	Load at yield F <sub>yk</sub> [kN]	Ultimate load F <sub>tk</sub> [kN]	Weight [kg/m]	Approval
R32-210 (R32L)	340	160	210	2.65	○ × △
R32-250	370	190	250	2.90	○ × △
R32-280 (R32N)	410	220	280	3.20	○ × △
R32-320	470	250	320	3.70	○ × △
R32-360 (R32S)	510	280	360	4.00	○ × △
R32-400	560	330	400	4.40	○ × △
R38-420	660	350	420	5.15	○ × △
R38-500 (R38N)	750	400	500	5.85	○ × △
R38-550	800	450	550	6.25	○ × △
R51-550 (R51L)	890	450	550	6.95	○ × △
R51-660	970	540	660	7.65	○ × △
R51-800 (R51N)	1,150	640	800	9.00	○ × △
T76-1200 (T76L)	1,610	1,000	1,200	12.60	
T76-1600 (T76N)	1,990	1,200	1,600	15.60	
T76-1900 (T76S)	2,360	1,500	1,900	18.50	

Lengths of delivery L = 2/3/4/6m

○ Germany: Z-14.4-674 & Z-34.13-208  
 × Austria: BMVIT-327.120/0010-IV/ST2/2012  
 △ Europe: ETA-12/0603

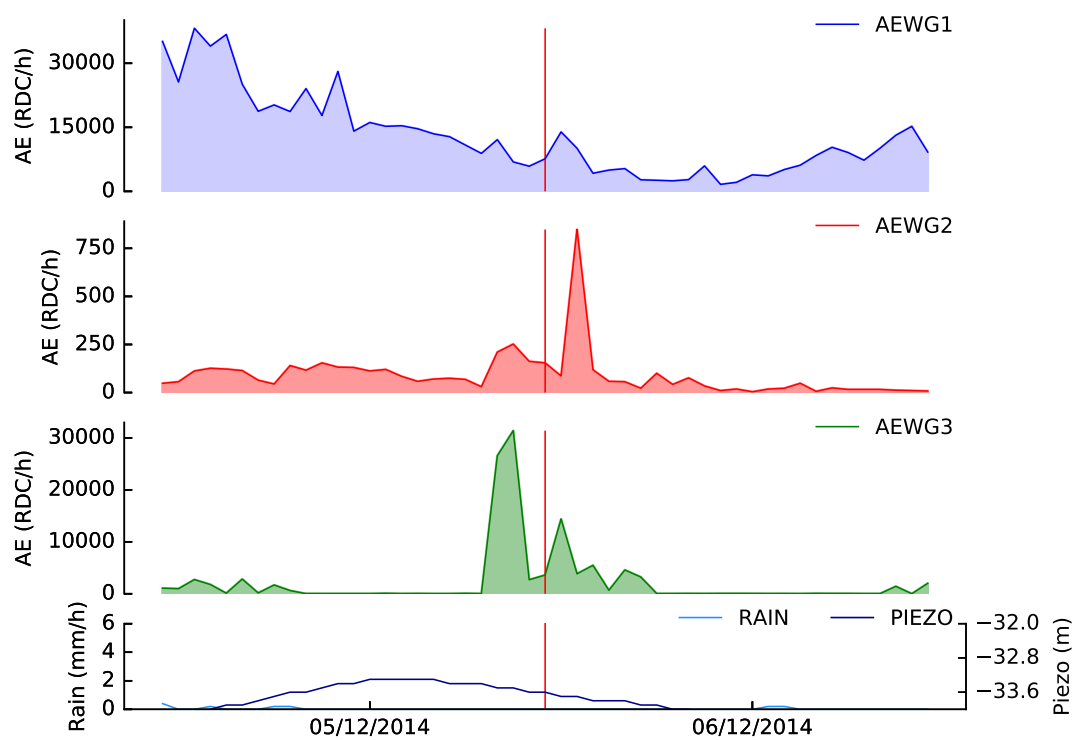
### Additional Information

German Approval DIBt Z-14.4-674 und Z-34.13-208 / Austrian Approval BMVIT-327.120/0010-IV/ST2/2012 / European Approval ETA-12/0603

# Appendix B

## Additional graphs

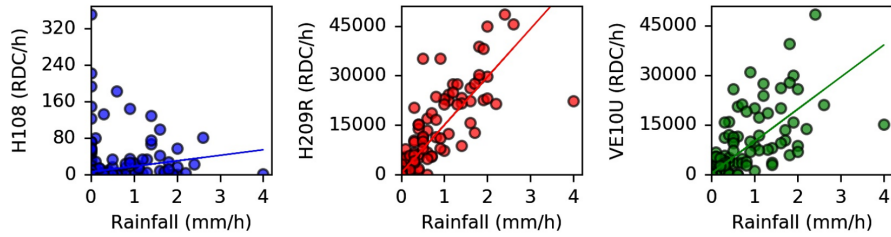
### PdM earthquake No.18



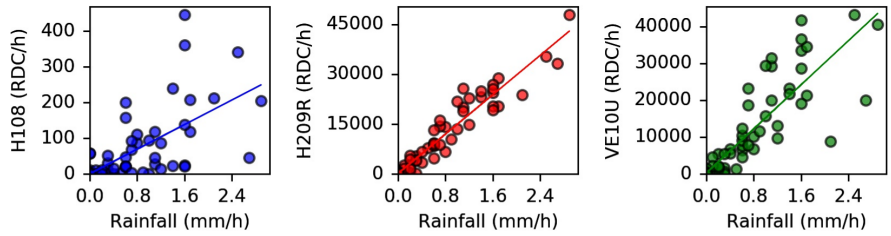
**Figure B.1:** The red line indicates the (rounded-up) time of earthquake No.18

# SART seepage events

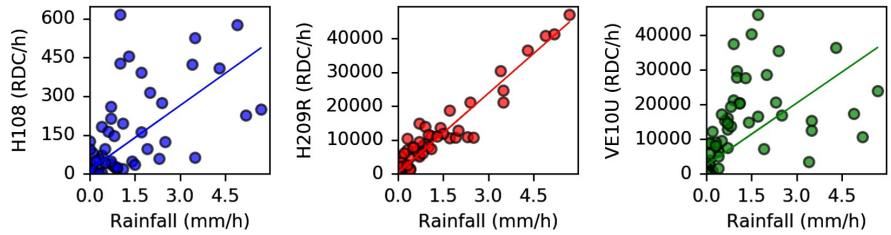
Event e06: 2015-10-04 to 2015-10-20



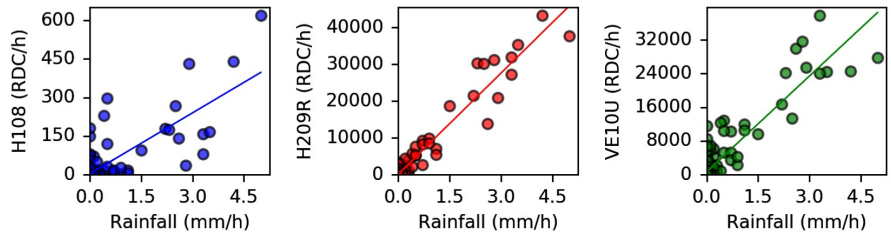
Event e07: 2015-11-29 to 2015-12-03



Event e08: 2016-01-29 to 2016-02-03



Event e09: 2016-02-15 to 2016-02-22



Event e10: 2016-04-16 to 2016-04-29

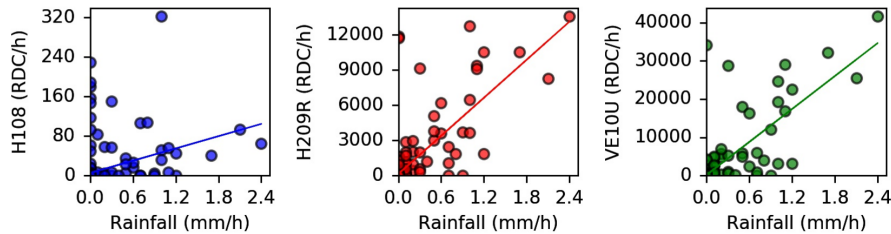


Figure B.2: SART seepage events

# Appendix C

## Additional tables

### PdM AE data distribution values

Series1	AEWG1	AEWG2	AEWG3
count	11262.000000	2185.000000	1293.000000
mean	96.504262	159.124027	3001.706110
std	540.623553	866.100798	10818.235367
min	1.000000	1.000000	1.000000
10%	1.000000	1.000000	1.000000
25%	4.000000	2.000000	3.000000
50%	14.000000	6.000000	13.000000
75%	48.750000	22.000000	77.000000
99%	1267.900000	3978.200000	56369.680000
max	19174.000000	14082.000000	163517.000000

Series 2	AEWG1	AEWG2	AEWG3
count	9750.000000	7485.000000	3312.000000
mean	5643.194564	630.389446	2892.198973
std	13236.185209	7432.065966	22063.118225
min	1.000000	1.000000	1.000000
10%	12.000000	2.000000	2.000000
25%	77.000000	4.000000	6.000000
50%	856.000000	16.000000	21.000000
75%	5587.750000	64.000000	104.000000
99%	69985.320000	5036.240000	98162.120000
max	252368.000000	266468.000000	489620.000000

## Test A - 1 second

MK2 RDC	MK1-WG1 RDC	MK1-WG2 RDC	MK1-WG3 RDC
31809	9766	24009	20792
31233	9528	22002	20762
31384	9472	22689	19581
31126	9274	20259	21064
31709	9031	21359	17515
31496	9244	21711	19319
31163	8708	22703	20075
31317	8835	22049	18932
30951	8540	22539	20642
30701	8951	22797	20704
32714	8426	21811	21141
31044	8478	20473	21890
30786	7999	22272	21143
30788	8005	24150	20157
30461	7461	20492	20811
32756	12529	22686	20573
32519	11592	20516	20536
30967	11295	20752	21338
30127	11578	20916	20722
32069	10657	22828	21228
31675	10556	23906	21135
31812	11057	22698	20346
30173	10990	21449	21661
29994	10509	21888	19805
29190	10497	23044	19559
31120	10405	23535	21826
31611	10626	21366	19141
31349	10328	19530	18856
31143	10412	20093	20276
31164	10491	23693	21072
31055	9787	22018	21686
31227	9950	22596	18302
29807	9995	22170	17850
30698	9539	21979	22039
30723	9656	24728	20155
31118	9879	21745	21247
29833	9241	21753	20827
28365	9293	23372	20451
29088	8993	22792	20419
30733	9184	22621	22334
28974	9258	21655	18302



30626	9150	22834	19413
30108	8949	23956	20503
30183	8861	22507	22989
30114	8987	25025	19213

---

## Test A - 10 seconds

MK2 RDC	MK1-WG1 RDC	MK1-WG2 RDC	MK1-WG3 RDC
235995	137447	180998	180267
212535	114795	198953	176872
217519	125083	187401	187814
218485	119718	181251	188700
220221	125161	185105	182865
220818	118192	183302	186099
222185	121273	195280	175476
224284	130544	193250	180485
225488	117997	199081	180308
225885	133464	189308	180584
226760	121330	178395	192022
229112	139370	186329	178112
229305	131667	186982	176456
229607	140261	185830	179409
240669	136699	192289	170413

---

## Test B - 1 second

B0 RDC	B1 RDC	B2 RDC	B3 RDC	B4 RDC	B5 RDC
33081	6321	2900	178	22446	14889
45104	3426	3144	236	22314	12636
42128	4431	3185	254	23237	16693
31878	2947	3382	364	21053	14385
37658	2948	3055	206	22230	14484
47925	5721	3306	185	23837	17810
40474	2792	2970	362	24194	15341
36437	2470	3511	230	23503	12095
51871	7144	2961	273	24384	11796
31518	7266	2683	195	25441	12007

## Test B - 10 seconds

B0 RDC	B1 RDC	B2 RDC	B3 RDC	B4 RDC	B5 RDC
117573	92246	94711	25262	190887	152328
246300	105785	77626	18327	214140	149478
226622	81122	65489	24702	231579	111274
168323	142344	75094	17747	182130	156192
202189	59610	75234	25145	187904	171026
215918	134768	95441	27056	226716	173047
224317	81632	98670	26861	155254	135177
167752	76827	87014	24600	218974	135519
153598	127105	78342	26992	157848	150985
250298	58361	83571	20534	217886	105345

## Test C

m	RDC
1.25	185940
1.25	159177
1.25	134936
1.25	135380
1.25	137877
2.25	158642
2.25	153857
2.25	152678
2.25	118276
2.25	131329
3.25	55560
3.25	60841
3.25	63981
3.25	80038
3.25	46453
4.25	66963
4.25	73041
4.25	70665
4.25	60274
4.25	41673
5.25	57263
5.25	88216
5.25	62796
5.25	82568
5.25	73032
6.25	45043
6.25	25555
6.25	28688
6.25	39532
6.25	15203
7.25	45764
7.25	68207
7.25	52235
7.25	33888
7.25	46930
8.25	28425
8.25	35654
8.25	28999
8.25	24434
8.25	17878
9.25	12522
9.25	38972

9.25	37827
9.25	17304
9.25	12986
10.25	2827
10.25	1444
10.25	1015
10.25	2452
10.25	1504
11.25	1306
11.25	277
11.25	992
11.25	1286
11.25	51

## Test D

m	AEWG1 RDC	AEWG2 RDC	AEWG3 RDC
0.2	101955	40151	49248
0.2	120851	43755	59932
0.2	122531	62107	70747
0.2	136195	89092	79254
0.2	137725	104330	59614
0.2	138180	105643	-
0.2	141881	108707	-
0.2	146318	113577	-
0.2	147331	120429	-
0.2	149915	126560	-
0.3	61565	80711	32082
0.3	65373	98608	40174
0.3	65984	101347	62267
0.3	67658	102333	62685
0.3	71798	112058	69807
0.3	80355	117042	70518
0.3	84099	122175	97357
0.3	93673	123249	99946
0.3	94904	127027	109303
0.3	99136	136904	120148
0.4	4730	6460	6602
0.4	10821	7417	7649
0.4	12494	8161	8785

0.4	13545	34946	9179
0.4	13635	35012	10668
0.4	14846	35639	10792
0.4	17236	43037	11317
0.4	17812	53387	12637
0.4	21047	55522	13274
0.4	21264	58609	13492
0.5	81	5034	106
0.5	145	6080	625
0.5	155	9870	679
0.5	488	12163	895
0.5	610	18196	2174
0.5	694	23877	2360
0.5	1029	25819	2389
0.5	1186	32958	4308
0.5	1881	38120	11284
0.5	1993	69837	-
1	0	230	-
1	84	354	-
1	95	634	-
1	109	1074	-
1	0	1164	-
1	0	2915	-
1	-	5666	-
1	-	6739	-
1	-	10330	-
1	-	30911	-
1.1	-	0	-
1.1	-	0	-

---

## Test E

Location	m	RDC
E1	0.3	259
E1	0.3	315
E1	0.3	419
E1	0.3	299
E1	0.3	464
E2	0.6	90
E2	0.6	187
E2	0.6	47
E2	0.6	157
E2	0.6	121
E3	1.1	12
E3	1.1	0
E3	1.1	0
E3	1.1	5
E3	1.1	0

## Test F1

	H108L	H209R	VE10U
seconds	RDC	RDC	RDC
0	0	0	0
5	97	24	0
10	6711	1617	0
15	1843	11005	0
20	21775	13744	0
25	14716	33322	0
30	33816	36450	0
35	12949	5065	0
40	3753	31804	0
45	9296	25398	0
50	1338	30490	0
55	778	30557	0
60	1664	9471	0
65	418	12669	0
70	1552	18145	0
75	6711	1238	0
80	1130	12476	0
85	24115	24769	0
90	11259	2902	0

95	10247	28853	0
100	16771	32017	0
105	5867	1815	0
110	598	1522	0
115	4771	3734	0
120	14773	2883	0

## Test F2

Part	H108L	H209R	VE10U
A	1589	3391	206
A	1907	2032	152
A	3154	2910	89
B	11	47	241
B	168	139	5
B	209	37	59

## Test F3

kg	RDC
10	0
10	0
10	0
10	0
10	0
60	0
60	0
60	0
60	0
60	0
80	0
80	0
80	0
80	0
80	0

# Appendix D

## Coding

Python version used: 2.7.11

List of modules used and their version: geopy 1.11.0, matplotlib 2.0.0rc2, numpy 1.11.0, pandas 0.19.2, python-dateutil 2.5.1, scipy 0.17.0

### PdM – Percentage of monitoring periods equal to 0 RDC/h

```
1 # coding: utf-8
2 import pandas as pd
3
4 db = pd.read_csv('pdm_data.csv', parse_dates=['datetime'], dayfirst=True,
5                 index_col='datetime', usecols=['datetime', 'AEWG1', 'AEWG2', 'AEWG3'])
6
7 df1 = db['2010-12-17': '2014-08-07']
8 df2 = db['2011-09-28': '2014-10-13']
9 df3 = db['2012-10-13': '2014-10-13']
10 df4 = db['2014-10-14': '2016-12-31']
11
12 def zeroes(df, sensor):
13     z = (df[sensor]==0).sum()
14     c = df[sensor].count()
15     p = float(z)/c
16     print round(p,2)
17
18 zeroes(df1, 'AEWG1') # Series 1, AEWG1
19 zeroes(df2, 'AEWG2') # Series 1, AEWG2
20 zeroes(df3, 'AEWG3') # Series 1, AEWG3
21 zeroes(df4, 'AEWG1') # Series 2, AEWG1
22 zeroes(df4, 'AEWG2') # Series 2, AEWG2
```



```

22 zeroes(df4, 'AEWG3') # Series 2, AEWG3
23
24 # ----- END of SCRIPT ----- #

```

## PdM – Daily and weekly trends

```

1 # coding: utf-8
2 import pandas as pd
3 import numpy as np
4 import datetime
5
6 db = pd.read_csv('pdm_data.csv', dayfirst=True, parse_dates=['datetime'],
7                 usecols=['datetime', 'AEWG1', 'AEWG2', 'AEWG3'],
8                 index_col='datetime')
9
10 # Select data from MK2 installation to tunnel closure & greater than 0 RDC/h
11 data = db.loc['2014-10-13_20:00:00': '2016-06-20_12:00:00']
12 data = data[data>0]
13
14 def extract_counts(df):
15     a,b,c = df['AEWG1', 'count'], df['AEWG2', 'count'], df['AEWG3', 'count']
16     return pd.DataFrame({'AEWG1':a, 'AEWG2':b, 'AEWG3':c})
17
18 # Daily trends
19 df = pd.DataFrame()
20 df = data.groupby([data.index.hour]).describe().unstack(level=1)
21 df1 = extract_counts(df)
22 df1.to_csv('ch4_dailyweekly1.csv', sep='\t')
23
24 # Weekly trends
25 df = pd.DataFrame()
26 df = data.groupby([data.index.weekday]).describe().unstack(level=1)
27 df1 = extract_counts(df)
28 df1.to_csv('ch4_dailyweekly2.csv', sep='\t')
29
30 # ----- END of SCRIPT ----- #

```

## PdM – Piezo events selection

```

1 # coding: utf-8
2 import pandas as pd
3 df = pd.read_csv('pdm_data.csv', parse_dates=['datetime'], dayfirst=True,
4                 index_col='datetime', usecols=['datetime', 'AEWG1', 'AEWG2',

```

```

5         'AEWG3', 'precip[mm]', 'PIEZ0-P22[m]'])
6
7 events = [
8     {'id': '01', 'xmin': '2014-11-05', 'xmax': '2014-12-15'},
9     {'id': '02', 'xmin': '2015-03-20', 'xmax': '2015-04-09'},
10    {'id': '03', 'xmin': '2015-05-12', 'xmax': '2015-05-19'},
11    {'id': '04', 'xmin': '2015-05-19', 'xmax': '2015-05-29'},
12    {'id': '05', 'xmin': '2015-06-14', 'xmax': '2015-06-30'},
13    {'id': '06', 'xmin': '2015-10-13', 'xmax': '2015-10-28'},
14    {'id': '07', 'xmin': '2016-02-27', 'xmax': '2016-03-18'},
15    {'id': '08', 'xmin': '2016-04-08', 'xmax': '2016-04-15'},
16    {'id': '09', 'xmin': '2016-04-18', 'xmax': '2016-04-22'},
17 ]
18
19 df1 = pd.DataFrame()
20 for e in events:
21     df1 = df1.append(df[e['xmin']:e['xmax']])
22
23 df1.to_csv('ch4_piezo_events.csv')
24
25 # ----- END of SCRIPT ----- #

```

## PdM – Earthquake events selection

```

1 # coding: utf-8
2 import pandas as pd
3 import datetime
4 from datetime import timedelta
5 from geopy.distance import great_circle
6
7 # Define rule for rounding to next hour
8 def round_to_hour(t):
9     delta = datetime.timedelta(minutes=t.minute%60,
10                               seconds=t.second,
11                               microseconds=t.microsecond)
12     t -= delta
13     if delta >= datetime.timedelta(minutes=0):
14         t += datetime.timedelta(minutes=60)
15     return t
16
17 # Earthquake data source: CRS-OGS staff (2013). Real Time Seismology of
18   the OGS Seismological Research Centre website (http://rts.crs.inogs.it)
19 # Research keys used:
20 # Lon [min, max] = [12.3767,13.0285]
21 # Lat [min, max] = [46.1730,46.6226]

```

```

21 # Mag [min, max] = [1,10]
22 # Beginning,end = '2010-12-17','2016-01-10'
23
24 ogs = pd.read_csv('OGS_data.csv', parse_dates=['Date'], dayfirst=True,
                    usecols={'Event_id','Date','Lat','Lon','Mag'}, index_col=False)
25 ogs.rename(columns={'Event_id':'EventID_OGS','Date':'Time(UTC)'},
             inplace=True)
26 ogs.drop_duplicates(subset=['Time(UTC)','Mag'], keep='last', inplace=True)
27 ogs['No.'] = ogs.index+1
28 ogs.set_index('EventID_OGS', inplace=True)
29
30 # Open Acoustic Emission data file
31 rdc = pd.read_csv('pdm_data.csv', parse_dates=['datetime'], dayfirst=True,
                    usecols=['datetime','AEWG1','AEWG2','AEWG3'], index_col='datetime')
32
33 # Calculate distance from Passo della Morte
34 pdm = (46.3978,12.7026)
35 index,lats,lons = ogs.index,ogs['Lat'],ogs['Lon']
36 for i,lat,lon in zip(index,lats,lons):
37     ptx = (lat, lon)
38     ogs.loc[i,'Distance(Km)'] = round((great_circle(pdm, ptx).km),1)
39
40 # Make a selection (ML >=2.5 and Distance <=20Km)
41 ogs = ogs[(ogs['Mag']>=2.5) & (ogs['Distance(Km)']<=20)]
42
43 # Convert time from UTC to Central European Time (UTC+1)
44 ogs['Time(UTC+01)'] = ogs['Time(UTC)']+datetime.timedelta(hours=1)
45 ogs.drop('Time(UTC)', axis=1, inplace=True)
46
47 # Round time to next hour
48 index = ogs.index
49 time = ogs['Time(UTC+01)']
50 for i,times in zip(index,time):
51     ogs.loc[i,'Time_round'] = round_to_hour(times)
52
53 # Extract corresponding RDC values
54 df = pd.DataFrame(columns=('AEWG1','AEWG2','AEWG3'))
55 time = ogs['Time_round']
56 for times in time:
57     df.loc[times] = rdc.loc[times]
58 ogs = ogs.merge(df, how='inner', left_on='Time_round', right_index=True)
59
60 ogs.sort_values('Time(UTC+01)')
61 ogs = ogs.reset_index()
62
63 ogs['No.'] = ogs.index+1

```

```

64
65 cols = list(ogs)
66 cols.insert(0, cols.pop(cols.index('No.')))
67 ogs = ogs.ix[:, cols]
68
69 # Save file
70 ogs.to_csv('ch4_earthquakes.csv', sep='\t', index=False)
71
72 # ----- END of SCRIPT ----- #

```

## SART – Seepage events

```

1 # coding: utf-8
2 import numpy as np
3 import pandas as pd
4 import matplotlib.pyplot as plt
5 import matplotlib.gridspec as gridspec
6 from mpl_toolkits.axes_grid1 import host_subplot
7 import mpl_toolkits.axisartist as AA
8 from matplotlib.ticker import MaxNLocator
9
10 # Define events dates
11 events = [
12     {'id': '01', 'xmin': '2015-09-02', 'xmax': '2015-09-09'},
13     {'id': '02', 'xmin': '2015-09-23', 'xmax': '2015-09-27'},
14     {'id': '03', 'xmin': '2015-10-04', 'xmax': '2015-10-20'},
15     {'id': '04', 'xmin': '2015-11-29', 'xmax': '2015-12-02'},
16     {'id': '05', 'xmin': '2016-01-29', 'xmax': '2016-02-04'},
17     {'id': '06', 'xmin': '2016-02-15', 'xmax': '2016-02-22'},
18     {'id': '07', 'xmin': '2016-04-16', 'xmax': '2016-04-29'},
19     {'id': '08', 'xmin': '2016-05-01', 'xmax': '2016-05-06'},
20     {'id': '09', 'xmin': '2016-05-12', 'xmax': '2016-05-21'},
21 ]
22
23 df1 = pd.DataFrame()
24 for e in events:
25     df1 = df1.append(df[e['xmin']:e['xmax']])
26
27 df1.to_csv('ch5_seepage_events.csv')
28
29 # ----- END of SCRIPT ----- #

```